Design Characterization of Newly Developed 3-Fluid Gas-Liquid Contactor for Liquid Desiccant Air Conditioning Systems with Ionic Liquid

イオン流体を活用したリキッドデシカント調湿空調システム用３流体気液接触器の開発と設計手法に関する研究

July 2020

Richard Jayson VARELA

ヴァレラ　リチャード　ジェイソン

Design Characterization of Newly Developed 3-Fluid Gas-Liquid Contactor for Liquid Desiccant Air Conditioning Systems with Ionic Liquid

イオン流体を活用したリキッドデシカント調湿空調システム用３流体気液接触器の開発と設計手法に関する研究

July 2020

Waseda University

Graduate School of Fundamental Science and Engineering

Department of Applied Mechanics

Research on Dynamics and Control of Mechanical Systems

Richard Jayson VARELA

ヴァレラ　リチャード　ジェイソン

Abstract

Due to global warming, global temperature readings are rising steadily. As a result, air conditioners are becoming a necessity in countries located in the tropical and subtropical zones but also those situated in the temperate zone. This consequently results in the extensive use of air conditioning systems. Conventional air conditioners use the vapor compression cycle to accomplish air cooling and dehumidification. This method of achieving cooling and dehumidification effect consumes an intensive amount of energy due to the deep cooling of the inlet air and reheating. It can be concluded that even though the vapor compression system is the widely used air conditioning technology, it is inefficient and contributes to high power generation, which can lead to high greenhouse gas emission and intensify global warming.

In order to prevent global warming, several countries have agreed to reduce greenhouse gas emissions by 80% by 2050. Japan is aiming for net-zero carbon dioxide emissions by 2050. The motivation of this research comes from using innovative and energy-efficient technologies in line with the drive of several international treaties to address critical environmental problems. One of the promising air conditioning alternatives which can address the inefficient dehumidification process of the vapor compression system is the liquid desiccant air conditioning system. This innovative technology is an open-cycle system and employs gas separation to efficiently dehumidify the supply air. Using this approach gives the advantage of direct and precise control of humidity in the air. The simultaneous temperature and humidity control in this system eliminate not only the energy used for deep cooling but also that for sensible heating. Moreover, the salt solutions used as liquid desiccants naturally disinfects the air from microbiological organisms such as bacteria and viruses. This is particularly essential as different kinds of viruses are becoming capable of causing a pandemic such as the current coronavirus. The liquid desiccant air conditioning system can assure as of a clean and better-quality air now and in the coming generations. However, the liquid desiccant air conditioning system is still a developing technology, and design control and optimization of this system are highly necessary considering relevant influencing factors.

Generally, there are two types of gas-liquid contactors: these are the 2-fluid and the 3-fluid gas-liquid contactors. An example of a 2-fluid gas-liquid contactor is the packed bed and for the 3-fluid gas-liquid contactor an example is the fin-tube gas-liquid contactor. The 3-fluid gas-liquid contactor is highly favored over the conventional 2-fluid gas-liquid contactors due to their capability to maintain high heat and mass transfer potential between the air and the liquid desiccant solution owing to the third fluid. However, 3-fluid gas-liquid contactors have limited application due to the corrosion property of commonly used liquid desiccants. If a non-corrosive liquid desiccant is developed, 3-fluid gas-liquid contactors made of high thermal conductivity metals would

be possible. This study introduces a new liquid desiccant that is not corrosive to aluminum. On the other hand, the physical phenomena in a 3-fluid gas-liquid contactor are more complicated compared to that of a 2-fluid gas-liquid contactor. For example, in the fin-tube gas-liquid contactor, the complex phenomenon of partial wetting occurs which has not been conclusively studied in previous literature. In the absence of information on the wetting characteristics and partial wetting of a liquid desiccant on the surface of a gas-liquid contactor, complete wetting of the contactor area is assumed in falling film models. The assumption of complete wetting remains to be a problem due to a lack of conclusive research and mathematical model for the partial wetting in falling film devices.

This research aims to clarify the wetting phenomenon of the new liquid desiccant on an aluminum fin-tube substrate, including other phenomena such as contact angle and wetting hysteresis, and derive a model for the partial wetting in 3-fluid gas-liquid contactors to more accurately predict, control, and optimize 3-fluid liquid desiccant air conditioning systems. With the partial wetting model, the other objective of this study is to develop a mathematical model for the heat, mass, and momentum transfer inside the 3-fluid gas-liquid contactor considering the effect of partial wetting. Another goal of this study is to improve the performance of the gas-liquid contactor by optimizing its size and structure. Part of this goal is aimed at clarifying the effect of the physical dimensions of the contactor, which is the length, height, and width, on the dehumidification performance and air pressure drop.

It was clarified that increasing the length, the height, or the width decreases the outlet air humidity ratio and outlet air temperature due to the increase in transfer area and contact time. On the other hand, increasing the length of the contactor increases the air pressure drop while increasing both the height and the width decreases the air pressure drop. A performance comparison between a 3-fluid gas-liquid contactor and a conventional 2-fluid gas-liquid contactor was carried out to clarify the advantage of the 3-fluid gas-liquid contactor. A size reduction of about 56% was obtained from the 3-fluid gas-liquid contactor in obtaining the smallest outlet air humidity ratio obtained by the 2-fluid gas-liquid contactor.

To summarize, due to the additional cooling medium, the superior performance of the 3-fluid gas-liquid contactor is proven over the conventional 2-fluid gas-liquid contactor. In addition, the partial wetting model is very useful for predicting more realistic heat, mass, and momentum transfer inside the gas-liquid contactor. With these, the liquid desiccant air conditioning system becomes a more competitive alternative to the conventional vapor compression air conditioning system. These achievements will greatly contribute to the progress of refrigeration and air conditioning engineering, thermal engineering, and mass transfer engineering.

Acknowledgment

This doctoral thesis would not have been possible without the help and support of many for whom I would like to express my sincere gratitude.

I would like to thank Dr. Nicanor Buenconsejo Jr. for his encouragement and assistance in my application for the Ministry of Education, Culture, Sports, Science and Technology (MEXT) scholarship. I am also grateful to Dr. Edwin Carcasona for his unconditional help in my application for the MEXT scholarship. My doctoral study in Japan would have not been possible without the firsthand support from the Japanese government.

I am deeply indebted to my supervisor, Prof. Kiyoshi Saito, for his guidance, advice, and financial support during the final years of my study. The success of this research study has been possible with his polishing and financial support after my scholarship.

I would like to thank Assoc. Prof. Seiichi Yamaguchi for the guidance and advice he has provided me. His knowledge and expertise on the field became the foundation of the humble beginnings of this work. I would also like to express my heartfelt gratitude to Asst. Prof. Niccolo Giannetti for his ideas and the many interesting discussions we have shared. I greatly appreciate the support and friendship that he has shared with me and my family.

I would like to thank the members of the Steering Committee, Prof. Emeritus Masafumi Katsuta, Assoc. Prof. Hiroshi Muto, and Prof. Yoshimura Amano, for their valuable comments and suggestions which have greatly improved the content of this thesis.

I would like to extend my appreciation to those who have been part of the desiccant team, namely Mr. Ota, Mr. Kobayashi, Mr. Uzusaka, Mr. Sato, Ms. Inui, Mr. Ogiwara, Ms. Chen, Mr. Hosho for their help in the construction of the experimental rigs and on the experimental work.

I wish to thank the staff of Saito Laboratory, Ms. Osaki and Ms. Kochi, for their help and patience with all the bureaucratic work and Japanese language translation.

I am extremely grateful to my loving wife, Engr. Daryl Anne, for her never-ending support, help, sacrifices, encouragement, and prayers. Without these, my whole doctoral study would not have been possible or exceedingly difficult emotionally.

I would like to express my appreciation to my fellow laboratory members and friends, Dr. Ohno, Mr. Ikumi, Dr. Jeong, Dr. Miyaoka, Mr. Nishiyama, Dr. Kimura, Dr. Arnas and Mirta, Lisa, Engr. Mark, Sholahudin, Engr. Carlo, Dr. Hifni, Dr. Yulianto, and Dr. Kim for their helpful ideas, support, and encouragement. The same goes for all the people that I have had an opportunity to meet, share thoughts, collaborate, and made this experience enjoyable and memorable.

I would like to thank my immediate family and my in-laws for the support, prayers, and for always making me and my family feel at home every time we go to the Philippines.

Above all, I would like to thank and praise the All-Knowing God for guiding me and giving me the strength to make this endeavor a success.

Dedication

I wholeheartedly dedicate this doctoral thesis to my wife, Daryl Anne, for her unfaltering love, support, and patience while I was working on this study which resulted in this humble fruit.

I, with my wife, also dedicate this work to my daughters Rianne Jayne and Danielle Akira, who have served as my inspiration and strength in this challenging but memorable journey.

Table of Contents

Chapter
1. Introduction……..……..……..18
1.1 Importance of the research……..……...……...…..18
1.2 Research background……..……...……..……..20
1.3 Previous research and problems…..……...…….....24
1.3.1 Corrosivity of liquid desiccants…….……...…….…24
1.3.2 Large and expensive components……..26
1.3.3 Limited overall research…….……...27
1.4 Research objectives……..……...…….……..30
1.5 Thesis outline……...……..…30

2. System and component description……..33
2.1 Introduction……...33
2.2 Conventional liquid desiccant air conditioning system…….….33
2.3 Liquid desiccant……34
2.4 Gas-liquid contactor……..36
2.5 New liquid desiccant air conditioning system……37
2.5.1 New Ionic Liquid…….38
2.5.2 New 3-fluid gas-liquid contactor…….39

3. Model conceptualization…….…….……42
3.1 Introduction……...42
3.2 Film wetting phenomena……...42
3.2.1 Theoretical formulation……...43
3.2.2 Direct observation from experiments……..43
3.2.3 Development of a semi-theoretical model……...44
3.3 Transport phenomena…….…….…….…….44
3.3.1 Heat, mass, and momentum transfer……44
3.3.2 Whole device model validation……...45
3.3.3 Performance analysis and volume minimization…….45

4. Falling film partial wetting model…….…...46
4.1 Introduction……...46
4.2 Importance of partial wetting model…..……46
4.3 Modeling approach…….…….…….…….47
4.4 Theoretical modeling…….48

5. Experiment and validation of the partial wetting model……...60

5.1 Introduction……..…….…..60
5.2 Experimental investigation of the wetting characteristics of the new IL……60
5.2.1 Experimental apparatus and procedures…….60
5.2.2 Visualization and analysis of the surface wetting……...64
5.2.3 Contact angle and contact angle hysteresis……68
5.2.4 Wetting hysteresis……..73
5.3 Validation of the theoretical partial wetting model…….…….…….…77

6. Semi-theoretical partial wetting model…….84
6.1 Introduction……...……..…..84
6.2 Semi-theoretical formulation…….....84
6.3 Prediction of the wetting ratio using the semi-theoretical model…….....85

7. Gas-liquid contactor model…….…….88
7.1 Introduction……...……..…..88
7.2 3-Fluid gas-liquid contactor model……88
7.2.1 Heat, mass, and momentum transfer geometry…….....89
7.2.2 Assumptions……..90
7.2.3 Governing equations……..90
7.2.4 Initial and boundary conditions……..98
7.2.5 Heat and mass transfer coefficients……99
7.2.6 Air pressure drop……..……102
7.2.7 Numerical analysis……..…….103

8. Experiment and validation of the 3-fluid gas-liquid contactor model…..…….....105
8.1 Introduction……...…….....105
8.2 Fin-tube liquid desiccant air conditioning system..…….....105
8.2.1 Experimental apparatus…….....105
8.2.2 Experimental results……..……..……109
8.2.3 Performance comparison between the new 3-fluid gas-liquid contactor and conventional packed bed contactor…….....111

9. Performance analysis of the 3-fluid gas-liquid contactor..…….....115
9.1 Introduction……115
9.2 Validation of the 3-fluid gas-liquid contactor model……...115
9.3 Parametric study and design characterization...…….....117
9.3.1 Effect of the gas-liquid contactor length...…….....118
9.3.2 Effect of the gas-liquid contactor height...…….....119
9.3.3 Effect of the gas-liquid contactor width……...121

9.4 Optimization……...123
9.4.1 Objective function……...123
9.4.2 Design parameters……...124
9.4.3 Constraint conditions……...124
9.4.4 Optimization method……...125
9.5 Optimization results……..128
9.5.1 Contactor size optimization at various air flow rates……128
9.5.2 Contactor size optimization at various inlet air humidity ratio……132
9.6 Advantage of the 3-fluid gas-liquid contactor…….....135

10. Conclusions and future plan……137
10.1 Conclusions……..……137
10.2 Future plan……..……..138

References……...……..139

Appendix……...148
1. Packed bed gas-liquid contactor model……..148
1.1 Simplified geometry for the air channel…..……148
1.2 Assumptions……149
1.3 Governing equations……...…….……..……..149
1.4 Initial conditions……..153
1.5 Heat and mass transfer coefficients……..153
1.6 Air pressure drop……156
1.7 Numerical analysis……..157

2. Experiment and validation of the packed bed gas-liquid contactor…...…….....159
2.1 Experimental apparatus…...……159
2.2 Experimental results……162
2.3 Effect of air flow rate on the overall heat and mass transfer coefficients……..164
2.4 Effect of air flow rate on the outlet air humidity ratio and temperature……165
2.5 Effect of solution flow rate on the overall heat and mass transfer coefficients….167
2.6 Effect of solution flow rate on the outlet air humidity ratio and temperature……168

3. Source code of the 3-fluid gas-liquid contactor……171

List of Figures

Fig. 1.1 Global temperature anomaly: (a) 1880 – 1884 and (b) 2015 – 2019[1)].....19
Fig. 1.2 Schematic diagram for a typical vapor compression cycle.....20
Fig. 1.3 Illustration of the air processes in a vapor compression system in a psychrometric chart.....21
Fig. 1.4 Comparison of the psychrometric processes between the vapor compression system and desiccant air conditioning system.....23
Fig. 1.5 Dehumidification and cooling in a typical liquid desiccant air conditioning system.....23
Fig. 1.6 (a) packed bed (2-fluid gas-liquid contactor), (b) fin-tube[9)] (3-fluid gas-liquid contactor).....24
Fig. 1.7 Packed bed-tube gas-liquid contactor[23)].....26
Fig. 1.8 General classifications of the decision variables selected for the optimization of liquid desiccant systems.....29

Fig. 2.1 Schematic diagram of a conventional 2-fluid liquid desiccant air conditioning system.....34
Fig. 2.2 Example of a 2-fluid gas-liquid contactor.....36
Fig. 2.3 Three main types of 3-fluid gas-liquid contactor[72)].....37
Fig. 2.4 Schematic diagram of an advanced 3-fluid liquid desiccant air conditioning system.....38
Fig. 2.5 Newly developed ionic liquid.....39
Fig. 2.6 New 3-fluid gas-liquid contactor made of aluminum.....40
Fig. 2.7 Single tube element of the 3-fluid gas-liquid contactor.....41

Fig. 3.1 Wetting phenomena, showing partial wetting, on the surface of a fin-tube substrate.....43
Fig. 3.2 Schematic diagram of the coupled heat and mass transfer between the gas and the liquid phases an (a) wetted wall and heat transfer on a (b) dry wall.....45

Fig. 4.1 Partial wetting on a flat vertical surface.....46
Fig. 4.2 Schematic of the 3-fluid gas-liquid contactor (left) and partial wetting on the surface of the fin-tube substrate (right).....47
Fig. 4.3 Schematic of the rivulet configuration along a fin-tube substrate.....49
Fig. 4.4 Representation of the advancing contact angle of the rivulet due to increasing flow rate.....54

Fig. 4.5 Specific energy per unit stream-wise length [J·m^{-2}] of pure water rivulet and uniform film configurations as a function of film Reynolds number; T=25°C, (a) decreasing ($\theta_0 = \theta_R$) and (b) increasing ($\theta_0 = \theta_A$) liquid flow rates.....55
Fig. 4.6 Specific energy per unit width and per unit stream-wise length [J·m^{-2}] of a pure water rivulet on a vertical fin-tube substrate. T=25°C, for (a) decreasing ($\theta_0 = \theta_R$) and (b) increasing ($\theta_0 = \theta_A$) liquid flow rates.....56
Fig. 4.7 Simulated local wetting behavior of pure water on a vertical fin-tube substrate. T=25°C, for (a) decreasing ($\theta_0 = \theta_R$) and (b) increasing ($\theta_0 = \theta_A$) liquid flow rates.....58
Fig. 4.8 Global wetting behavior of water on a vertical fin-tube substrate, T=25°C.....59

Fig. 5.1 (a) Photo and (b) schematic diagram of the visualization apparatus.....61
Fig. 5.2 (a) Photo of the single aluminum fin with tubes, (b) tube horizontal and vertical pitch, and (c) tube outer diameter.....61
Fig. 5.3 (a) Phot of the distributor and (b) illustration of the distributor cross-section.....62
Fig. 5.4 Image processing output: (a) raw, (b) cropped, (c) wetted area traced, (d) dry areas removed, and (e) tube areas removed.....63
Fig. 5.5 Surface wetting at 0% IL mass fraction for gradually increasing (→) and decreasing (←) solution flow rates.....65
Fig. 5.6 Surface wetting at 34% IL mass fraction for gradually increasing (→) and decreasing (←) solution flow rates.....65
Fig. 5.7 Surface wetting at 45% IL mass fraction 66
Fig. 5.8 Surface wetting at 60% IL mass fraction 67
Fig. 5.9 Surface wetting at 75% IL mass fraction …….....67
Fig. 5.10 Illustration of the (a) static and (b) dynamic contact angles of water on an aluminum plate.....69
Fig. 5.11 Contact angle (static and dynamic) meter.....70
Fig. 5.12 Graphical illustration of the contact angles (static θ_S, advancing θ_A, receding θ_R, and hysteresis θ_H) of the IL solution on an aluminum plate.....71
Fig. 5.13 Comparison between the experimental data and predicted results of the advancing and receding contact angle.....71
Fig. 5.14 Computer Numerical Control surface roughness tester.....73
Fig. 5.15 Wetting ratio of the IL solution on the aluminum substrate as a function of solution mass flow rate: (a) 0%, (b) 34%, 45%, 60%, and 75% IL mass fraction.....76
Fig. 5.16 Specific energy per unit stream-wise length [J·m^{-2}] of rivulet and uniform film configurations as a function of film Reynolds number; T = 34°C, X_{IL} = 34%, for (a) decreasing ($\theta_0 = \theta_R$) and (b) increasing ($\theta_0 = \theta_A$) liquid flow rates.....78
Fig. 5.17 Specific energy per unit width and per unit stream-wise length [J·m^{-2}] of an ionic liquid flow on a vertical aluminum fin of an internally-cooled contactor. T = 34°C, X_{IL} = 34%, as a function of the wetting ratio WR for (a) decreasing ($\theta_0 = \theta_R$) and (b) increasing ($\theta_0 = \theta_A$) liquid flow rates……79

Fig. 5.18 Comparison between theoretical predictions (using Eq. (4.18)) and experimental results for the wetting ratio of water on the fin-tube.....80
Fig. 5.19 Comparison between theoretical predictions (using Eq. (4.18)) and experimental results for the wetting ratio on the fin-tube substrate: (a) 34%, (b) 45%, (c) 60%, and (d) 75% IL mass fraction.....83

Fig. 6.1 Comparison between predictions (using Eq. (6.5)) and experimental results for the wetting ratio on the fin-tube substrate: (a) 34%, (b) 45%, (c) 60%, and (d) 75% IL mass fraction.....87

Fig. 7.1 (a) Illustration of the elemental control volume, (b) front view of the control volume, (c) side view of the control volume.....89
Fig. 7.2 Heat and mass transfers on a: (a) horizontal tube, and (b) vertical fin.....90
Fig. 7.3 Schematic diagram of the heat and mass transfer flows on a: (a) wetted wall and (b) dry wall.....91
Fig. 7.4 Schematic diagram of the heat and mass transfer flow with equivalent moisture circuit for mass diffusion.....92
Fig. 7.5 Schematic diagram of the heat and mass transfer flow with equivalent thermal circuits on wet and dry walls.....94
Fig. 7.6 (a) 3-Fluid gas-liquid contactor, (b) front view of control volume, and (c) side view of the control volume.....104

Fig. 8.1 Photo of the experimental apparatus.....106
Fig. 8.2 Schematic diagram of the 3-fluid liquid desiccant air conditioning system.....106
Fig. 8.3 Photo of the 3-fluid gas-liquid contactor: (a) isometric, (b) front, (c) side, and (c) back views.....108
Fig. 8.4 Construction of the 3-fluid contactor: (a) tube details and (b) fin details.....108
Fig. 8.5 Dehumidification performance comparison between the 3-fluid and packed bed liquid desiccant air conditioning system.....112
Fig. 8.6 Air pressure drop comparison between the 3-fluid gas-liquid and packed bed contactors.....113
Fig. 8.7 Air pressure drop though fin-tube contactor as the air velocity increases.....114

Fig. 9.1 Comparison between the experimental data and predicted results for the: (a) outlet air humidity ratio and (b) outlet air temperature from the 3-fluid liquid desiccant system.....116
Fig. 9.2 Comparison between the experimental data and predicted air pressure drop.....117
Fig. 9.3 Effect of the contactor length on the: (a) outlet air humidity ratio, (b) air pressure drop, and (c) wetting ratio.....119

Fig. 9.4 Effect of the contactor height on the: a) outlet air humidity ratio, (b) air pressure drop, and (c) wetting ratio.....121
Fig. 9.5 Effect of the contactor width on the: a) outlet air humidity ratio, (b) air pressure drop, and (c) wetting ratio.....123
Fig. 9.6 Flow chart of the GA-based optimization of the contactor size.....127
Fig. 9.7(a) Outlet air humidity ratio, (b) air pressure drop, (c) minimum volume, (d) wetting ratio, and (e) dimension pattern at varying inlet air flow rate.....132
Fig. 9.8(a) Outlet air humidity ratio, (b) air pressure drop, (c) minimum volume, and (d) wetting ratio at varying inlet air humidity ratio.....135
Fig. 9.9 Performance comparison of 3-fluid and conventional 2-fluid (no cooling water) gas-liquid contactor.....136

Fig. 1.1 (a) Structured packed bed and (b) differential control element for the packed bed.....148
Fig. 1.2 Illustration of the: (1) actual geometry and (2) simplified geometry of air channel inside the structured packed bed.....149
Fig. 1.3 Concentration profiles of water species in the air and solution.....150
Fig. 1.4 Illustration of the liquid film falling on the inclined corrugated sheets of the packed bed.....152
Fig. 1.5 Equivalent circuits for the heat and mass transfers between the air and solution.....156
Fig. 1.6 Illustration of the: (a) differential control element and (b) stencil for the conservation equations of the adiabatic packed bed.....158

Fig. 2.1 Schematic diagram of the packed bed liquid desiccant air conditioning system.....159
Fig. 2.2 Photo of the test section.....160
Fig. 2.3 Construction of the structured packed bed gas-liquid contactor.....160
Fig. 2.4 Photo of the LiCl solution distributor.....160
Fig. 2.5 Photo of the (a) air and (b) solution condition control sections.....161
Fig. 2.6 Effect of air velocity on the overall (a) heat and (b) mass transfer coefficients..165
Fig. 2.7 Effect of the air velocity on the outlet air (a) humidity ratio and (b) temperature of the dehumidification process.....166
Fig. 2.8 Effect of the air velocity on the outlet air (a) humidity ratio and (b) temperature of the regeneration process.....167
Fig. 2.9 Effect of solution flow rate on the overall (a) heat and (b) mass transfer coefficients.....168
Fig. 2.10 Effect of the solution flow rate on the outlet air (a) humidity ratio and (b) temperature of the dehumidification process.....169

Fig. 2.11 Effect of the solution flow rate on the outlet air (a) humidity ratio and (b) temperature of the regeneration process.....170

List of Tables

Table 1.1 Previous gas-liquid contactors and liquid desiccants.....25

Table 2.1 Range for selected thermophysical properties of aqueous IL.....39
Table 2.2 Dimensions of the fin-tube gas-liquid contactor.....40

Table 5.1 Dimensions of the fin and tubes.....62
Table 5.2 Details of the distributors.....62
Table 5.3 Specifications of the measuring instruments.....63
Table 5.4 Wetting visualization experimental data.....64
Table 5.5 Static, advancing, dynamic contact angles, and contact angle hysteresis of the IL solution on an aluminum plate.....69
Table 5.6 Surface roughness of the aluminum substrate.....72

Table 6.1 Characteristic coefficients of the semi-theoretical formulation.....85

Table 8.1 Detailed dimensions of the 3-fluid gas-liquid contactor.....108
Table 8.2 Fluid properties and specifications of their measuring instruments.....108
Table 8.3 Dehumidification experimental data.....109
Table 8.4 Regeneration experimental data.....110

Table 9.1 Inlet conditions of the parametric study.....117
Table 9.2 Search range of the design parameters.....124
Table 9.3 Conditions for the contactor size optimization at various air flow rates.....128
Table 9.4 Conditions for volume optimization at various inlet air humidity ratio……...132
Table 9.5 Conditions for the performance calculation of a 3-fluid and a conventional 2-fluid gas-liquid contactor.....135

Table 1 Specifications of the measuring instruments.....162
Table 2 Dehumidification experimental data.....162
Table 3 Regeneration experimental data.....163

Nomenclature

A	area, cross-sectional area, m^2
d	distance between opening, m; diameter, m
c_p	constant pressure specific heat, $J \cdot kg^{-1} \cdot K^{-1}$
C	characteristic coefficient
C_{sa}	contact surface area per unit volume, $m^2 \cdot m^3$
CR	crossover rate
D	tube diameter, m; mass diffusion coefficient, $m^2 \cdot s^{-1}$
DP	dewpoint temperature, °C
e	energy per unit area, $J \cdot m^{-2}$
E	Energy per unit stream-wise length, $J \cdot m^{-1}$
f	friction factor
F	flow rate, $L \cdot m^{-1}$
FS	full scale
g	standard gravitational acceleration, $m \cdot s^2$
G	geometric function of the contact angle, mass flux, $kg \cdot m^{-2}$
GA	genetic algorithm
h	enthalpy, $kJ \cdot kg^{-1}$
h_h	heat transfer coefficient, $kW \cdot m^{-2} \cdot K^{-1}$
h_m	mass transfer coefficient, $kg \cdot s^{-1}$
h, H	Height, m
IL	Ionic Liquid
j	mass flux, $kg \cdot m^{-2} \cdot s^{-1}$
l, L	Length, m
$\dot{m}$	mass flow rate, $g \cdot s^{-1}$ or $kg \cdot s^{-1}$
MG	maximum generation
MR	mutation rate
n	number of openings, number of sheets
N	number of tubes in the transversal direction
N_f	number of fins
N_{tc}	number of tube columns
N_{tr}	number of tube rows
P	pitch, m; perimeter, m
$\Delta P, P$	pressure drop, pressure loss
PS	population size
q	heat flux, $kW \cdot m^{-2}$
R	tube radius, m
R_a	arithmetic mean roughness, μm

R_p maximum peak height, μm
R_v maximum valley depth, μm
R_z maximum height, μm
RD relative density
S interface, m
T thickness, opening thickness, m
T temperature, °C
u velocity, $m \cdot s^{-1}$
V volume, μL, m^3
w opening width, m
W width, m; wetting
WR wetting ratio
WS surface wetting
x streamwise direction, horizontal direction; humidity ratio, $kg \cdot kg(DA)^{-1}$ or $g \cdot kg(DA)^{-1}$
X mass fraction, - or %
y transversal direction, vertical direction
z normal direction, depth direction

Greek symbols
Δ dimensionless thickness
δ thickness, m
ε surface roughness, m
η efficiency
γ geometric function of the contact angle
Γ mass flow rate per unit width, $kg \cdot m^{-1} \cdot s^{-1}$
λ transversal unit length, m; thermal conductivity, $kW \cdot m^{-1} \cdot K^{-1}$
μ dynamic viscosity, Pa·s
ω geometric variable
ρ density, $kg \cdot m^3$
ψ geometric function of the contact angle
σ surface tension, $J \cdot m^{-2}$
θ contact angle, °

Subscripts
0 representative variable for advancing or receding
a air
A advancing
ac air channel
ave average

b	breaking, base
c	condensation, cross-sectional
cw	cooling water
d	decreasing
dp	dewpoint
dry	dry
D	dynamic
e	effective
exp	experiment
f	fin
g	gas
gb	gas bulk
ge	gas equilibrium
gl	gas-liquid interface
gs	gas-solid interface
h	horizontal, hydraulic
H	hysteresis
i	increasing
icw	inlet cooling water
ig	inlet gas
il	inlet liquid
iw	inner wall
k	kinematic
l	liquid
lb	liquid bulk
lg	liquid-gas interface
ls	liquid-solid interface
lv	liquid-vapor interface
max	maximum
min	minimum
o	outer
oa	outlet air
og	outlet gas
ol	outlet liquid
ocw	outlet cooling water
ow	outer wall
PT	plate tilt
R	receding
riv	rivulet
s	solution, sheet

s, S	static
sg	solid-gas interface
sl	solid-liquid interface
sv	solid-vapor interface
t	tube
ti	tube inner
to	tube outer
tw	tube wall
uf	uniform film
v	vertical, vaporization
w	wall, wetted
wet	wet

Dimensionless numbers

Ga	Galileo number
Nu	Nusselt number
Pr	Prandtl number
Re	Reynolds number
Sc	Schmidt number
Sh	Sherwood number
We	Weber number

1. Introduction

1.1 Importance of the research

Due to global warming, temperature readings all around the world are rising steadily. According to the National Aeronautics and Space Administration or NASA[1)], the average global temperature on Earth has increased by more than 1°C since 1880. Two-thirds of the warming has occurred since 1975, at a rate of roughly 0.15 - 0.20°C per decade[1)]. But how would a one degree Celsius of warming be alarming considering that daily temperatures change by many degrees everywhere around the globe? That is because the global temperature reading represents the average over the entire surface of the planet. It depends on how much energy the Earth receives from the Sun and how much it radiates back into outer space. The amount of energy radiated by the planet depends on the chemical composition of the atmosphere, particularly the amount of heat-trapping greenhouse gases. A one-degree change in global temperature is significant because it requires an immense amount of heat to warm all the solid, liquid, and gas matter of the earth by that much. In the most recent Ice Age, which reached peaked conditions about 18,000 years ago, the global temperature dropped by 5°C and that was all it took to cover a large part of North America by about 12,000 feet thick ice[2)].

Fig. 1.1 shows the global temperature records from 1880 – 1884 (Fig. 1.1(a)) and from 2015 – 2019 (Fig. 1.1(b)). The maps depict how much a region is warmer or colder compared to the average temperature for that region from 1951 – 1980 (base period, 0°C). It is evident in Fig. 1.1(a) that most regions are white followed by several blue colors and a few orange colors. This means that the global average temperatures from 1880 – 1884 are mostly similar to the baseline period of 1951 – 1980, with several colder regions and a few warmer regions. On the other hand, the temperature map in Fig. 1.1(b) depicts mostly orange and red colors. The average temperatures increased dramatically compared to the baseline period. It is apparent that there is a rapid global warming four decades since 1980 compared to ten decades since 1880. Global warming is caused by excessive heat trapping due to the increased concentration of greenhouse gases in the Earth's atmosphere.

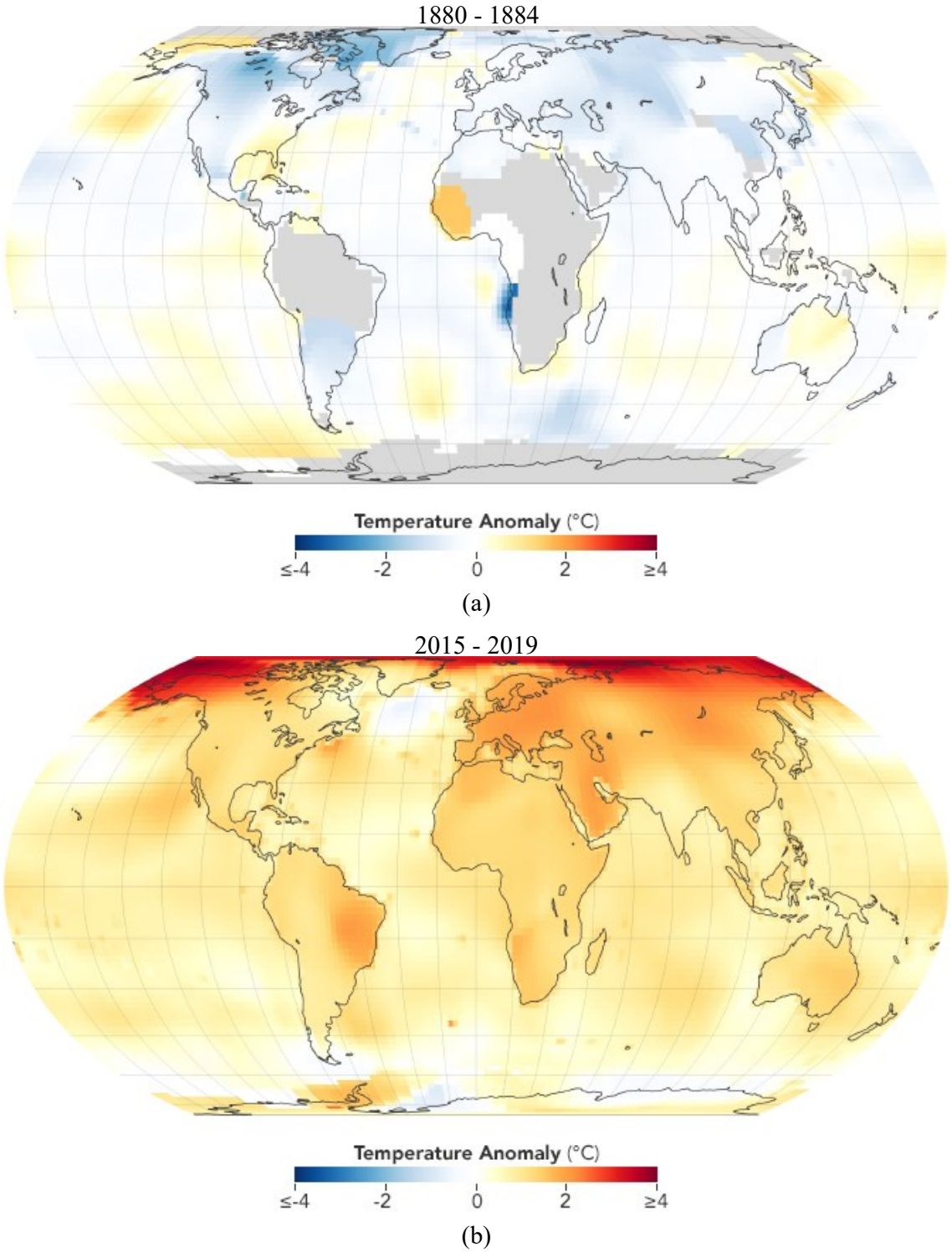

Fig. 1.1 Global temperature anomaly: (a) 1880 – 1884 and (b) 2015 – 2019[1)].

In countries located in the tropical and subtropical zones, air conditioners are used to control the temperature and humidity of the air inside buildings and residential spaces. However, due to the increase in global temperatures, air conditioners are also becoming

a necessity in countries situated in the temperate zone. These result in the extensive use of air conditioning systems in the three mentioned climate zones.

1.2 Research background

The first recorded use[3)] of air conditioning system dates back to 1902 when Willis H. Carrier invented the first mechanical air conditioning system to control the temperature and humidity, at the publishing company he worked for. The system sends ambient air through cold water filled coils to cool the air and at the same time to remove moisture from the air.

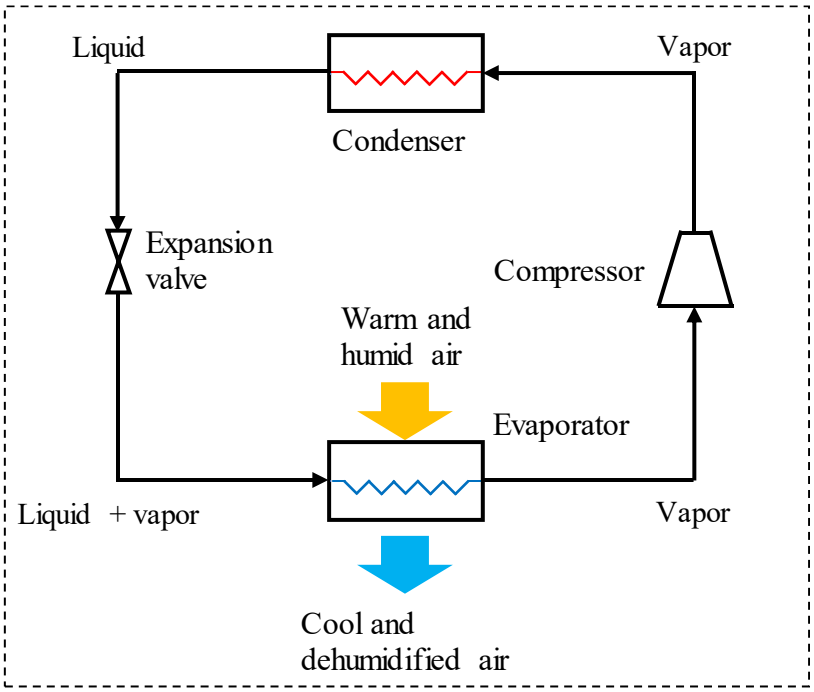

Fig. 1.2 Schematic diagram for a typical vapor compression cycle.

Modern air conditioners (ACs) use the vapor compression cycle to accomplish air cooling and dehumidification. The vapor compression cycle forces the refrigerant (working fluid) to circulate in a closed thermodynamic system and uses its phase change property to control its temperature and pressure. Fig. 1.2 illustrates a schematic diagram for a typical vapor compression cycle. A typical vapor compression cycle has four basic components: a compressor, a condenser, an expansion valve, and an evaporator. In the vapor compression, the refrigerant at a saturated vapor state is compressed to a higher pressure by the compressor, increasing its temperature in the process. Now at a superheated vapor state, the refrigerant is condensed to a saturated liquid by the cooling air passing through the outside surface of the condenser coils. Then, the saturated liquid refrigerant undergoes a rapid reduction in pressure, and thereby temperature, which results in a mixture of the refrigerant in liquid and vapor states. The low-temperature

refrigerant mixture is available for heat exchange and returns to a saturated vapor state after absorbing heat in the evaporator. This cyclic change in temperature enables the refrigerant to absorb heat from the air-conditioned space and release it to the outdoor air.

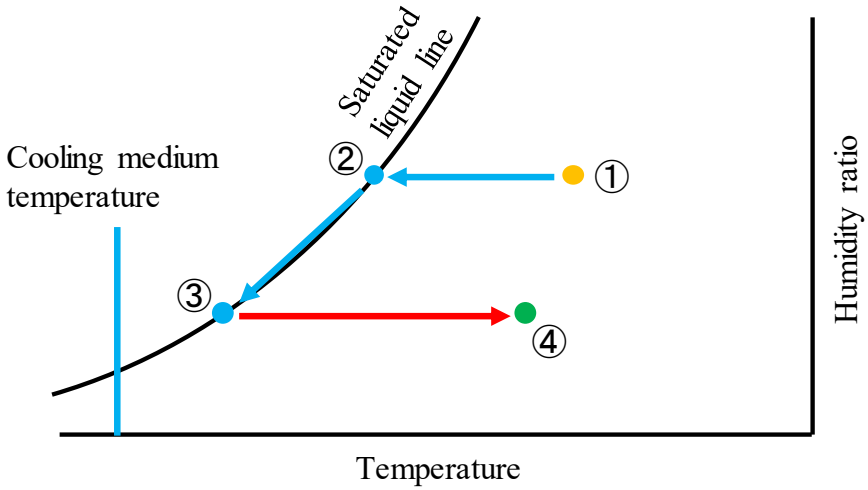

Fig. 1.3 Illustration of the air processes in a vapor compression system in a psychrometric chart.

In conventional vapor compression systems, the air undergoes three psychrometric processes to achieve cooling and dehumidification. Fig. 1.3 schematically illustrates the three processes (① - ②, ② - ③, and ③ - ④) in a psychrometric chart. For example, air at a psychrometric state point ① is supplied to the evaporator to be cooled and dehumidified to state point ④. To accomplish the required air condition, the vapor compression system has to cool the supply air to the dewpoint temperature. In this example, state point ② represents the dewpoint temperature of the air. Water vapor from the air can be condensed since the dewpoint temperature is reached and it will continue as long as the air temperature is equal or below the dewpoint temperature. Dehumidification is achieved by further cooling the air to around to state point ③. The resulting water condensate wets the cooling coils and can lead to corrosion and microbial growth such as fungi and bacteria, which can cause undesirable health problems. The method for realizing dehumidification effect by cooling the supply air from state point ① to state point ③ is generally known, in the air conditioning field, as “deep cooling”. Deep cooling consumes an intensive amount of energy and is inefficient. Moreover, the resulting temperature of the air is not suitable for thermal comfort and needs to be reheated to a comfortable level such as at state point ④. This sensible reheating of the air

from state point ③ to ④ further adds to the energy consumption of the vapor compression system. It can be concluded that even though the vapor compression system is the widely used air conditioning technology, it is not energy efficient for humidity control and contributes to high energy generation from the power sector, which can lead to increased greenhouse gas emission and intensify global warming.

The motivation of this research comes from the potential of using innovative and energy-efficient technologies in line with the drive of several international treaties to address critical environmental problems. This is in reference to the Kyoto Protocol, the Paris Agreement, and the European Union Low Carbon 2050 which aims to reduce greenhouse gas emissions, to combat climate change, and to reduce greenhouse gas emission by 80% (compared to 1990 level) by 2050, respectively.

One of the promising air conditioning alternatives which can address the inefficient humidity control of the vapor compression system is the desiccant air conditioning system. This innovative technology is a type of an open-cycle absorption system and employs gas separation to efficiently dehumidify the supply air. The operation takes place at atmospheric pressure, eliminating the use of vacuumed/pressurized vessels. Using this approach gives the advantage of direct and precise control of humidity in the air without the need for deep cooling. The humidity control above dew point temperature (state point ① - ③ in Fig. 1.4) in this system eliminates not only the energy used for deep cooling but also that for sensible heating. Moreover, since the sorptive medium takes directly the moisture from the air, water condensate and the problems along with it are avoided. Conversely, after the dehumidification process, the sorptive medium becomes diluted and must undergo a regeneration process to bring it back to the thermodynamic state where its equilibrium vapor pressure is lower than that of the process air. This process is commonly performed by a heat source, which extracts the moisture gained by the sorptive medium from the dehumidification process. As the temperature level required for regenerating the sorptive medium is relatively low, desiccant air conditioning systems can be thermally driven by other heat sources such as low-grade solar energy and waste heat.

Desiccant air conditioning systems are generally classified based on the type of desiccant employed in the system. Desiccants have high hygroscopic properties making them highly applicable for mass transfer processes. There are two types of desiccant used in the desiccant air conditioning system: the solid desiccant[4)] and the liquid desiccant[5)]. Compared to solid desiccants, liquid desiccants have the advantages of greater moisture capacity[6)], lower regeneration temperatures[7)], and better indoor air quality[8)]. This gives the liquid desiccant air conditioning system the capacity to more accurately control the air humidity than the solid desiccant system.

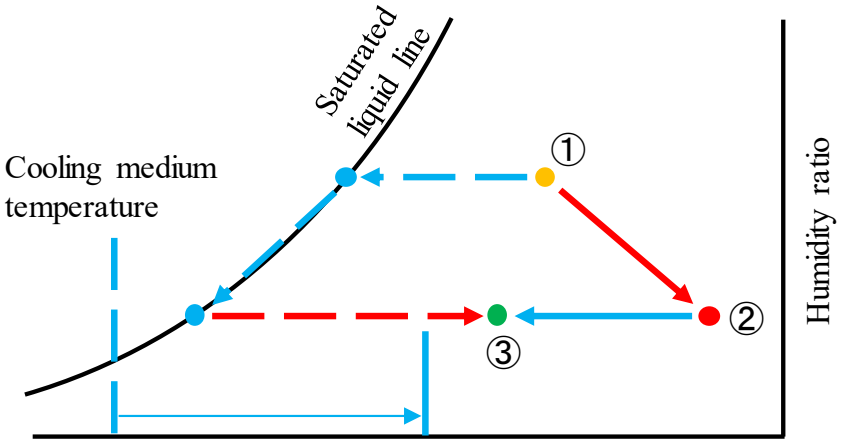

Fig. 1.4 Comparison of the psychrometric processes between the vapor compression system and desiccant air conditioning system.

Fig. 1.5 shows the dehumidification and cooling process in the components of a typical liquid desiccant air conditioning system. The dehumidification process takes place in the dehumidifier or generally known as a gas-liquid contactor. Warm and humid air is blown into the dehumidifier where it undergoes simultaneous heat and mass transfer through direct contact with the cold and concentrated liquid desiccant solution. The humid air is dehumidified through gas separation by absorption into the concentrated solution. This process is accompanied by the release of heat due to the condensation, resulting in a higher temperature process air. The cooling process is necessary to bring the supply air to thermal comfort.

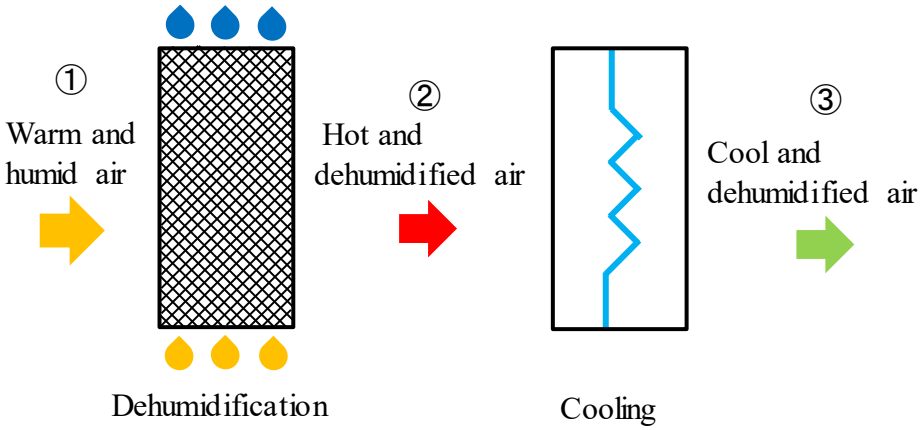

Fig. 1.5 Dehumidification and cooling in a typical liquid desiccant air conditioning system.

1.3 Previous research and problems

There are two general types of gas-liquid contactors in liquid desiccant air conditioning systems. These are the 2-fluid flow (adiabatic) gas-liquid contactor and the 3-fluid flow (internally cooled/heated) gas-liquid. An example of an adiabatic contactor is the packed bed[5] shown in Fig. 1.6(a) and one example of an internally cooled/heated contactor is the fin-tube[9] shown in Fig. 1.6(b). The main difference between these two types of contactors is the number of interacting fluids inside the contactor. In these two contactors, the physical material is also different from the other with the adiabatic made of cellulose paper and the fin-tube made of stainless steel.

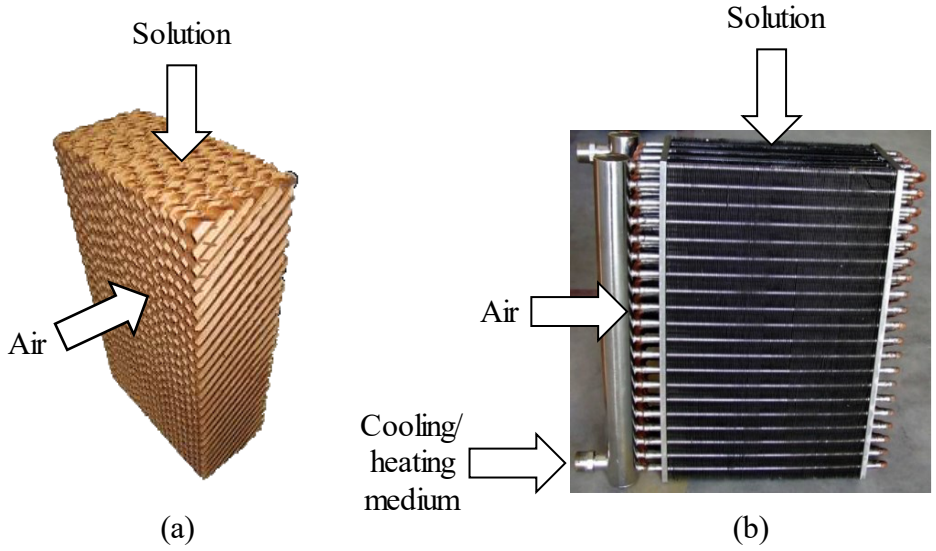

Fig. 1.6 (a) packed bed (2-fluid gas-liquid contactor), (b) fin-tube[9] (3-fluid gas-liquid contactor).

1.3.1 Corrosivity of liquid desiccants

Liquid desiccants are substances with high hygroscopic properties and due to this capability, they are utilized as working fluids in absorption systems especially in liquid desiccant air conditioning systems. Conventionally used liquid desiccants for air conditioning applications are mono-ethylene glycol (MEG)[10], triethylene glycol (TEG)[11], lithium bromide (LiBr)[9),12], calcium chloride (CaCl)[13], and lithium chloride (LiCl)[5),14),15]. These liquid desiccants have limited applications to gas-liquid contactors made of metal due to their corrosion properties. The selection of a suitable liquid desiccant depends on several factors that can be categorized as those related to heat and mass transfer potential, compatibility (in terms of corrosion) with the gas-liquid contactor, safety, purchasing cost, and operational cost. In general, an ideal liquid desiccant is defined as having low vapor pressure, high thermal conductivity, non-corrosive to heat exchangers made of metal, low crystallization point, low volatility, non-flammable, low

viscosity, and low cost. Low vapor pressure assures that the liquid desiccant would have high mass transfer potential with the gas mixture, while low viscosity translates to low pumping power and low operational cost. If a non-corrosive liquid desiccant is available, high thermal conductivity metals can be used as materials for the gas-liquid contactor and the application of 3-fluid flow configuration would be possible.

Three-fluid gas-liquid contactors have the advantages of higher heat and mass transfer performance due to the addition of direct control of the solution temperature and the vapor pressure, as an effect of controlling the temperature, owing to the third cooling/heating medium[16)-20)]. However, their application is limited due to the corrosion property of commonly used liquid desiccants. For example, in Fig. 1.6(b), corrosion is present on the outside surface of the fin and tubes due to the incompatibility of the liquid desiccant used with stainless steel. This makes the cellulose packed bed, usually structured, as the heavily relied gas-liquid contactor for liquid desiccant air conditioning systems.

A list of previously used gas-liquid contactors and liquid desiccants in the literature is given in Table 1.1. Notice that the packed bed gas-liquid contactor is used freely with any type of liquid desiccant since it does not corrode. However, the process is adiabatic, in other words, the interacting fluids inside the gas-liquid contactor are limited to two fluids.

Table 1.1 Previous gas-liquid contactors and liquid desiccants.

Gas-liquid contactor	Adiabatic/ Internally cooled	Liquid desiccant	Corrosion
Packed bed[11)]	Adiabatic	TEG	Absent
Packed bed[21)]	Adiabatic	LiBr	Absent
Packed bed[22)]	Adiabatic	$CaCl_2$	Absent
Packed bed[5),20)]	Adiabatic	LiCl	Absent
Packed bed + aluminum tube[23)]	Internally cooled	$CaCl_2$	Present
Packed bed + polyethylene tube[24)]	Internally cooled	LiCl	Absent
Packed bed + titanium tube[24)]	Internally cooled	LiCl	Absent
Polypropylene plates[15),25)]	Internally cooled	LiCl	Absent
Stainless steel Fin-tube[9)]	Internally cooled	LiBr	Present
Electroplated fin-tube[17)]	Internally cooled	LiCl	Absent

In some studies, plastics and metals were used for the gas-liquid contactor to take advantage of the 3-fluid flow configuration. Bansal et al.[23)] applied internal cooling through 3-fluid configuration by inserting aluminum coils inside the packed bed. Fig. 1.7 shows the structure of the packed bed-tube gas-liquid contactor. The liquid desiccant used was $CaCl_2$. Since aluminum can suffer corrosion against $CaCl_2$[26)], it is logical to say that there could be corrosion on the outer surface of the aluminum coils even though it was not directly mentioned in their paper. Gommed et al.[24)] used layers of polyethylene and

titanium tubes below the structured packed to achieve internal cooling and improve the performance of the gas-liquid contactor. Both polyethylene and titanium tubes exhibited no corrosion with the LiCl liquid desiccant. Other studies used parallel plate heat exchangers as a gas-liquid contactor. Liu et al.[25] and Kessling et al.[15] employed polypropylene plates as a gas-liquid contactor and paired it with LiCl. Since polypropylene is plastic, there was no corrosion reported with the LiCl liquid desiccant. A few studies have used fin-tube gas-liquid contactor, which has been reported by Liu et al[27] to have superior performance compared to the packed bed-tube and parallel plate gas-liquid contactors. Zhang et al.[9] investigated the operating performance of a stainless-steel fin-tube gas-liquid contactor. However, with the LiBr liquid desiccant, corrosion is highly likely since stainless steel is vulnerable to corrosion as reported by Guiñon et al.[28] To avoid corrosion on the surface of the gas-liquid contactor, Luo et al.[17] used electroplated fin-tube contactor with LiCl. They tested a sample electroplated fin together with a copper and stainless steel 304 The electroplated fin proved to be resistant to corrosion against LiCl, while both the copper and stainless steel 304 showed corrosion on the surface.

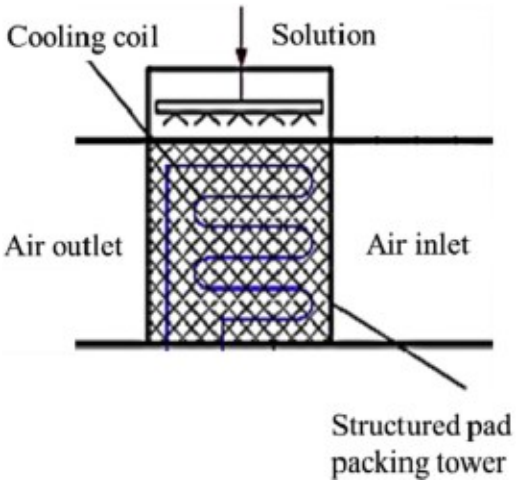

Fig. 1.7 Packed bed-tube gas-liquid contactor[23].

1.3.2 Large and expensive components

It is apparent that to avoid the problem of corrosion, the adiabatic packed bed has been widely used as a gas-liquid contactor. However, it needs to be paired with an extra heat exchanger to precool or preheat the liquid desiccant solution before entering the dehumidifier or regenerator, respectively. The combined packed bed contactor and precooler components (Fig. 1.5) not only makes the system large but also expensive.

If non-corrosive liquid desiccants are developed, high thermal conductivity metals can be used as materials for the gas-liquid contactor and the application of 3-fluid flow configuration would be possible. This will eliminate the necessity of using an extra

component for liquid desiccant cooling and will lead to space and cost savings for the liquid desiccant air conditioning system.

In some investigations, researchers have used titanium[24] and electroplated fin-tube gas-liquid contactors[17]. However, both are expensive and are less employed in actual liquid desiccant air conditioning systems. If non-corrosive liquid desiccants are available, inexpensive metals such as aluminum can be used as materials for the gas-liquid contactor.

1.3.3 Limited overall research

Liquid desiccant air conditioning systems are still a developing technology and comprehensive experimental, mathematical, and optimization studies of such systems are highly necessary. Given the complexity of the heat, mass, and momentum transfer, and the variability of the component design, material, as well as the new developments of liquid desiccants, no conclusive mathematical model is available yet for this kind of systems.

Limited research on wettability

In general, the sorptive solution flows as a gravity-driven falling film with controlled liquid desiccant mass fraction and temperature before being directly contacted with the process or regeneration air. The interaction of the fluid with the solid structure and gaseous phase generates active interfaces where heat and mass transfer is realized with an effectiveness that is directly related to the extension of these interfaces. The extension of these interfaces in the transversal direction to the flow is an aftermath of the wetting ability of the liquid on the solid substrate in the given gaseous environment.

The wettability, which is the degree of wetting, can be determined by balancing the effects of the adhesive and cohesive forces of the liquid on the solid substrate. However, accurate information about these forces is usually not available as a priori. In the absence of information about the wetting characteristics (critical film thickness, contact angle, wetting patterns, etc.) of a liquid desiccant on the surface of the gas-liquid contactor, complete wetting of the contactor are is assumed[29] as a simplification in falling film models. Theoretical models for transport phenomena of the gas-liquid contactor presented in previous literature rely on the assumption of complete wetting and uniform film thickness due to the lack of conclusive research and mathematical model for the prediction of the surface wetting in the gas-liquid contactor. However, this is usually not the case as film breakage and dry spot formation commonly occur on the surface of the gas-liquid contactor[30]. Without proper calculation of the wetted area, the assumption of complete wetting can overestimate the heat and mass transfer performance of the gas-liquid contactor[29].

Limited optimization studies

The constant push toward computer digitalization has propelled both simulation and optimization; and armed by the current advancement in computing power, various optimization problems and techniques have been realized. Optimization seeks to improve the performance of a product, a process, or a system by minimizing or maximizing an objective that is subject to certain conditions. In optimal design problems, the size of a product or component is usually minimized to reduce its initial or capital cost and save space.

To gain insight on the previous optimization studies on liquid desiccant air conditioning systems, a literature review is conducted. The key phrase "liquid desiccant optimization" is searched for on the Web of Science, selecting all its databases from 1990 to 2019. Out of 179 search results, 31 results[31)-61)], including both journal papers and conference proceedings, were selected relevant to the optimization of liquid desiccant air conditioning systems. The objective of these studies is similar to each other and that is either to optimize the performance, efficiency, effectiveness, energy consumption, exergy, or the annual running cost of the system. The studies differ according to the selection of decision variables which are grouped into four general classifications listed as follows:

1. Operating condition – includes the temperature and mass flow rates of the gas, the solution, and the cooling/heating fluid if there is, the concentration of the liquid desiccant in the solution, cooling and dehumidification loads, exhaust gas recirculation and process gas recirculation.

2. Component – includes the comparison of the adiabatic and internally cooled gas-liquid contactors, comparison between the use of heat exchanger or electric heater, use of solar collector, cooling coil, pre-cooler, and pre-heater.

3. Structure – includes the variation in length and height of the gas-liquid contactor.

4. Flow configuration – includes the comparison between counterflow and crossflow configuration of the gas and the solution.

Fig. 1.8 illustrates the number of papers per year for each classification of the decision variables. It can be observed from the graph that there are only a few studies conducted on the optimization of liquid desiccant air conditioning systems before the year 2010. However, for the following years, there have been yearly publications on the optimization of these systems indicating the increased interest of researchers on the topic. The majority of these optimization studies focus on the selection of the operating condition as decision variables. The results from these optimization studies are useful not only because they can be used as a basis for future systems but also for current operating

systems as well. On the other hand, optimizations selecting the component, structure, and flow configurations as decision variables have practical applications for future systems since it is difficult to change the type of component, the structure, or the flow configuration of currently operating systems compared to changing the operating conditions. However, it does not indicate that optimization selecting the structure or the flow configuration as decision variables over the operating conditions is less important since these parameters also have a high impact on the improvement of the system. Especially, the optimization of the structure of the gas-liquid contactor is necessary for miniaturization purposes and to be competitive against vapor compression systems in terms of size and compactness. Liquid desiccant air conditioning systems must be small enough and compact for them to be a viable option not only for building utilization but also for residential applications.

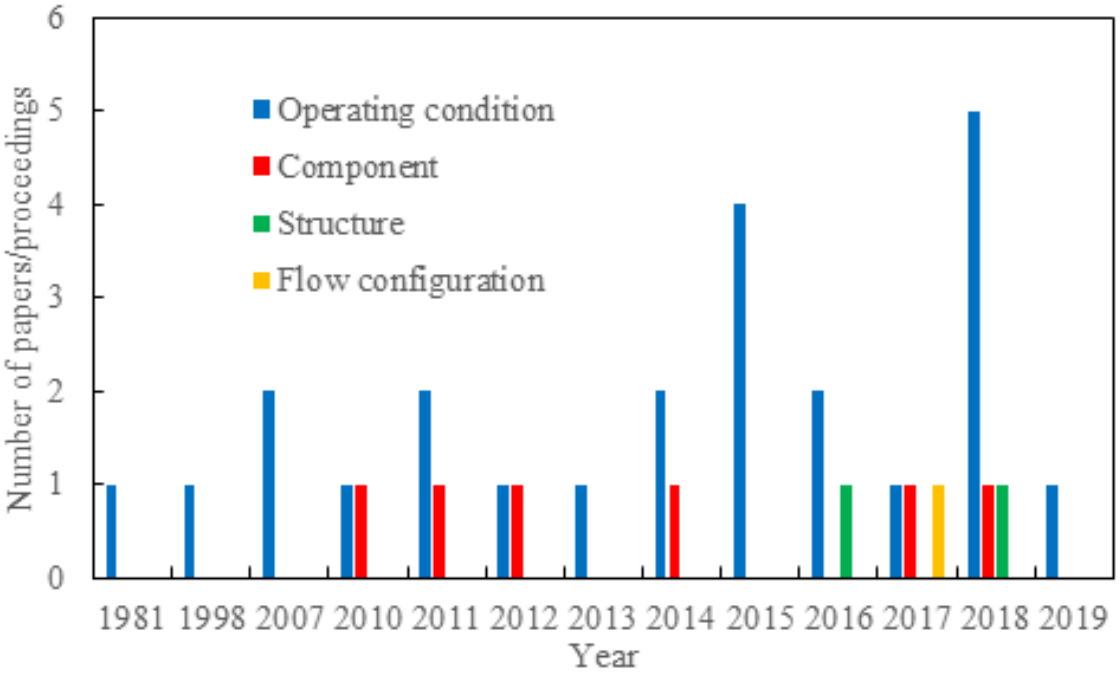

Fig. 1.8 General classifications of the decision variables selected for the optimization of liquid desiccant systems.

Previous studies on the structure optimization of gas-liquid contactors have focused on the influence of geometrical parameters and not on the overall design of the structure. For example, the study of Liang and Zeng[61] focused on the effect of the length and inner diameter of a hollow fiber membrane-based liquid desiccant module on the annual cost and entropy generation. They found that the inner diameter of the fiber has the most significant effect on the performance of the module. On the other hand, Fakhrabadi and Kowsary[52] investigated the effect of the length and height of a membrane-based liquid desiccant dehumidifier on its cooling capacity. They found an optimum range for these parameters which can give an optimum cooling capacity at a

constant fan power. In these studies, the optimal design of the gas-liquid contactor has not been discussed and a criterion for miniaturization has not been achieved. This research work takes motivation from the lack of information on the optimal design of gas-liquid contactors used in liquid desiccant air conditioning systems.

1.4 Research objectives

The following are the objectives of this study:

1. Propose a new ionic liquid and investigate its wetting characteristics on a new aluminum 3-fluid gas-liquid contactor.

2. Develop a model for predicting the wetting of the new ionic liquid on the newly developed aluminum 3-fluid gas-liquid contactor and validate the model with experimental data.

3. Develop a mathematical model for the new 3-fluid gas-liquid contactor considering partial wetting and validate the model with experimental data.

4. Analyze the effect of the dimensions on the performance of the 3-fluid gas-liquid contactor for design characterization.

5. Clarify the advantages of the new 3-fluid gas-liquid contactor.

1.5 Thesis outline

The doctoral thesis is divided into ten chapters. The following discussions serve as a roadmap for the dissertation and roughly explains the content of each chapter:

Chapter 1 clarifies the position of the research by describing the importance, background, purpose, previous studies, and current problems in the research area. It establishes the areas that will be investigated and provides a review of what has been done by other researchers. The problems, research gasps, and limitations of the previous research are pointed out, which served as the basis for the motivation of the study. The application of the study for future design and improvement of gas-liquid contactors are also presented.

Chapter 2 describes in detail the liquid desiccant air conditioning system. The basic liquid desiccant cycle is explained, and the major components of the system are identified. The essential principles and physical phenomena occurring inside the gas-liquid contactor of a liquid desiccant air conditioning system are discussed. The difference between a conventional 2-fluid and a 3-fluid liquid desiccant air conditioning is identified and elaborated. The newly developed ionic liquid that is not corrosive to aluminum is

introduced. This made the development of a 3-fluid gas-liquid contactor made of aluminum possible.

Chapter 3 describes the model conceptualization by explaining the necessary steps for the modeling of the 3-fluid gas-liquid contactor. The importance of wetting phenomena in modeling the performance of falling film devices is explained. Theoretical modeling of the partial wetting is briefly introduced. Data gathering for the wettability of the proposed ionic liquid on a fin-tube test section and contact angle of the ionic liquid on an aluminum surface are shortly discussed. Semi-theoretical modeling of the partial wetting is briefly explained.

Chapter 4 explains in detail the development of the theoretical falling film partial wetting model. The partial wetting on the fin and tube surface was modeled applying the Principle of Minimum Energy to the uniform film and rivulet. This resulted in a general theory for determining the minimum film thickness that would ensure complete wetting and subsequently, for estimating the surface wetting.

Chapter 5 presents the experimental apparatus for the investigation of the wetting characteristics of the new ionic liquid. Experimental data on the wettability of the new ionic liquid on the single aluminum fin with tubes were gathered and surface wetting was estimated through image processing. The principles of minimum wetting rates and film stability, and their relationship on the occurrence of wetting hysteresis were explained and the factors affecting wetting hysteresis were identified. The static and dynamic contact angles of the ionic liquid on an aluminum surface were also gathered. Contact angle hysteresis of the ionic liquid was evaluated and the factors causing its occurrence were identified. The surface wetting experimental data was compared with the results from the theoretical partial wetting model.

Chapter 6 explains the semi-theoretical formulation of partial wetting. It was clarified from the comparison of the wetting ratio between the experiment and theoretical partial wetting model that the theoretical model can be improved further by designating characteristic coefficients to represent other factors not accounted for in the partial wetting model. Hence, a semi-theoretical partial wetting model was developed by fitting the characteristic coefficients to the to surface wetting experimental data. An improved degree of accuracy for the prediction of the surface wetting was obtained from the semi-theoretical partial wetting model.

Chapter 7 presents the modeling of the 3-fluid gas-liquid contactor. The inclusion of the partial wetting model provides a potential improvement in the mathematical model of the heat and mass transfer in the 3-fluid gas-liquid contactors by adopting a more realistic prediction of the wettability inside the contactor. With the mathematical model

of the 3-fluid gas-liquid contactor, prediction, simulation, and various optimization problems are possible.

Chapter 8 describes the experimental apparatus for the 3-fluid liquid desiccant air conditioning system. Experimental data for the dehumidification and regeneration process were gathered at various air velocity and solution mass flux. The effect of the air velocity and solution mass flux on the heat and mass transfer coefficients, and on the air humidity ratio and temperature were analyzed and explained. The dehumidification performance of the 3-fluid gas-liquid contactor was compared with the performance of a 2-fluid packed contactor and the superiority of the 3-fluid gas-liquid contactor in terms of dehumidification was clarified.

Chapter 9 presents the validation of the 3-fluid gas-liquid contactor model and performance analysis of the parametric and optimization studies. The effect of the dimensional parameters to the outlet air humidity ratio, outlet air temperature, air pressure drop, and wetting ratio was clarified. Case optimization of the 3-fluid gas-liquid contactor was conducted to minimize the volume of the contactor and its initial cost. The optimum volume of the contactor was calculated at various inlet air flow rate at a constant solution flow rate while setting a constraint for the outlet air humidity ratio and pressure drop. Also, the optimal volume of the contactor was calculated at various inlet air humidity ratio, which represents different climatic conditions. A performance comparison between a 3-fluid gas-liquid contactor and a conventional 2-fluid gas-liquid contactor was carried out to clarify the advantage of the 3-fluid gas-liquid contactor.

Chapter 10 gives the conclusions obtained from the study and other possible work in the future. It was clarified that increasing the length, the height, or the width of the gas-liquid contactor decreases the outlet air humidity ratio and outlet air temperature due to the increase in transfer area and contact time. On the other hand, increasing the length of the contactor increases the air pressure drop while increasing both the height and the width decreases the air pressure drop. For the wetting ratio, increasing the length and width of the contactor decreases the wetting ratio since these parameters affect the solution flow rate per unit area. While changes in the height of the contactor do not significantly affect the wetting ratio. From the performance comparison between 2-fluid and 3-fluid gas-liquid contactor, it was found that size reduction of about 56% can be obtained from the 3-fluid gas-liquid contactor in obtaining the smallest outlet air humidity ratio obtained by the 2-fluid gas-liquid contactor. Due to the additional cooling medium, the superior performance of the 3-fluid gas-liquid contactor is proven against conventional 2-fluid gas-liquid contactors.

2. System and component description

2.1 Introduction

Liquid desiccant systems are based on the basic principles of an open-absorption cycle, which means that the associated thermodynamic process occurs at atmospheric temperature. This innovative technology uses the hygroscopic properties of the liquid desiccant and the direct contact heat and mass transfer between the gas and liquid phases inside the gas-liquid contactor to precisely control the temperature and humidity of the gas mixture. Based on the two general classifications of gas-liquid contactors, the liquid desiccant air conditioning system can be categorized into types: the 2-fluid liquid desiccant air conditioning system and the 3-fluid liquid desiccant air conditioning system.

2.2 Conventional liquid desiccant air conditioning system

Fig. 2.1 shows the basic cycle of a conventional 2-fluid liquid desiccant air conditioning system. The system consists four major components, namely, two gas-liquid contactors (one air dehumidifier and one solution regenerator) and two solution-liquid heat exchangers (one solution precooler and one solution preheater). In the dehumidifier, there are only two interacting fluids, thus, the name 2-fluid liquid desiccant air conditioning system. Concentrated liquid desiccant solution is drawn from the storage tank and is passed through the solution precooler to be adjusted to the required temperature before entering the dehumidifier. The solution precooler may be supplied with chilled water or it can be an evaporator of a heat pump. A solution distributor, mounted at the top of the gas-liquid contactor, dispenses the solution to the dehumidifier. The solution falls from the top of the dehumidifier as liquid films acted upon by gravity. It makes direct contact with the warm and humid air blown horizontally by a fan, depicting a crossflow configuration. In some cases, the air is blown from the bottom of the gas-liquid contactor and makes contact with the free-falling solution in counter-current flow. When the air makes contact with the solution, coupled heat and mass transfer between the air and the solution occurs. Water vapor separates from the air mixture and is absorbed by the concentrated solution at a rate dependent on the diffusivity of the air and solution. The process involves the release of the latent heat of condensation by the air, which is transferred to the solution. The liquid desiccant solution absorbs both the sensible heat, due to the difference in temperature between the air and solution, and the latent heat of condensation from the air. This increases the solution temperature and vapor pressure, which decreases the heat and mass transfer potential of the solution. The diluted solution exits the dehumidifier and is collected by a storage tank. Through simultaneous heat and mass transfer with the solution, cool and less humid air is supplied to the air-conditioned space.

The diluted solution needs to be regenerated in order to bring the liquid desiccant to its required inlet conditions, and hence, to continuously perform the air conditioning process in the dehumidifier. The regeneration process starts by pumping the diluted solution from the diluted solution storage tank to the solution preheater to raise the solution temperature and vapor pressure. Hot water, waste heat from the condenser of a heat pump, or solar heat can be used to heat the solution. Bringing the vapor pressure of the diluted solution higher than the ambient air entering the regenerator guarantees that mass transfer would be from the solution to the air. The distributor dispenses the high-temperature solution at the top of the regenerator. Ambient air, which is at a lower temperature and vapor pressure than the solution, is supplied to the regenerator. In this case, the air and the solution flow in the same manner as they do in the dehumidifier. Since the partial pressure of the water species in the solution is higher compared to those in the air, water species in the solution is desorbed by diffusion and mixes with the air. This is accompanied by the release of the latent heat of vaporization by the solution, which is transferred to the regeneration air. The re-concentrated solution is collected by the storage tank completing the liquid desiccant cycle.

The system should continuously repeat the dehumidification and regeneration liquid desiccant cycle in order to achieve the required concentration of the liquid desiccant in the solution before entering the dehumidifier.

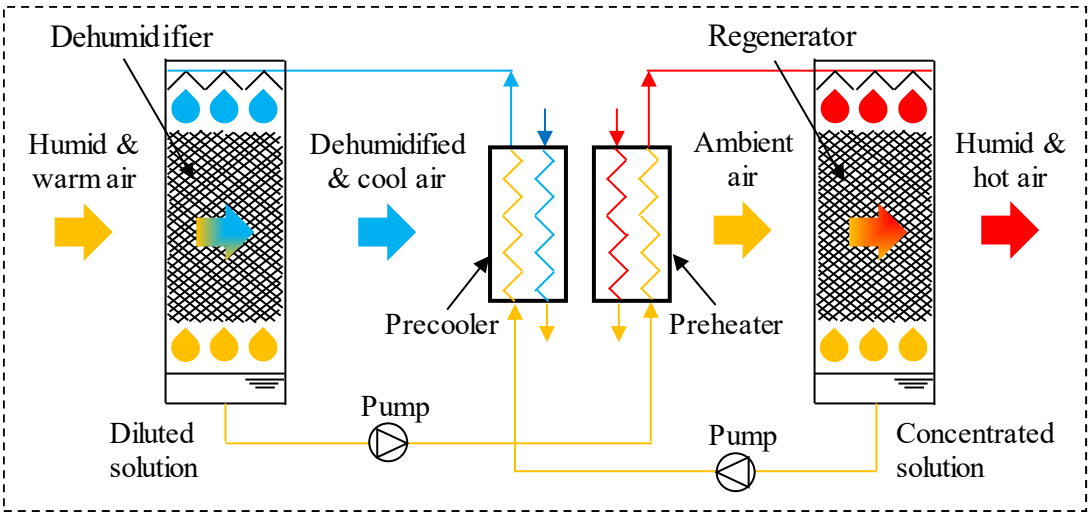

Fig. 2.1 Schematic diagram of a conventional 2-fluid liquid desiccant air conditioning system.

2.3 Liquid desiccant

Like solid desiccants, liquid desiccants are special chemicals that are utilized in sorption systems due to their high hygroscopic properties. They exhibit lower vapor pressure than water at the same temperature, allowing air or other gas mixtures contacting

them to be dehumidified. Liquid desiccants generally have higher moisture capacity compared to solid desiccants, which means they can remove a higher amount of moisture per unit weight of desiccant. They also have lower regeneration temperatures[7] and provide better indoor air quality[8] compared to solid desiccants. The selection of a suitable liquid desiccant depends on several factors that can be categorized as those related to heat and mass transfer potential, compatibility (in terms of corrosion) with the gas-liquid contactor, safety, purchasing cost, and operational cost. In general, an ideal liquid desiccant is defined as having low vapor pressure, high thermal conductivity, non-corrosive to heat exchangers made of metal, low crystallization point, low volatility, non-flammable, low viscosity, and low cost. Low vapor pressure assures that the liquid desiccant would have high mass transfer potential with the gas mixture, while low viscosity translates to low pumping power and low operational cost.

Types of liquid desiccants

Glycols: These organic chemicals are the earliest liquid desiccants used for liquid desiccant systems. Mono ethylene glycol (MEG)[10] and triethylene glycol (TEG) [11,62,63,64,65] are the two commonly used glycols as a liquid desiccant. The problem with using glycols is that they have very low vapor pressure that causes some of the glycol to evaporate into the air. While organic compounds such as MEG and TEG are nontoxic[66], the amount of glycol in the liquid desiccant solution decreases and requires periodic replacement. Moreover, diffused glycol does not only contaminate the air but also the surfaces of the system components, which is unacceptable in air conditioning systems. Due to these reasons and the limitation of using glycols at low temperature to avoid high evaporation rates, the use of glycols became obsolete in modern liquid desiccant air conditioning systems.

Hygroscopic salts: Hygroscopic salts are chemical compounds that have a high affinity to water. The most commonly used hygroscopic salts are lithium bromide (LiBr) [9,12], calcium chloride (CaCl)[14], lithium chloride (LiCl)[5,20,15], and ionic liquids (IL). Salt solutions of LiBr, CaCl, and LiCl have high corrosion properties to metals, which limits their use to cellulose gas-liquid contactors. They also possess solubility problems at low concentrations and crystallization issues at high concentrations[67]. On the other hand, ILs are solvents that are generally liquid at room temperature and exhibit low to no corrosion to metals[68]. They have low vapor pressure but also have high thermal and chemical stability, and excellent solubility[69], making them highly applicable for absorption processes such as in liquid desiccant systems and compression-absorption hybrid systems[70].

2.4 Gas-liquid contactor

Gas-liquid contactors are devices used to transfer heat and mass between a gas phase and a liquid phase by direct contact. In liquid desiccant systems, they function as a dehumidifier when heat and mass are transferred from the gas mixture to the liquid desiccant solution or as a regenerator when heat and mass are vice versa. Gas-liquid contactors are categorized as 2-fluid (adiabatic) or as 3-fluid (internally cooled/heated) gas-liquid contactors.

Types of gas-liquid contactors

Conventional gas-liquid contactor: Conventional 2-fluid or adiabatic gas-liquid contactors provide heat and mass transfer between the gas mixture and the liquid desiccant solution only. When heat and mass are transferred to the solution, its temperature increases (lowers its heat transfer potential) and the liquid desiccant concentration decreases. As a result, the equilibrium vapor pressure of the liquid desiccant solution increases and lowers the mass transfer potential of the solution. Among the commonly used 2-fluid gas-liquid contactors are the random packing[71] the structured packed bed shown in Fig. 2.2.

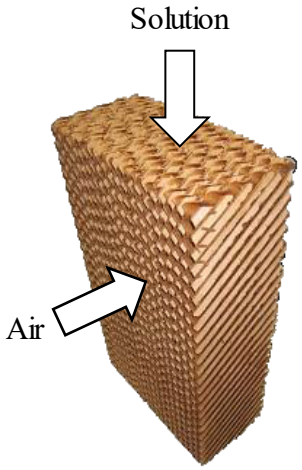

Fig. 2.2 Example of a 2-fluid gas-liquid contactor.

3-fluid gas-liquid contactors: 3-fluid gas-liquid contactors are designed to allow heat transfer between three fluids. In addition to the direct contact heat and mass between the gas and liquid phases, a third fluid exchanges heat with the gas and liquid phases without directly contacting both fluids similar to that in a non-mixing heat exchanger. In liquid desiccant systems, the third fluid provides internal cooling or heating especially for the liquid desiccant solution to keep it at high heat and mass transfer potential. Among the various designs of 3-fluid gas-liquid contactors, they can be categorized into 3 main types as shown in Fig. 2.3: parallel plate, fin-tube, and packed bed-tube. Liu et al.[72] have

numerically compared the performance of these three types of 3-fluid gas-liquid contactors and their results revealed that the fin-tube type is superior against the other types because it can provide higher heat and mass transfer capacities at the same contactor volume.

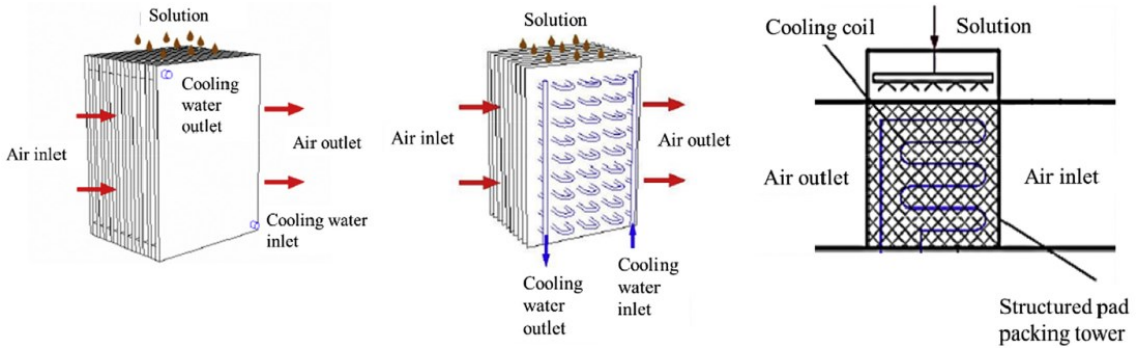

Fig. 2.3 Three main types of 3-fluid gas-liquid contactor[72].

2.5 New liquid desiccant air conditioning system

The new system is a 3-fluid liquid desiccant air conditioning system, which follows the same fundamental liquid desiccant cycle as the conventional liquid desiccant system. The major components are similar to a conventional liquid desiccant air conditioning system with a difference in the type of gas-liquid contactor. As previously discussed, there are only two interacting fluids in the gas-liquid contactor of the conventional liquid desiccant air conditioning system. On the other hand, the new liquid desiccant air conditioning system uses a new fin-tube gas-liquid contactor which incorporates 3-fluid flows.

Fig. 2.4 presents a schematic diagram of a new 3-fluid liquid desiccant air conditioning system. The dehumidifier incorporates a cooling medium, which enters the coil from the bottom and exits at the top. In addition to the coupled heat and mass between the air and the solution, the air and the solution is internally cooled by the cooling medium. As a result, the temperature and vapor pressure between the air and solution inside the 3-fluid gas-liquid contactor are kept close to the inlet condition. This improves the heat and mass transfer performance of the gas-liquid contactor.

On the other hand, the regenerator is added with a heating medium, which flows counter currently with the solution the same as with that in the dehumidifier. The heating medium keeps the solution at high temperature and vapor pressure. This results in an improved regeneration performance of the gas-liquid contactor.

Due to the high thermal conductivity of metals, they are commonly used as 3-fluid gas-liquid contactors. However, their applications are limited due to the natural corrosion

property of most liquid desiccants. If a non-corrosive liquid desiccant is developed, high thermal conductivity and inexpensive metals can be used as materials for the gas-liquid contactor and the application of 3-fluid flow configuration would be possible.

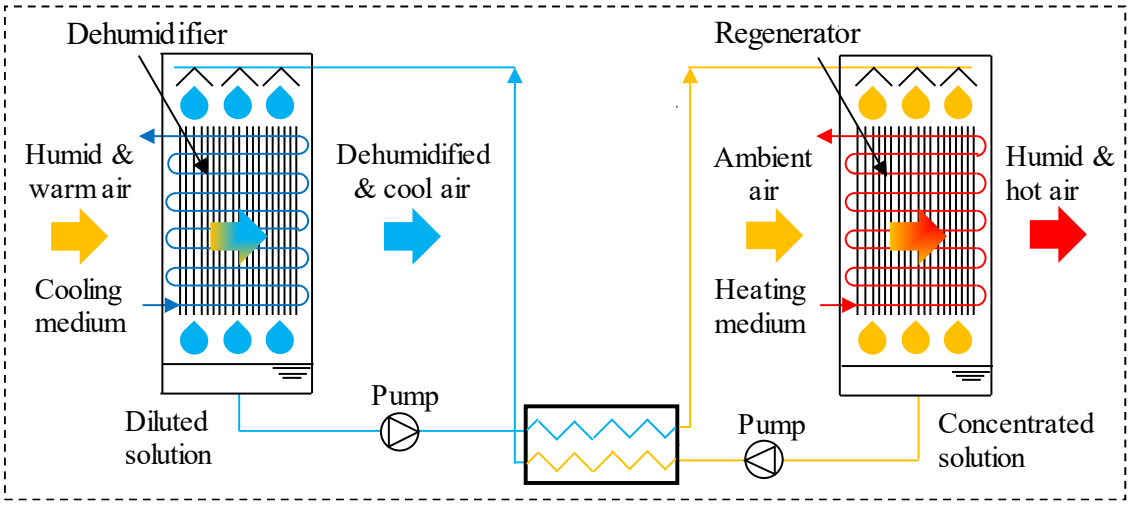

Fig. 2.4 Schematic diagram of an advanced 3-fluid liquid desiccant air conditioning system.

2.5.1 New Ionic Liquid

This research introduces a new ionic liquid developed together with Evonik Industries. The new IL, as shown in Fig. 2.5, is not corrosive to aluminum. Table 2.1 presents the range values for the density ρ, surface tension σ, and dynamic viscosity μ of aqueous IL between the range of IL mass fraction of 0~75%.

In falling film devices, the liquid can flow as a single film or as rivulets. Therefore, knowing the wetting characteristics of a liquid on the surface of a certain material, where the flow regime could change from complete to partial wetting, is highly important as the wettability of the liquid dictates the transfer performance of the device. In liquid desiccant systems, as the transfer processes occur at the phase interfaces, the absence of information about the wetting characteristics of a liquid desiccant on the surface of a gas-liquid contactor results in large deviations in the estimation of the heat and mass transfer inside the gas-liquid contactor[29]. In Chapter 5, the wetting properties, contact angle, contact angle hysteresis, wetting hysteresis of the new IL on an aluminum fin-tube substrate are investigated. Visualization of the wetting characteristics of the new IL provides an understanding of the wetting phenomena inside a gas-liquid contactor and guides the modeling of the surface wetting on the fin and tube surfaces.

Fig. 2.5 Newly developed ionic liquid.

Table 2.1 Range for selected thermophysical properties of aqueous IL.

X_{IL} (% mass)	ρ (kg·m^{-3})	σ (N·m^{-1})	μ (Pa·s)
0~75	1000~1150	0.072~0.039	0.001~0.020

2.5.2 New 3-fluid gas-liquid contactor

A new 3-fluid gas-liquid contactor was developed as a fin-tube structure as shown in Fig. 2.6. The new 3-fluid gas-liquid contactor is made of aluminum, which was made possible because of the newly developed IL. Table 2.2 lists the basic dimensions of the 3-fluid fin-tube contactor. In Chapter 8, the detailed specifications of the 3-fluid gas-liquid contactor are provided together with its performance investigation in the actual liquid desiccant air conditioning system.

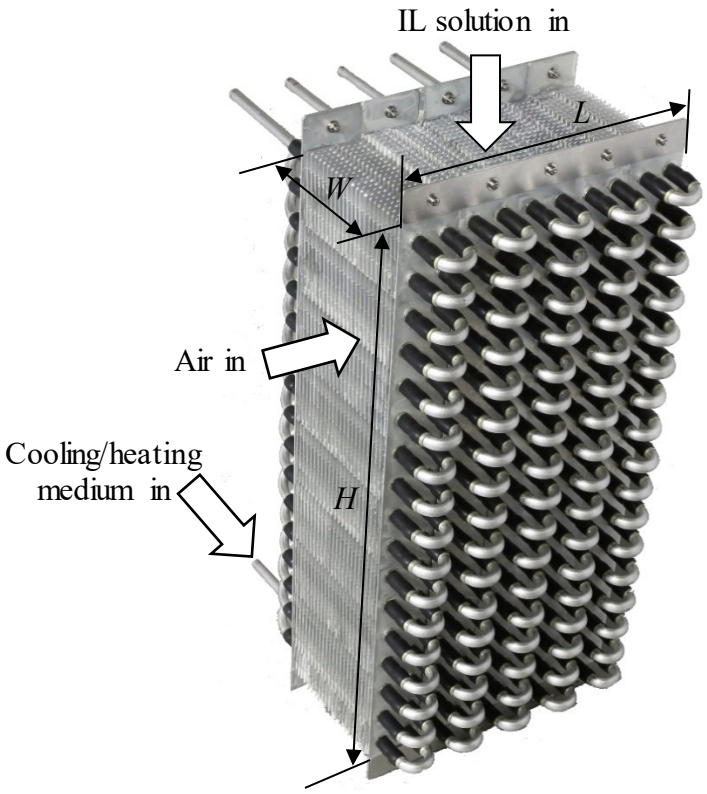

Fig. 2.6 New 3-fluid gas-liquid contactor made of aluminum.

Table 2.2 Dimensions of the fin-tube gas-liquid contactor.

Dimension	Symbol	Value
Length (air flow direction)	L	200×10^{-3} m
Height (solution flow direction)	H	400×10^{-3} m
Width (cooling/heating medium flow direction)	W	100×10^{-3} m

The design features of this 3-fluid gas-liquid contactor are essentially evident in each tube element as illustrated in Fig. 2.7. This element enables flexible structural arrangements according to the specific application and operative conditions. Adjusting the length, height, and width of the contactor corresponds to changes in the number of elements in the direction of the dimension and the performance of the gas-liquid contactor. This design investigation is ultimately explored in Chapter 9, where a volume minimization design problem based on a genetic algorithm is presented.

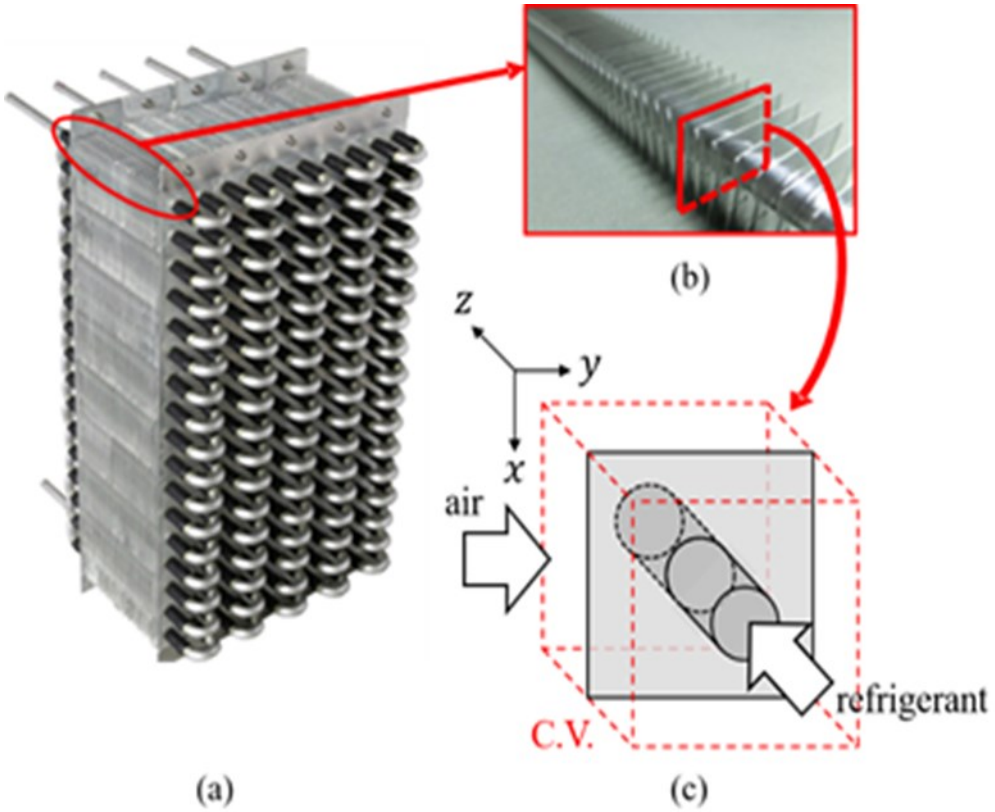

Fig. 2.7 Single tube element of the 3-fluid gas-liquid contactor.

Advanced design and control, which leads to the effective development of a thermal technology, is based on the availability of a reliable model for the transport processes in the main components of the system. In desiccant systems, the gas-liquid contactor enables the heat and mass transfer that is required for meeting the system capacity and the target conditions. In the case of the new 3-fluid gas-liquid contactor, heat, mass, and film flow are directly coupled in complex interrelations. These need to be clarified and accurately predicted in a broad range of conditions.

3. Model conceptualization

3.1 Introduction

The importance of wetting phenomena can be found in many industrial applications such as in the chemical industry (e.g. painting), construction (e.g. waterproofing), absorption system, distillation columns, and more. For example, in falling film devices, knowing the wetting characteristics of a liquid on the surface of the device is important as the wettability of the falling film on the solid surface dictates the transfer capacity of the device.

Accordingly, the modeling procedure is structured with reference to the following conceptualization.

3.2 Film wetting phenomena

Inside the gas-liquid contactor of a liquid desiccant system, the liquid desiccant solution can flow as a single falling film or as rivulets on the fin and tube surfaces. Film instabilities can cause a uniform falling film to break into rivulets and produce partial wetting on the solid substrate as shown in Fig. 3.1. For example, absorption of water vapor from the air to the liquid solution can increase the surface wetting and evaporation of water from the liquid solution can decrease the liquid wetting on the surface of the substrate. Also, cooling and heating of the solid substrate can lead to thermocapillary extension and contraction of the liquid film[73)], respectively. Variation in falling film configurations can produce different surface wetting and wetting patterns that can significantly affect the heat and mass transfer between the gas and liquid phases. These show that without proper prediction of the surface wetting inside the gas-liquid contactor, estimation of the heat and mass transfer between the gas and liquid phases would be highly inaccurate.

Fig. 3.1 Wetting phenomena, showing partial wetting, on the surface of a fin-tube substrate.

A general model with a wide range of applicability and high accuracy is targeted for being implemented in reliable and large spectrum analysis of the three-fluid contactor.

3.2.1 Theoretical formulation

Firstly, the mathematical framework is obtained from the Principle of Minimum energy applied to the simplified flow patterns of a thin film with uniform thickness (providing complete wetting of the surface) and a rivulet (ensuring only partial wetting of the transfer surface) with a circular cross-section shape under the influence of capillary and inertial forces. This results in a general, although simplified, theory for capturing film breaking and estimating partial wetting.

3.2.2 Direct observation from experiments

Subsequently, experimental data for validating the partial wetting model are collected on a dedicated test section by implementing binary image processing on photos captured during quasi-static wetting-dewetting cycles. Additionally, the measurement of contact angle hysteresis on the same solid substrate provides the necessary information for a direct comparison between theory and experiments. The direct observation of the phenomenon on a wide range of IL mass fraction provides a first comparison and a clearer phenomenological understanding of falling film wetting characteristics guides the following modeling development toward a more accurate estimation of film rupture and partial wetting.

3.2.3 Development of a semi-theoretical model

Consequently, semi-theoretical modeling of partial wetting is developed based on the previous experimental results. An increased degree of accuracy in predicting the wetting characteristics of the IL desiccant solution over the aluminum substrate is achieved through the definition and tuning of specific characteristic coefficients acting on the magnitude of the effects at play, while consistently maintaining the shape of the equations extracted by the theoretical model. The discrepancy from the unitary value of these constant coefficients from the fitting to the experimental data encloses the effect of the simplifying assumptions introduced in the theoretical formulation. The advantage of using the semi-theoretical model over the theoretical model to predict the wetting ratio of the IL on the actual 3-fluid gas-liquid contactor is also pointed out. This model enables accurate evaluation of the wetting characteristics of the sorptive solution to be combined with a heat and mass transfer transport model for conducting transfer performance analysis and optimization procedures.

3.3 Transport phenomena

3.3.1 Heat, mass, and momentum transfer

Falling films are employed as transport media in various falling film devices such as in absorption towers, film evaporators, and gas-liquid contactors. In gas-liquid contactors, coupled heat and mass transfer occur between the gas and liquid phases as shown in Fig. 3.2. The heat, mass, and momentum transfer processes between the gas and the liquid are affected by various factors, one of which is the wetting behavior of the falling liquid film.

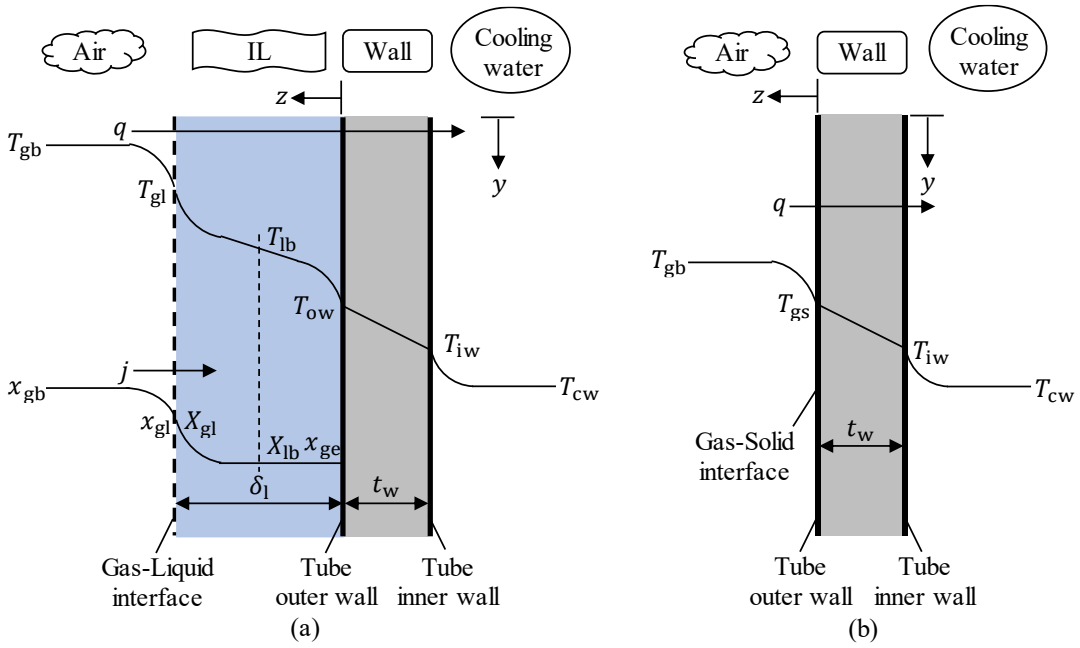

Fig. 3.2 Schematic diagram of the coupled heat and mass transfer between the gas and the liquid phases an (a) wetted wall and heat transfer on a (b) dry wall.

The modeling of the 3-fluid gas-liquid contactor is thus constructed. Heat and mass transfer geometry, assumptions, governing equations, initial and boundary conditions, heat and mass transfer coefficients, air pressure drop, and the numerical approach are described.

3.3.2 Whole device model validation

A detailed discussion of the 3-fluid gas-liquid contactor and the respective experimental apparatus is given. A thorough consideration of the gas-liquid contactors, liquid desiccants, distributors, experimental methods and procedures, and measuring instruments is carried out. The experimental results are also summarized and discussed. This provides the validation of the mathematical model of 3-fluid fin-tube gas-liquid contactor.

3.3.3 Performance analysis and volume minimization

Performance analysis of the 3-fluid gas-liquid contactor is comprehensively conducted under the effect of different design dimensions of the gas-liquid contactor. An optimization method used for minimizing the size of the 3-fluid gas-liquid contactor for a given dehumidification capacity is presented. The advantages of the 3-fluid gas-liquid contactor over conventional 2-fluid contactor are finally demonstrated and the actual application of the 3-fluid gas-liquid contactor in the actual industrial system is described.

4. Falling film partial wetting model

4.1 Introduction

The assumption of complete wetting remains to be an issue in gas-liquid contactors due to the lack of conclusive research and mathematical model for the prediction of the partial wetting. Therefore, it is necessary to develop a model for predicting the surface wetting inside the gas-liquid contactor for accurate performance evaluation, design, and optimization of the falling film device. In general, clarifying the wetting characteristics of a falling liquid film on a solid surface is complex, which requires extensive theoretical and experimental investigation to deeply understand the liquid's wetting patterns, contact angle, and critical film thickness to name a few.

In the absence of information about the wetting characteristics of a liquid desiccant on the surface of a gas-liquid contactor, complete wetting of the contactor area is assumed as a simplification in falling film models. However, this is usually not the case as film breakage and dry spots can occur[30]. Without proper calculation of the wetted area, the assumption of complete wetting can overestimate the heat and mass transfer performance inside the gas-liquid contactor[29].

4.2 Importance of partial wetting model

Wetting deals with the study of how a liquid deposited on a solid or liquid substrate spreads out[74]. In dynamic wetting processes, the definition can be extended to the study of the wetting properties of flowing films on solid surfaces (Fig. 4.1) such as in multiphase-flow devices.

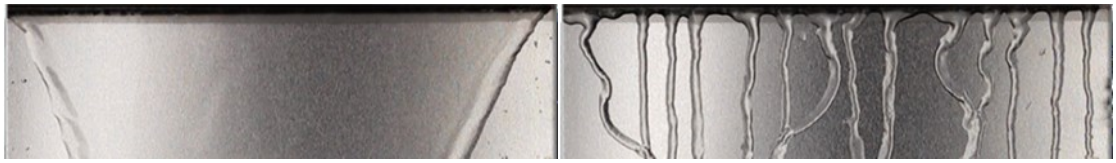

Fig. 4.1 Partial wetting on a flat vertical surface.

Primarily, it is important to investigate the wetting properties of a liquid on a substrate as various pairs of liquid and solid surface may exhibit different wetting characteristics. Inside the gas-liquid contactor of a liquid desiccant air conditioning system, the solution can flow as a single falling film or as rivulets falling on the fin and tube surfaces as shown in the right of Fig. 4.2. As the performance of desiccant systems is strongly associated with the transport performances of the contactor, it is necessary to be able to estimate the extension of the transfer interfaces within the contactor for properly defining the operation strategy of these systems. Additionally, the transfer

performance of the tertiary cooling/heating medium needs to be evaluated considering its interrelations with the gas and the liquid.

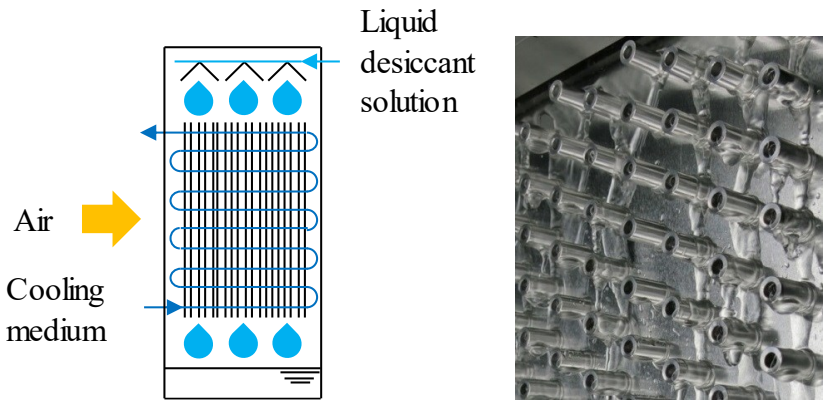

Fig. 4.2 Schematic of the 3-fluid gas-liquid contactor (left) and partial wetting on the surface of the fin-tube substrate (right).

4.3 Modeling approach

Flow systems are irreversible due to the resistances and the imperfections distributed over different scales and encountered along the flow path. There is an extensive range of characteristic scales at play that affect the flow behavior including turbulence, tensile effects, interfacial dynamics, and affinity between the liquid, solid substrate, and gaseous environment. Thus, the collection of sufficiently detailed information that exhaustively includes these effects in a deterministic (Newtonian) model of forces, resistances, and fluxes is often unlikely.

The presence of dynamic and deformable phase-interfaces and related discontinuities of fluid properties, multi-phase flows are characterized by a higher degree of complexity in deriving the governing transport and conservation equations. However, despite this difficulty, the theoretical background of multiphase systems still relies on the classical laws of thermodynamics, fluid mechanics, and principles of heat and mass transfer. Heterogeneous or multi-phase flows exhibit important engineering characteristics to realize intense heat and mass transfer processes. These can be described as the aftermath of thermodynamic instability by which the homogeneous/single-phase fluid splits into two or more sub-systems in equilibrium[75]. The physical structure of the flow eventually determines the transfer resistances of the specific technical device, and eventually, capacity, size, and power requirements of the system.

Given this viewpoint, variational methods (principles, theorems, and approximate procedures), including Helmholtz's minimum dissipation theorem[76], Hamilton's principle of least action[77)-78], Onsager's principle of minimum energy[79)-80], the principles of maximum and minimum entropy generation[81], Prigogine's theorem[82], and the

Constructal Law[83)], were proven as useful (although of debated legitimacy[84)-86)]) tools to obtain local and global solutions for problems that are less accessible from the standpoint of conservation principles and Newton's law. This is because they provide descriptions of the system's physical quantities independently from the selected frame of reference. For example, Zivi[87)] applied Prigogine's theorem to an idealized two-phase flow to analyze the steady-state value of the vapor void fraction. More recently, Giannetti et al.[88)] applied the same Theorem including the effect of surface tension within small-sized channels to predict the void fraction and flow transition between idealized annular and stratified flow patterns. Brauner et al.[89)] employed the principle of minimum energy to predict the interfacial configuration of a stratified two-phase flow. The same approach was used by Chakrabarti et al.[90)] to develop a model for predicting the pressure drop in a liquid-liquid (kerosene-water) flow through a horizontal pipe. Paulus et al.[91)] showed the consistency between the assumption of equal pressure drops and the tendency toward a condition that extremizes the rate of entropy production for the laminar flow distribution of a specified overall flowrate between two parallel ducts. Recently, Daibirian et al.[92)] investigated a computational algorithm to predict two-phase flow splitting and corresponding pressure drop in looped lines for the oil and gas industry.

4.4 Theoretical modeling

The modeling approach employed is based on the following principles:

1) the definition of the ideal geometry of two flow configurations; a uniform film fully wetting the solid substrate and a rivulet with a circular cross-section shape (Fig. 4.3):

2) the hydrodynamic description established by the solution of the stream-wise momentum equation under the assumptions of Nusselt integral theory (Eq. (4.2)): isothermal flow with constant properties, under the assumption that the momentum transfer is dominated by viscous forces without convection, in the absence of inertia and pressure forces, and no shear stress is generated at the gas-liquid interface[93)-96)].

3) the variational method developed in a previous paper[97)] with reference to the Principle of Minimum Energy[98)], which can predict its wettability over the 3-fluid gas-liquid contactor under analysis (Eq. (4.1)) and, beyond this, defines the limit of stability of a uniform film (Eq.(4.3)); where E defines the energetic contents of the flow and ω determines the flow configuration of the rivulet.

The analysis is applied to a fully developed, steady, and laminar flow configuration, under the assumption that neither the fluid distribution at the inlet nor the size of the test section, affect the results obtained. It is further assumed that the liquid film is characterized by a uniform thickness and surface tension (hence excluding thermo-distill-capillarity effects on the flow). The calculation is, thus, performed with respect to

the smallest symmetrical section of the fin-tube test section (Fig. 4.3), which is used to characterize the wetting behavior of the whole fin.

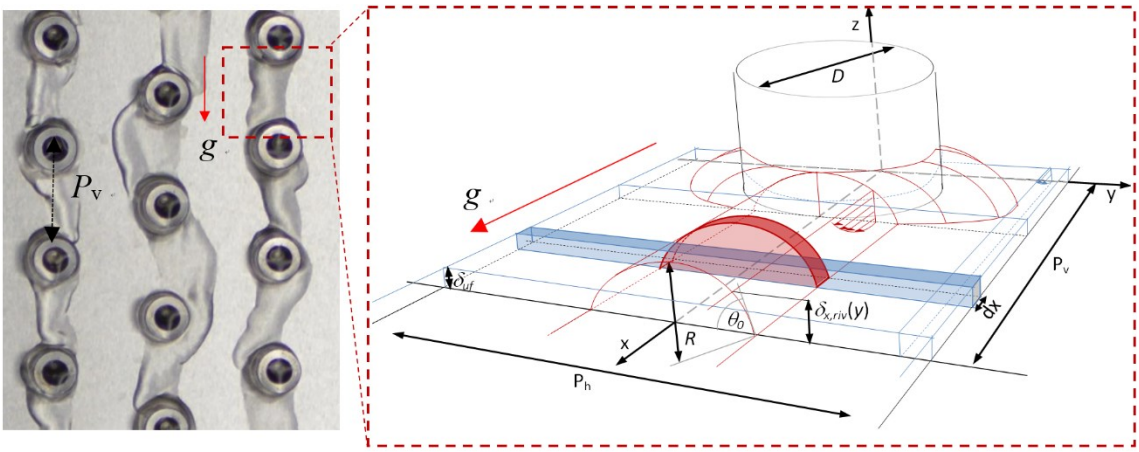

Fig. 4.3 Schematic of the rivulet configuration along a fin-tube substrate.

$$\frac{\partial E_{\mathrm{riv}}}{\partial \omega} = 0, \qquad \frac{\partial^2 E_{\mathrm{riv}}}{\partial \omega^2} > 0 \qquad (\mathrm{J\cdot m^{-1}}) \qquad (4.1)$$

$$\mu \frac{\partial^2 \mu}{\partial z^2} = -\rho g \qquad (\mathrm{kg\cdot m^{-2}\cdot s^{-2}}) \qquad (4.2)$$

$$E_{\mathrm{riv}} = E_{\mathrm{uf}} \qquad (\mathrm{J\cdot m^{-1}}) \qquad (4.3)$$

The mass flow rate per unit substrate width is expressed (Eq.(4.4)) by considering complete and uniform wetting as follows:

$$\Gamma(x) = \frac{2\dot{m}}{N\left(P_{\mathrm{h}} - 2\sqrt{Dx - x^2}\right)} \qquad (\mathrm{kg\cdot m^{-1}\cdot s^{-1}}) \qquad (4.4)$$

Furthermore, the solution of Eq. (4.2) for the boundary conditions imposing no slip at the solid substrate ($u = 0$ at $z = 0$) and no shear stress at the free interface ($\partial u/\partial z = 0$ at $z = \delta_{\mathrm{uf}}$) leads to Eq. (4.5).

$$u(z) = \frac{\rho g}{2\mu}(2\delta_{\mathrm{uf}} z - z^2) \qquad (\mathrm{m\cdot s^{-1}}) \qquad (4.5)$$

Continuity leads to the expression of the film thickness written in Eq. (4.7). It is hereby assumed that the thickness of the liquid film is uniquely determined in the y direction as given in Eqs. (4.4) - (4.6). This assumption also applies when the liquid film is flowing around the tube.

$$\Gamma_{\mathrm{uf}} = \int_0^{\delta_{\mathrm{uf}}} \frac{\rho^2 g}{2\mu}(2\delta_{\mathrm{uf}} z - z^2)dz = \frac{1}{3}\frac{\rho^2 g}{\mu}\delta_{\mathrm{uf}}^3 \qquad (\mathrm{kg\cdot m^{-1}\cdot s^{-1}}) \qquad (4.6)$$

which yields

$$\delta_{\mathrm{uf}}(x) = \left(\frac{3\mu\Gamma}{\rho^2 g}\right)^{1/3} \qquad (\mathrm{m}) \qquad (4.7)$$

The principle of minimum energy is used to determine the stability of the liquid film on the fin surface and to define the wetting area. Generally, the affinity between the solid-liquid phases, liquid properties, flow configuration, and solid surface features control the evolution of the wetting configuration. Particularly, the conflicting effects of gravity and surface tension (the first forcing towards flowing configurations and iso-potential flat interfaces while the second tends to create stationary spherical phase boundaries) establish a limit of configuration-stability that in certain operative conditions is associated with hysteresis phenomena[99]. The common contributions to the energy content of flow include kinetic, potential, internal, and surface energies. However, for the aim of determining the stable wetting configuration and the transition between complete and partial wetting, the potential and internal energies have a negligible influence on the thermodynamic system under analysis. Specifically, the variation on the flow wettability (identified below by the geometrical parameter *WR*, Eq. (4.15)) due to temperature variations and vice versa are negligible, and gravity acts uniformly on the vertical flow, independent on the flow wettability. Mathematically, the conceptual derivation presented in Eq. (4.1) and the equivalence in Eq. (4.3) are not affected by the gravitational potential energy and internal energy contributions. Thus, the energy of the liquid film and the corresponding rivulet configuration is estimated as the sum of the surface tension and the kinetic energy (Eq. (4.8)) as follows:

$$e = \frac{E}{\lambda} = \frac{1}{\lambda}(E_{\mathrm{k}} + E_{\mathrm{s}}) = \frac{1}{\lambda}\left(\int_A \frac{1}{2}\rho u^2 dA + \int_S \sigma dS\right) \qquad (\mathrm{J\cdot m^{-2}}) \qquad (4.8)$$

The energy of the uniform liquid film and that of the ruptured film flowing in a stable rivulet configuration are calculated under the assumption that the velocity profile in Eq. (4.5) also applies to the rivulet cross-section in Eq. (4.10).

The development of Eq. (4.8) for the rivulet cross section per unit transversal length λ, gives Eq. (4.9).

$$e_{\mathrm{uf}} = \frac{\rho}{2\lambda}\int_0^{\delta_{\mathrm{uf}}} \left[\frac{\rho g}{2\mu}(2\delta_{\mathrm{uf}} z - z^2)\right]^2 dz + \sigma_{\mathrm{sl}} + \sigma_{\mathrm{gl}} \qquad (\mathrm{J\cdot m^{-2}}) \qquad (4.9)$$

The cross section of the rivulet configuration is approximated by a circular segment of radius R cutting the solid substrate with an angle equal to the contact angle of the specific solid-liquid pair θ_0.

$$\delta_{\mathrm{riv}}(y) = R(\cos\theta - \cos\theta_0) \quad \text{(m)} \qquad (4.10)$$

The expression of the sum of kinetic and surface tension energy of the rivulet configuration is given by Eq. (4.11).

$$\begin{aligned} e_{\mathrm{riv}} &= \frac{\rho}{\lambda}\int_0^{Rsin\theta_0}\int_0^{\delta_{\mathrm{riv}}(y)}\left[\frac{\rho g}{2\mu}(2\delta_{\mathrm{uf}}z - z^2)\right]^2 dzdy + \frac{2Rsin\theta_0}{\lambda}\sigma_{\mathrm{sl}} \\ &\quad + \frac{2R\theta_0}{\lambda}\sigma_{\mathrm{gl}} + \frac{2\lambda - Rsin\theta_0}{\lambda}\sigma_{\mathrm{sg}} \quad (\mathrm{J\cdot m^{-2}}) \qquad (4.11) \\ &= \frac{2}{15\lambda}\frac{\rho^3 g^2}{\mu^2}R^6\psi(\theta_0) + \frac{2\sigma_{\mathrm{gl}}Rsin\theta_0}{\lambda}\left[\frac{\theta_0}{sin\theta_0} - cos\theta_0\right] + \sigma_{\mathrm{sg}} \end{aligned}$$

where

$$\begin{aligned} \psi(\theta_0) &= \int_0^{\theta_0}(\cos\theta - \cos\theta_0)^5\cos\theta\, d\theta \\ &= \theta_0\left(\frac{5}{16} + \frac{15}{4}\cos^2\theta_0 + \frac{5}{2}\cos^4\theta_0\right) \qquad (4.12) \\ &\quad - \sin\theta_0\left(\frac{113}{48}\cos\theta_0 + \frac{97}{24}\cos^3\theta_0 + \frac{1}{6}\cos^5\theta_0\right) \end{aligned}$$

The specific flow rate of this flow configuration (Eq. (4.13)) is obtained under the previously mentioned assumption that the velocity profile in Eq. (4.5) also applied to the rivulet cross-section.

$$\Gamma_{\mathrm{riv}} = \frac{\dot{m}_{\mathrm{riv}}}{P_{\mathrm{h}}} = \frac{2}{P_{\mathrm{h}}}\int_0^{Rsin\theta_0}\int_0^{\delta_{\mathrm{riv}}(y)}\rho u(z)dzdy = \frac{2}{3P_{\mathrm{h}}}\frac{\rho^2 g}{\mu}R^4\gamma(\theta_0) \quad (\mathrm{kg\cdot m^{-1}\cdot s^{-1}}) \quad (4.13)$$

where

$$\gamma(\theta_0) = \int_0^{\theta_0} (\cos\theta - \cos\theta_0)^3 \cos\theta \, d\theta$$
$$= -\frac{1}{4}\cos^3\theta_0 \sin\theta_0 - \frac{13}{8}\cos\theta_0 \sin\theta_0 - \frac{3}{2}\theta_0 \sin^2\theta_0 + \frac{15}{8}\theta_0 \tag{4.14}$$

The wettability of the flow is defined as the ratio of the wetted extension of the surface (corresponding to the solid-liquid interface) to the reference transversal unit length λ. A geometric parameter, called "wetting ratio" *WR*, is thus introduced and treated as a generalized variable under the variational approach hereby implemented. The latter is identified as that yielding minimal rivulet energy (Eq. (4.11)) when minimized with respect to the geometric variable ω matching, in this case, the parameter describing the wet part of the solid substrate *WR* (Eq. (4.15)).

$$WR = \frac{2R\sin\theta_0}{P_\mathrm{h} - 2\sqrt{Dx - x^2}}, \qquad 0 \le x \le D$$
$$WR = \frac{2R\sin\theta_0}{P_\mathrm{h}}, \qquad D < x \le P_\mathrm{v} \tag{4.15}$$

Given that the surface tension is considered constant, it is assumed that the cross section of the rivulet is approximated by a segment of a circle with a contact angle θ_0 as shown in Fig. 4.3. The surface tension equilibrium is assured by the Young-Depree relation. The mass balance between the two flow configurations yields a relation (Eq. (4.16)) between the rivulet radius *R*, the uniform film thickness δ_{uf}, and the parameter used to estimate the wet part of the surface *WR*.

$$\frac{\delta_{\mathrm{uf}}}{R} = WR\frac{\gamma(\theta_0)}{\sin\theta_0} \tag{4.16}$$

Plugging this relationship in Eq. (4.11) and Eq. (4.16), the specific energy of the rivulet becomes

$$e_{\mathrm{riv}} = \frac{1}{15}\frac{\rho^3 g^2}{\mu^2} R^5 WR \frac{\psi(\theta_0)}{\sin\theta_0} + WR\sigma_{\mathrm{gl}}\left[\frac{\theta_0}{\sin\theta_0} - \cos\theta_0\right] + \sigma_{\mathrm{sg}}$$
$$= \frac{1}{15}\frac{\rho^3 g^2}{\mu^2} WR^{-\frac{2}{3}} \left[\frac{\sin\theta_0}{\gamma(\theta_0)}\right]^{\frac{5}{3}} {\delta_{\mathrm{uf}}}^5 \frac{\psi(\theta_0)}{\sin\theta_0} \qquad (\mathrm{J\cdot m^{-2}}) \tag{4.17}$$
$$+ WR\sigma_{\mathrm{gl}}\left[\frac{\theta_0}{\sin\theta_0} - \cos\theta_0\right] + \sigma_{\mathrm{gl}}$$

The following is hence obtained when solving for *WR*

$$WR = \left\{ \frac{2}{45} \frac{\psi(\theta_0)}{\sin\theta_0} \left[\frac{\theta_0}{\sin\theta_0} - \cos\theta_0 \right]^{-1} \right\}^{3/5} \frac{\sin\theta_0}{\gamma(\theta_0)} \left(\frac{9}{4} \frac{\mathrm{Re}}{\mathrm{We}^3} \right)^{1/5} \tag{4.18}$$

Equation (4.3) represents the stability criterion of the uniform film yielding to the estimation of the minimum wetting rate that assures the complete wetting of the solid substrate. Eq. (4.21) is obtained by equating the energy of the rivulet in the extremum condition obtained for a wetting given by Eq. (4.18) and the film energy in Eq. (4.9).

$$\frac{3}{5} \left(\frac{3}{4} \frac{\mathrm{Re}}{\mathrm{We}^3} \right)^{1/3} + 1 - \cos\theta_0 - G(\theta_0) \left(\frac{3}{4} \frac{\mathrm{Re}}{\mathrm{We}^3} \right)^{1/5} = 0 \tag{4.19}$$

where

$$G(\theta_0) = \frac{5}{2} \left[\frac{\sin\theta_0}{\gamma(\theta_0)} \right] \left[\frac{2\psi(\theta_0)}{3\sin\theta_0} \right]^{2/5} \left[\frac{\theta_0}{\sin\theta_0} - \cos\theta_0 \right]^{2/5} \tag{4.20}$$

With a given contact angle, the related geometrical functions ($\gamma(\theta_0)$), $\psi(\theta_0)$ and $G(\theta_0)$) of the rivulet, and the thermophysical properties of the liquid, the stability of the film and the wetting ability of the rivulet can be estimated.

Equation (4.21) represents the stability criterion of the uniform film (analytical details are given in Giannetti et al.[97] yielding to the estimation of the minimum Reynolds number (Eq. (4.22)) that assures the complete wetting of the solid substrate.

$$\Delta_b^5 + (1 - \cos\theta_0) - G(\theta_0)\Delta_b^3 = 0, \qquad \Delta_b = \left(\frac{\rho^3 g^2}{15\sigma\mu^2} \right) \delta_{\mathrm{uf,b}} \tag{4.21}$$

$$\mathrm{Re_b} = \left(\frac{3g\mu^4}{4^5 15^3 \rho\sigma^3} \right) \Delta_b^3 = 6.77\mathrm{Ga}^{1/5}\Delta_b^3 \tag{4.22}$$

Hence, when the film flowrate is lower than that yielding the minimum Reynolds number in Eq. (4.22), the film is assumed to be broken and the local wetting ratio *WR* can be estimated by Eq. (4.18).

As the liquid must indeed advance or retreat at the three-phase contact line in order to enlarge or reduce the solid-liquid interface of the flowing rivulet, these situations are distinguished by utilizing the advancing and receding contact angles (Fig. 4.4) for increasing and decreasing flow rates, respectively.

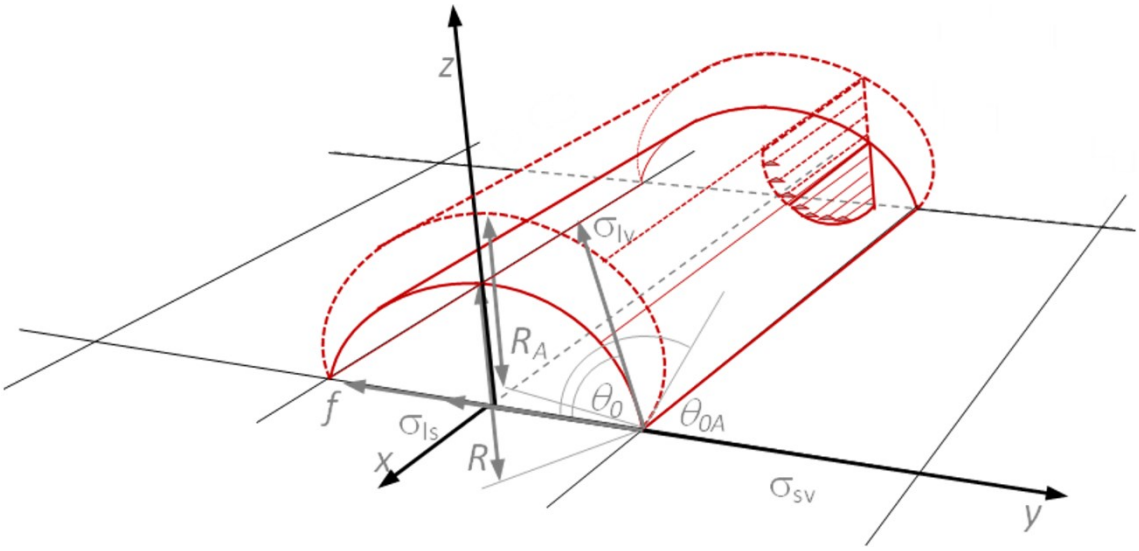

Fig. 4.4 Representation of the advancing contact angle of the rivulet due to increasing flow rate.

The direct outcomes of Eqs. (4.21) and (4.19) are shown in Fig. 4.5 and Fig. 4.6, respectively. Fig. 4.5 illustrates the film and rivulet energies (and their difference) over a comprehensive range of Reynolds number ranging from zero to the condition of complete wetting. This condition is hereby always associated with a film with uniform thickness δ_{uf}.

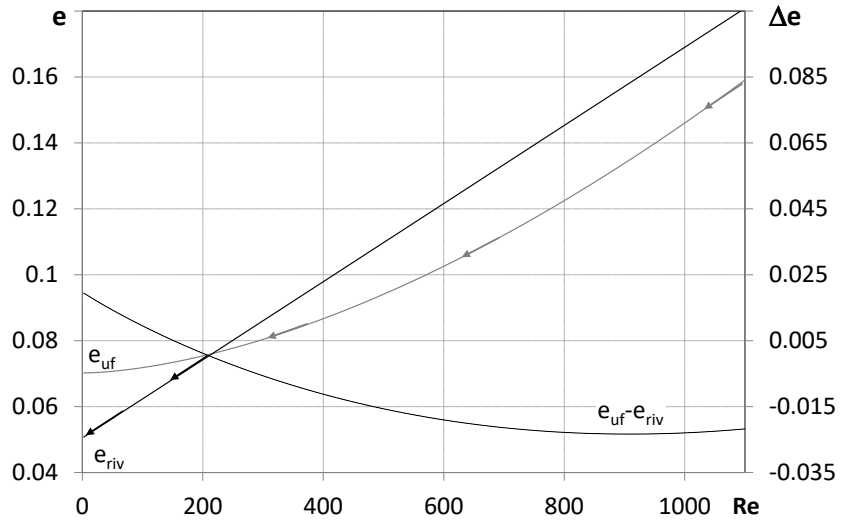

(a)

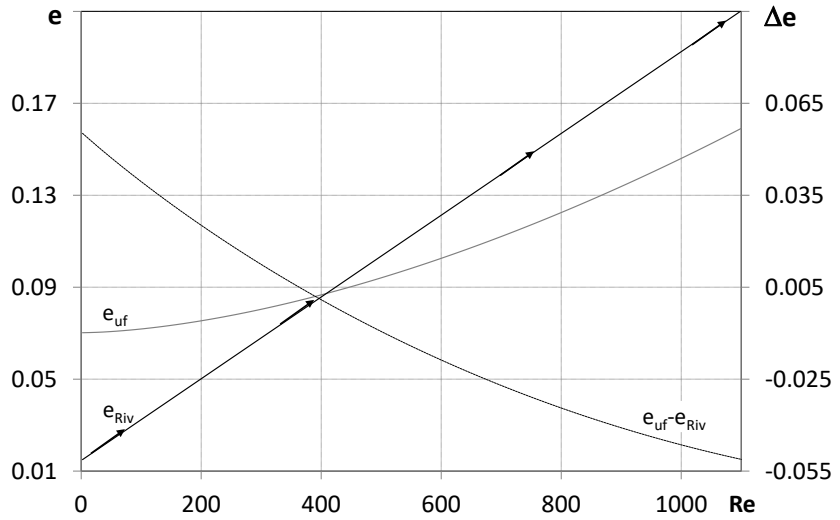

(b)

Fig. 4.5 Specific energy per unit stream-wise length [J·m^{-2}] of pure water rivulet and uniform film configurations as a function of film Reynolds number; T=25ºC, (a) decreasing ($\theta_0 = \theta_R$) and (b) increasing ($\theta_0 = \theta_A$) liquid flow rates.

Quasi-statically decreasing the mass flowrate starting from a uniform film configuration, complete wetting of the surface is maintained until the minimum critical wetting rate is reached (Eq. (4.22)). Thereupon, the flow will break, switching to the rivulet configuration with a contact angle θ_0 equal to the receding value θ_R. As plotted in Fig. 4.5, for a certain value of surface tension σ_{gl} and Reynolds number equal to or below 200, the rivulet configuration has lower energy than the film flow configuration and becomes stable for a wetting ratio of about 0.4 (Fig. 4.4(a)). In these graphs, the energy of the two configurations is quantified up to the value of σ_{gl}, which is not directly available in the literature. Nonetheless, this quantity does not influence the results and analysis of this investigation.

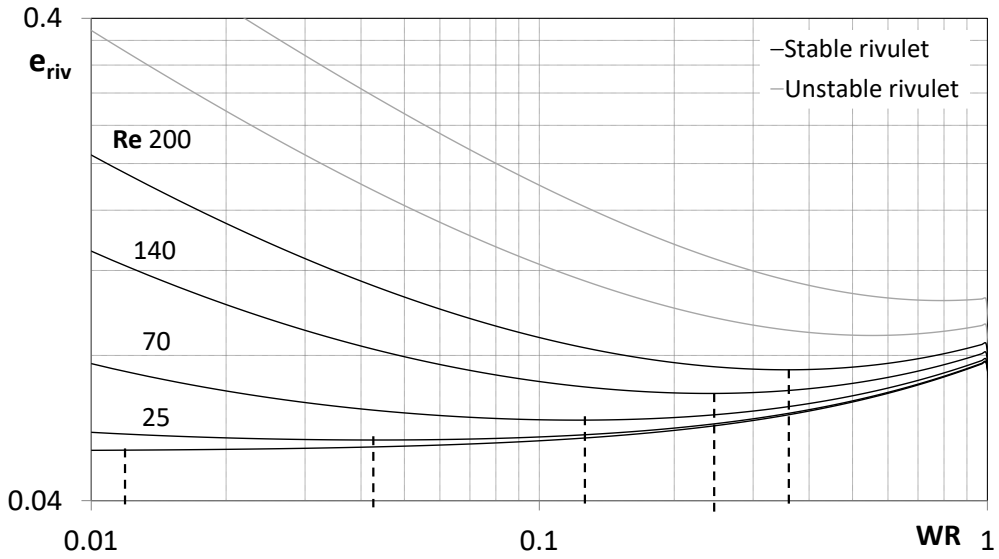

(a)

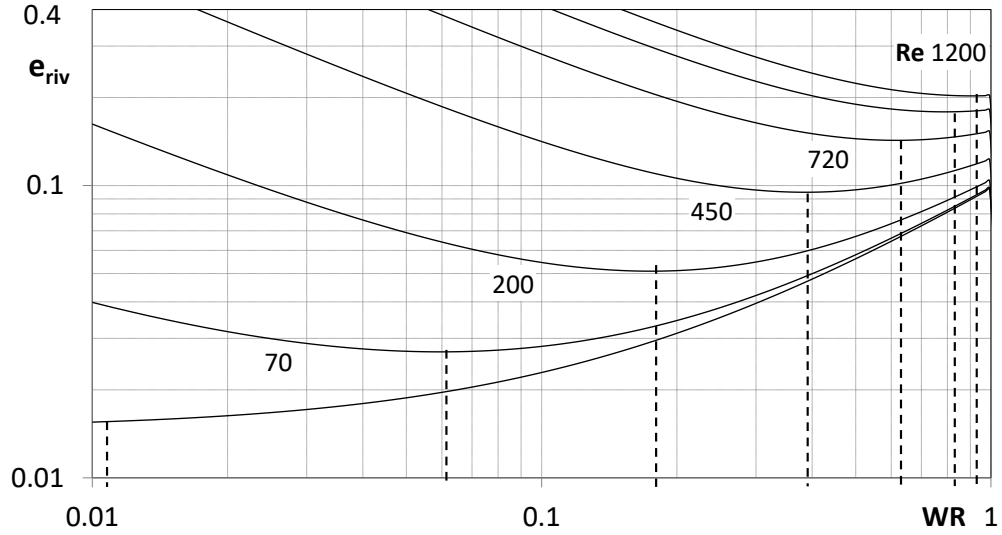

(b)

Fig. 4.6 Specific energy per unit width and per unit stream-wise length [J·m^{-2}] of a pure water rivulet on a vertical fin-tube substrate. T=25ºC, for (a) decreasing ($\theta_0 = \theta_R$) and (b) increasing ($\theta_0 = \theta_A$) liquid flow rates.

As the stable rivulet configuration corresponds to e, minimum of its thermodynamic potential (local minimum energy) for increasing mass flow rates, the rivulet configuration is maintained (Fig. 4.5(a)) until the rivulet solid-liquid interface covers the whole surface (WR = 1 in Fig. 4.6(b)). In this case, the advancing contact angle θ_A is used in the calculation. Consequently, the values of the WR for increasing Reynolds number corresponds to the abscissa of the local minima in Fig. 4.6(b).

Fig. 4.7(a) shows the local wetting behavior for decreasing Reynolds number, locally based on the critical condition and stable wetting ratio expressed by Eq. (4.19) and (4.18), respectively, when the receding value of the contact angle θ_R is used. When the film Reynolds number decreases to the point where the local rivulet energy is lower than the local uniform film configuration, the wetting ratio is given by Eq. (4.18). Fig. 4.7(b) is obtained for increasing liquid mass flow rates and using the advancing contact angle θ_A, making evidence of the wetting ability of the flowing liquid when the rivulet configuration is maintained until complete wetting is reached.

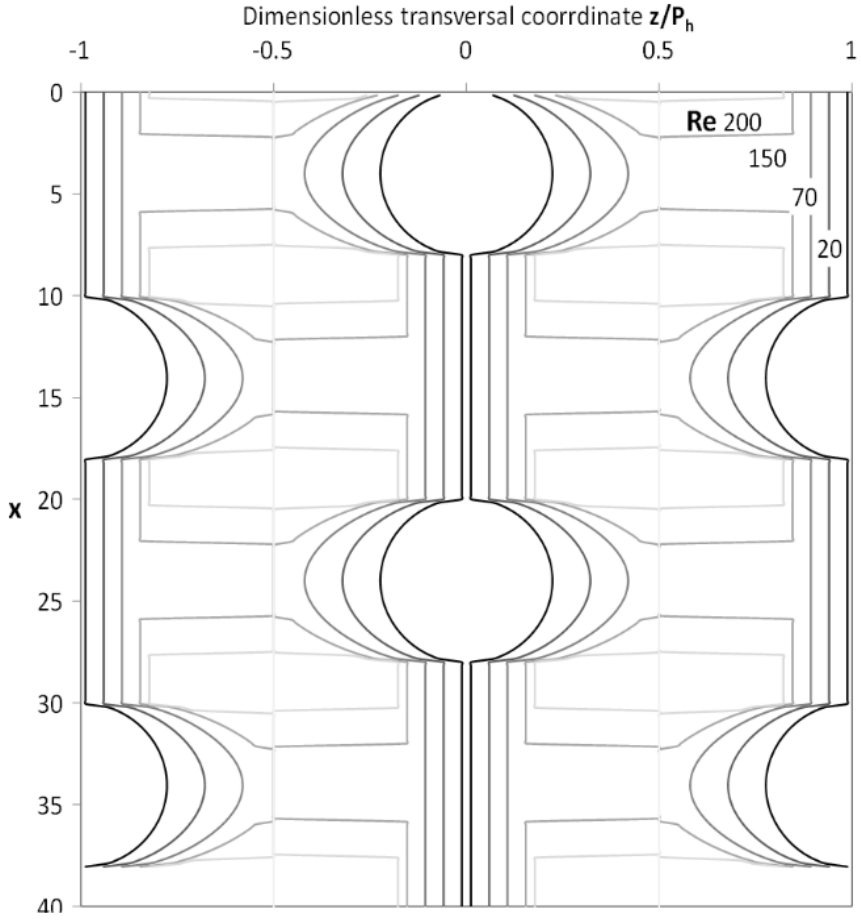

(a)

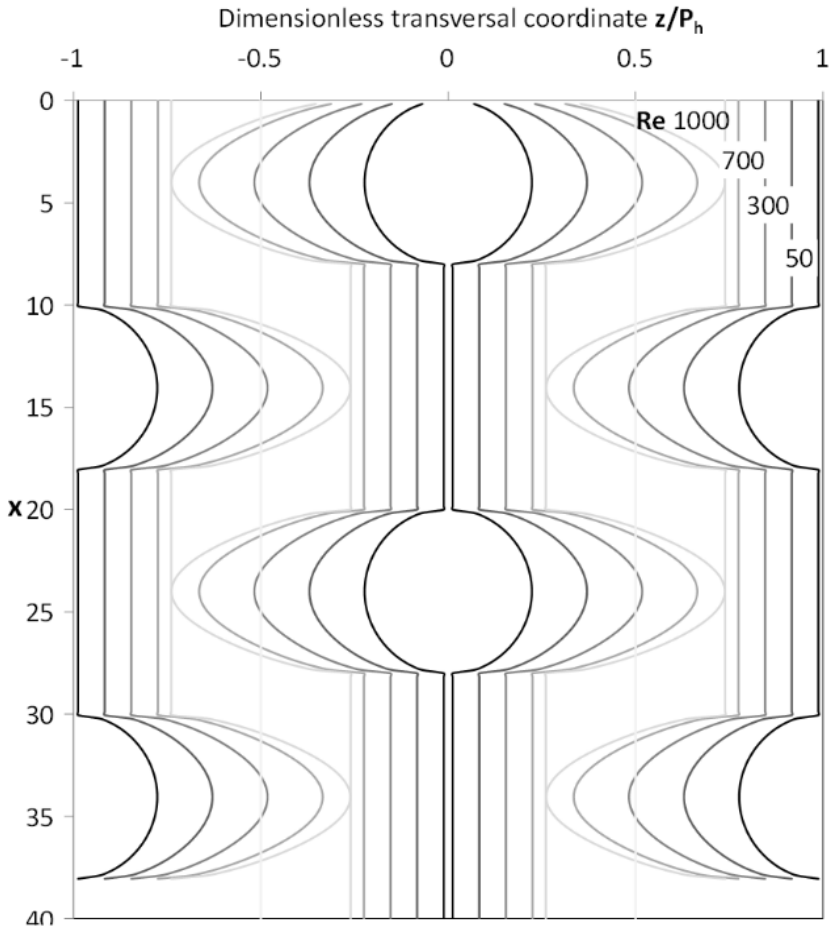

(b)

Fig. 4.7 Simulated local wetting behavior of pure water on a vertical fin-tube substrate. T=25°C, for (a) decreasing ($\theta_0 = \theta_R$) and (b) increasing ($\theta_0 = \theta_A$) liquid flow rates.

The surface wetting WS (Eq. (4.23)) is obtained from the integration of the local WR in the stream-wise direction for a span equal to the vertical pitch P_v measured between tube centers.

$$WS = \int_0^{P_v} WR dx \tag{4.23}$$

Fig. 4.8 illustrates the resulting wetting hysteresis along a wetting-dewetting cycle. The hysteresis phenomenon can be separated into two main contributions. The first is related to the contact angle hysteresis and the second is the thermodynamic stability of the two flow configurations, which affects the first contribution.

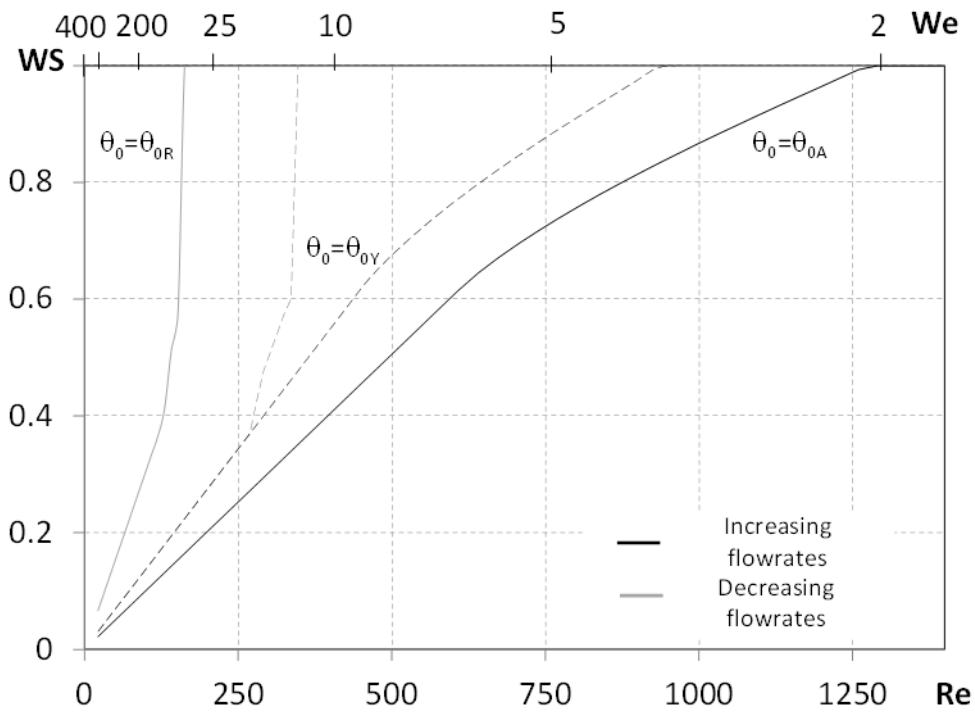

Fig. 4.8 Global wetting behavior of water on a vertical fin-tube substrate, T=25°C.

5. Experiment and validation of the partial wetting model

5.1 Introduction

To validate the falling film partial wetting model, an experimental apparatus was built to understand the wetting characteristics of the new IL. A single aluminum fin was mounted on the test section of the experimental apparatus to visualize the wetting phenomenon. The aluminum fin was embedded with banks of tubes to include their effect on the wettability. Since it is difficult to investigate the wetting phenomena inside an actual fin-tube contactor due to its compact design, the construction of the flow visualization apparatus became more essential.

The experimental data were analyzed, and different wetting patterns were observed. Data on the contact angle, including the static and dynamic contact angles of the IL, were also gathered. The contact angle hysteresis of the IL solution on the aluminum surface was evaluated and the factors causing its occurrence were identified. Furthermore, wetting hysteresis on the single aluminum fin with tubes was investigated. The principles of minimum wetting rates and film stability, and their relationship on the occurrence of wetting hysteresis were analyzed and the factors affecting the wetting hysteresis were identified

5.2 Experimental investigation of the wetting characteristics of the new IL

5.2.1 Experimental apparatus and procedures

Fig. 5.1(a) shows a photo of the experimental apparatus and Fig. 5.1(b) illustrates a schematic diagram of the wetting visualization apparatus. The manually constructed experimental setup is composed of a solution tank at the top for IL solution storage, a distributor, a test section where the single fin is mounted, a solution reservoir, and a solution pump.

Fig. 5.2 presents the aluminum fin with banks of tubes arranged in a staggered configuration. It also emphasizes the tube diameter D, the horizontal pitch P_h, and vertical pitch P_v measured between the tube centers. On the other hand, Table 5.1 provides the dimensions of the fin and tubes.

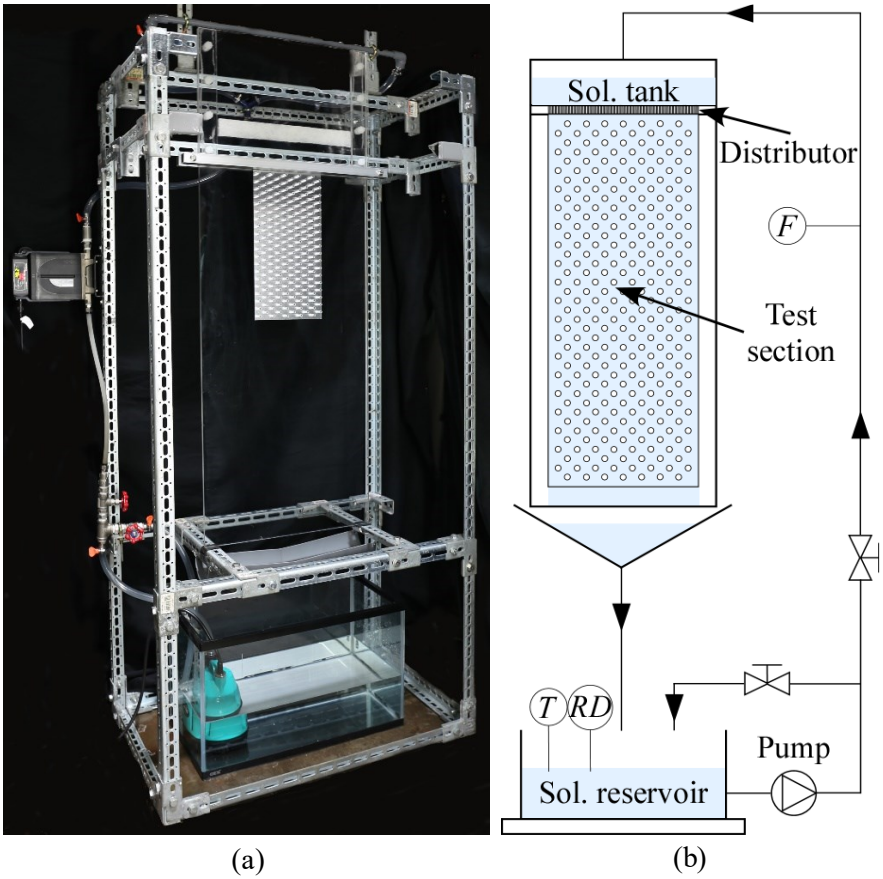

Fig. 5.1 (a) Photo and (b) schematic diagram of the visualization apparatus.

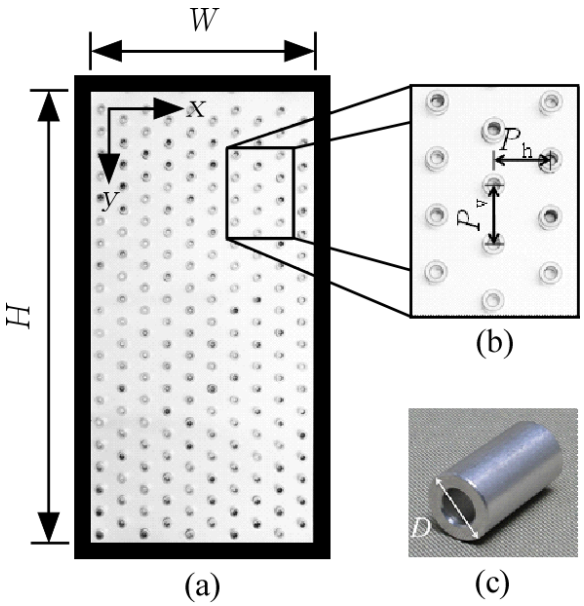

Fig. 5.2 (a) Photo of the single aluminum fin with tubes, (b) tube horizontal and vertical pitch, and (c) tube outer diameter.

Table 5.1 Dimensions of the fin and tubes.

Parameter	Value
W	200×10^{-3} m
H	400×10^{-3} m
P_h	20×10^{-3} m
P_v	20×10^{-3} m
D	7.95×10^{-3} m

Fig. 5.3(a) shows a photo and Fig. 5.3(b) illustrates the cross-section of the distributor. The distributor is made of acrylic with slits in the transverse direction, where the solution passes.

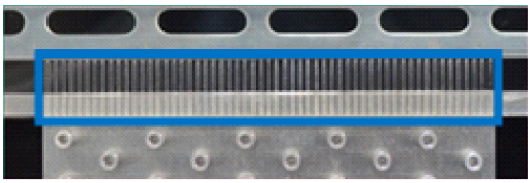

(a)

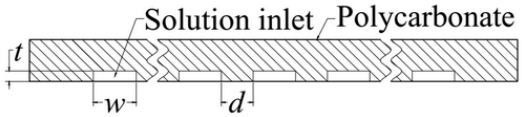

(b)

Fig. 5.3 (a) Phot of the distributor and (b) illustration of the distributor cross-section.

Two types of distributors were investigated during the experimental work. Distributor 1 has a smaller slit area compared to distributor 2 but has a longer distance between slits. Table 5.2 gives the details of both distributors.

Table 5.2 Details of the distributors.

Parameter		Value
Distributor 1	Opening thickness, t	0.5×10^{-3} m
	Opening width, w	2×10^{-3} m
	Distance between opening, d	1.5×10^{-3} m
	Number of openings, n	57
Distributor 2	Opening thickness, t	0.6×10^{-3} m
	Opening width, w	2.5×10^{-3} m
	Distance between opening, d	0.5×10^{-3} m
	Number of openings, n	66

The wetting visualization experiment is started by preparing an aqueous solution with the required IL mass fraction and circulating it in the whole system at a sufficient flow rate to completely wet the test section. Then, the test section is allowed to dewet naturally. This cycle of wetting and dewetting is performed five times to remove dust and

other impurities from the test section before the data gathering is conducted. Next, with the pump operating, the flow control valve is adjusted to obtain the desired solution flow rate. When the wetted area in the test section is at the steady-state condition, data gathering is started by taking photos of the test section. Just after a photo is taken, the solution temperature and relative density are measured for that wetting data. Data gathering was carried out at various solution flow rates in increasing and decreasing trends at an ambient temperature of approximately 34°C. Batch experiments were conducted at various IL mass fractions in the solution.

After the images are taken, image processing is done to estimate the wetting fraction/wetting ratio. Fig. 5.4 illustrates the output of each step in the image processing. The process is started by trimming down the raw image so that the only left is the image of the aluminum fin-tube substrate. Next, the boundaries of the liquid film and rivulets on the substrate are traced. Then, the areas which are not part of the liquid film and rivulets, these include the dry area and static droplets, are removed. Next, the resulting image is converted to a black and white scale with black representing the wetted area and white representing the dry area. Finally, the tube areas are deleted using dummy tubes.

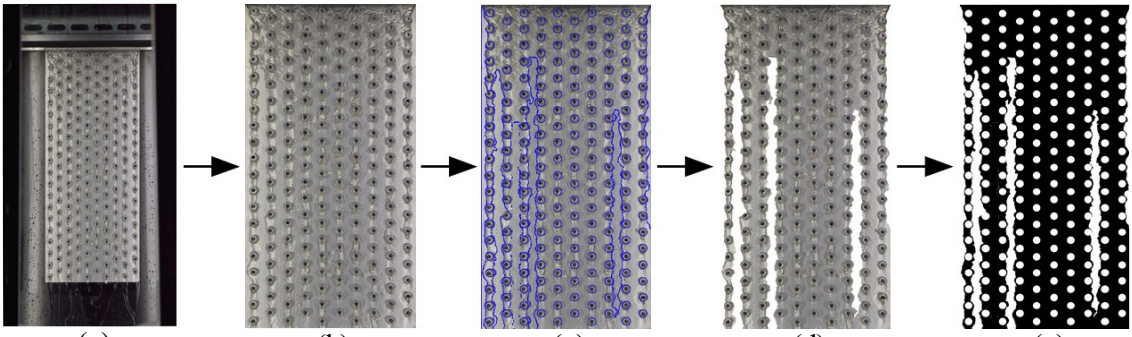

Fig. 5.4 Image processing output: (a) raw, (b) cropped, (c) wetted area traced, (d) dry areas removed, and (e) tube areas removed.

Table 5.3 summarizes the specifications of the instruments used to measure the fluid properties during the visualization experiments. It was observed that the Coriolis flow sensor does not give accurate readings for solution flow rates below 1 $L \cdot min^{-1}$, this was verified by collecting an amount of solution at the outlet of the test section and dividing it by the time it took for that solution to be gathered. Due to this, the latter-mentioned evaluation method was used to record solution flow rates below 1 $L \cdot min^{-1}$.

Table 5.3 Specifications of the measuring instruments.

Property	Measuring instrument	Range	Accuracy
F	Coriolis flow sensor	0~20 $L \cdot m^{-1}$	0-25% of FS: ±1% of FS
T	T type thermocouple	-50~350°C	±1°C (-50~99.9°C)

RD	Specific gravity hydrometer	1.06~1.12, 1.12~1.18	±0.001

5.2.2 Visualization and analysis of the surface wetting

Table 5.4 lists selected experimental results from the wetting visualization experiments. In this table, letters (a) to (e) are data for the increasing flow rate condition while letters (f) to (j) are for the decreasing flow rate condition.

Table 5.4 Wetting visualization experimental data.

X	Parameter	Increasing (a)	(b)	(c)	(d)	(e)	Decreasing (f)	(g)	(h)	(i)	(j)
0	*WR*	0.0893	0.3661	0.6183	0.8976	0.9614	0.9589	0.9147	0.6117	0.3264	0.2366
	Γ	0.0063	0.043	0.0840	0.1523	0.2858	0.0703	0.0441	0.0283	0.0074	0.0052
	Re	20.26	200.36	400.09	739.83	1394.2	342.23	215.02	146.29	37.19	25.8
	We	426.73	8.64	2.80	1.03	0.36	3.74	8.14	16.59	157.02	287.36
34	*WR*	0.2888	0.447	0.643	0.8268	0.97	0.966	0.8438	0.7558	0.6092	0.5658
	Γ	0.185	0.0546	0.0838	0.1434	0.2865	0.1658	0.1004	0.0537	0.0387	0.0229
	Re	27.02	76.49	127.18	207.39	388.94	224.99	142.34	76.16	61.02	36.05
	We	36.25	5.99	2.81	1.19	0.38	0.95	2.16	6.12	10.19	24.48
45	*WR*	0.2499	0.4505	0.6059	0.7949	0.99	0.9498	0.8254	0.6494	0.4801	0.3741
	Γ	0.0097	0.0532	0.064	0.1261	0.3422	0.2207	0.0747	0.0499	0.0249	0.0092
	Re	7.39	35.94	42.29	97.83	252.91	72.2	41.43	22.6	8.47	6.21
	We	116.4	7.08	5.45	1.62	0.32	2.34	5.9	15.06	77.35	132.25
60	*WR*	0.3581	0.4176	0.6847	0.8874	0.9554	0.9787	0.8805	0.7436	0.6005	0.5992
	Γ	0.0142	0.0294	0.0601	0.1178	0.1592	0.1781	0.0665	0.0375	0.0268	0.0158
	Re	6.04	15.67	25.57	63.67	81.73	96.25	33.3	18.77	14.1	7.84
	We	73.21	19.64	6.60	1.97	1.21	0.99	5.24	13.62	23.4	57.21
75	*WR*	0.4907	0.5907	0.6914	0.8921	0.9537	0.9528	0.8492	0.7956	0.7417	0.6944
	Γ	0.0301	0.034	0.0523	0.0712	0.0863	0.0669	0.023	0.0223	0.0169	0.0102
	Re	5.50	7.24	11.15	16.71	17.1	14.91	5.18	4.88	3.49	1.98
	We	26.04	20.16	9.83	5.64	4.36	6.38	37.57	40.15	65.11	153.78

The next set of figures illustrates the wetting on the aluminum fin-tube substrate for the selected experimental data presented in Table 5.4.

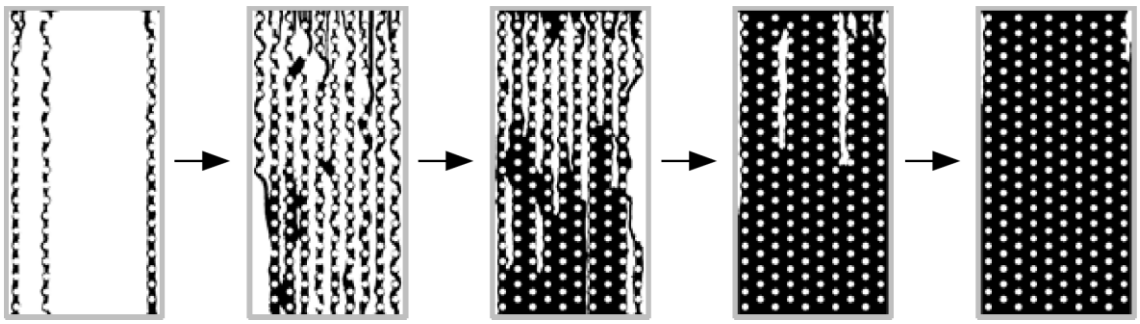

(a) (b) (c) (d) (e)

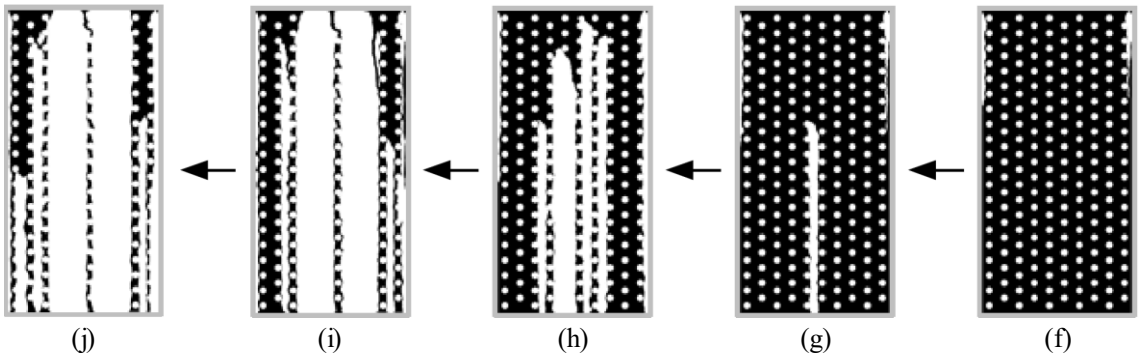

Fig. 5.5 Surface wetting at 0% IL mass fraction for gradually increasing (→) and decreasing (←) solution flow rates.

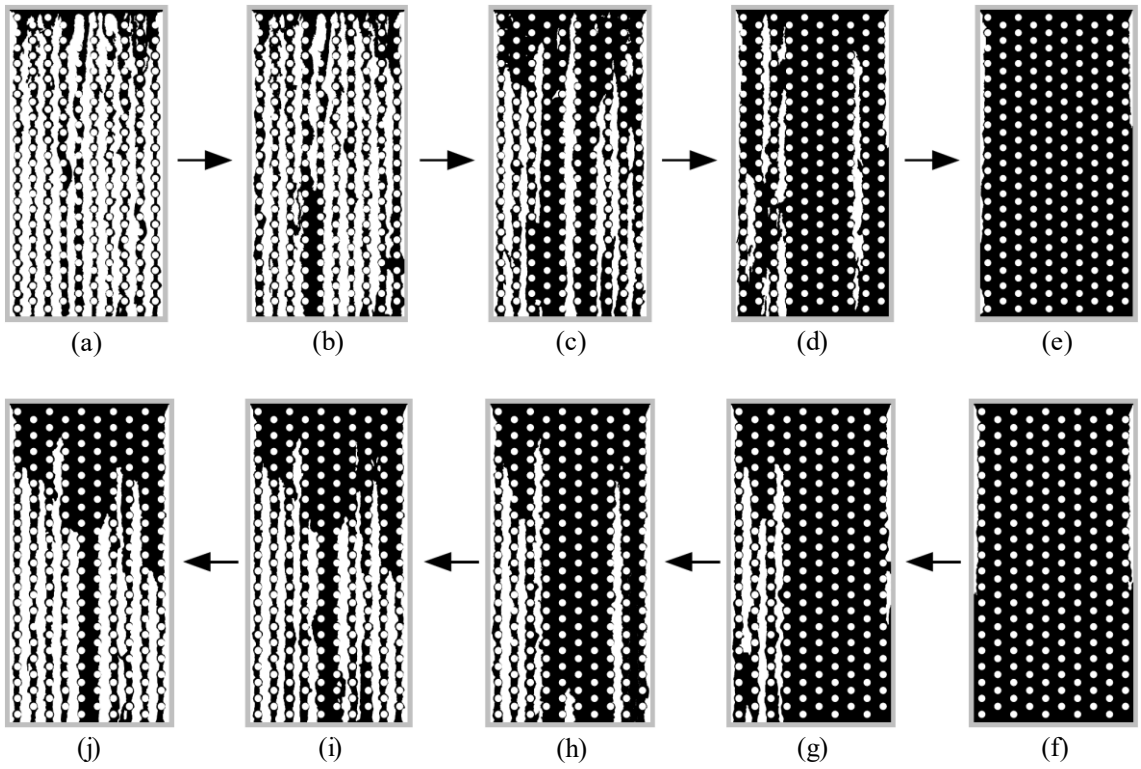

Fig. 5.6 Surface wetting at 34% IL mass fraction for gradually increasing (→) and decreasing (←) solution flow rates.

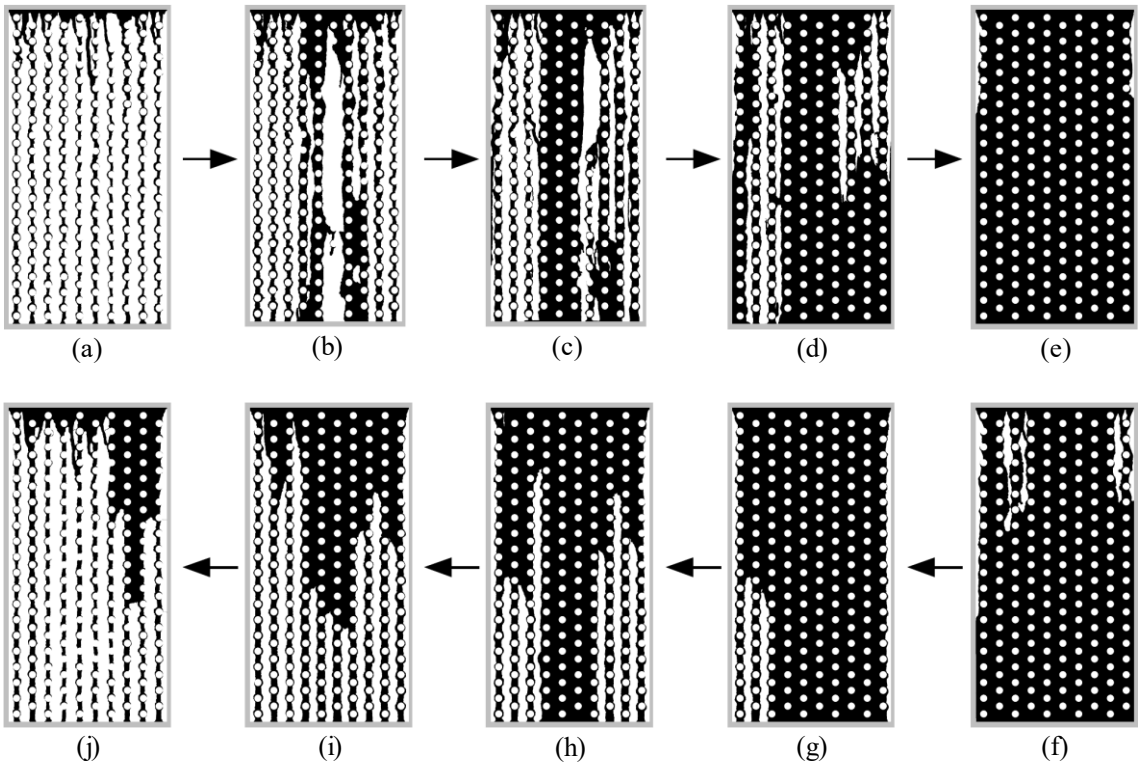

Fig. 5.7 Surface wetting at 45% IL mass fraction for gradually increasing (→) and decreasing (←) solution flow rates.

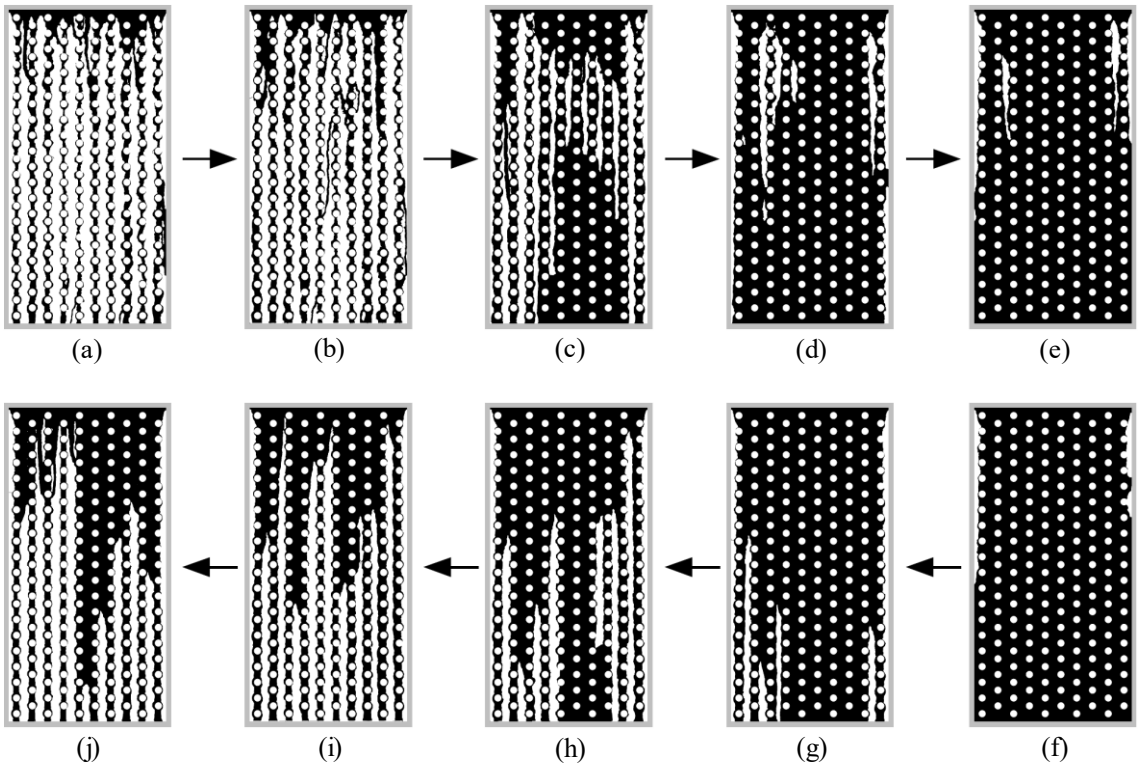

Fig. 5.8 Surface wetting at 60% IL mass fraction for gradually increasing (→) and decreasing (←) solution flow rates.

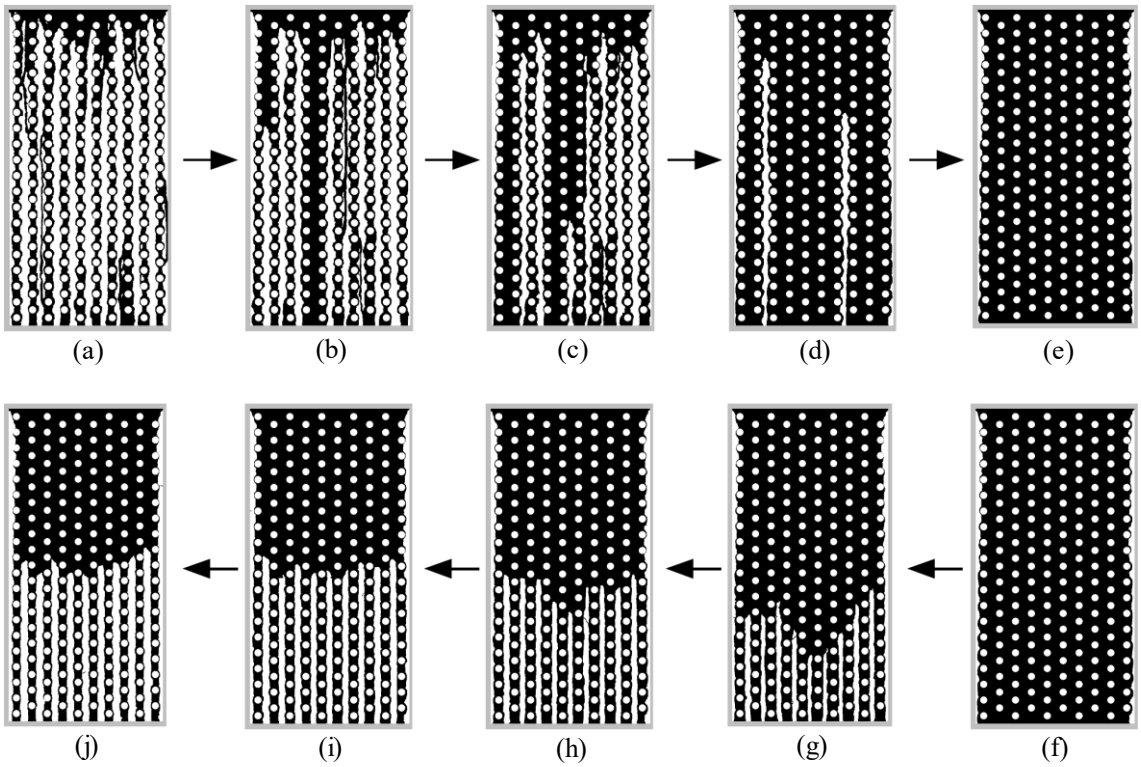

Fig. 5.9 Surface wetting at 75% IL mass fraction for gradually increasing (→) and decreasing (←) solution flow rates.

Thinning and breaking of the liquid film

In falling film technology, the "critical film thickness" is the minimum thickness of the film where it remains stable and does not break into small streams or rivulets. According to de Gennes[100], when a liquid film becomes very thin (approaches to zero), the film lowers its energy by splitting into rivulets, which leads to partial wetting. Thus, for a liquid film to completely wet a solid surface, its critical film thickness must be maintained.

Thinning and breaking of the falling film are observed in most of the experimental results. At first, film breaking appears to be random especially at low Reynolds number. Then, a more organized film breaking is observed for the decreasing flow rate condition at 75% IL mass fraction. Here, the solution trickled from the top of the test section as a single film, which covers approximately half of the substrate, and ruptured into vertical rivulets following the arrangement of the tubes. Higher viscosity and weaker surface tension of the IL solution at higher IL mass fractions are the reasons associated with this occurrence, which improved the spreading and wettability of the solution and aided the

film to flow in a smooth and organized pattern. In actual systems, this wetting behavior is desirable as it produces high heat and mass transfer potential between the gas and liquid by providing a wider contact area and longer gas-liquid contact time.

Dewetting and rewetting of the solid substrate

In principle, the concept of thinning and breaking of a film is similar to dewetting. In fact, film thinning and breaking is a consequence of film instability where the film dewets the surface and form dry spots. However, dewetting through conventional drying (evaporation) is different from dewetting through thinning and breaking as the former leaves behind a residue of stains while the latter brings all impurities along with the liquid[100]. Rewetting, on the other hand, is the reestablishment of liquid contact by a previously dewetted surface or the merging of rivulets from a previously single film down the line of flow.

Dewetting and rewetting of the solid substrate are seen in Fig. 5.6(c), Fig. 5.7(b) ~ (d), Fig. 5.8(c) ~ (e), and Fig. 5.8(h). The factors that might control the ability of the solution to rewet the substrate as soon as dry spots are formed to avoid dewetting are still to be identified. A direct investigation is necessary to clarify these factors as it can help in the improvement of the design of fin-tube contactors and their operating conditions.

Merging of small rivulets and formation of larger rivulets

Another wetting pattern that is observed from the experimental results is the merging of adjacent rivulets and the formation of larger rivulets. Small rivulets flow from the top of the test section and join to form larger rivulets. This is particularly noticeable at low flow rates and low IL mass fractions of increasing flow rate condition. Examples are Fig. 5.5(c) and (d), and Fig. 5.6(b). Usually, this does not occur in decreasing flow rate condition as the film starts at a fully wetted substrate. If the film eventually breaks and reestablishes down the flow line, it would be a case of dewetting and rewetting. Although this kind of wetting pattern occurred only within a narrow range of the operating conditions, it is of high engineering interest, and knowing the factors that can enhance the merging of the rivulets is important for the improvement of the wetting condition inside the contactor.

5.2.3 Contact angle and contact angle hysteresis

Contact angle

From a macroscopic point of view, the contact angle of a liquid droplet deposited on a solid surface is the angle formed by the solid-liquid interface and the liquid-gas interface as shown in Fig. 5.10. Specifically, on the left figure, the angle is called the

static contact angle θ_S since it is measured in a state where the three-phase contact line is in a static condition. Such is the case for droplets deposited on a horizontal surface and at a fixed volume. When the contact angle is measured just before the three-phase contact line has moved, due to either external forces or change in drop size, the contact angle is called the dynamic contact angle θ_D. There are two ways dynamic contact angles occur. First is when the volume of the droplet, resting on a horizontal solid surface, increase or decrease, this is known as the inflation[101]. The other is when the angle of the surface, where the drop of a fixed volume is deposited; changes relative to the horizontal axis. In both cases, two types of contact angles are formed depending on the movement of the three-phase contact line. In the case of changing the surface angle, the contact angle measured just before the drop rolled down the surface is the advancing contact angle θ_A (downhill side of Fig. 5.10(b)) and the decreasing contact angle θ_R (uphill side of Fig. 5.10(b).

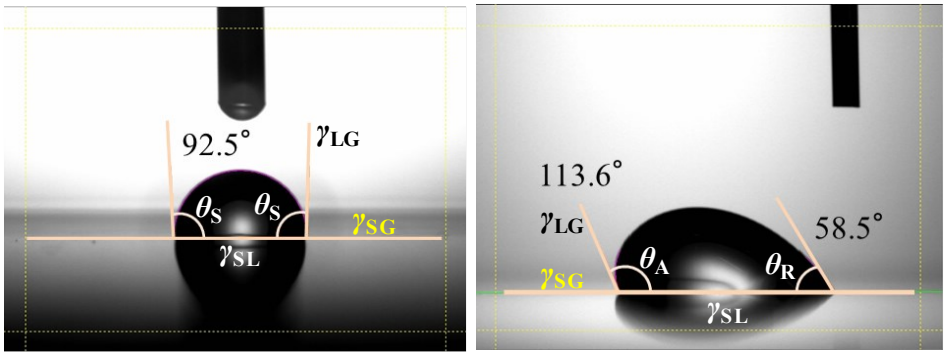

(a) (b)

Fig. 5.10 Illustration of the (a) static and (b) dynamic contact angles of water on an aluminum plate.

Table 5.5 Static, advancing, dynamic contact angles, and contact angle hysteresis of the IL solution on an aluminum plate.

X_{IL}, %	Static contact angle		Dynamic contact angle				
	V, μL	θ_S, °	V, μL	θ_{PT}, °	θ_A, °	θ_R, °	θ_H, °
0.0	5.0	97.7	10.1	79	107.1	80.3	26.8
12.8	5..0	87.9	10.0	83	105.9	84.9	21.0
21.3	5.3	85.4	10.2	59	99.8	66.3	33.5
32.0	2.0	82.3	10.1	48	86.3	58.8	27.5
39.9	5.8	77.3	12.0	34	83.4	59.2	24.2
50.8	4.3	75.2	11.1	34	78.0	49.4	28.6
62.4	2.3	72.9	9.8	33	74.7	54.7	20.0
69.7	2.6	67.9	10.5	42	79.3	47.5	31.8
75.5	2.2	67.8	10.7	37	74.2	47.3	26.9

Table 5.5 summarizes the experimental data for the contact angles of the IL solution at various IL mass fractions. The contact angles were measured by the contact angle meter shown in Fig. 5.11 at controlled room temperature approximately within 22~25°C.

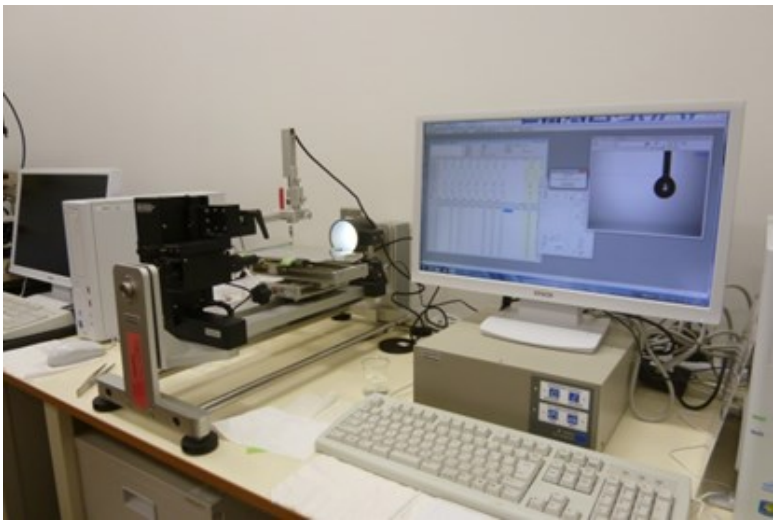

Fig. 5.11 Contact angle (static and dynamic) meter.

Fig. 5.12 illustrates the static, advancing, receding, and contact angle hysteresis summarized in Table 5.5. De Gennes[100] classified a liquid as “mostly wetting” if its static contact angle on a solid surface is less than or equal to 90° and “mostly non-wetting” if the static contact angle is more than 90°. In the experimental data, only pure water has a static contact angle of more than 90°. Based on the trend of the static contact angle, the solution will have a static contact angle of more than 90° at IL mass fractions lower than 11.8%. These conclude that the IL solution is mostly wetting on the aluminum substrate at IL mass fraction of 11.8% or higher.

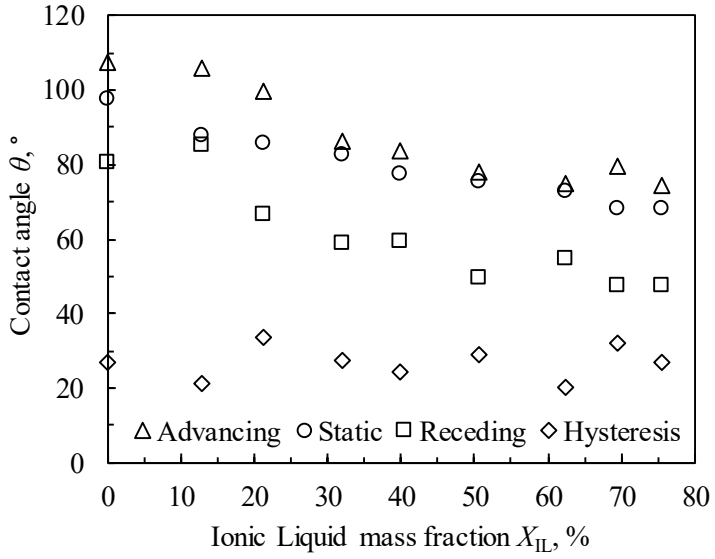

Fig. 5.12 Graphical illustration of the contact angles (static θ_S, advancing θ_A, receding θ_R, and hysteresis θ_H) of the IL solution on an aluminum plate.

A regression analysis was carried out with the experimental data on the advancing and receding contact angles presented in Table 5.5. The polynomial regression of the experimental data for advancing and receding contact angles results in the quadratic functions of the IL mass fraction X_{IL} expressed by the following equations.

$$\theta_A = 1.94 - 0.0149X_{IL} + 0.00008X_{IL}^2 \quad (°) \quad (5.1)$$

$$\theta_R = 1.48 - 0.0150X_{IL} + 0.00008X_{IL}^2 \quad (°) \quad (5.2)$$

Fig. 5.13 shows a comparison between the experimental data and the predicted results (from Eqs. (5.1) and (5.2)) of the advancing and receding contact angle. The mean absolute percentage error between the experimental data and predicted results is 3.2% for the advancing contact angle and 5.6% for the receding contact angle.

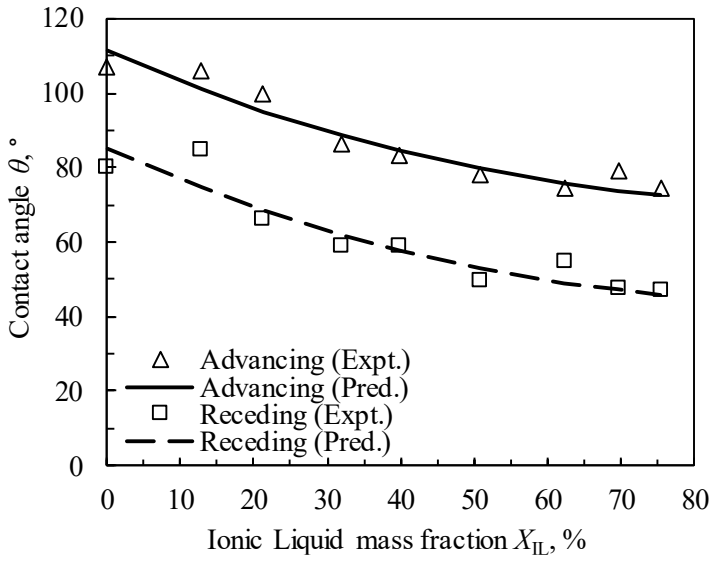

Fig. 5.13 Comparison between the experimental data and predicted results of the advancing and receding contact angle.

Contact angle hysteresis

Butt et al.[69] defined contact angle hysteresis θ_H as the measure of the degree at which line pinning and the history of the system determine the macroscopic contact angle. On the other hand, Johnson and Dettre[102] described it as a balance between the vibrational energy of a drop and the heights of the energy barriers that allowed metastable states. Mathematically, contact angle hysteresis is the difference between the advancing and receding contact angles. Contact angle hysteresis is caused by both or either of these two major factors:

1. Chemical (heterogeneity, existence of dirt, dust, and other foreign particles).
2. Physical (surface roughness, existence of pores, and other surface irregularities).

In the wetting experiment, the aluminum fin-tube substrate underwent a series of complete wetting and dewetting to ensure as much as possible that no dirt or other foreign particles remain on the test section. Therefore, contact angle hysteresis in the surface wetting experiment can be assumed to be mainly caused by the surface roughness of the aluminum substrate.

Table 5.6 lists the surface roughness parameters of the aluminum fin-tube substrate mounted on the test section. The values for the parameters were measured by a Computer Numerical Control surface roughness tester similar to that shown in Fig. 5.14. According to the International Organization for Standardization (ISO), the arithmetic mean roughness of 0.317 μm is below the middle value of the roughness grade. On the other hand, a surface is described to be "good" if it gives a contact angle hysteresis of less than 5° and "rough" if it gives more than 50°[100]. As illustrated in Fig. 5.12, the contact angle hysteresis of the IL solution on the aluminum substrate is between 20 and 33.5°, with an average value of 26.7°. Summarizing all this information about the aluminum fin-tube substrate, it can be concluded that the aluminum substrate is slightly to moderately rough. Therefore, the assumption that the contact angle hysteresis of the IL solution is significantly caused by the aluminum substrate is proven since the aluminum substrate does not have a smooth surface.

Table 5.6 Surface roughness of the aluminum substrate.

Roughness parameter	Unit	Value
Arithmetic mean roughness, R_a	μm	0.317
Maximum peak height, R_p	μm	1.191
Maximum valley depth, R_v	μm	0.851
Maximum height, R_z	μm	2.042

Fig. 5.14 Computer Numerical Control surface roughness tester.

5.2.4 Wetting hysteresis

Wetting hysteresis is a complex phenomenon that requires a detailed experimental investigation. Many studies about the wetting hysteresis phenomenon have used the concept of contact angle hysteresis to describe wetting hysteresis. For example, de Jonghe and Chatain[103], Shanahan[104], Jin and Koplik[105], Kabov and Zaitsev[106], Soolaman and Yu[107], and Chang et al.[101] have used the term wetting hysteresis to describe the difference between the advancing and receding contact angles. Similarly, Emelyanenko et al.[108] defined wetting hysteresis as the difference between cos θ_A and cos θ_R. Clearly, it can be argued that there is a misconception about the phenomenon of wetting hysteresis. The wetting hysteresis needs to be clarified and differentiated from contact angle hysteresis.

Minimum wetting rates

An experimental study by Hobler[109] led to the discovery of three minimum wetting rates for which a falling film does not break. He concluded that these wetting rates are in the order of magnitude as shown in Eq. (5.3).

$$\Gamma_{\min,0} > \Gamma_{\min,1} > \Gamma_{\min,2} \tag{5.3}$$

where $\Gamma_{\min,0}$ is the minimum wetting rate in the regime of gradually increasing flow rate on a previously dry surface, $\Gamma_{\min,1}$ is the minimum wetting rate in the regime of gradually increasing flow rate on an initially wet surface, and $\Gamma_{\min,2}$ is the minimum wetting rate in the regime of gradually decreasing flow rate.

This means that applying the least mass flow rate that can achieve complete wetting in the decreasing flow rate condition will produce partial wetting when applied in the increasing flow rate condition, and thus, wetting hysteresis is created between the two flow conditions. For system applications, decreasing flow rate condition is advantageous as it requires lesser pumping power to achieve complete wetting compared to increasing flow rate condition. Moreover, the thinner films produced in the decreasing flow rate condition promote larger heat and mass transfer compared to thicker films.

Film stability

Picknett and Bexon[110] classified the variation of a droplet shape (as a function of time) into two extreme modes, namely the constant area mode and the constant contact angle mode. In the constant area mode, the contact area between the liquid and the solid surface remains the same while evaporation takes place, this is known as “pinning”. As a result, the drop compensates by lowering its contact angle. In the contact angle mode, the contact angle remains unchanged as the drop volume and contact area decreases, this is known as “shrinking”. They have confirmed that during an evaporation process, pinning dominates until the contact angle decreases to a constant value at which point the mode switches to shrinking. The following principles of film stability can be related to the wetting hysteresis. Pinning can be related to the gradual decrease of the mass flow rate in the gradually decreasing flow rate condition where a single film is maintained. Until the film becomes too thin that decreasing further the mass flow rate results in film breaking and partial wetting otherwise known as shrinking in film stability terms.

To summarize the whole wetting-dewetting process, after the substrate is completely wetted at increasing flow rate condition, the film continues to completely wet the surface as the mass flow rate decreases until the critical film thickness is reached. This results in two different minimum wetting rates between the increasing and decreasing flow rate conditions.

Experimental analysis of the wetting hysteresis

Fig. 5.15 shows the wetting ratio of the IL solution on the aluminum substrate for both increasing (△ markers) and decreasing (▽ markers) flow rate conditions. The arrows inside the graphs serve as a rough guide for the wetting trend of the increasing and decreasing conditions. The wetting hysteresis can be estimated by measuring the vertical distance between two collinear data in the graph. The wettability of the aluminum substrate increases as the IL mass fraction increases as depicted by the steeper wetting curves, which become closer and closer to the origin.

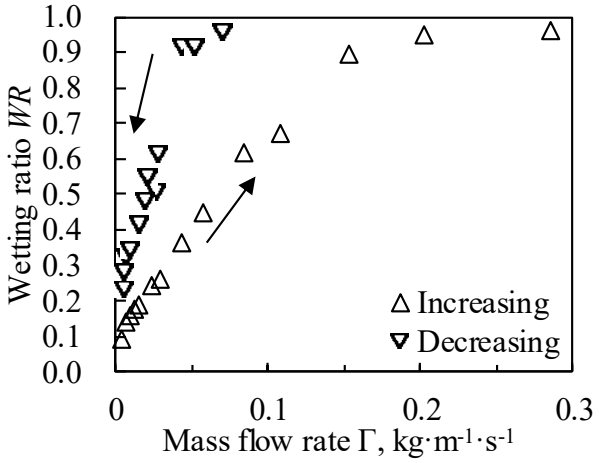
Wetting ratio WR
1.0
0.9
0.8
0.7
0.6
0.5
0.4
0.3
0.2
0.1
0.0
0
0.1
0.2
0.3
Mass flow rate Γ, kg·m-1·s-1
Increasing
Decreasing

(a)

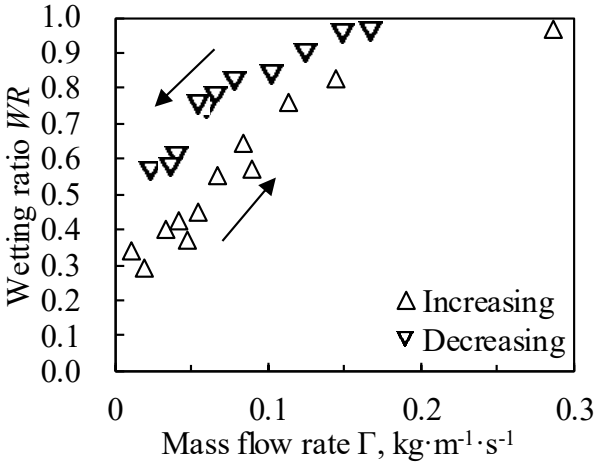
Wetting ratio WR
1.0
0.9
0.8
0.7
0.6
0.5
0.4
0.3
0.2
0.1
0.0
0
0.1
0.2
0.3
Mass flow rate Γ, kg·m-1·s-1
Increasing
Decreasing

(b)

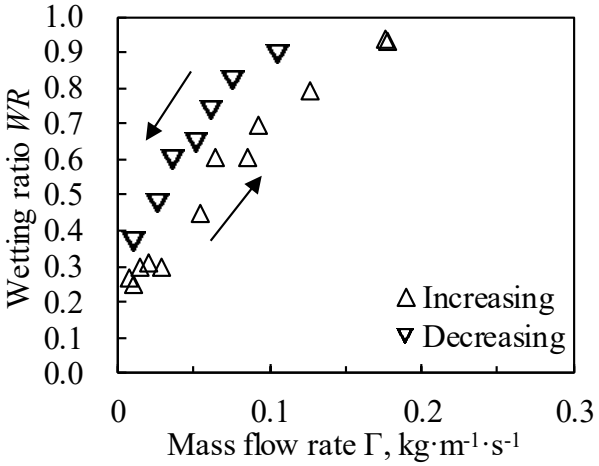
Wetting ratio WR
1.0
0.9
0.8
0.7
0.6
0.5
0.4
0.3
0.2
0.1
0.0
0
0.1
0.2
0.3
Mass flow rate Γ, kg·m-1·s-1
Increasing
Decreasing

(c)

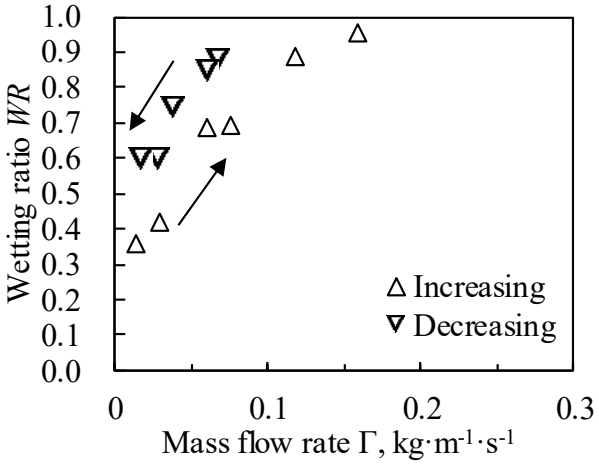

(d)

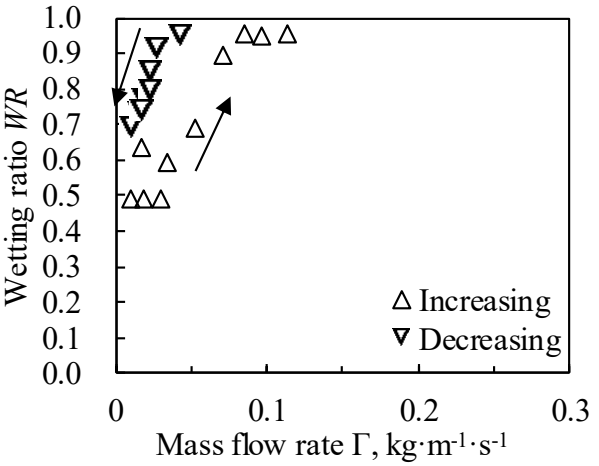

(e)

Fig. 5.15 Wetting ratio of the IL solution on the aluminum substrate as a function of solution mass flow rate: (a) 0%, (b) 34%, 45%, 60%, and 75% IL mass fraction.

Based on the above experimental observation, the wetting hysteresis W_{h} can be defined as the difference between the wetting of a liquid at the same mass flow rate flowing at increasing and decreasing flow rate conditions. It measures how much a liquid at decreasing flow rate condition exceeds the wetting of that liquid at the same flow rate flowing at increasing flow rate condition. This can be expressed by the following equation:

$$W_{\mathrm{h}} = WR_{\mathrm{d}} - WR_{\mathrm{i}} \tag{5.4}$$

where WR_{d} and WR_{i} represent the wetting ratio (at equal liquid mass flow rate) for decreasing and increasing mass flow rate condition.

Wetting hysteresis is a complex phenomenon that is caused by many factors including the contact angle hysteresis. The same factors that produce contact angle hysteresis also influence the occurrence of wetting hysteresis. Based on the different parameters that were experimentally investigated, the key factors that contributed to the wetting hysteresis are as follows:

1. Surface roughness
2. Chemical heterogeneity
3. Liquid desiccant mass fraction
4. Distributor opening

The presence of surface roughness or chemical heterogeneity creates contact angle hysteresis, which consequently affects the wetting hysteresis. On the other hand, variations in the mass fraction of the liquid desiccant produce different minimum wetting rates and create wetting hysteresis. The construction of the distributor and the way the fluid is dispersed affects the width and thickness of the film. Thus, using distributors that have different openings generate wetting hysteresis. In the wetting experiments, the effect of the distributor opening can be considered as not significant as there were only two kinds of distributors used and their configurations are not significantly different from each other. Therefore, it can be concluded that the two factors that mainly contribute the wetting hysteresis are the surface roughness and the liquid desiccant mass fraction.

5.3 Validation of the theoretical partial wetting model

Calculations were performed using the thermo-physical properties of the IL and the equations of the advancing and receding contact angles given in Eqs. (5.1) and (5.2). The predictions from Eqs. (4.21) and (4.18) are shown in Fig. 5.16 and Fig. 5.17, respectively. Fig. 5.16 depicts the film and rivulet energies from zero to complete wetting. When the mass flow rate of a uniform film is quasi-statically decreased, complete wetting of the surface is maintained until the film minimum critical flowrate (Eq. (4.22)) is reached. Subsequently, the film breaks, switching to a rivulet configuration of defined geometry with a wetting ratio WR, which is approximated by Eq. (4.18).

In the case of an isothermal liquid and substrate, for a solution concentration of 34% of IL (Fig. 5.16) and at a Reynolds number equal or lower than 95, the rivulet configuration exhibits lower energy and is stable for a wetting ratio of approximately 0.35 (Fig. 5.17). A further decrease in the mass flowrate reduces the extension of the rivulet, and it follows the path identified by the configurations of minimum energy (Fig. 5.16(b)) with a contact angle corresponding to the measured value of the receding contact angle θ_R (Eq. (5.2)). Grey lines represent the energy of the rivulet at Reynolds numbers wherein the uniform film configuration results to be stable.

The rivulet configuration is a stable configuration characterized by a local minimum-energy condition. Thus, with respect to increasing mass flow rates, the rivulet configuration is maintained (Fig. 5.16(b)) until the rivulet base completely covers the surface (WR = 1 in Fig. 5.17(a)). In this case, the advancing contact angle θ_A (Eq. (5.1)) is used in the calculation.

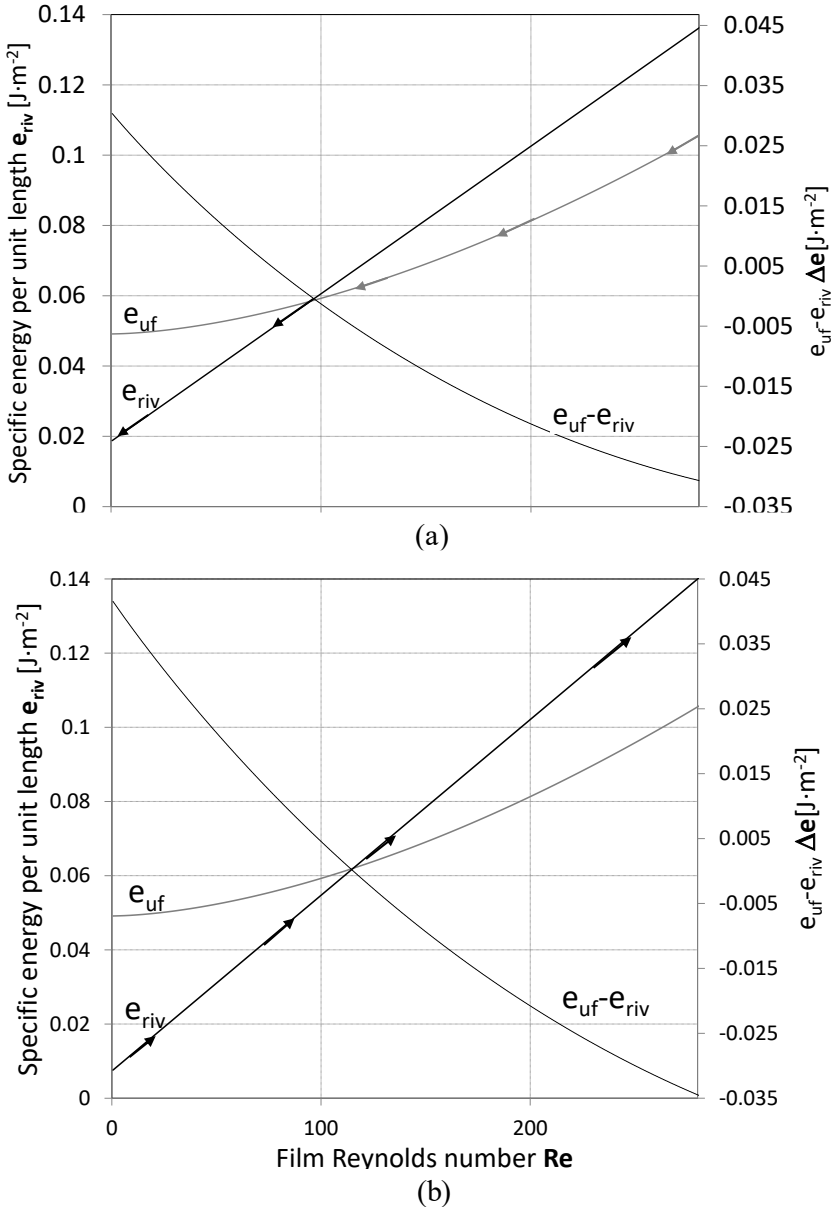

Fig. 5.16 Specific energy per unit stream-wise length [J·m^{-2}] of rivulet and uniform film configurations as a function of film Reynolds number; T = 34°C, X_{IL} = 34%, for (a) decreasing ($\theta_0 = \theta_R$) and (b) increasing ($\theta_0 = \theta_A$) liquid flow rates.

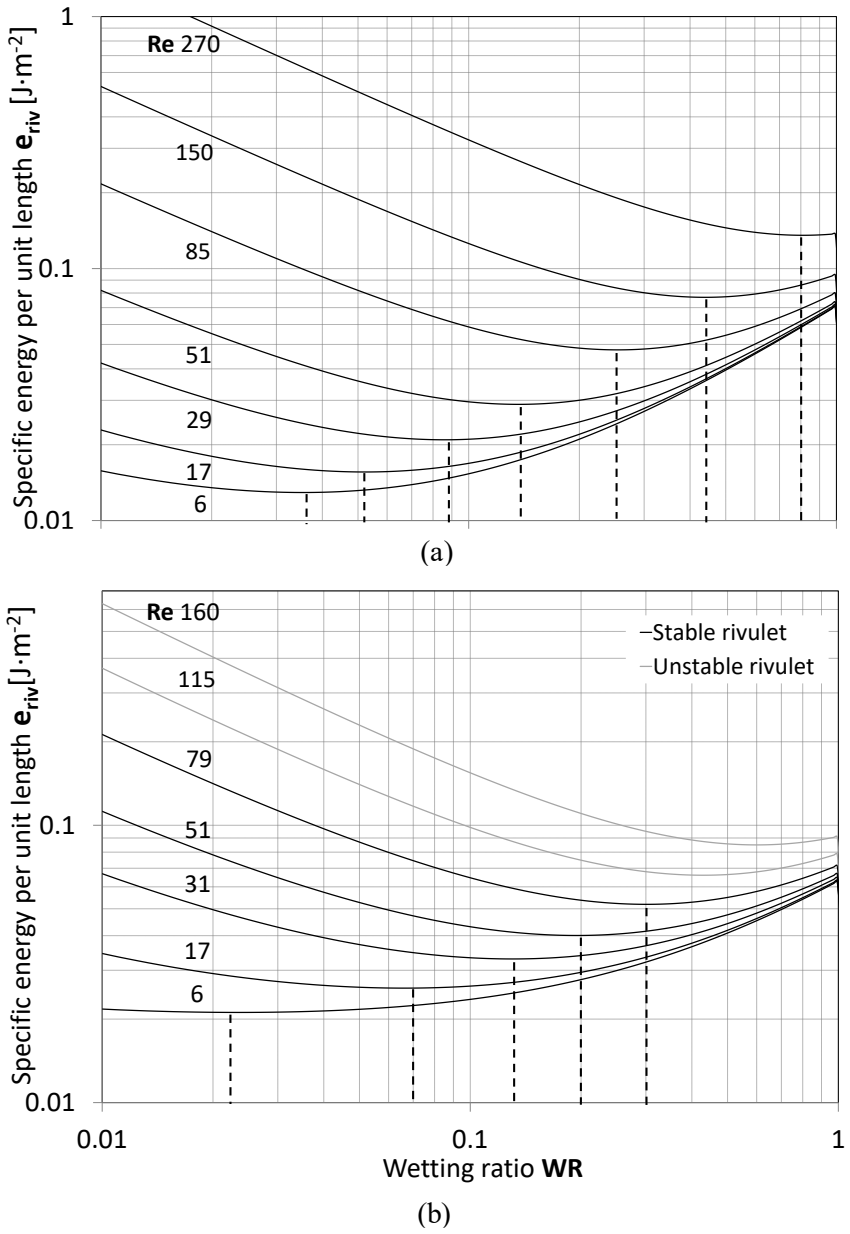

Fig. 5.17 Specific energy per unit width and per unit stream-wise length [J·m^{-2}] of an ionic liquid flow on a vertical aluminum fin of an internally-cooled contactor. T = 34°C, X_{IL} = 34%, as a function of the wetting ratio WR for (a) decreasing ($\theta_0 = \theta_R$) and (b) increasing ($\theta_0 = \theta_A$) liquid flow rates

A direct comparison between theoretical results and experimental data is performed to preliminarily screen the potential of the modeling approach when it is applied to different fluid compositions and properties. The theoretical results are compared and validated with the experimental data measured at a solution temperature of approximately 34ºC and IL mass fractions from 34~75%.

Fig. 5.18 shows a comparison of the theoretical and experimental results of the wetting ratio *WR* for pure water (0% IL mass fraction) at solution Reynolds number ranging up to 1500. The figure clearly shows the ability of the model to theoretically predict the wetting ability of the liquid on the aluminum fin-tube substrate. Furthermore, the model can predict the wetting hysteresis phenomenon of the solution on the same aluminum surface for increasing and decreasing flowrate conditions.

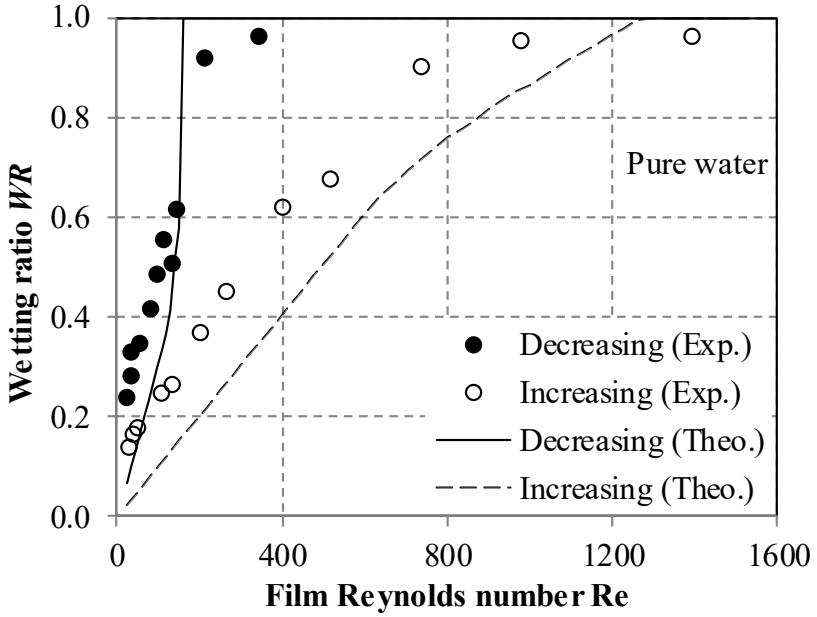

Fig. 5.18 Comparison between theoretical predictions (using Eq. (4.18)) and experimental results for the wetting ratio of water on the fin-tube.

It is important to note that the experimental data exhibit a higher wetting ratio than the theoretical calculations, particularly at low liquid Reynolds numbers. This deviation may have occurred due to the effect of imperfect liquid delivery by the distributor, which locally increased the mass flow rate per unit surface width.

A comparison between the theoretical and experimental results of the *WR* along the wetting-dewetting cycles at solution concentrations ranging from 34% to 75% (IL mass fraction) are shown in Fig. 5.19. Additionally, as shown in the figure, it is clear that the model predicts the difference in wetting ability of the liquid on the aluminum fin-tube substrate for increasing and decreasing mass flowrate conditions or the wetting hysteresis.

The results emphasize that wetting hysteresis also occurs on an ideally smooth surface characterized by a unique value of the contact angle θ_0, although it is intensified by the contact angle hysteresis phenomenon. Furthermore, the wettability of the desiccant solution improves with the increase in the IL mass fraction X_{IL}. Correspondingly, the film stability (quantified as Re_b or minimum wetting rate) is expanded to lower Reynolds

number, and the hysteresis behavior is less substantial. This is related to the effect of a higher IL mass fraction on the thermo-physical properties of the solution, which yields lower values of the contact angle and surface tension along with higher viscosity and density. Nevertheless, it is not possible to state the advantage of operating at higher IL mass fractions in absolute terms because the film thickness for a given flow rate is negatively affected by an increased viscosity, in conjunction with a lower thermal conductivity at higher mass fractions. Additionally, the experimental results confirm that the minimum solution Reynolds number required to reach the fully wetted surface moves to lower values when the IL mass fraction increases for both advancing and receding contact angles, as theoretically predicted by the model. The behavior is linked to a higher viscosity and lower surface tension at higher X_{IL} and increases in its wettability, and it allows the solution to flow more smoothly in a more organized pattern.

The quantitative analysis of the results indicates that the aluminum substrate is fully wetted at the IL mass fraction of 34% at increasing solution flowrate when the solution Reynolds number reaches approximately 340. Furthermore, it returns to a partially wetted condition (gradually decreasing the solution flowrate) when the solution Reynolds number decreases to approximately 100. At higher IL mass fractions (for example at 45%), complete wetting occurs at a Reynolds number of approximately 210 at increasing solution flowrate, and the film rupture occurs when the solution Reynolds number decreases to 60.

The predicted values for the pair of minimum wetting Re are 150 and 40 at 60% IL mass fraction and 60 and 20 at 75% IL mass fraction.

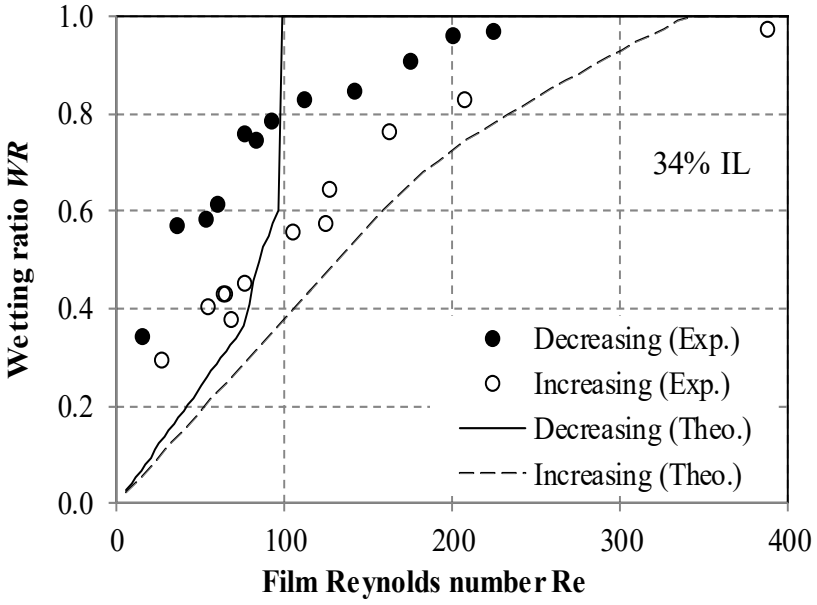

(a)

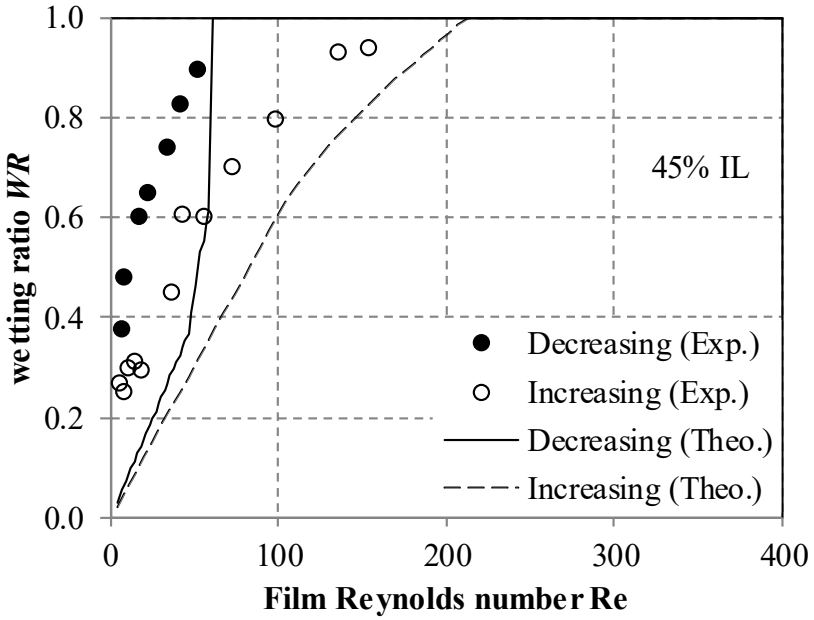
1.0
0.8
0.6
0.4
0.2
0.0
wetting ratio WR
45% IL
Decreasing (Exp.)
Increasing (Exp.)
Decreasing (Theo.)
Increasing (Theo.)
0
100
200
300
400
Film Reynolds number Re

(b)

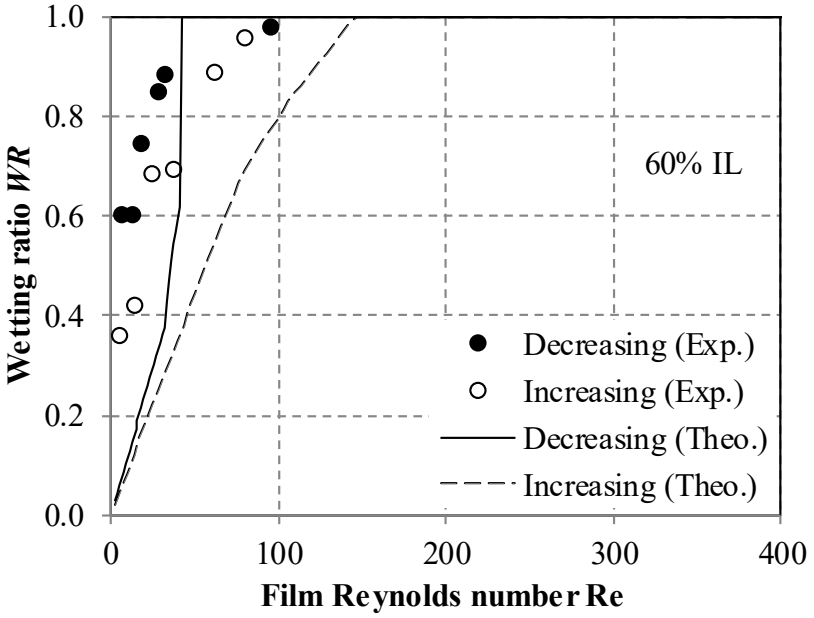
1.0
0.8
0.6
0.4
0.2
0.0
Wetting ratio WR
60% IL
Decreasing (Exp.)
Increasing (Exp.)
Decreasing (Theo.)
Increasing (Theo.)
0
100
200
300
400
Film Reynolds number Re

(c)

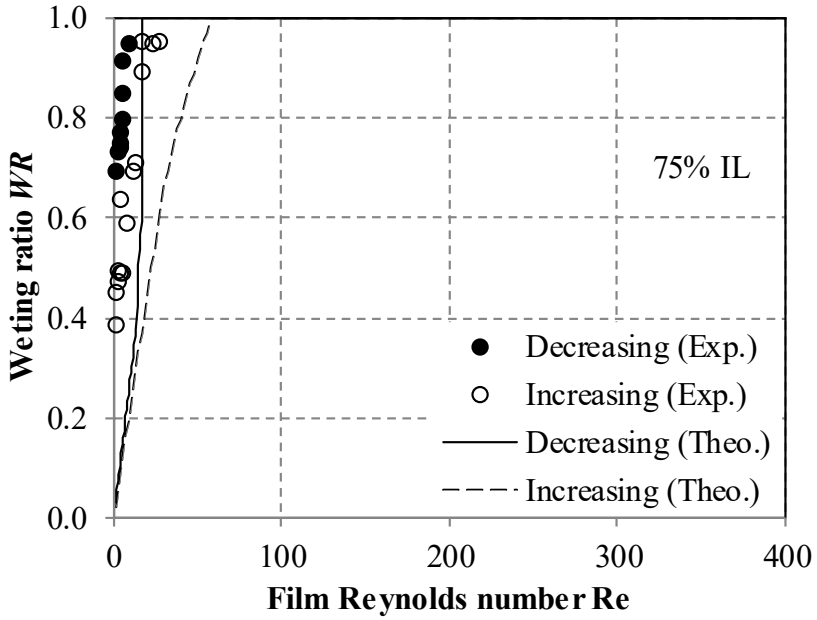

(d)

Fig. 5.19 Comparison between theoretical predictions (using Eq. (4.18)) and experimental results for the wetting ratio on the fin-tube substrate: (a) 34%, (b) 45%, (c) 60%, and (d) 75% IL mass fraction.

Generally, the theoretical values are in good agreement when compared with the experimental data considering the complexity of the phenomenon in the actual experiment. Although there are discrepancies between theoretical and experimental values, the developed model exhibits a fair capability to predict the wetting characteristics of the water/IL solution on an aluminum fin-tube gas-liquid contactor over a wide range of IL concentrations.

6. Semi-theoretical partial wetting model

6.1 Introduction

An increased degree of accuracy in predicting the wetting characteristics of the desiccant solution over the aluminum substrate is achieved through the definition and tuning of specific characteristic coefficients acting on the magnitude of the effects at play, while consistently maintaining the shape of the equations extracted by the theoretical model. The difference between these constant coefficients fitted to the experimental data to minimize the deviation of the model and the original theoretical values enclose the effect of the simplifying assumptions by considering the flow configurations, such as Nusselt velocity profile, absence of waves at the free interface, dynamic values of the contact angle and effect of the staggered tube array.

6.2 Semi-theoretical formulation

Equations (4.7) and (4.8) are first assessed to achieve a semi-theoretical form that better approximates film stability over a comprehensive range of IL mass fractions. Equation (4.21) expresses a univocal relationship $\Delta_b = \varphi_b(\theta_0)$ between Δ_b and the contact angle θ_0 that is approximated by Eq. (6.1) with a deviation below 1% in the range of interest as follows:

$$\Delta_b = 0.20 \ln \theta_0 + 0.69 \tag{6.1}$$

Yielding the following handling formulation of the minimum Reynolds number for the stability of the uniform film configuration.

$$\mathrm{Re}_b = 0.054 \mathrm{Ga}_b^{1/5} (\ln \theta_0 + 3.45)^3 \tag{6.2}$$

The theoretical shape of the film stability criterion expressed in Eq. (4.21) is maintained, and by introducing the characteristic coefficients C_0 (takes in consideration the other factors such as the distributor effect, etc.) and C_1 (considers the effects of heat and mass transfer) a semi-theoretical formulation of the minimum Reynolds number able to ensure complete wetting of the substrate is achieved as follows:

$$\mathrm{Re}_b = 0.054 C_0 \mathrm{Ga}_b^{C_1/5} (\ln \theta_0 + 3.45)^3 \tag{6.3}$$

The characteristic coefficients C_2, C_3, and C_4, are introduced in Eq.(6.4) to match the wetting behavior, actual flow geometry, and the effect of heat and mass transfer on Weber and Reynolds number, respectively.

$$WR \approx 0.27 C_2 \theta_0^{-1.24 C_4} \left(\frac{\mathrm{Re}_{\mathrm{lb}}}{\mathrm{We}_{\mathrm{lb}}^3} \right)^{C_3/5} \tag{6.4}$$

The deviation of the experimental data from the predicted results of Eqs. (6.3) and (6.4) is minimized, and the values summarized in Table 6.1 are obtained.

Table 6.1 Characteristic coefficients of the semi-theoretical formulation.

C_0	C_1	C_2	C_3	C_4
0.47	1.28	3.07	0.35	0.73

The value of these coefficients represents the deviation of the semi-theoretical correlation from the modeling of the theoretical equations and the assumptions introduced in their formulation. Specifically, C_0 and C_2 are related to the simplified geometry of the two flow configurations, which ignore waviness and more complex cross-sectional shapes. C_4 represents the limitation of the assumption of a single value of contact angle throughout the flow along the whole fin. Finally, C_3 and C_1 evaluate the importance of effects other than kinetics and surface tension (such as heat and mass transfer or friction with the gaseous phase).

If the film Reynolds number is greater than the critical Reynolds number, it is assured based on the stability criterion that the film completely wets the entire surface; otherwise if the film Reynolds number is lesser than the critical Reynolds number, it is assumed that there is partial wetting of the surface and the wetting ratio is estimated as follows:

$$WR = 0.83 \theta_0^{-0.90} \left(\frac{\mathrm{Re}_{\mathrm{lb}}}{\mathrm{We}_{\mathrm{lb}}^3} \right)^{0.07} \tag{6.5}$$

6.3 Prediction of the wetting ratio using the semi-theoretical model

Fig. 6.1 shows the predicted results from the semi-theoretical model of the partial wetting, which are graphed together with the experimental data. The semi-theoretical model clearly shows improved prediction capability compared to the theoretical model. Especially for the decreasing flow rates, the predicted results follow the experimental results accordingly as shown in Fig. 6.1(a) – (d) compared to Fig. 5.19(a) – (d). Moreover, using Eq. (6.5) the wetting hysterias between increasing and decreasing flow rates can be estimated more accurately.

By considering the effect of other factors which contributes to the actual wetting phenomena, especially the effect of the distributor on the wetting behavior, and the contact angle variation along the flow direction, the wettability of the IL solution on the

aluminum substrate is more accurately predicted for the entire range of IL mass fraction. This commends the use of the semi-theoretical model in predicting the wettability in the actual 3-fluid gas-liquid contactor.

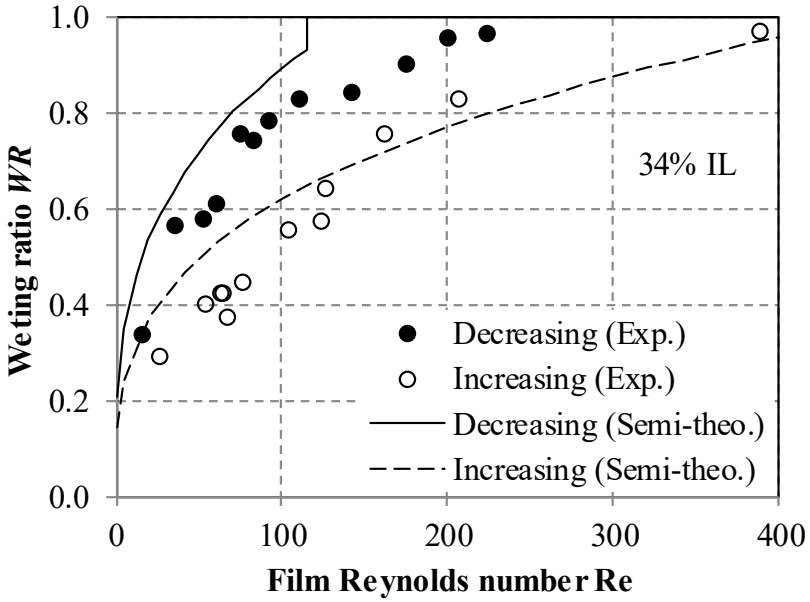

(a)

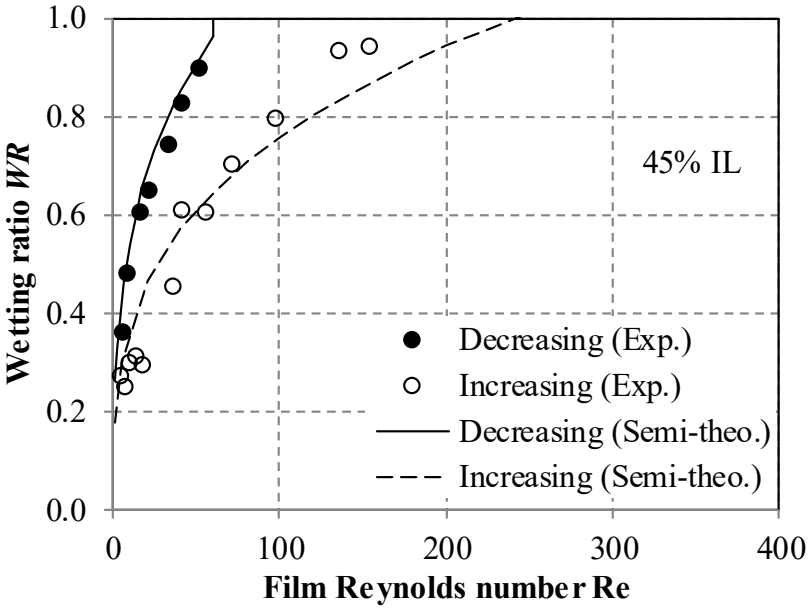

(b)

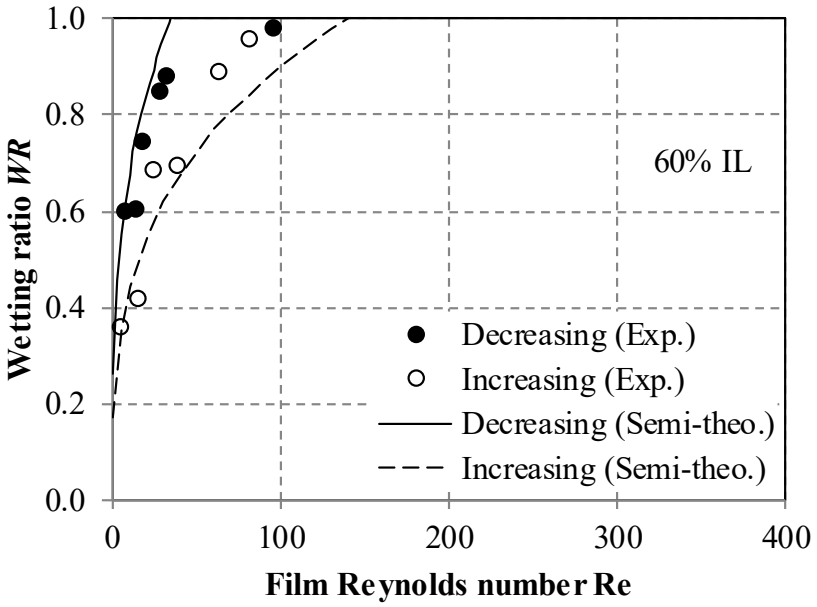

(c)

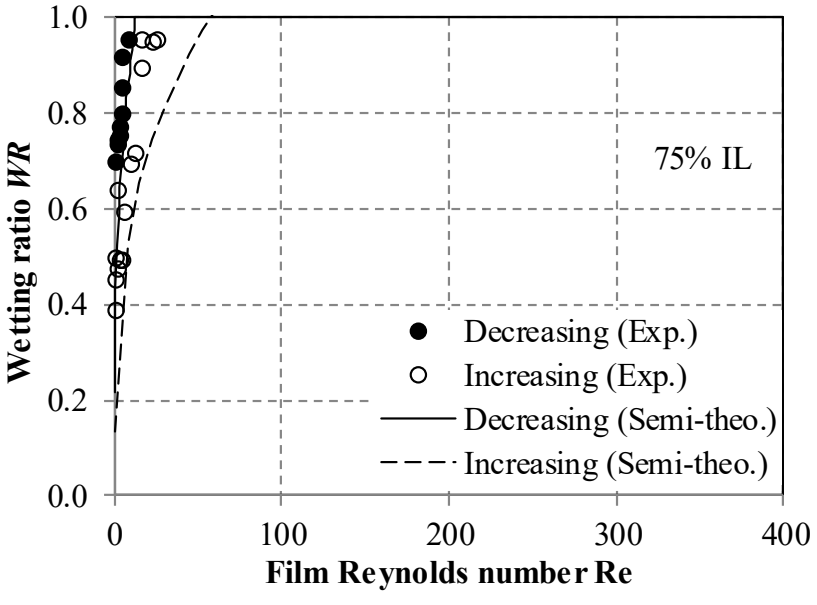

(d)

Fig. 6.1 Comparison between predictions (using Eq. (6.5)) and experimental results for the wetting ratio on the fin-tube substrate: (a) 34%, (b) 45%, (c) 60%, and (d) 75% IL mass fraction.

7. Gas-liquid contactor model

7.1 Introduction

This chapter explains the development, fundamental theories, and principles adopted in the mathematical modeling of the 3-fluid gas-liquid contactor. If the system is not yet built, modeling and simulation provide several benefits such as consumption of lesser time and money in clarifying the performance of the system, and prevention of possible risk and harm to both humans and equipment. Moreover, with the mathematical models, parametric studies outside the range and conditions investigated in the experiments can be carried out and control strategies can be developed for a new system.

In liquid desiccant systems, mathematical models may vary depending on the type of gas-liquid contactor and the liquid desiccant used. As an example, the mathematical model for a 3-fluid gas-liquid contactor would differ from that of a conventional 2-fluid packed bed contactor because of the structural and transport differences. Additionally, the difference in thermophysical properties and wetting characteristics of various working fluids have to be considered in the mathematical modeling.

Factors such as the complex structure of the fin-tube gas-liquid contactor which incorporates a 3-fluid flow configuration, occurrence of partial wetting, and complex wetting patterns inside the contactor, have all contributed to the complexity in modeling the heat, mass, and momentum transfer inside the 3-fluid gas-liquid contactor. In addition to this, a newly developed ionic liquid desiccant was used in this research, and thus, its thermophysical properties and wetting characteristics on the gas-liquid contactor need to be formulated and clarified, respectively. As no conclusive wetting theory is yet available in the literature, this constitutes one of the novelties of this research along with the inclusion of the partial wetting model for predicting the wetted area of the contactor. In some studies[30], it was found that not all parts of the contactor area can be wetted by a certain amount of solution flow rates, and the assumption of complete wetting in falling film models can result in significant errors in the predicted results[29]. The development of the partial wetting model provides a potential improvement in the mathematical model of the heat and mass transfer in the 3-fluid gas-liquid contactors by adopting a more realistic prediction of the wettability inside the gas-liquid contactor.

7.2 3-Fluid gas-liquid contactor model

The 3-fluid gas-liquid contactor is modeled by analyzing the elemental control volume shown in Fig. 7.1, and by applying the conservation laws to the control volume. The elemental control volume was determined based on the fin and tube spacing of the 3-fluid gas-liquid contactor, which was designed in accordance with the manufacturing standards of fin-tube heat exchangers.

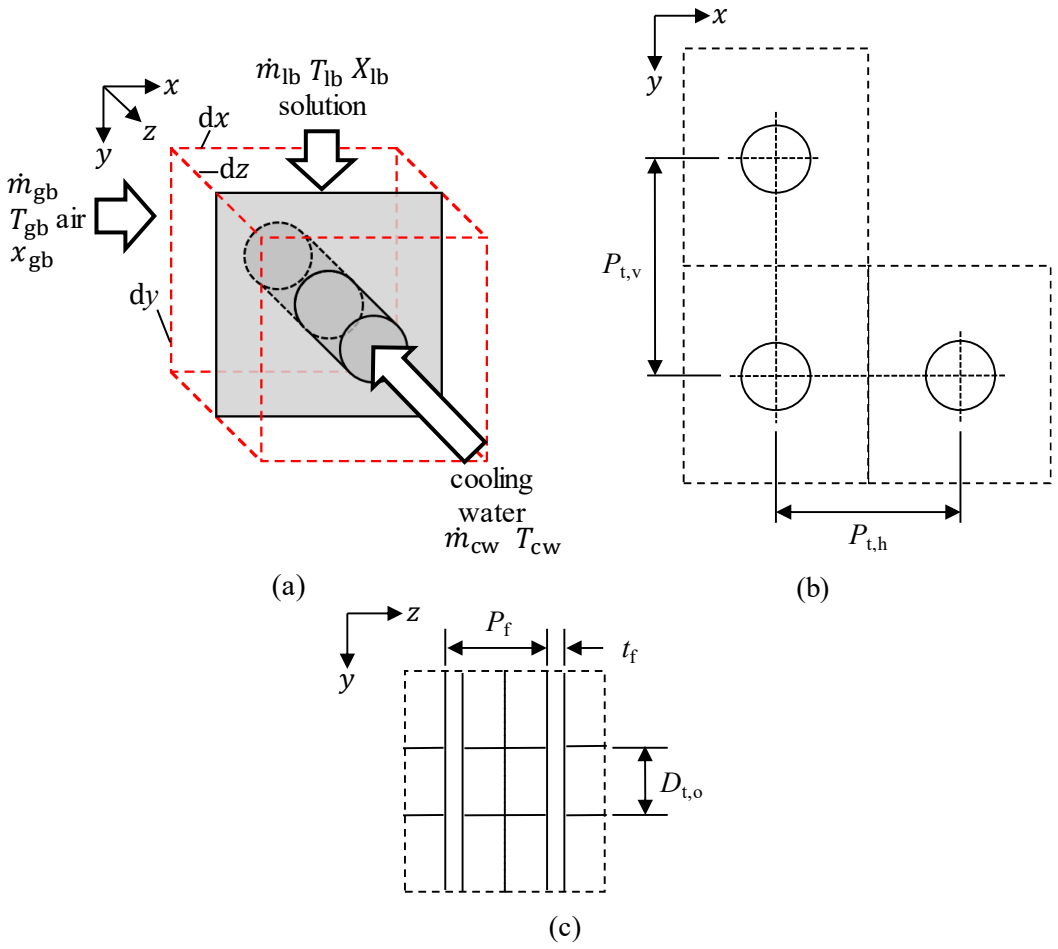

Fig. 7.1 (a) Illustration of the elemental control volume, (b) front view of the control volume, (c) side view of the control volume.

7.2.1 Heat, mass, and momentum transfer geometry

Heat and mass transfers inside the fin-tube contactor, specifically in the control volume, occurs across two geometries; first, across the round horizontal tube and the other across the vertical fin. The schematic of the heat and mass transfer flows in these two geometries are described in Fig. 7.2(a) and Fig. 7.2 (b), respectively. Modeling of the heat and mass transfers on a horizontal tube alone is complicated, and even more for combined tube and fin geometries because of the difference in geometrical shapes and the falling film configurations produced by the corresponding geometries. In mathematical models of a liquid falling on vertically stacked horizontal tubes, the tubes are assumed as if they are connected depicting a hollow vertical plate[111)-113)]. The film is assumed to fall on the outside surface of the vertical plate while the cooling medium flows inside the vertical plate.

The modeling approach in this study is envisioned at replicating the actual phenomena occurring inside the 3-fluid gas-liquid contactor. To realize this, both fin and tube geometries are retained with the consideration that the liquid is falling only on the vertical fin, and the wetted area on the surface of the tube is added to the wetted area of the fin. This consideration is the bases upon which the momentum conservation for the falling film is established. The fact that the cooling medium is flowing inside the tube and heat transfer towards the cooling medium through the hollow cylinder is implemented.

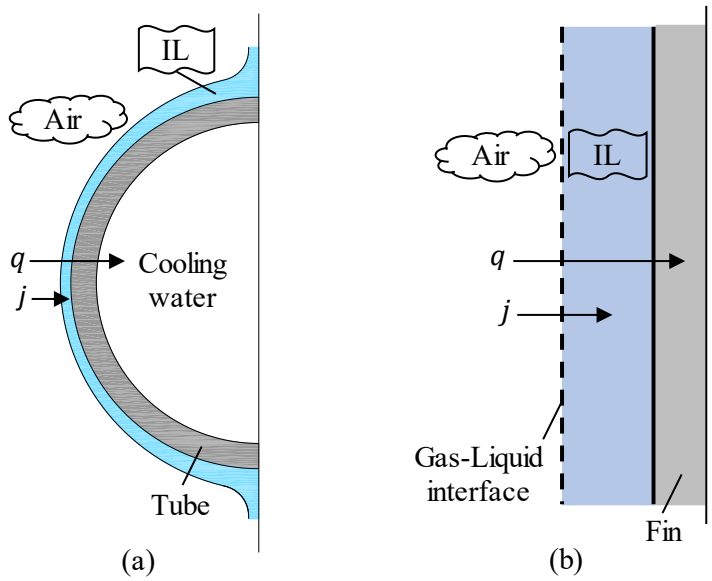

Fig. 7.2 Heat and mass transfers on a: (a) horizontal tube, and (b) vertical fin.

7.2.2 Assumptions

The following assumptions were applied in the mathematical analysis of the 3-fluid gas-liquid contactor:

(a) Transfer flow is steady-state and one-dimensional.

(b) The temperature profile of the air is fully developed.

(c) The flow of the solution is laminar, non-wavy, and fully developed.

(d) Thermodynamic equilibrium exists, and no shear force is acting on the gas-liquid interface.

(e) Mass transport across the falling film is by diffusion only, mass transfer by convection is not considered.

(f) Diffusion-thermo (Dufour) and thermo-diffusion (Soret) effects are neglected.

(g) There is no chemical reaction and viscous dissipation.

7.2.3 Governing equations

Coupled heat and mass transfer on a wet spot while heat transfer and mass transfer by condensation on a dry spot are considered in this mathematical model. Fig. 7.3

illustrates the schematic diagram of the one-dimensional transfer flow on a wetted and dry wall.

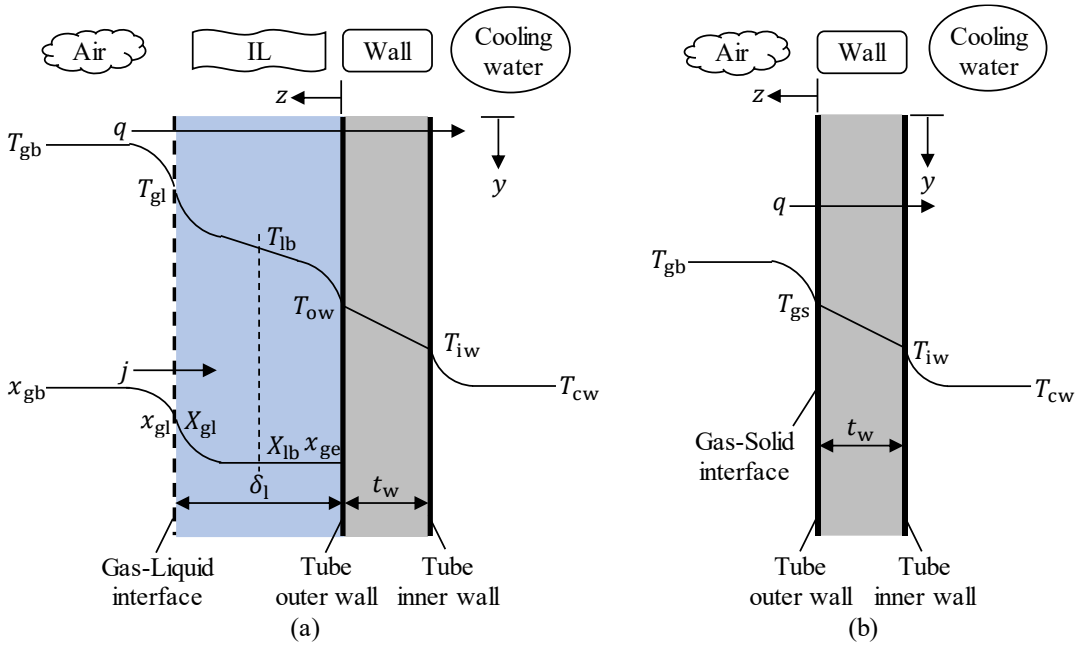

Fig. 7.3 Schematic diagram of the heat and mass transfer flows on a: (a) wetted wall and (b) dry wall.

Applying the assumptions listed in the previous section, the directions of the working fluids in Fig. 7.1, and the heat and mass transfer flow in Fig. 7.3, the governing mass, energy, and momentum equations are derived and expressed in semi-discrete partial differential forms. The system of equations is fully discretized using forward difference method for the air and solution, and backward difference method for the cooling water.

Governing equations for the air

The mass flow rate of dry air $\dot{m}_{gb}$ is conserved in each control volume as expressed by Eq (7.1). For moist air, the change in the water mass fraction of the air in the x direction is balanced by the water vapor transferred from the air to the solution through the gas-liquid interface and the water condensed from the air (Eq. (7.2)).

$$\frac{\partial \dot{m}_{gb}}{\partial x} = 0 \qquad (\mathrm{kg \cdot s^{-1}}) \quad (7.1)$$

$$\dot{m}_{gb} \frac{\partial x_{gb}}{\partial x} = -j_{gb-gl} A_{gl} - \dot{m}_{gb-dp} \qquad (\mathrm{kg \cdot s^{-1}}) \quad (7.2)$$

$j_{gb\text{-}gl}$ denotes the water vapor diffusion mass flux from the gas bulk to the gas-liquid interface, which is described as

$$j_{\mathrm{gb-gl}} = h_{\mathrm{m,gb-gl}}\rho_{\mathrm{gb}}\left(x_{\mathrm{gb}} - x_{\mathrm{gl}}\right) \quad (\mathrm{kg\cdot m^{-2}\cdot s^{-1}}) \quad (7.3)$$

where $h_{\mathrm{m,gb\text{-}gl}}$ ($\mathrm{m\cdot s^{-1}}$) is the gas-side mass transfer coefficient explained in Section 7.2.5 and ρ_{gb} ($\mathrm{kg\cdot m^{-3}}$) is the density of the gas bulk determined based on ASHRAE[6]. x_{gb} ($\mathrm{kg\cdot kg(DA)^{-1}}$) is the water mass fraction of the gas bulk and x_{gl} ($\mathrm{kg\cdot kg(DA)^{-1}}$) is the water mass fraction at the gas-liquid interface, which is determined by relating the overall water mass fraction difference with the gas-side water mass fraction difference as illustrated in Fig. 7.4 and expressed by the next equation.

$$h_{\mathrm{m,gb-lb}}\left(x_{\mathrm{gb}} - x_{\mathrm{ge}}\right) = h_{\mathrm{m,gb-gl}}A_{\mathrm{gl}}\rho_{\mathrm{gb}}\left(x_{\mathrm{gb}} - x_{\mathrm{gl}}\right) \quad (\mathrm{kg\cdot s^{-1}}) \quad (7.4)$$

$h_{\mathrm{m,gb\text{-}lb}}$ ($\mathrm{kg\cdot s^{-1}}$) is the overall mass transfer coefficient discussed in Section 7.2.5 and x_{ge} ($\mathrm{kg\cdot kg(DA)^{-1}}$) is the equilibrium water mass fraction of the liquid bulk, which is estimated as a function of the temperature and IL mass fraction of the IL solution.

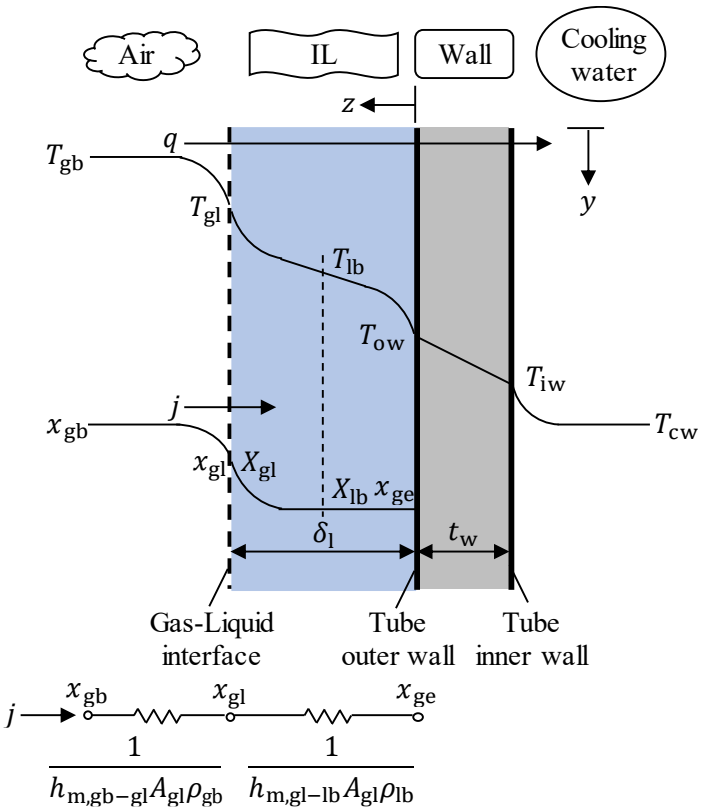

Fig. 7.4 Schematic diagram of the heat and mass transfer flow with equivalent moisture circuit for mass diffusion.

A_{gl} in Eq. (7.2) indicates the area of the gas-liquid interface or simply the wetted area, which is approximated by

$$A_{\mathrm{gl}} = WR\left(A_{\mathrm{t,ow}} + A_{\mathrm{f}}\right) \quad (\mathrm{m^2}) \quad (7.5)$$

where $A_{t,ow}$ (m^2)and A_f (m^2) denote the tube outer-wall and fin areas, respectively, and WR is the wetting ratio.

$\dot{m}_{gb\text{-}dp}$ in Eq. (7.2) is the water condensation rate determined by the following equation.

$$\dot{m}_{gb-dp} = \dot{m}_{gb}(x_{gb} - x_{dp}) \quad (kg \cdot s^{-1}) \quad (7.6)$$

Here, x_{dp} ($kg \cdot kg(DA)^{-1}$) is the humidity ratio of the gas bulk at dewpoint temperature and is estimated as a function of the air dewpoint temperature and pressure. The above equation indicates that condensation occurs as a result of the gas bulk temperature going below or equal to its dewpoint temperature.

The conservation of energy for the moving air is the change in energy in the x direction equated to the conductive and diffusive transports transversal to the flow direction. In the case of partial wetting, heat is conducted both to the wet and dry surfaces of the fin and tube.

$$\dot{m}_{gb}\frac{\partial h_{gb}}{\partial x} = -A_{gl}(q_{gb-gl} + j_{gb-gl}h_c) - \dot{m}_{gb-dp}h_c - q_{gb-gs}A_{gs} \quad (kW) \quad (7.7)$$

where h_{gb} ($kJ \cdot kg^{-1}$) is the enthalpy of the gas bulk and h_c ($kJ \cdot kg^{-1}$) is the enthalpy of condensation for the dehumidification process, which is equivalently the enthalpy of vaporization h_v ($kJ \cdot kg^{-1}$) for the regeneration process. $q_{gb\text{-}gl}$ and $q_{gb\text{-}gs}$ represent the heat flux from the gas bulk to the gas-liquid interface and from the gas bulk to the gas-solid interface and are expressed by Eq. (7.8) and Eq. (7.9), respectively.

$$q_{gb-gl} = h_{h,gb-gl}(T_{gb} - T_{gl}) \quad (kW \cdot m^{-2}) \quad (7.8)$$

$$q_{gb-gs} = h_{h,gb-gs}(T_{gb} - T_{ow}) \quad (kW \cdot m^{-2}) \quad (7.9)$$

$h_{h,gb\text{-}gl}$ ($kW \cdot m^{-2} \cdot K^{-1}$) and $h_{h,gb\text{-}gs}$ ($kW \cdot m^{-2} \cdot K^{-1}$)are the heat transfer coefficients from the gas bulk to the gas-liquid and gas-solid interfaces, respectively, and are both explained in Section 7.2.5.

T_{gl} (°C) and T_{ow} (°C) are the gas-liquid and the tube outer-wall temperatures, respectively, which are estimated by considering the overall temperature difference and the local temperature difference for each phase or element as illustrated in Fig. 7.5. Alternatively, for T_{gl}, the temperature difference between the gas bulk and the liquid bulk can be equated to the gas-side temperature difference similar to the approach used to estimate x_{gl}.

$$h_{h,gb-lb}(T_{gb} - T_{lb}) = h_{h,gb-gl}A_{gl}(T_{gb} - T_{gl}) \quad (kW) \quad (7.10)$$

$h_{h,gb\text{-}lb}$ (kW·K^{-1}) is the heat transfer coefficient from the gas bulk through the liquid bulk described in Section 7.2.5 and T_{lb} (°C) is the liquid bulk temperature.

On the other hand, T_{ow} can be determined by relating the overall temperature difference to the temperature difference of the inner wall and the outer wall (Eq. (7.12)). This requires calculating first the tube inner wall temperature T_{iw} (°C) from the overall one-dimensional heat transfer rate as expressed by the following equation.

$$h_{h,gb-cw}(T_{gb} - T_{cw}) = h_{h,cw}A_{t,iw}(T_{iw} - T_{cw}) \quad \text{(kW)} \qquad (7.11)$$

Here, $h_{h,gb\text{-}cw}$ (kW·K^{-1}) is the overall heat transfer coefficient and $h_{h,gb\text{-}cw}$ (kW·m^{-2} K^{-1}) is the cooling water heat transfer coefficient, which are both explained in Section 7.2.5 and T_{iw} (°C) is the tube inner wall temperature.

Using T_{iw} to estimate T_{ow},

$$h_{h,gb-cw}(T_{gb} - T_{cw}) = h_{h,w}A_{t,ow}(T_{ow} - T_{iw}) \quad \text{(kW)} \qquad (7.12)$$

where $h_{h,w}$ (kW·m^{-2} K^{-1}) is the tube wall heat transfer coefficient discussed in Section 7.2.5.

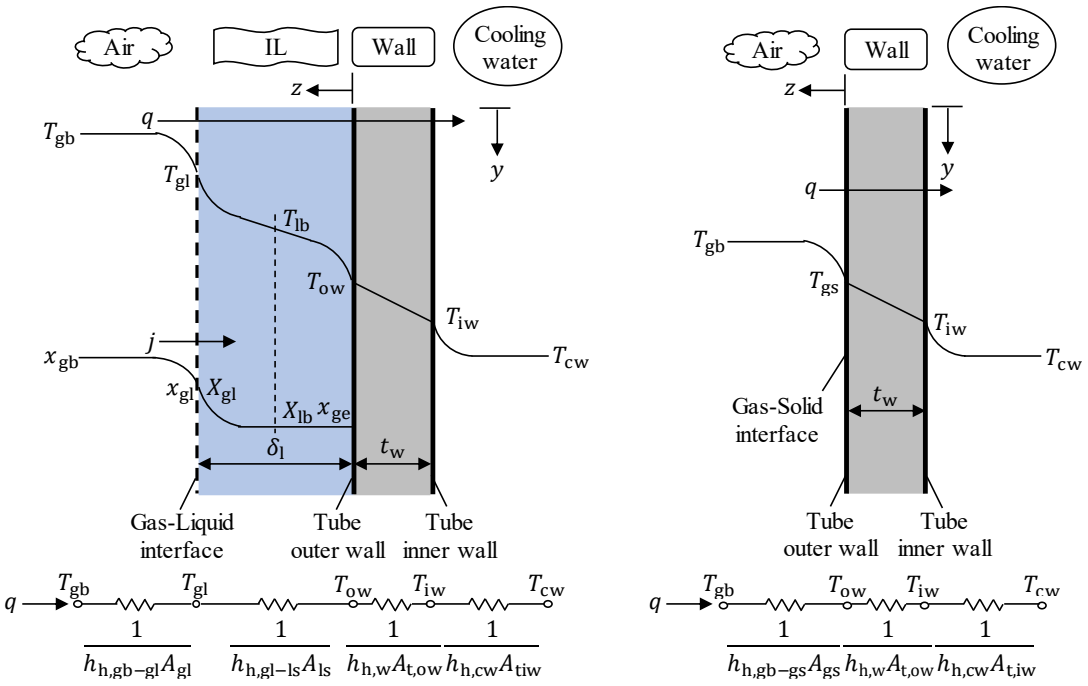

Fig. 7.5 Schematic diagram of the heat and mass transfer flow with equivalent thermal circuits on wet and dry walls.

The symbol A_{gs} is the area covered by the gas-solid interface or the dry area defined by

$$A_{\mathrm{gs}} = (1.0 - WR)\left(A_{\mathrm{t,ow}} + \eta_{\mathrm{f}} A_{\mathrm{f}}\right) \quad (\mathrm{m}^2) \quad (7.13)$$

where η_{f} is the fin efficiency, which is calculated by the following formula[117]:

$$\eta_{\mathrm{f}} = \left\{1 + h_{\mathrm{h}} \frac{\left(D_{\mathrm{f}} - D_{\mathrm{t,o}}\right)^2}{6\lambda_{\mathrm{t}} t_{\mathrm{f}}} \left(\frac{D_{\mathrm{f}}}{D_{\mathrm{t,o}}}\right)^{0.5}\right\}^{-1} \quad (7.14)$$

h_{h} (kW·m^{-2}·K^{-1}) is the symbol for the heat transfer coefficient, which is either of the air or the IL solution. $D_{\mathrm{t,o}}$ (m), λ_{t} (kW·m^{-1}·K^{-1}), and t_{f} (m) are the tube outer diameter, tube thermal conductivity, and the fin thickness, respectively. D_{f} (m) is the fin equivalent diameter described as follows:

$$D_{\mathrm{f}} = \left(\frac{4}{\pi} dxdy\right)^{0.5} \quad (\mathrm{m}) \quad (7.15)$$

Governing equations for aqueous ionic liquid

In falling film liquid desiccant systems, the gas and the liquid generally have short contact time that the solute barely has a chance to cross the interface and it diffuses only slightly into the liquid bulk. Here, diffusion behaves as if the film is infinitely thick and a concentration boundary layer is produced near the interface. The mass transfer model presented in Fig. 7.3 is based on this theory suggested by Higbie in 1935 known as the "Penetration Theory"[114)-115)]. Applying this theory, the conservation of mass for the liquid bulk is the mass diffusion into the film defined as

$$\frac{\partial \dot{m}_{\mathrm{lb}}}{\partial y} = j_{\mathrm{gl-lb}} A_{\mathrm{gl}} + \dot{m}_{\mathrm{gb-dp}} \quad (\mathrm{kg \cdot s^{-1}}) \quad (7.16)$$

where $\dot{m}_{\mathrm{lb}}$ (kg·s^{-1}) is the liquid bulk mass flow rate and $j_{\mathrm{gl\text{-}lb}}$ represents the diffusion mass flux of water species from the gas-liquid interface to the liquid bulk expressed as

$$j_{\mathrm{gl-lb}} = h_{\mathrm{m,gl-lb}} \rho_{\mathrm{lb}} \left(X_{\mathrm{gl}} - X_{\mathrm{lb}}\right) \quad (\mathrm{kg \cdot m^{-2} \cdot s^{-1}}) \quad (7.17)$$

Here, ρ_{lb} (kg m^{-3}) is the density if the liquid bulk and X_{gl} (kg(IL) kg(sol)$^{-1}$) is the IL mass fraction at the gas-liquid interface. $h_{\mathrm{m,gl\text{-}lb}}$ (m·s^{-1}) is the mass transfer coefficient from the gas-liquid interface to the liquid bulk discussed in Section 7.2.5.

The conservation of mass for the IL in the liquid bulk is given by

$$\frac{\partial (\dot{m}_{\mathrm{lb}} X_{\mathrm{lb}})}{\partial y} = 0 \quad (\mathrm{kg \cdot s^{-1}}) \quad (7.18)$$

where X_{lb} (kg(IL) kg(sol)$^{-1}$) is the IL mass fraction in the liquid bulk.

The conservation of energy for the liquid bulk is defined as the change in energy in the y direction equated to the net conductive transport to or from the liquid bulk, that is

$$\frac{\partial(\dot{m}_{\mathrm{lb}}h_{\mathrm{lb}})}{\partial y} = A_{\mathrm{gl}}\left(q_{\mathrm{gl-lb}} + j_{\mathrm{gl-lb}}h_{\mathrm{c}}\right) + \dot{m}_{\mathrm{gb-dp}}h_{\mathrm{c}} - q_{\mathrm{lb-ls}}A_{\mathrm{ls}} \qquad \text{(kW)} \quad (7.19)$$

where h_{lb} (kJ·kg^{-1}) is the enthalpy of the liquid bulk and $q_{\mathrm{gl\text{-}lb}}$ denotes the heat flux from the gas-liquid to the liquid bulk and is defined as

$$q_{\mathrm{gl-lb}} = h_{\mathrm{h,gl-ls}}\left(T_{\mathrm{gl}} - T_{\mathrm{lb}}\right) \qquad \text{(kW·m}^{-2}\text{)} \quad (7.20)$$

$h_{\mathrm{h,gl\text{-}ls}}$ (kW·m^{-2}·K^{-1}) indicates the heat transfer coefficient from the gas-liquid to the liquid-solid interface, tackled in Section 7.2.5.

$q_{\mathrm{lb\text{-}ls}}$, which is represented by Eq. (7.21), is the heat flux from the liquid bulk to the liquid-solid interface.

$$q_{\mathrm{lb-ls}} = h_{\mathrm{h,gl-ls}}(T_{\mathrm{lb}} - T_{\mathrm{ow}}) \qquad \text{(kW·m}^{-2}\text{)} \quad (7.21)$$

A_{ls} is the liquid-solid interfacial area determined by the following equation.

$$A_{\mathrm{ls}} = WR\left(A_{\mathrm{t,ow}} + \eta_{\mathrm{f}}A_{\mathrm{f}}\right) \qquad \text{(m}^2\text{)} \quad (7.22)$$

Assuming negligible inertia, Nusselt's solution for a falling film is given by the balance between the viscous and gravity forces,

$$\mu_{\mathrm{l}}\frac{\partial^2 u_{\mathrm{l}}}{\partial z^2} = -\rho_{\mathrm{l}}g \qquad \text{(kg·m}^{-2}\text{·s}^{-2}\text{)} \quad (7.23)$$

Integrating Eq. (7.23) results to

$$\frac{\partial u_{\mathrm{l}}}{\partial z} = -\frac{\rho_{\mathrm{l}}g}{\mu_{\mathrm{l}}}z + c_1 \qquad \text{(s}^{-1}\text{)} \quad (7.24)$$

Substituting the boundary condition for u_{l} at the gas-liquid interface provided in Eq. (7.40), which is defined by the laminar and fully developed solution flow assumptions, gives the expression for c_1

$$c_1 = \frac{\rho_{\mathrm{l}}g}{\mu_{\mathrm{l}}}\delta_{\mathrm{l}} \qquad \text{(s}^{-1}\text{)} \quad (7.25)$$

Now, integrating Eq. (7.26)

$$u_{\mathrm{l}} = -\frac{\rho_{\mathrm{l}} g}{\mu_{\mathrm{l}}}\frac{z^2}{2} + c_1 z + c_2 \qquad (\mathrm{m\cdot s^{-1}}) \qquad (7.26)$$

Substituting the expression for c_1 derived earlier and the boundary condition for u_{l} at the liquid-solid interface written in Eq. (7.39) yields the equation for the velocity profile of the falling film

$$u_{\mathrm{l}} = \frac{\rho_{\mathrm{l}} g}{\mu_{\mathrm{l}}}\left(\delta_{\mathrm{l}} z - \frac{z^2}{2}\right) \qquad (\mathrm{m\cdot s^{-1}}) \qquad (7.27)$$

The maximum velocity $u_{\mathrm{l,max}}$ is the value at the outermost part of the film ($z = \delta_{\mathrm{l}}$). Substituting $z = \delta_{\mathrm{l}}$ to the velocity profile gives the equation for $u_{\mathrm{l,max}}$

$$u_{\mathrm{l,max}} = \frac{\rho_{\mathrm{l}} g \delta_{\mathrm{l}}^2}{2\mu_{\mathrm{l}}} \qquad (\mathrm{m\cdot s^{-1}}) \qquad (7.28)$$

The average velocity for half parabolic velocity profile of the fully developed liquid film is then

$$u_{\mathrm{l,ave}} = \frac{2}{3} u_{\mathrm{l,max}} = \frac{\rho_{\mathrm{l}} g \delta_{\mathrm{l}}^2}{3\mu_{\mathrm{l}}} \qquad (\mathrm{m\cdot s^{-1}}) \qquad (7.29)$$

The mass flow rate of the liquid film per unit length of the contactor is given by the expression

$$\Gamma_{\mathrm{l}} = \frac{\dot{m}_{\mathrm{l}}}{L} \qquad (\mathrm{kg\cdot m^{-1}\cdot s^{-1}}) \qquad (7.30)$$

This time, considering the continuity of Γ_{l} across the falling film

$$\Gamma_{\mathrm{l}} = \int_0^{\delta_{\mathrm{l}}} \rho_{\mathrm{l}} u_{\mathrm{l}} dz = \frac{\rho_{\mathrm{l}}^2 g}{\mu_{\mathrm{l}}} \int_0^{\delta_{\mathrm{l}}} \left(\delta_{\mathrm{l}} z - \frac{z^2}{2}\right) dz \qquad (\mathrm{kg\cdot m^{-1}\cdot s^{-1}}) \qquad (7.31)$$

Taking the integral of the above expression gives the equation of the film thickness

$$\delta_{\mathrm{l}} = \left(\frac{3\mu_{\mathrm{l}}\Gamma_{\mathrm{l}}}{\rho_{\mathrm{l}}^2 g}\right)^{1/3} \qquad (\mathrm{m}) \qquad (7.32)$$

Governing equations for the cooling/heating water

The conservation of mass for the cooling water is the net change in the mass flow rate of the cooling water $\dot{m}_{\mathrm{cw}}$ within a control volume, written in equation form as

$$\frac{\partial \dot{m}_{\mathrm{cw}}}{\partial z} = 0 \qquad (\mathrm{kg \cdot s^{-1}}) \quad (7.33)$$

The energy conservation, on the other hand, is the balance between the change in energy of the cooling water in the z direction and the net conductive transport to or from the cooling water through the tube.

$$\frac{\partial (\dot{m}_{\mathrm{cw}} h_{\mathrm{cw}})}{\partial z} = q_{\mathrm{iw-cw}} A_{\mathrm{t,iw}} \qquad (\mathrm{kW}) \quad (7.34)$$

Here, h_{cw} ($\mathrm{kJ \cdot kg^{-1}}$) is the enthalpy of the cooling water and $A_{\mathrm{t,iw}}$ ($\mathrm{m^2}$) is the area of the tube inner wall. $q_{\mathrm{iw-cw}}$ denotes the heat flux from the tube inner wall to the cooling water expressed by the following equation

$$q_{\mathrm{iw-cw}} = h_{\mathrm{h,cw}} (T_{\mathrm{iw}} - T_{\mathrm{cw}}) \qquad (\mathrm{kW \cdot m^{-2}}) \quad (7.35)$$

where $h_{\mathrm{h,cw}}$ ($\mathrm{kW \cdot m^{-2} \cdot K^{-1}}$) indicates the heat transfer coefficient of the cooling water, which is treated in Section 7.2.5, and T_{cw} (°C) is the cooling water temperature.

7.2.4 Initial and boundary conditions

Initial conditions are important to solve the system of equations derived in the previous section. These initial or input conditions depend on the experimental conditions. On the other hand, the boundary conditions have specific applications and some of them are part of the assumptions. The initial and boundary conditions are listed mathematically below.

Initial conditions

At the air inlet or $x = 0$,

$$T_{\mathrm{gb}} = T_{\mathrm{ig}},\ T_{\mathrm{dp,gb}} = T_{\mathrm{dp,ig}},\ x_{\mathrm{gb}} = x_{\mathrm{ig}},\ u_{\mathrm{gb}} = u_{\mathrm{ig}} \qquad (7.36)$$

where $T_{\mathrm{dp,gb}}$ and $T_{\mathrm{dp,ig}}$ are the gas bulk and inlet gas dewpoint temperatures, respectively.

At the solution inlet or $y = 0$,

$$T_{\mathrm{lb}} = T_{\mathrm{il}},\ \dot{m}_{\mathrm{lb}} = \dot{m}_{\mathrm{il}},\ X_{\mathrm{lb}} = X_{\mathrm{il}} \qquad (7.37)$$

where $\dot{m}_{\mathrm{il}}$ is the inlet liquid mass flow rate.

At the cooling water inlet ($y = H$ and $z = W$),

$$T_{\mathrm{cw}} = T_{\mathrm{icw}},\ \dot{m}_{\mathrm{cw}} = \dot{m}_{\mathrm{icw}} \qquad (7.38)$$

where T_{cw}, T_{icw}, and $\dot{m}_{icw}$ are the cooling water temperature, inlet cooling water temperature, and inlet cooling water mass flow rate, respectively.

Boundary conditions

Assuming a fully developed and non-wavy falling film, the boundary condition at the liquid-solid interface or $z = 0$, as shown in Fig. 7.3, are the following:

$$T_l = T_{ow},\ X_l = X_{lb},\ u_l = 0 \tag{7.39}$$

At the gas-liquid interface or $z = \delta_l$, the boundary conditions are

$$T_l = T_{gl},\ X_l = X_{gl},\ u_l = u_{l,max},\ \frac{\partial u_l}{\partial z} = 0 \tag{7.40}$$

7.2.5 Heat and mass transfer coefficients

To solve the heat and mass transfer terms, it is necessary to determine the heat and mass transfer coefficients corresponding to each term. This includes the heat and mass transfer coefficients of the air and IL solution, the heat transfer coefficient of the tube and cooling water, and the overall heat and mass transfer coefficients. Highly applicable correlations for the air, liquid desiccant solution, and cooling water were selected from the literature to estimate the heat and mass transfer coefficients.

Gas-side heat and mass transfer coefficients

Generally, for laminar flow in rectangular ducts, the gas-side heat transfer coefficient $h_{h,gb\text{-}gl}$ ($kW \cdot m^{-2} \cdot K^{-1}$) can be estimated from the Nusselt number correlation Nu = 7.54 for constant wall temperature and Nu = 8.24 for constant heat flux[116]. A more applicable correlation for the Nusselt number specific for plate-fin and tube heat exchangers and considering the effect of liquid condensate was obtained by Fujii and Seshimo[117]. Categorized into low and high Reynolds number, the Nusselt number correlation for low gas bulk Reynolds number Re_{gb} defined within the range of 100 ~ 400 is expressed as

$$Nu_{gb} = \frac{h_{h,gb-gl} d_{h,gb}}{\lambda_{gb}} = 2.1 Re_{gb} \left(\frac{d_{h,gb}}{2dx} \right)^{0.38} \tag{7.41}$$

For higher Reynolds number defined within the range of 400 ~ 750, the Nusselt number correlation is

$$Nu_{gb} = \frac{h_{h,gb-gl} d_{h,gb}}{\lambda_{gb}} = 0.12 Re_{gb}^{0.64} \tag{7.42}$$

The hydraulic diameter of the gas bulk $d_{\mathrm{h,gb}}$ (m) differs in dry $d_{\mathrm{h,gb,dry}}$ and wetted $d_{\mathrm{h,gb,wet}}$ areas and varies according to the film thickness defined as follows

$$d_{\mathrm{h,gb,dry}} = \frac{4A_{\mathrm{c,dry}}}{P_{\mathrm{w,dry}}} = \frac{4[(P_{\mathrm{f}} - t_{\mathrm{f}})dy - P_{\mathrm{f}}D_{\mathrm{to}}]}{2(dy + P_{\mathrm{f}})} \quad \text{(m)} \qquad (7.43)$$

$$d_{\mathrm{h,gb,wet}} = \frac{4A_{\mathrm{c,wet}}}{P_{\mathrm{w,wet}}} = \frac{4[(p_{\mathrm{f}} - t_{\mathrm{f}})dy - P_{\mathrm{f}}D_{\mathrm{to}} - 2\delta_{\mathrm{l}}dy]}{2[dy + (P_{\mathrm{f}} - 2\delta_{\mathrm{l}})]} \quad \text{(m)} \qquad (7.44)$$

Similarly, the $\mathrm{Re}_{\mathrm{gb}}$ also differs in dry $\mathrm{Re}_{\mathrm{gb,dry}}$ and wet $\mathrm{Re}_{\mathrm{gb,wet}}$ areas,

$$\mathrm{Re}_{\mathrm{gb,dry}} = \frac{\rho_{\mathrm{gb}} u_{\mathrm{gb,dry}} d_{\mathrm{h,gb,dry}}}{\mu_{\mathrm{gb}}} \qquad (7.45)$$

$$\mathrm{Re}_{\mathrm{gb,wet}} = \frac{\rho_{\mathrm{gb}} u_{\mathrm{gb,wet}} d_{\mathrm{h,gb,wet}}}{\mu_{\mathrm{gb}}} \qquad (7.46)$$

where μ_{gb} (Pa·s) is the gas bulk dynamic viscosity determined from ASHRAE[7] as a function of the gas bulk's temperature and humidity ratio. $u_{\mathrm{gb,dry}}$ and $u_{\mathrm{gb,wet}}$ are the gas bulk effective velocity in dry and wet areas described by the following equations:

$$u_{\mathrm{gb,dry}} = \frac{\dot{m}_{\mathrm{gb}}}{\rho_{\mathrm{gb}}[(P_{\mathrm{f}} - t_{\mathrm{f}})dy - P_{\mathrm{f}}D_{\mathrm{to}}]} \quad (\mathrm{m \cdot s^{-1}}) \qquad (7.47)$$

$$u_{\mathrm{gb,wet}} = \frac{\dot{m}_{\mathrm{gb}}}{\rho_{\mathrm{gb}}[(P_{\mathrm{f}} - t_{\mathrm{f}})dy - P_{\mathrm{f}}D_{\mathrm{to}} - 2\delta_{\mathrm{l}}dy]} \quad (\mathrm{m \cdot s^{-1}}) \qquad (7.48)$$

The gas-side mass transfer coefficient $h_{\mathrm{h,gb\text{-}gl}}$ ($\mathrm{m \cdot s^{-1}}$) can be estimated using the gas-side heat transfer coefficient and relevant gas physical properties. Reynolds analogy correlates the heat, mass, and momentum transport coefficients and is found to be accurate for gases by experiments. On the other hand, due to the practical usefulness of Reynolds analogy, many researchers have extended the method to estimate the mass transfer coefficient of liquids. The most recognized extension is the Chilton-Colburn analogy[115]. For heat and mass transfer relationship, Reynolds analogy is written as

$$h_{\mathrm{h,gb-gl}} = \frac{h_{\mathrm{m,gb-gl}}}{\rho_{\mathrm{gb}} c_{\mathrm{p,gb}}} \quad (\mathrm{kW \cdot m^{-2} \cdot K^{-1}}) \qquad (7.49)$$

where $c_{\mathrm{p,gb}}$ ($\mathrm{J \cdot kg^{-1} \cdot K^{-1}}$) indicates the constant pressure specific heat of the gas bulk estimated from ASHRAE[6].

Liquid-side heat and mass transfer coefficients

The liquid-side heat transfer coefficient $h_{\mathrm{h,gl\text{-}ls}}$ (kW·m^{-2}·K^{-1}) is determined based on the Nusselt number correlation of Karami et al.[118] The heat transport model assumes viscous sublayers near the gas-liquid and liquid-solid interfaces and is expressed as

$$\mathrm{Nu_{lb}} = \frac{h_{\mathrm{h,gl-ls}}\delta_{\mathrm{l}}}{\lambda_{\mathrm{lb}}} = 0.4764\mathrm{Re_{lb}^{0.0477}Pr_{lb}^{0.334}} \tag{7.50}$$

where $\mathrm{Nu_{lb}}$ denotes the Nusselt number of the liquid bulk and λ_{lb} (kW·m^{-1}·K^{-1}) is the thermal conductivity of the liquid bulk estimated as a function of the temperature and IL mass fraction of the aqueous IL. $\mathrm{Re_{lb}}$, is the Reynolds number of the liquid bulk and $\mathrm{Pr_{lb}}$ is the Prandtl number of liquid bulk calculated as a function of the temperature and IL mass fraction of the aqueous IL.

There are several applicable ways to determine the liquid-side mass transfer coefficient $h_{\mathrm{h,gl\text{-}lb}}$. One of which is by employing the Chilton-Colburn analogy introduced earlier. The other methods are non-empirical formulations of the mass transfer coefficient as a function of the diffusion coefficient. The simplest theoretical formulation, the Film Theory[114)-115)], assumes a stagnant film near the gas-liquid interface undisturbed by the liquid bulk. It says that the mass transfer coefficient is proportional to the mass diffusion coefficient and inversely proportional to the film thickness, $h_{\mathrm{h,gl\text{-}lb}} = D_{\mathrm{lb}}/\delta_{\mathrm{l}}$. The other method is given by the Penetration Theory explained Section 7.2.3. This model is better physically since it considers mass transfer across the gas-liquid interface depending on the velocity of the liquid. Using this approach, the liquid-side mass transfer coefficient is

$$h_{\mathrm{m,gl-lb}} = 2\sqrt{\frac{u_{\mathrm{l,max}}D_{\mathrm{lb}}}{\pi dy}} \qquad (\mathrm{m\cdot s^{-1}}) \tag{7.51}$$

where D_{lb} (m^2·s^{-1}) is formulated as a function of the liquid bulk IL mass fraction.

Tube heat transfer coefficient

The tube wall heat transfer coefficient $h_{\mathrm{h,w}}$ is estimated using the thermal conductivity λ_{w} (0.236 kW·m^{-1}·K^{-1}) of the aluminum tube as

$$h_{\mathrm{h,w}} = \frac{2\pi\lambda_{\mathrm{w}}P_{\mathrm{f}}}{\ln(D_{\mathrm{to}}/D_{\mathrm{ti}})} \qquad (\mathrm{kW\cdot m^{-2}\cdot K^{-1}}) \tag{7.52}$$

where D_{ti} (m) represents the tube inner diameter.

Cooling/heating water heat transfer coefficient

For the cooling water heat transfer coefficient $h_{\mathrm{h,cw}}$ (kW·m^{-2}·K^{-1}), the Nusselt number correlation of Gnielinski[119] is used, which is valid for $\mathrm{Re_{cw}} \leq 2 \times 10^4$.

$$\mathrm{Nu_{cw}} = \frac{h_{\mathrm{h,cw}} d_{\mathrm{h,cw}}}{\lambda_{\mathrm{cw}}} = \frac{(f_{\mathrm{cw}}/8)(\mathrm{Re_{cw}} - 1000)\mathrm{Pr_{cw}}}{1 + 12.7(f_{\mathrm{cw}}/8)^{1/2}\left(\mathrm{Pr_{cw}^{2/3}} - 1\right)} \tag{7.53}$$

where $\mathrm{Nu_{cw}}$ denotes the Nusselt number of the cooling water and λ_{cw} (kW·m^{-1}·K^{-1}), $\mathrm{Re_{cw}}$, and $\mathrm{Pr_{cw}}$ are the thermal conductivity, the Reynolds number, and the Prandtl number of the cooling water estimated according to the JSME Steam Tables[120].

$d_{\mathrm{h,cw}}$ (m) represents the hydraulic diameter of the cooling/heating water, which is equal to the inner diameter of the tube. On the other hand, f_{cw} is the friction factor of the cooling water and is defined as

$$f_{\mathrm{cw}} = \mathrm{Re_{cw}}^{-1/4} \tag{7.54}$$

Overall heat and mass transfer coefficients

Considering first the summation of heat transfer resistance across the gas-liquid interface as shown in Fig. 7.5,

$$\frac{1}{h_{\mathrm{h,gb-ls}}} = \frac{1}{h_{\mathrm{h,gb-gl}} A_{\mathrm{gl}}} + \frac{1}{h_{\mathrm{h,gl-ls}} A_{\mathrm{ls}}} \quad (\mathrm{K \cdot kW^{-1}}) \tag{7.55}$$

Similarly, the overall mass transfer coefficient $h_{\mathrm{m,gb\text{-}lb}}$ across the gas-liquid interface (Fig. 7.4) is obtained applying the mass transfer terms

$$\frac{1}{h_{\mathrm{m,gb-lb}}} = \frac{1}{h_{\mathrm{m,gb-gl}} A_{\mathrm{gl}} \rho_{\mathrm{gb}}} + \frac{1}{h_{\mathrm{m,gl-lb}} A_{\mathrm{gl}} \rho_{\mathrm{lb}}} \quad (\mathrm{s \cdot kg^{-1}}) \tag{7.56}$$

Now, the overall heat transfer coefficient $h_{\mathrm{h,gb\text{-}cw}}$ is derived by considering the one-dimensional heat transfer from the gas bulk to the cooling water both on dry and wetted areas as shown in Fig. 7.5. Since the heat transfer across the gas-liquid interface $h_{\mathrm{h,gb\text{-}ls}}$ (Eq. (7.55))is already known, this is added to the other resistances to get $h_{\mathrm{h,gb\text{-}cw}}$

$$\frac{1}{h_{\mathrm{h,gb-cw}}} = \frac{1}{\dfrac{1}{h_{\mathrm{h,gb-gs}} A_{\mathrm{gs}} + h_{\mathrm{h,gl-ls}}} + \dfrac{1}{h_{\mathrm{h,w}} A_{\mathrm{t,ow}}} + \dfrac{1}{h_{\mathrm{h,cw}} A_{\mathrm{t,iw}}}} \quad (\mathrm{K \cdot kW^{-1}}) \tag{7.57}$$

7.2.6 Air pressure drop

The pressure drop is a necessary parameter in optimization studies of air conditioning systems due to its contribution to the power consumption of the system. To

determine the pressure loss of the air through each control volume, the relationship of the friction factor to the pressure drop is used, which is defined as

$$\Delta P_{\mathrm{gb}} = -\frac{f_{\mathrm{gb}}\rho_{\mathrm{gb}}dx}{2}\left(\frac{u_{\mathrm{gb,dry}}^2(1-WR)}{d_{\mathrm{h,gb,dry}}} + \frac{u_{\mathrm{gb,wet}}^2 WR}{d_{\mathrm{h,gb,wet}}}\right) \quad \text{(Pa)} \qquad (7.58)$$

where ΔP_{gb} is the pressure drop of the gas bulk and f_{gb} is the Darcy friction factor of the gas bulk. Note that the total air pressure drop across a single control volume is the sum of the specific pressure drop in dry and wetted areas. Initially, the total pressure drop across a unit control volume was estimated assuming the smallest hydraulic diameter, which is that of a wetted area. However, this resulted to predicted values for the air pressure drop that are significantly higher compared to the experimental results. On the contrary, lower pressure drop values were predicted when estimated using the largest hydraulic diameter, which is that of a dry area. When estimated using the air pressure drop both in dry and wetted areas, predicted values are close to the experimental results.

Instead of the general correlation for rectangular ducts, f_{gb} is obtained employing the correlations obtained by Fujii and Seshimo[117], which were validated using their experimental results from a plate-fin and tube considering the effect of liquid condensate. These friction factor correlations are expressed as follows:

$$f_{\mathrm{gb}}\left(\frac{2dx}{\mathrm{Re}_{\mathrm{gb}}d_{\mathrm{h,gb}}}\right) = 0.43 + 35.1\left(\frac{\mathrm{Re}_{\mathrm{gb}}d_{\mathrm{h,gb}}}{2dx}\right)^{-1.07} \qquad 100 \le \mathrm{Re}_{\mathrm{gb}} \le 400 \qquad (7.59)$$

$$f_{\mathrm{gb}} = 0.26 + 27.0\left(\mathrm{Re}_{\mathrm{gb}}\right)^{-1.27} \qquad 400 \le \mathrm{Re}_{\mathrm{gb}} \le 750 \qquad (7.60)$$

7.2.7 Numerical analysis

The partial differential terms in the governing equations have to be discretized for the mathematical model to be suitable for numerical computation. Assuming that the three fluids are continuous, the conservative partial differential terms can be discretized either by finite volume or finite difference methods.

The spatial derivatives from the governing equations are transformed into finite differences and a system of algebraic equations or discrete equations are derived, which can be implemented into a computer code. The integrals of the air and IL solution are approximated by the forward difference method while the integrals of the cooling water are approximated by the backward difference method. In addition, a convergence scheme is employed for the refrigerant, in this case water, since it enters from the bottom of the contactor and exits at the top (see Fig. 7.6). The Newton-Raphson algorithm is used to approximate the exact solution (inlet water condition) within the specified error.

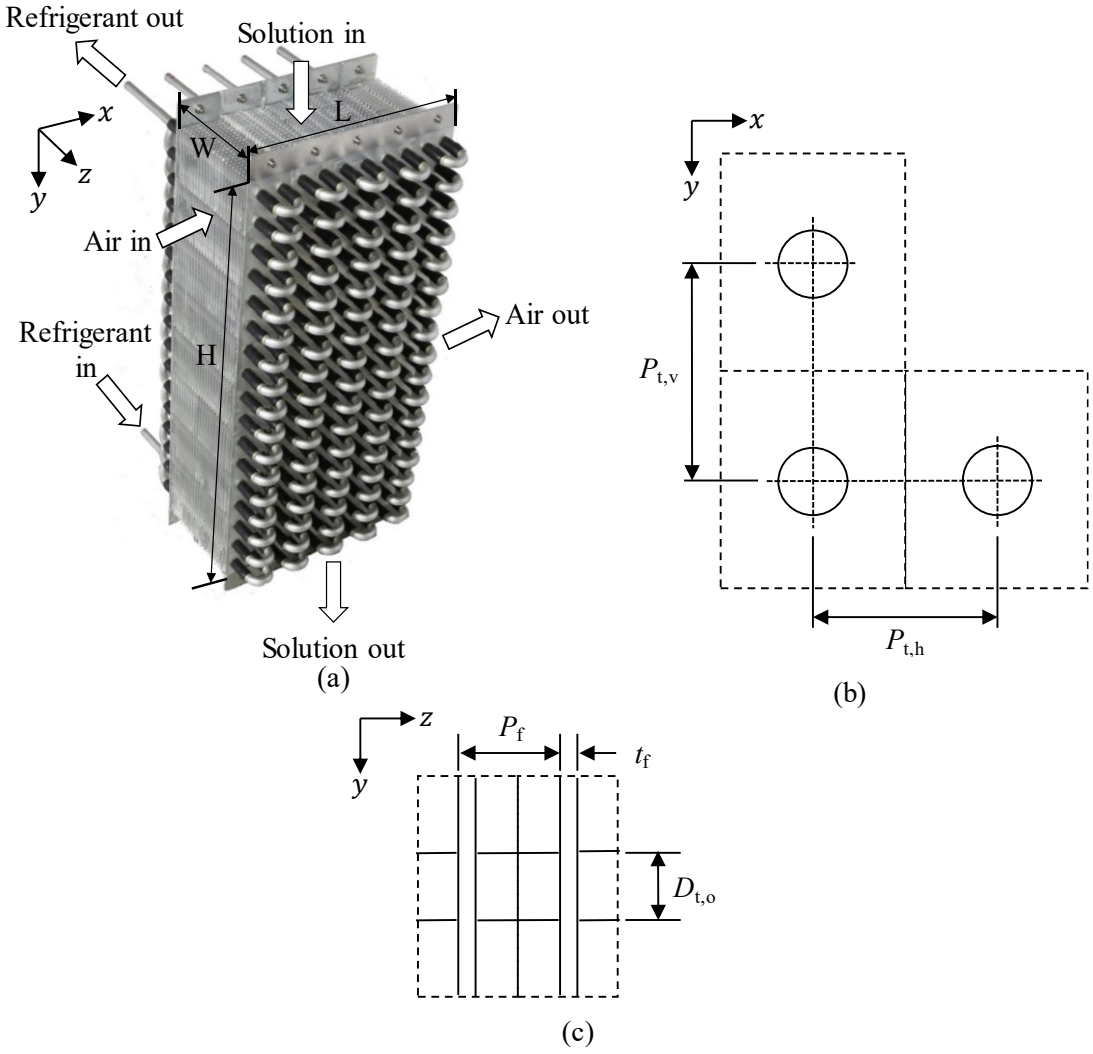

Fig. 7.6 (a) 3-Fluid gas-liquid contactor, (b) front view of control volume, and (c) side view of the control volume.

8. Experiment and validation of the 3-fluid gas-liquid contactor model

8.1 Introduction

An experimental apparatus was built to test and evaluate the performance of the new 3-fluid gas-liquid contactor. Experimental data at various air and solution flow rates were gathered from the fin-tube liquid desiccant air conditioning system. These results support the objectives of the research by serving as concrete materials for the clarification of the important phenomena, trends, and the validation of the 3-fluid gas-liquid mathematical model. The dehumidification and pressure drop performance of the 3-fluid gas-liquid contactor is compared with the performance of the 2-fluid packed bed contactor.

8.2 Fin-tube liquid desiccant air conditioning system

8.2.1 Experimental apparatus

Fig. 8.1 shows a photo of the experimental set-up for the 3-fluid liquid desiccant air conditioning system. A schematic diagram of the liquid desiccant air conditioning system is illustrated in Fig. 8.2. The liquid desiccant system is divided into three parts: the process side, the solution control unit, and the regeneration side. The inlet air for both the dehumidification and regeneration sides, which are represented by the large arrows in light blue and orange colors, is supplied by a separate air handling. The new ionic liquid (IL) desiccant was used as the liquid desiccant in this system.

Fig. 8.1 Photo of the experimental apparatus.

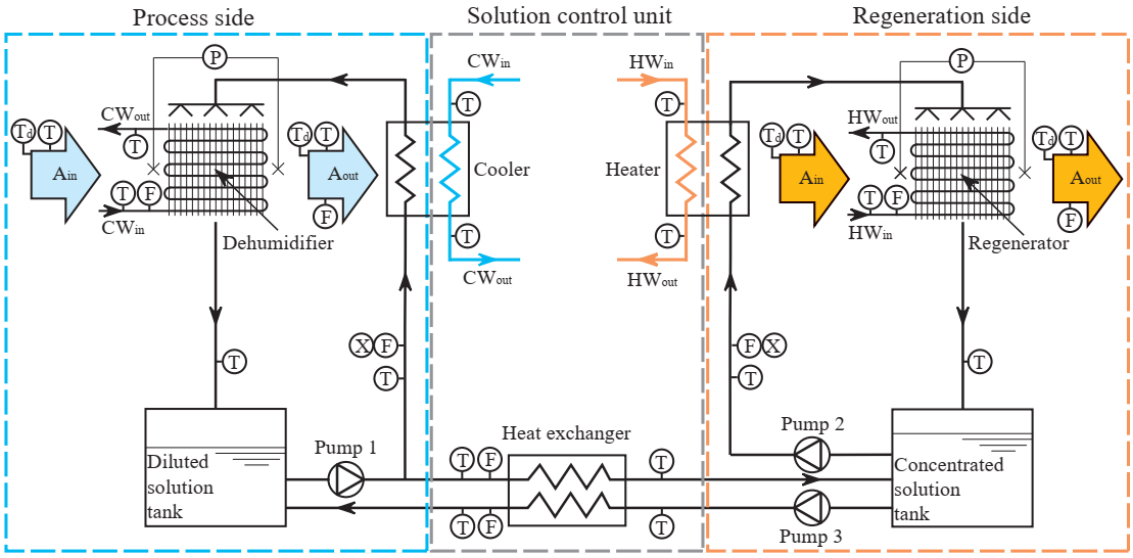

Fig. 8.2 Schematic diagram of the 3-fluid liquid desiccant air conditioning system.

Fig. 8.3 shows the isometric, side, and front views of the 3-fluid gas-liquid contactor. The 3-fluid gas-liquid contactor is different in terms of material, construction, and the number of interacting fluids compared with a conventional packed bed gas-liquid contactor. This type of gas-liquid contactor is generally known as an internally cooled/heated gas-liquid contactor because it incorporates an extra working fluid along with the air and solution. The purpose of the third fluid is to remove the sensible and latent heat absorbed by the solution from the air.

In the gas-liquid contactor, the air is blown horizontally through the length of the contactor by a blower and the solution flows vertically along the height of the contactor through the influence of gravity depicting a crossflow configuration between the two directly contacting fluids. There are five channels of cooling water with the inlet at the bottom and outlet at the top of the contactor. Higher effectiveness and energy recovery can be realized by making the cooling water and desiccant solution enter on opposite sides or counterflow instead of parallel flow; and since the two working fluids are not in direct contact with each other, solution carryover by the cooling water is not possible.

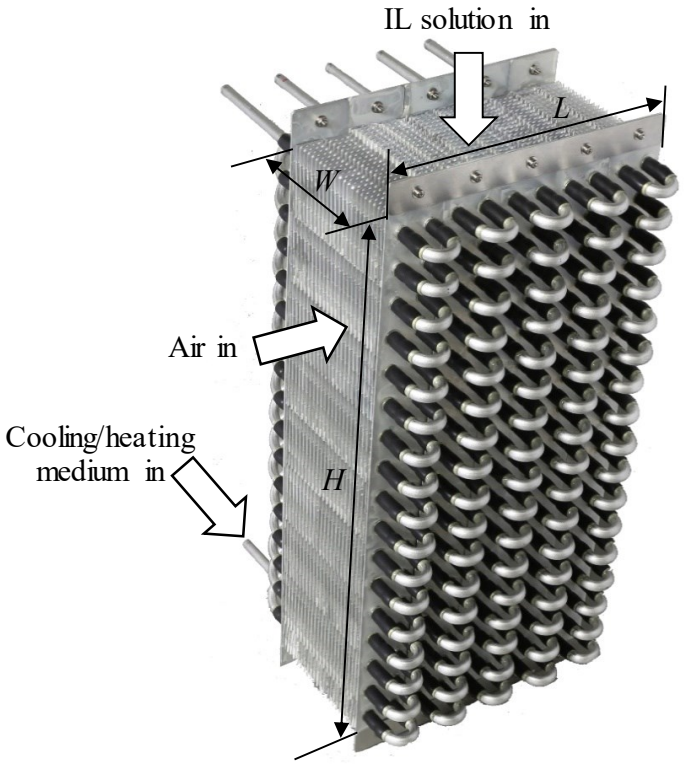

(a)

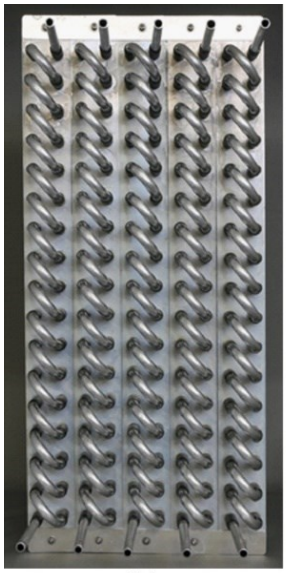

(b)

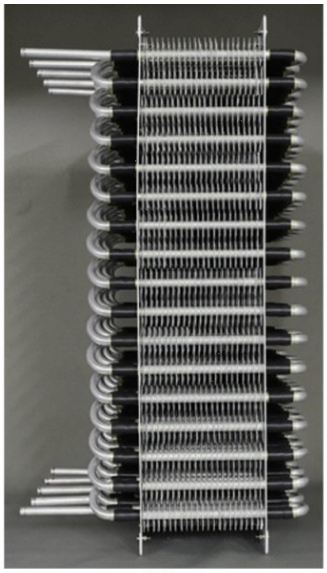

(c)

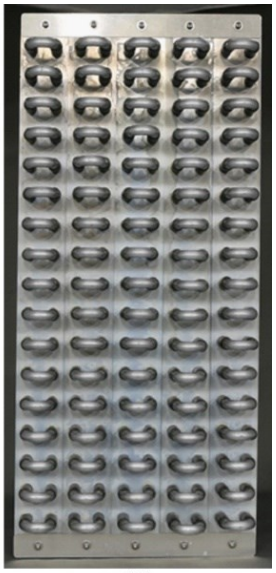

(d)

Fig. 8.3 Photo of the 3-fluid gas-liquid contactor: (a) isometric, (b) front, (c) side, and (c) back views.

Table 8.1 lists the detailed dimensions and Fig. 8.4 illustrates the construction of the fin-tube contactor. The surface contact area of the fin-tube contactor is approximately 451 $m^2 \cdot m^{-3}$.

Table 8.1 Detailed dimensions of the 3-fluid gas-liquid contactor.

Parameter	Symbol	Dimension
Length (air flow direction)	L	200×10^{-3} m
Height (solution flow direction)	H	400×10^{-3} m
Width (refrigerant flow direction)	W	100×10^{-3} m
Fin thickness	t_f	0.1×10^{-3} m
Fin pitch	P_f	4.42×10^{-3} m
Number of fins	N_f	23
Tube outer diameter	$D_{t,o}$	7.38×10^{-3} m
Tube wall thickness	t_{tw}	1×10^{-3} m
Number of tube columns (horizontal array)	N_{tc}	10
Number of tube rows (vertical array)	N_{tr}	17
Tube horizontal pitch	$P_{t,h}$	20×10^{-3} m
Tube vertical pitch	$P_{t,v}$	20×10^{-3} m

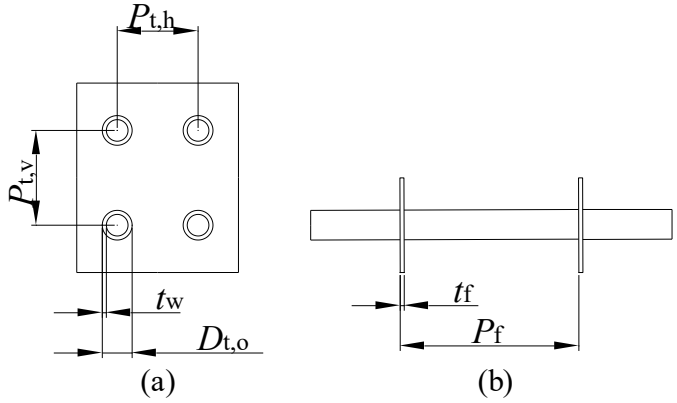

Fig. 8.4 Construction of the 3-fluid contactor: (a) tube details and (b) fin details.

The fluid property symbols indicated in Fig. 8.2 represent the points where the properties are measured. Table 8.2 summarizes the fluid properties and the specifications of the instruments used to measure each fluid property. One of the conventional methods used to calculate the mass fraction of a liquid desiccant in a solution is through its density and temperature. However, due to the small changes in IL density, this approach produced inaccurate results in the current system. Thus, a more accurate method was adopted for calculating the IL mass fraction by using the solutions refractive index and temperature.

Table 8.2 Fluid properties and specifications of their measuring instruments.

Parameter	Measuring instrument	Accuracy

Air dry-bulb temperature	Class 1 type T thermocouple	±0.5°C
Air dew point temperature	Chilled mirror hygrometer	±0.2°C
Air velocity	Hot wire anemometer	±0.2v or 0.015 m·s^{-1}
Air pressure drop	Differential pressure gauge	≥200 Pa: ±1.0%FS <200 Pa: ±1.5%FS
Solution temperature	Class A Platinum RTD	±0.15°C+0.002T
Solution refractive index	Process refractometer	±0.0002
Solution flow rate • inlet of both the process and regeneration sides • solution-to-solution heat exchanger	Coriolis flow meter	±0.12% 0~25%FS: ±1%FS 25~100%FS: ±4%Rdg.
Cooling/Heating water temperature	Class A Platinum RTD	±0.15°C+0.002T
Cooling/Heating water flow rate	Electromagnetic flow meter	±0.5%

8.2.2 Experimental results

The results from the dehumidification and regeneration experiments are organized in Table 8.3 and Table 8.4. In these tables, there are four sets of experimental data for air dehumidification and one for solution regeneration. The first two sets for air dehumidification investigate the influence of the air velocity while the solution mass flux is fixed at 0.5 and 2.0 kg·m^{-2}·s^{-1} and the cooling water flow rate held at 0.1 kg·s^{-1}. The next two explore the effect of the solution mass flux at a constant air velocity of 1.5 m·s^{-1} and at cooling water flow rates of 0.03 and 0.1 kg·s^{-1}. For solution regeneration, the influence of the solution mass flux is investigated while the air velocity and the cooling water flow rate are fixed at 1.5 m·s^{-1} and 0.04 kg·s^{-1}, respectively.

In the dehumidification side, two conditions for the air inlet humidity ratio and temperature were investigated; one at ambient summer condition in Tokyo and the other at a precooled condition. The intention of investigating at precooled inlet condition is to clarify the dehumidification performance of the system at low air inlet temperature and humidity ratio. The results show that at the same air velocity and solution mass flux, the same dehumidification capacity can be achieved for both inlet air conditions.

Table 8.3 Dehumidification experimental data.

u_{gb}	T_{ig}	T_{og}	x_{ig}	x_{og}	G_{il}	T_{il}	T_{ol}	X_{il}	X_{ol}	T_{icw}	T_{ocw}
G_{il} = 0.50 kg·m^{-2}·s^{-1}, $\dot{m}_{icw}$ = 0.10 kg·s^{-1}											
0.28	34.05	18.62	19.59	7.14	0.48	17.59	18.77	75.53	74.31	17.02	18.25
0.48	33.94	18.84	19.47	9.07	0.49	17.55	19.54	75.37	73.66	16.99	18.92
0.92	33.88	20.79	19.59	11.50	0.48	17.58	20.55	74.95	72.37	17.07	20.03
1.49	34.03	22.19	19.53	13.21	0.50	17.30	22.39	74.95	71.87	16.92	20.91

1.53	34.13	22.04	19.53	13.51	0.50	17.50	22.24	75.35	72.32	16.94	20.89
2.06	33.90	23.11	19.41	14.27	0.50	17.66	23.50	75.23	71.76	17.07	21.81
2.50	34.17	23.74	19.47	14.92	0.50	17.47	24.32	75.15	71.43	16.86	22.11
2.92	34.09	24.20	19.29	15.55	0.52	17.65	24.35	74.79	71.40	17.07	22.36
G_{il} = 2.00 kg·m^{-2}·s^{-1}, $\dot{m}_{icw}$ = 0.10 kg·s^{-1}											
0.24	33.71	18.76	19.13	7.04	1.99	17.35	18.48	75.11	74.87	17.13	18.08
0.46	33.85	18.37	19.32	8.71	2.00	17.25	19.20	75.15	74.74	17.00	18.47
0.97	34.25	20.05	19.72	10.73	2.03	17.32	20.71	75.22	74.49	17.04	19.63
1.47	34.10	21.44	19.29	12.19	2.00	17.41	22.43	75.05	74.17	17.17	20.57
u_{gb} = 1.50 m·s^{-1}, $\dot{m}_{icw}$ = 0.03 kg·s^{-1}											
1.47	22.00	20.72	14.78	11.13	0.75	17.41	21.49	75.19	73.93	17.23	21.04
1.49	21.75	20.75	14.82	10.77	1.01	17.14	21.63	74.94	73.89	17.17	20.70
1.48	22.03	20.59	14.92	10.73	1.46	17.20	21.43	75.06	74.32	17.20	20.61
1.49	22.09	20.46	15.16	10.32	2.01	17.35	21.58	74.94	74.31	17.31	20.61
1.47	22.21	20.34	14.97	9.56	3.94	18.60	21.05	75.41	75.05	17.23	20.80
u_{gb} = 1.50 m·s^{-1}, $\dot{m}_{icw}$ = 0.10 kg·s^{-1}											
1.48	21.81	18.66	15.06	11.31	0.23	17.52	20.53	75.19	71.14	16.92	18.74
1.46	22.18	19.78	15.01	10.49	0.49	17.31	20.33	74.95	72.61	16.95	18.95
1.49	22.01	19.21	14.87	10.46	0.76	17.21	20.18	75.01	73.50	16.86	18.78
1.50	21.64	19.67	15.06	10.25	1.04	17.09	20.13	74.93	73.71	16.96	18.87
1.47	22.05	19.44	14.78	9.98	1.51	17.33	20.03	75.07	74.24	17.16	18.93
1.51	22.40	19.21	15.01	9.79	2.00	17.33	20.07	74.92	74.23	17.06	18.97
1.45	21.99	19.14	14.92	9.53	3.00	17.68	19.88	75.01	74.54	17.07	18.81
1.48	22.15	18.93	14.97	9.13	3.94	17.94	19.80	74.97	74.58	16.91	18.80
1.48	22.07	19.20	15.11	8.74	5.02	18.30	19.74	75.15	74.82	16.94	18.99
1.49	34.15	21.90	19.29	14.97	0	-	-	-	-	17.07	20.67
1.49	34.03	22.19	19.53	13.21	0.50	17.30	22.39	74.95	71.87	16.92	20.91
1.50	33.87	21.94	19.23	12.67	0.77	17.16	22.54	75.65	73.52	16.93	20.76
1.50	33.65	22.38	19.53	12.71	0.97	17.15	22.70	75.01	73.26	17.02	20.94
1.49	33.99	22.19	19.47	11.95	1.92	17.16	22.17	74.96	73.98	16.84	20.73
1.50	33.90	21.21	18.65	10.46	3.06	17.54	21.90	74.93	74.25	16.88	20.52

Table 8.4 Regeneration experimental data.

u_{gb}	T_{ig}	T_{og}	x_{ig}	x_{og}	G_{il}	T_{il}	T_{ol}	X_{il}	X_{ol}	T_{icw}	T_{ocw}
u_{gb} = 1.50 m·s^{-1}, $\dot{m}_{icw}$ = 0.04 kg·s^{-1}											
1.45	34.12	43.74	19.21	20.69	1.06	49.89	45.01	76.10	76.47	50.19	45.70
1.47	34.79	44.31	19.20	22.16	1.45	50.88	45.28	75.83	76.37	51.60	46.82
1.47	34.07	44.63	19.28	21.61	1.80	50.37	46.01	76.05	76.39	50.81	46.71
1.50	33.86	44.12	19.22	22.89	2.46	50.05	45.66	75.97	76.38	51.17	46.71
1.51	33.76	43.51	19.90	23.15	3.03	49.74	45.52	75.89	76.17	50.59	46.41
1.50	34.29	44.57	19.78	23.48	3.52	50.37	46.26	76.27	76.56	51.67	46.90
1.50	33.75	44.43	19.55	24.89	3.97	50.15	46.31	76.15	76.51	51.67	47.22
1.51	34.27	44.62	19.13	23.48	4.51	50.02	46.29	76.18	76.44	51.67	46.84
1.51	34.13	44.78	19.11	23.30	5.02	50.08	46.80	75.86	76.08	51.78	47.42
1.50	34.35	44.95	19.17	24.28	5.50	50.04	46.50	76.20	76.45	51.66	47.04

8.2.3 Performance comparison between the new 3-fluid gas-liquid contactor and conventional packed bed contactor

Dehumidification performance comparison

The main purpose of a liquid desiccant air conditioning system is to supply air at a comfortable temperature and humidity ratio consuming less power as much as possible. Therefore, one of the most important criteria for comparing different kinds of liquid desiccant air conditioning systems is the dehumidification performance.

Fig. 8.5 shows the comparison of the dehumidification performance of the 3-fluid gas-liquid contactor and the packed bed contactor discussed in Appendix 2. It is evident from the graphs that the 3-fluid liquid desiccant air conditioning system can reach a lower outlet air humidity ratio and temperature at smaller solution flow rates compared to the packed bed liquid desiccant system. For example, an outlet air humidity ratio of 12.7 and 10.4 $g \cdot kg(DA)^{-1}$ was achieved by the 3-fluid liquid desiccant system at solution mass flux of 15.4 and 61.2 $g \cdot s^{-1}$ compared to 41.6 and 99.6 $g \cdot s^{-1}$ for the same outlet humidity ratio for the packed bed liquid desiccant system. Due to the capability of the 3-fluid liquid desiccant system to maintain the mass transfer potential of the solution, low air outlet humidity ratio can be achieved even at low flow rates.

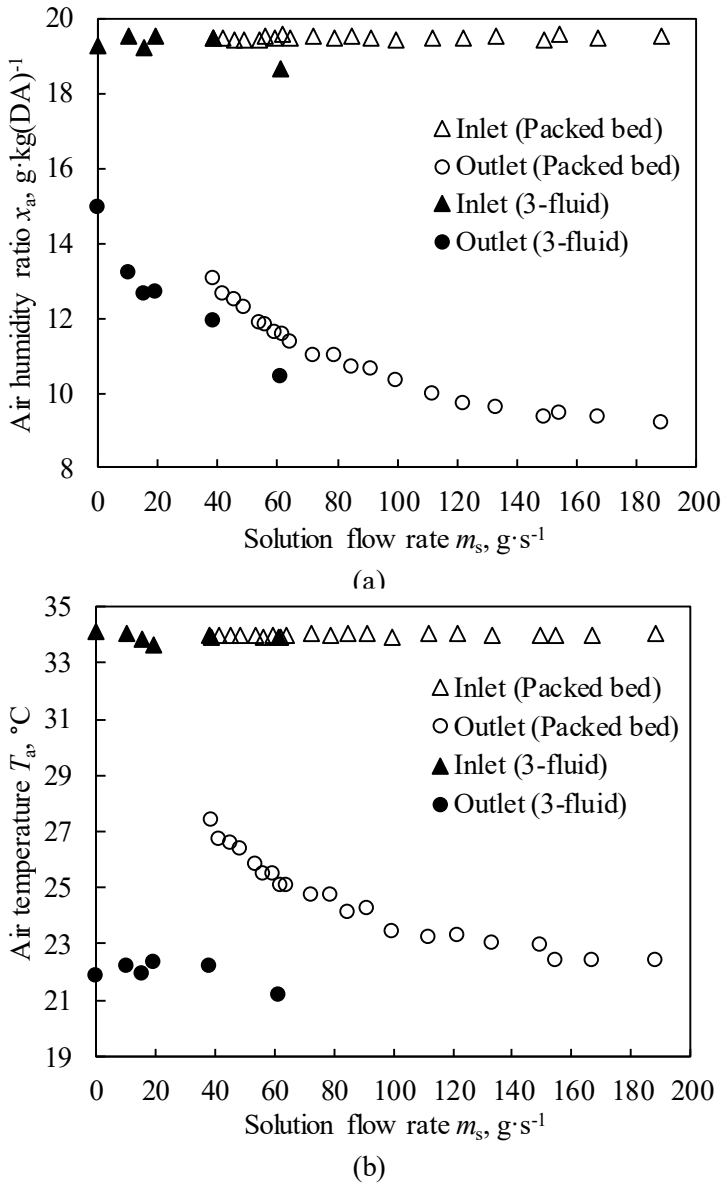

Fig. 8.5 Dehumidification performance comparison between the 3-fluid and packed bed liquid desiccant air conditioning system.

The magnitude of the difference between the outlet air temperature of the two systems is greater compared to the difference between the outlet air humidity ratio. The 3-fluid liquid desiccant air conditioning system obtained an outlet air temperature of 22.19°C at 15.4 g·s^{-1} which was not obtained by the packed bed liquid desiccant system even at its largest solution flow rate of 188 g·s^{-1}. This is possible because of the cooling water which maintains the heat transfer potential between the air and the solution. It is evident, however, that the trend of the outlet air temperature from the 3-fluid liquid desiccant system is different compared to the trend that is followed by the outlet air temperature of the packed bed liquid desiccant system. This suggests that the cooling

water of the 3-fluid liquid desiccant system is efficient in removing the sensible heat even when the 3-fluid gas-liquid contactor is not fully wetted by the solution. On the other hand, the dehumidification performance of the 3-fluid liquid desiccant system is heavily affected by the solution mass flux, which dictates the wetting ratio inside the 3-fluid gas-liquid contactor. However, it is verified from the data that water condensation occurs as shown by the plot at 0 $g \cdot s^{-1}$ solution flow rate. Is evident that the outlet air humidity ratio deceased, suggesting the occurrence of water condensation. For the packed bed liquid desiccant system, the trend is similar for both outlet air properties since heat and mass transfer is purely between the air and the solution due to the absence of an extra cooling or heating medium.

Air pressure drop comparison

Fig. 8.6 shows the air pressure drop comparison between the fin-tube contactor and the packed bed contactor as the solution flow rate increases. The air pressure drop increase through the 3-fluid contactor is significantly higher compared to the air pressure drop through the packed contactor due to the narrower distance between each fin of the 3-fluid gas-liquid contactor. The distance between the fins of the 3-fluid gas-liquid contactor is at 4 mm while the distance between the sheets of the packed bed contactor is at 7 mm. The presence of tubes inside the 3-fluid gas-liquid contactor also contributed to the air pressure drop.

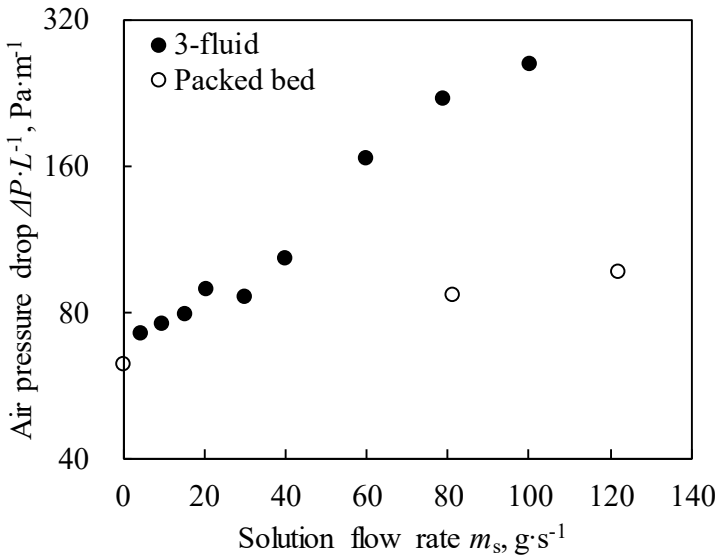

Fig. 8.6 Air pressure drop comparison between the 3-fluid gas-liquid and packed bed contactors.

Fig. 8.7 presents the experimental data for the air pressure drop through the 3-fluid gas-liquid contactor as the air flow rate increases. As expected, the air pressure drop increased as the air velocity increased. Higher air pressure drops result in larger fan power

requirements; hence, the air flow rate should be properly selected based on the system requirement.

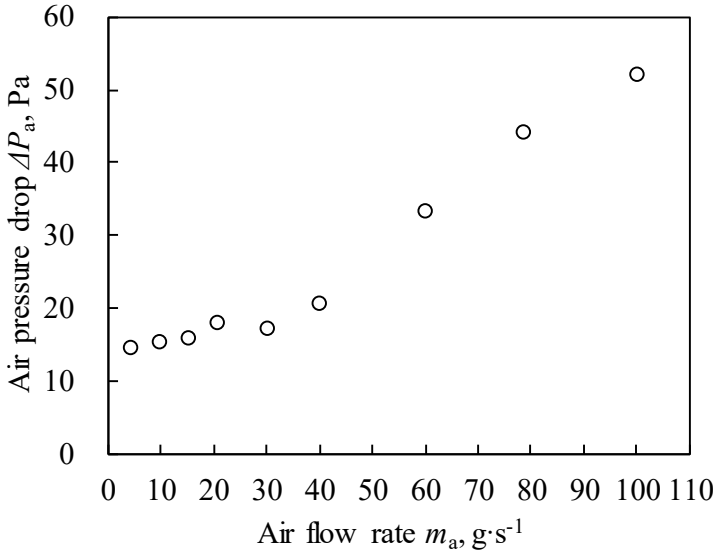

Fig. 8.7 Air pressure drop though fin-tube contactor as the air velocity increases.

9. Performance analysis of the 3-fluid gas-liquid contactor

9.1 Introduction

The mathematical model for the 3-fluid gas-liquid contactor presented in Chapter 7 was coded in C++ language. With the computer program of the 3-fluid gas-liquid contactor, prediction, simulation, and various optimization problems are made possible. Prediction of the outlet conditions was implemented using the experimental data as the input conditions. The predicted outlet conditions were validated by comparison with those of the experimental data. Parametric calculations were carried out to investigate and clarify the effect of the dimensional parameters to the outlet air humidity ratio, outlet air temperature, air pressure drop, and wetting ratio. Optimization of the gas-liquid contactor by volume minimization was carried out by applying relevant constraints.

9.2 Validation of the 3-fluid gas-liquid contactor model

The mathematical model of the 3-fluid liquid desiccant air conditioning system is validated to assess the reliability of the mathematical model in predicting the operation of the system. The calculated results from the computer program were compared with the outlet conditions from the experimental data and the deviations between the predicted and experimental results were estimated and analyzed.

Fig. 9.1(a) shows the comparison of the experimental data and predicted results for the outlet air humidity ratio. The mathematical model fairly predicts the outlet air humidity ratio with most of the deviations between the experimental data and calculated results within ±20%. The mean absolute percentage error for all the data is 15.60%. This discrepancy between the experimental data and predicted values can be ascribed to the underestimation of the wetting ratio ((9.3), which limited the mass transfer between the air and the IL solution. Nevertheless, the deviation is at an acceptable level considering the complicated transport phenomena and wetting characteristics occurring inside the 3-fluid gas-liquid contactor.

Fig. 9.1(b) presents the comparison of the experimental and predicted results for the outlet air temperature. The predicted results for the outlet air temperature agree well with the experimental data with deviations mostly within ±15% and a mean absolute percentage error of 9.34%. Based on the following comparisons, it can be concluded that the mathematical model for the 3-fluid liquid desiccant air conditioning system can satisfactorily predict the outlet air humidity ratio and outlet air temperature considering the complex heat and mass transfer and partial wetting inside the 3-fluid gas-liquid contactor.

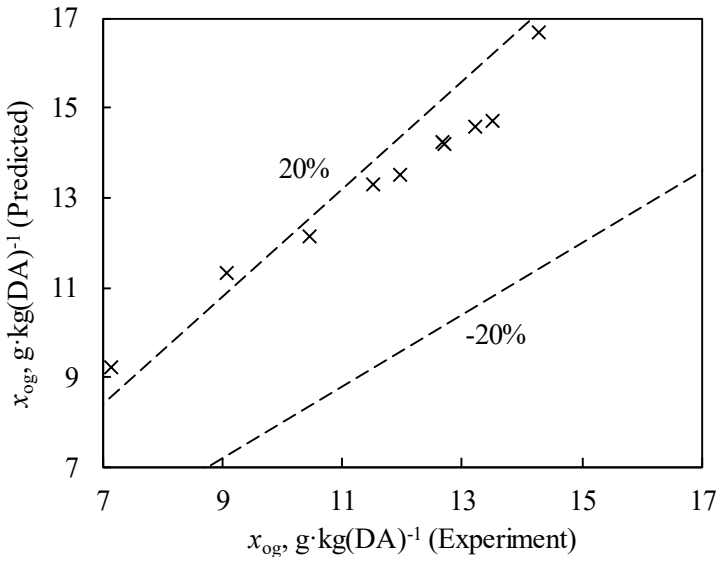

(a)

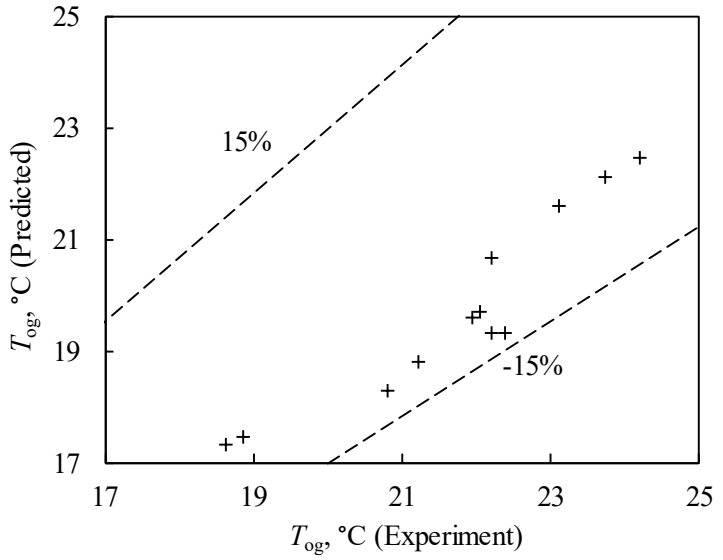

(b)

Fig. 9.1 Comparison between the experimental data and predicted results for the: (a) outlet air humidity ratio and (b) outlet air temperature from the 3-fluid liquid desiccant system.

Fig. 9.2 depicts the comparison of the air pressure drop from the experimental data and the air pressure drop model. It is evident that the predicted values from the air pressure drop model closely match the experimental data with most of the discrepancies within ±20%.

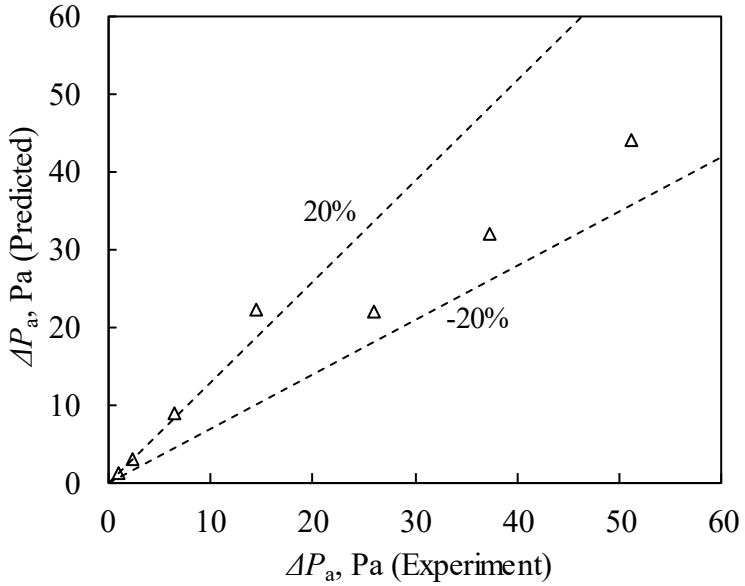

Fig. 9.2 Comparison between the experimental data and predicted air pressure drop.

9.3 Parametric study and design characterization

A parametric study of the dimensional parameters was carried to clarify the effect of the length, the height, and the width on the heat and mass transfer performance, air pressure drop, and wetting ratio. In these parametric studies, the dimension of the non-variable parameters is set at 0.4 m for the entire range of the variable dimension. Simulation were performed for 3 values of inlet solution flow rates (0.06 $kg \cdot s^{-1}$, 0.34 $kg \cdot s^{-1}$, 0.64 $kg \cdot s^{-1}$) as presented in Table 9.1. These solution flow rates represent low wetting (WR =28%, Re_s = 1.12), average wetting (WR = 57%, Re_s = 5.88), and complete wetting (WR = 100%, Re_s = 10.92) on the actual size of the 3-fluid gas-liquid contactor. The results help to understand the design and performance characteristics of the 3-fluid contactor.

Table 9.1 Inlet conditions of the parametric study.

Inlet conditions	Parameter	Value
Air	Temperature T_a	34°C
	Humidity ratio x_a	19.5 $g \cdot kg(DA)^{-1}$
	Mass flow rate $\dot{m}_a$	0.033 $kg \cdot s^{-1}$
Solution	Temperature T_s	17.5
	IL mass fraction X_{IL}	75%
	Mass flow rate $\dot{m}_s$	0.06, 0.34, 0.64 $kg \cdot s^{-1}$
Cooling water	Temperature T_{cw}	17.0°C
	Mass flow rate $\dot{m}_{cw}$	0.1 $kg \cdot s^{-1}$

9.3.1. Effect of the gas-liquid contactor length

Fig. 9.3(a) shows the effect of the contactor length on the outlet air humidity ratio. The outlet air humidity ratio decreases as the length of the contactor increases. This is due to the increase in contactor area and contact time between the air and solution even though the wetting ratio decreases as shown in Fig. 9.3(c). At solution mass flow rate of 0.64 $kg \cdot s^{-1}$, the trend is flat because the solution flow rate is too large that the outlet air humidity ratio reaches the equilibrium humidity ratio of the IL solution.

In contrast with the outlet air humidity ratio, the air pressure drop increases as the length increases as depicted in Fig. 9.3(b). The increase in air pressure drop is due to the longer air flow path and is a common phenomenon for heat exchangers. It can be observed that at approximately L = 0.24 m, the air pressure drop of the higher solution flow rates is smaller compared to those of the lower solution flow rates. This is because as the solution flow rate increases, the air mass flow rate decreases due to increasing dehumidification performance (Fig. 9.3(a)). As a result, the effective air velocity and Reynolds number decrease, which decreases the air pressure drop. Therefore, balancing the contrasting effect of the length on the air humidity ratio and pressure drop is necessary for the proper selection of the gas-liquid contactor length.

As mentioned earlier, the wetting ratio (Fig. 9.3(c)) decreases as the length of the contactor increases. This is because the total solution, which is set constant, is distributed to a wider area as the length increases which reduces the wetting ratio.

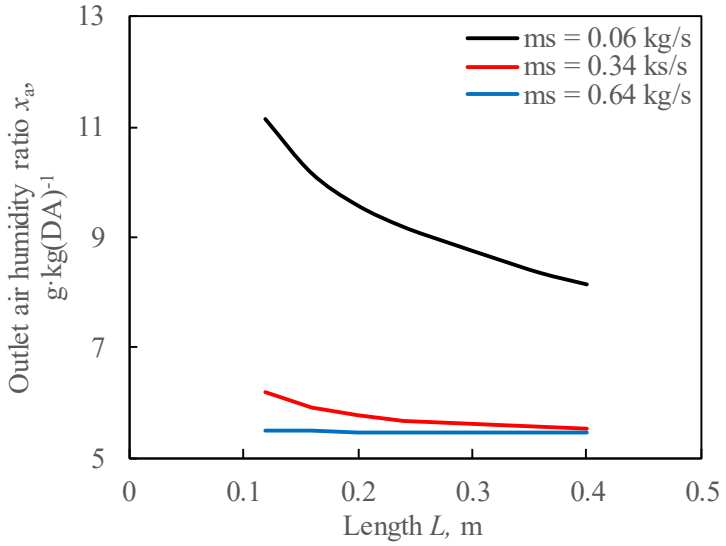

(a)

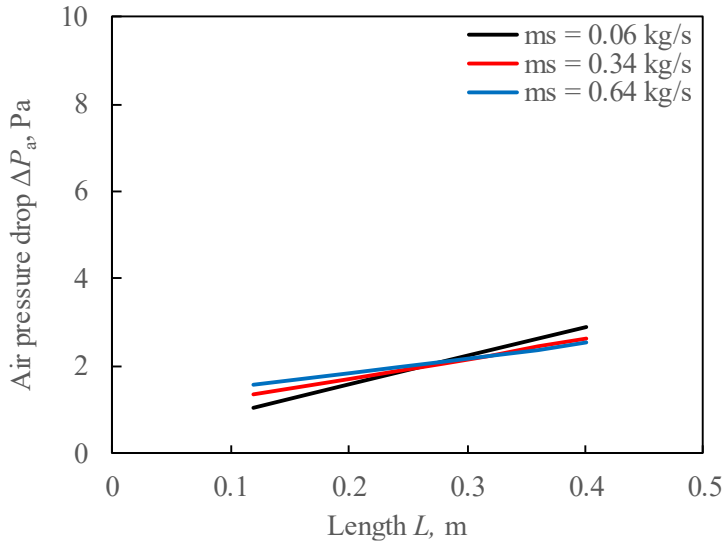

(b)

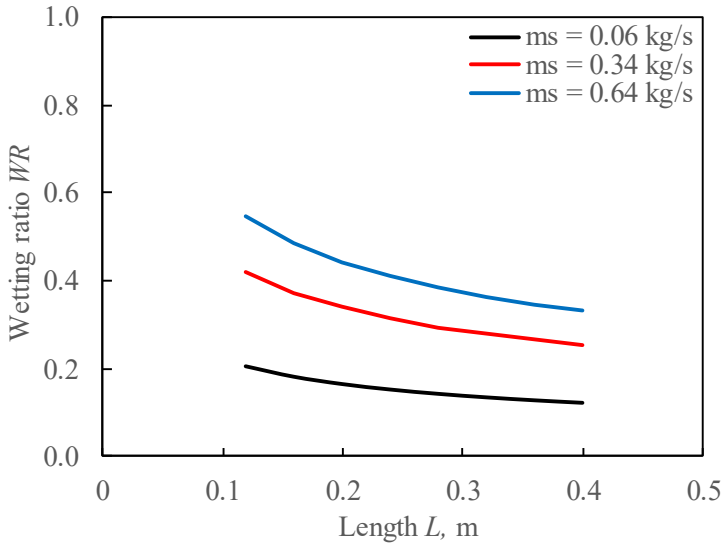

(c)

Fig. 9.3 Effect of the contactor length on the: (a) outlet air humidity ratio, (b) air pressure drop, and (c) wetting ratio.

9.3.2. Effect of the gas-liquid contactor height

Fig. 9.4(a) shows the effect of the contactor height on the outlet air humidity ratio. The outlet air humidity ratio decreases as the height of the contactor increases. Again, this can be explained by the increase in the contactor area and contact time between the air and solution. It can be observed that the effect of the contactor height on the outlet humidity ratio is more significant at low solution flow rate compared to the contactor length.

Contrary to the effect of the length, the air pressure drop decreases as the height increases (Fig. 9.4(b)). The improvement in both dehumidification and pressure drop performances become a double advantage for the height and desirable for improving the system performance.

On the other hand, the wetting ratio (Fig. 9.4(c)) is not significantly affected by the increase in height as the top area of the contactor is unchanged.

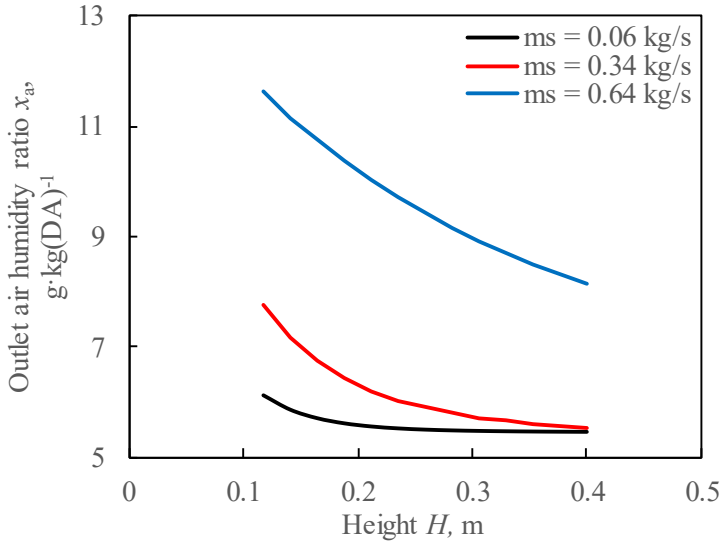

(a)

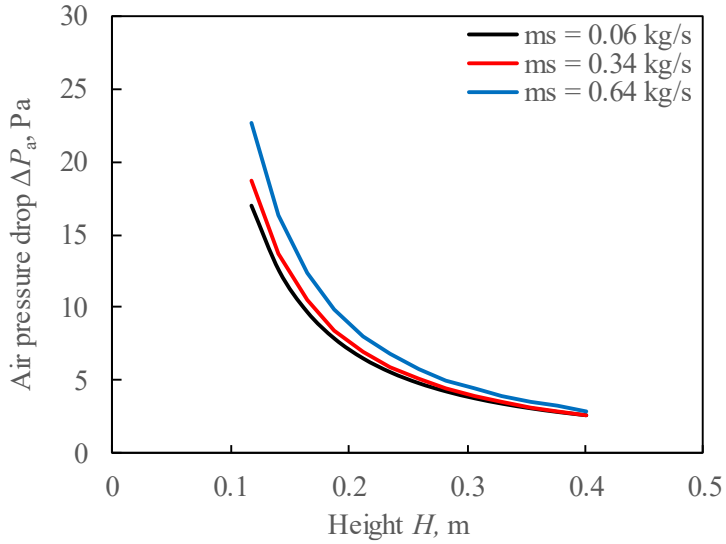

(b)

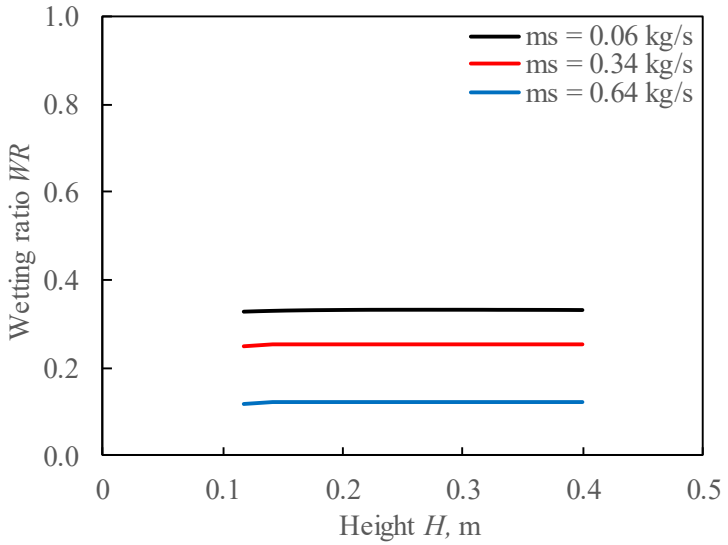

(c)

Fig. 9.4 Effect of the contactor height on the: a) outlet air humidity ratio, (b) air pressure drop, and (c) wetting ratio.

9.3.3. Effect of the gas-liquid contactor width

Fig. 9.5(a) shows the effect of the contactor width on the outlet air humidity ratio. Dehumidification improves due to the increase in the contact area.

Similar to the effect of the height, the air pressure drop (Fig. 9.5(b)) decreases as the width increases. This is due to the increase of the entrance area of the air which is inversely proportional to the pressure drop.

On the other hand, due to the increase in the top area of the contactor where the solution enters, the wetting ratio (Fig. 9.5(c)) decreases as the width of the contactor increases.

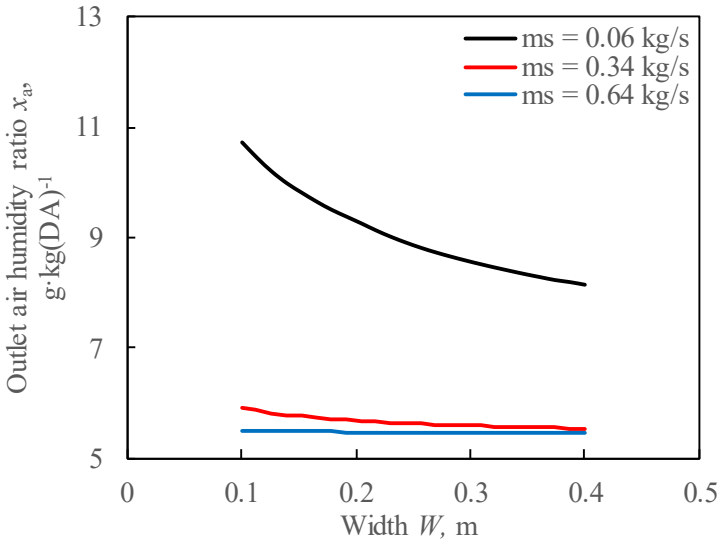
ms = 0.06 kg/s
ms = 0.34 kg/s
ms = 0.64 kg/s
Outlet air humidity ratio x_a, g·kg(DA)$^{-1}$
13
11
9
7
5
0
0.1
0.2
0.3
0.4
0.5
Width W, m

(a)

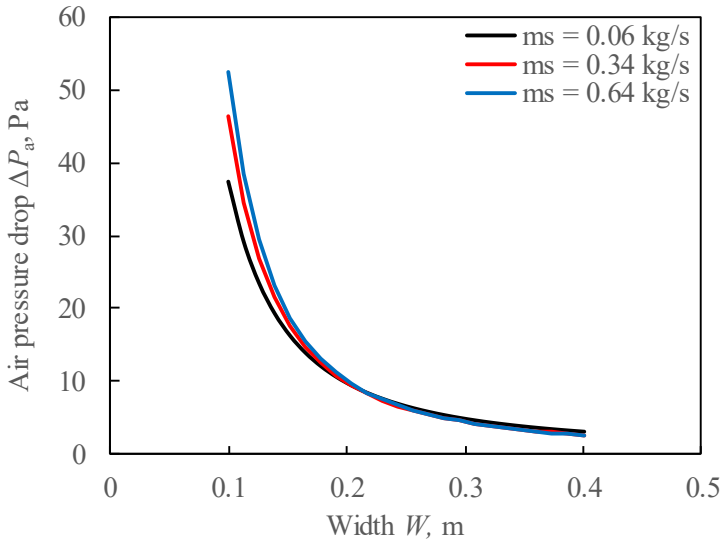
ms = 0.06 kg/s
ms = 0.34 kg/s
ms = 0.64 kg/s
Air pressure drop ΔP_a, Pa
60
50
40
30
20
10
0
0
0.1
0.2
0.3
0.4
0.5
Width W, m

(b)

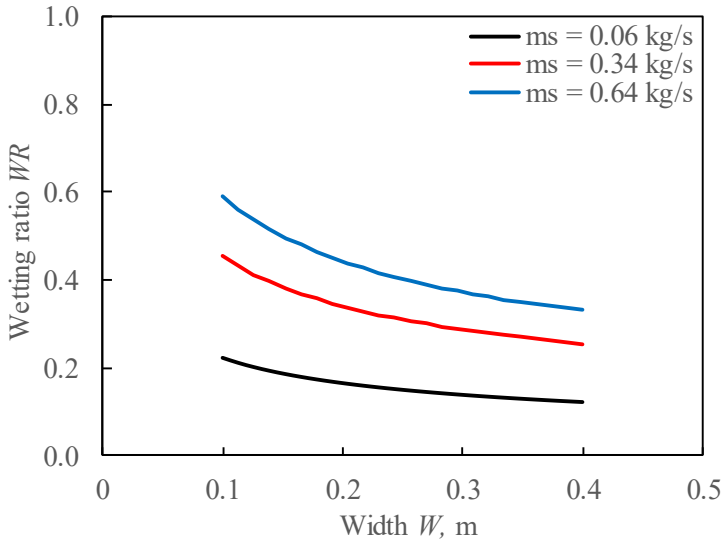

(c)

Fig. 9.5 Effect of the contactor width on the: a) outlet air humidity ratio, (b) air pressure drop, and (c) wetting ratio.

9.4 Optimization

As discussed in Chapter 1, limited studies have been published on the performance optimization of liquid desiccant systems. Optimization of the gas-liquid contactor is a complex process that involves the selection of the objective function, significant design parameters, and constraint conditions. Also, a proper selection of the optimization technique has to be undertaken as some optimization algorithms can give a local optimum value instead of the global optimum value. In this optimization endeavor, the structure of the gas-liquid contactor is optimized by manipulating the relevant design parameters while subjecting to the specific system constraints explained in detail in the following sections.

9.4.1. Objective function

The objective of the optimization is to minimize the volume of the gas-liquid contactor. The volume is chosen as the objective of the optimization because by minimizing the volume, the principal cost of the contactor can be minimized, and system miniaturization can be realized.

The following equation represents the objective function:

$$V = L \times W \times H \qquad (m^{-3}) \qquad (9.1)$$

where V denotes the volume of the gas-liquid contactor and L (m), W (m), and H (m) are the length, width, and height of the contactor, respectively.

9.4.2. Design parameters

The structural parameters for the fin-tube contactor are listed in Table 8.1. In accordance with the objective function, the length, the width, and the height are automatically selected as design parameters as they directly affect the objective function, while the other geometrical parameters are assumed constant.

Table 9.2 summarizes the design parameters and their search ranges. The lower bound of the search range is the smallest dimension of the original 3-fluid gas-liquid contactor and the upper bound is the largest dimension. The design parameters are manipulated by increasing or decreasing the number of control volumes in search of the set of dimensions that satisfies both the objective function and constraints.

Table 9.2 Search range of the design parameters.

Design parameter	Search range
L	0.1~0.4 m
W	0.1~0.4 m
H	0.1~0.4 m

9.4.3. Constraint conditions

Many optimal design problems contain both or either of the structural dimensions and performance constraints. In the optimization case here, the dimensional constraints are already considered along with the definition of the design parameters. On the other hand, the performance constraints are usually a trade-off between the output and the power consumption. Optimization problems containing two or more constraint conditions are called “multiconstraint optimization”.

The main purpose of liquid desiccant air conditioning systems is to produce, in an efficient way, a comfortable air humidity ratio that would be otherwise be delivered by the conventional vapor compression system inefficiently. Therefore, the outlet air humidity ratio constitutes to be an important constraint condition, which is represented by the inequality as follows:

$$x_{\mathrm{og}} \leq x_{\mathrm{og,exp}} \tag{9.2}$$

In the miniaturization of the gas-liquid contactor, when the dimensions are decreased, the air pressure drop increases due to the constriction of the flow area. If the air pressure drop increases, the fan power consumption also increases, and the purpose of the liquid desiccant system to minimize the energy consumption is compromised. To prevent the conflicting effect of the component miniaturization from compromising the performance of the system, the air pressure drop can be regulated according to the specific limitation of the system. This is given by the inequality constraint below.

$$\Delta P_{\mathrm{gb}} \leq \Delta P_{\mathrm{gb,exp}} \tag{9.3}$$

9.4.4. Optimization method

Genetic Algorithm (GA) was employed to implement the optimization problem. Genetic algorithms are pseudo-stochastic search methods which combine the theories of natural selection and genetics. They are pseudo-stochastic in the sense that the mechanisms of random selection and survival of the fittest are both exploited to select the initial and new set of populations. The most basic GA was developed by John Holland with the help of his colleagues and students, most notably David Goldberg. From then, many improvements have already been made by other researchers including the vector evaluated GA (VEGA) of Schaffer and the non-dominated sorting GA I and II (NSGA-I and NSGA-II) of Srinivas and Deb[121] and Deb et al.[122], respectively.

Applications of GA in thermal systems optimization have suggested a robust ability to successfully predict the optimal value of the objective function[123]. Specifically, GA has been used to geometrically optimize heat exchangers allowing them to perform more efficiently. In liquid desiccant systems, the application of GA for optimization is limited. Among these are the optimization of the energy and economic performance with the solar collector area and heating water flow rate as operation parameters of Qi et al.[44], and the minimization of energy consumption with inlet conditions as control parameters of Ge et al.[38], Zhang et al.[57], and Wang et al.[47] These studies have focused on the minimization of the energy consumption. There is no study carried out on optimizing the size and shape of the contactor, which will not only realize possible savings in energy consumption but also savings in the capital cost of producing new gas-liquid contactors. Therefore, this optimization study applies the power of GA to search for the optimal dimensions of the gas-liquid contactor while satisfying the specified system constraints.

Fig. 9.6 illustrates the flow chart of the GA-based optimization of the contactor size. The first step of the optimization process is to initialize the input conditions for the liquid desiccant system. Next, the *population size* and *maximum generation* are defined. The *population size* describes the maximum array of *individuals* in the data structure Then, the boundary conditions or the search ranges for the design parameters are declared. The GA creates a *population* as an array of *individuals* or *chromosomes*, based on the number of *population size* and from the lower and upper bound of the design parameters, for each generation until the *maximum generation* is reached. The *population* is composed of sets of *chromosomes*, each set is a potential solution to the design problem. Each *chromosome* is represented by a string of *genes* that hold the characteristics of that *chromosome*. The initial *population* is randomly generated from the search range and are assigned initial

fitness values of zero. Next, the *evaluation* operator evaluates each set of solutions by implementing the objective function and assigning the result as the new *fitness value* of each set.

Then, the for-loop structure is executed, and the condition inside the structure is evaluated. The next step in the flow chart is executed if the current number of *generations* is less than the *maximum generation*; otherwise, the program terminates. Next, the output results are calculated by implementing the mathematical model 3-fluid gas-liquid contactor presented in Chapter 7. Then, the if-else statement, which contains the constraint conditions, is executed. If the constraints are satisfied, the program proceeds to write the results from the current calculation; otherwise, the procedure after the input-output stream is implemented. The next three procedures are called the GA operators and are responsible for the reproduction of a pool of *offspring* which become *parents* of the next *generation*. The *selection* operator chooses *parents* from the current *population* which mate and combine to create *off-springs*. In the optimization case here, the Rank Selection method is implemented to select a pair of *parents* for reproduction. The lower the *fitness value* of the *parent*, the higher its possibility of being selected. The *crossover* operator mates the selected pairs of *parents* according to the defined *crossover* probability. The One Point Crossover method is used to randomly select a *crossover point* wherein the *parents* create *off-springs* by exchanging their genetic material on one side of the *crossover point*. The *mutation* operator randomly selects one or more *chromosomes* in a solution set and randomly modifies one or more *genes* replacing the selected *chromosomes* with different values. *Mutation* helps maintain diversity within the *population* and prevent premature convergence to the local optima. The combined effect of *selection*, *crossover*, and *mutation* lead to a higher possibility of convergence to the global solution. The new *generation* of *population* is evaluated and assigned with *fitness values* for the *selection* process of the next *generation*. Lastly, the number of *generations* is updated based on the increment, and the flow returns to the condition statement. The termination condition is evaluated, and the process repeats as long as the condition remains true.

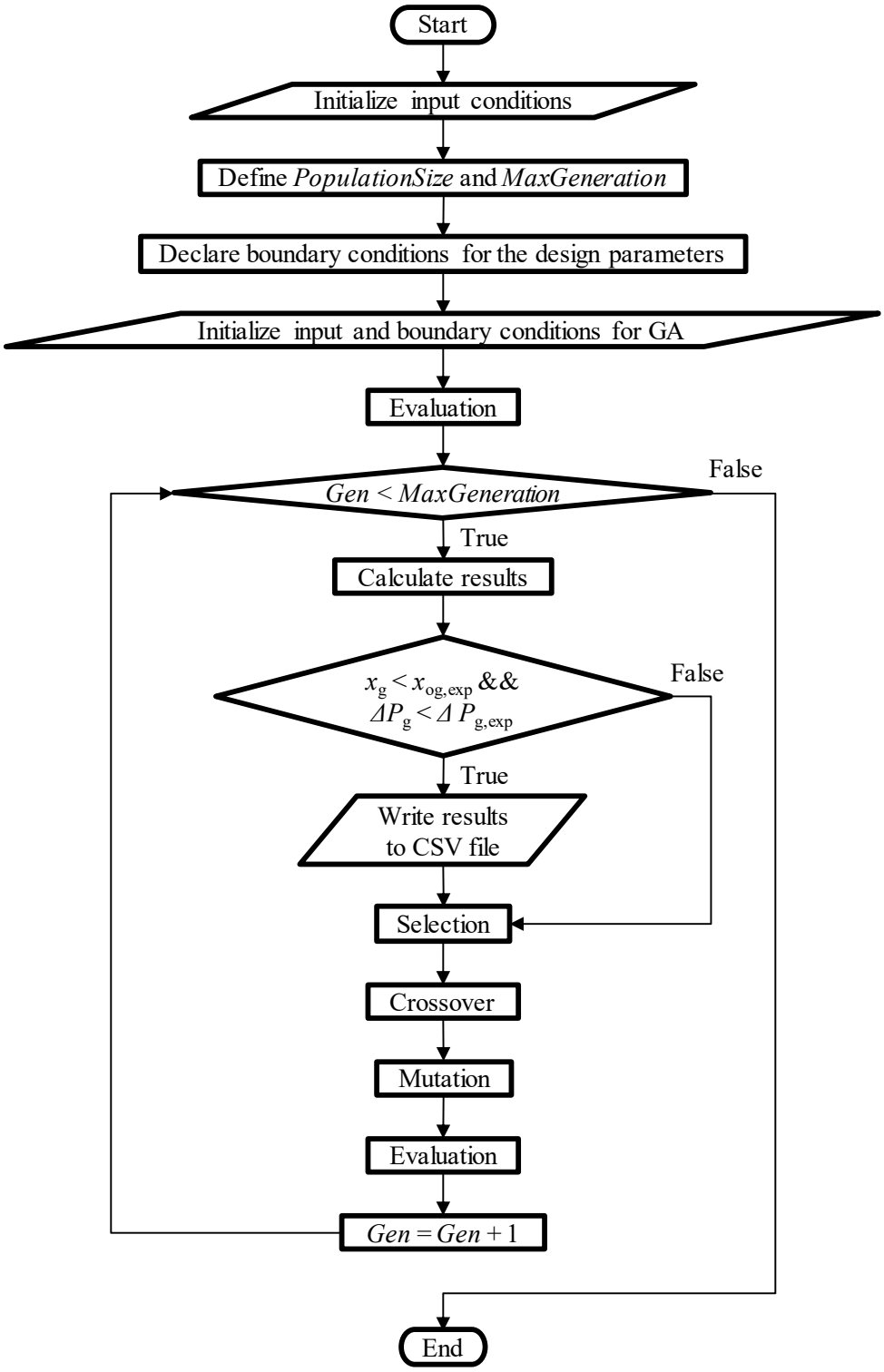

Fig. 9.6 Flow chart of the GA-based optimization of the contactor size.

9.5 Optimization results

9.5.1 Contactor size optimization at various air flow rates

The air flow rate is an important parameter in estimating the ventilation requirement of air-conditioned space. As the air flow rate affects the air pressure drop and dehumidification performance, it is necessary to know the optimal volume for a required ventilation rate, outlet air humidity ratio, and air pressure drop. Hence, an optimization study was carried out to determine the optimum size of the 3-fluid contactor for a required outlet air humidity ratio and air pressure drop.

Table 9.3 summarizes the conditions for the contactor size optimization at various inlet air flow rates. The ambient air condition during summer in Tokyo was selected as the inlet air condition. The air mass flow rate is varied starting from 0.011 $kg \cdot s^{-1}$ (0.5 $m \cdot s^{-1}$) until the value that satisfies the outlet air humidity ratio and air pressure drop constraints within the range of the dimensions (0.1~0.4 m).

Table 9.3 Conditions for the contactor size optimization at various air flow rates.

Conditions	Parameter	Value
Inlet air	Temperature T_a	34°C
	Humidity ratio x_a	19.5 $g \cdot kg(DA)^{-1}$
	Mass flow rate $\dot{m}_a$	0.011~0.11 $kg \cdot s^{-1}$
Inlet solution	Temperature T_s	17.5
	IL mass fraction X_{IL}	75%
	Mass flow rate $\dot{m}_s$	0.06 $kg \cdot s^{-1}$
Inlet cooling water	Temperature T_{cw}	17.0°C
	Mass flow rate $\dot{m}_{cw}$	0.1 $kg \cdot s^{-1}$
Constraints	Outlet air humidity ratio x_{oa}	12.59 $g \cdot kg(DA)^{-1}$
	Air pressure drop ΔP_a	23.15 Pa
GA	Population size *PS*	2000
	Maximum generation *MG*	100
	Crossover rate *CR*	0.9
	Mutation rate *MR*	0.1

Fig. 9.7(a) shows the calculation results for the outlet air humidity ratio at various inlet air flow rates. It can be observed that the results are slightly lower at smaller air flow rates compared to those at higher air flow rates. Since the solution flow rate is set constant, the air to solution ratio is smaller at low flow rates resulting in slightly lower outlet air humidity ratio.

Fig. 9.7(b) presents the results for air pressure drop at various inlet air flow rates. In this optimization problem, the factors heavily affecting the pressure drop is the air flow rate and the air entrance area. The effect of the solution film thickness is not significant in this calculation since the solution flow rate is set at a constant value. Therefore, the

results for air pressure drop is generally a trade-off between increasing air flow rate and increasing air entrance area. At low flow rates, this trade-off balances each other resulting in stable values of the air pressure drop. As depicted in Fig. 9.7 (e), the selection pattern of the dimensions at low inlet air flow rates is organized (the height is the only dimension changing) compared to higher inlet air flow rates. In this regime, the air pressure drop should increase as the inlet air flow rate increases but the increase in height almost equally balances this effect. At higher inlet air flow rates, the air pressure drop behavior becomes random as the dimension pattern becomes random relative to that at lower air flow rates.

Fig. 9.7(c) depicts the optimal volume of the 3-fluid gas-liquid contactor at various inlet air flow rates. The plot shows all the results that satisfied the outlet air humidity ratio and air pressure drop constraints for the entire range of the dimensions. The solid line represents the volume of the original 3-fluid gas-liquid contactor, which is equal to 0.008 m^3. This means that if the original volume of the 3-fluid gas-liquid contactor is taken as a constraint, the other constraints will only be satisfied until an inlet air flow rate of 0.034 $kg \cdot s^{-1}$ (1.5 $m \cdot s^{-1}$), which is the same condition as the original size of the contactor. The resulting optimal size of the contactor is exactly the original size of the 3-fluid gas-liquid contactor (L=0.2 m, H=0.4 m, W=0.1 m, V=0.008 m^3), which suggests that the current structure and size of the 3-fluid gas-liquid contactor is optimal.

Fig. 9.7(d) shows the resulting wetting ratio from the optimal volume of the 3-fluid gas-liquid contactor at various inlet air flow rates. The graphs depict that the wetting ratio roughly stays the same at lower air flow rates before gradually decreasing as the inlet air flow rate increases. In the same region where the wetting ratio remains unchanged, the length and the width of the contactor are also unchanged, which means that the solution entrance area is constant at this range; hence, the wetting ratio is not significantly affected.

Fig. 9.7(e) shows the selection pattern of the gas-liquid contactor dimensions at various inlet air flow rates. The behavior of the dimension selection is important as it gives an idea of how the other parameter will behave. In fact, the dimension pattern has already been used to explain the behavior of the air pressure drop and wetting ratio since they are significantly affected by the structure of the gas-liquid contactor. As already mentioned, the selection pattern for the dimensions is more organized at low inlet air flow rates compared to higher air flow rates. The selection follows a pattern wherein the height is increased first followed by the width, and lastly by the length. This behavior is consistent with the design characteristics from the parametric study and both results corroborate each other. To recall, both change in height and width has a double advantage to the dehumidification performance and air pressure drop.

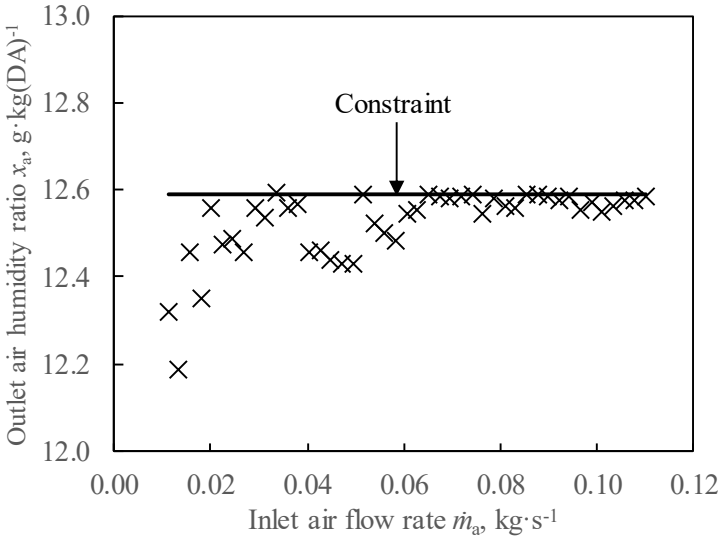
13.0
12.8
12.6
12.4
12.2
12.0
Constraint
Outlet air humidity ratio x_a, g·kg(DA)$^{-1}$
0.00
0.02
0.04
0.06
0.08
0.10
0.12
Inlet air flow rate $\dot{m}_a$, kg·s^{-1}

(a)

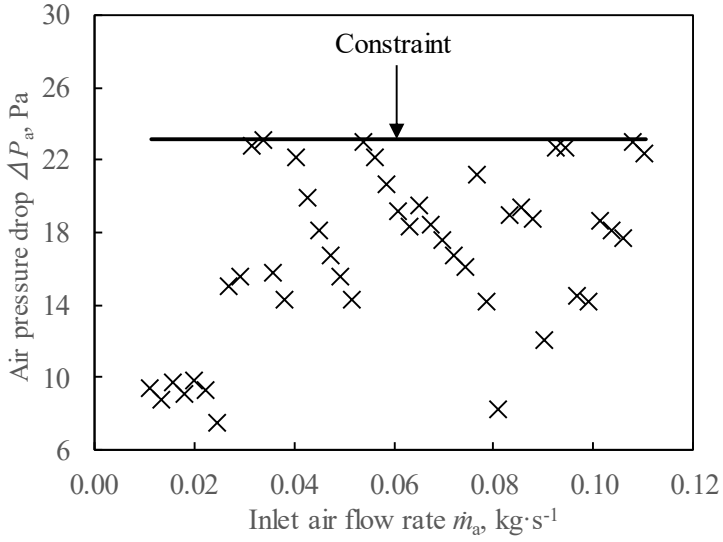
30
26
22
18
14
10
6
Constraint
Air pressure drop ΔP_a, Pa
0.00
0.02
0.04
0.06
0.08
0.10
0.12
Inlet air flow rate $\dot{m}_a$, kg·s^{-1}

(b)

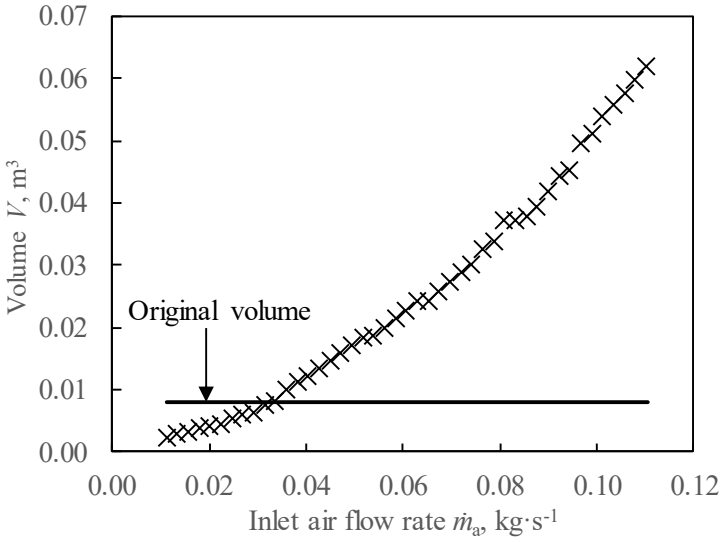
0.07
0.06
0.05
0.04
0.03
0.02
0.01
0.00
Volume V, m³
Original volume
0.00
0.02
0.04
0.06
0.08
0.10
0.12
Inlet air flow rate ṁa, kg·s-1

(c)

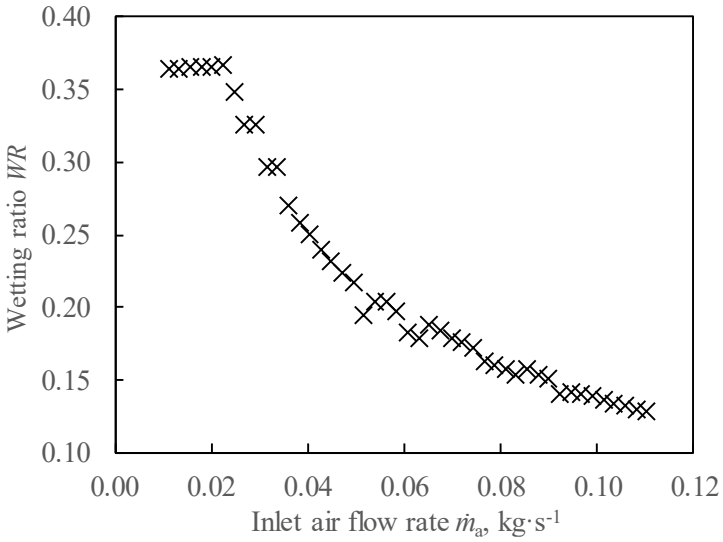
0.40
0.35
0.30
0.25
0.20
0.15
0.10
Wetting ratio WR
0.00
0.02
0.04
0.06
0.08
0.10
0.12
Inlet air flow rate ṁa, kg·s-1

(d)

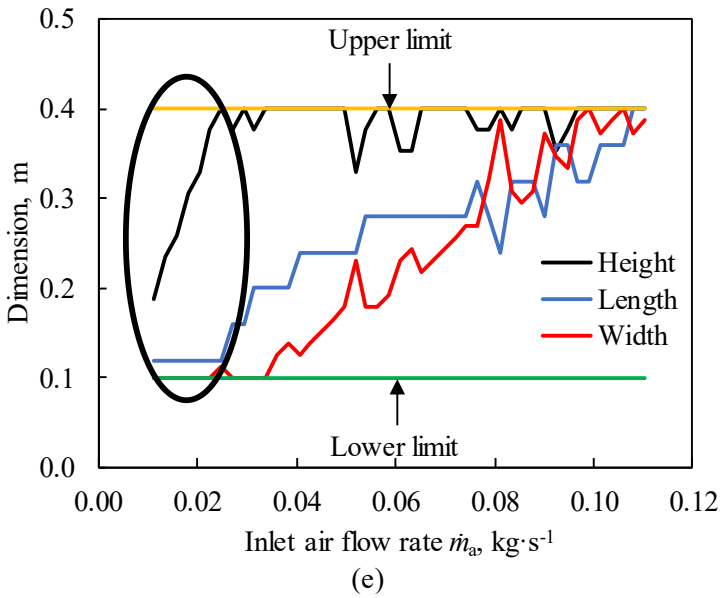

Fig. 9.7(a) Outlet air humidity ratio, (b) air pressure drop, (c) minimum volume, (d) wetting ratio, and (e) dimension pattern at varying inlet air flow rate.

9.5.2 Contactor size optimization at various inlet air humidity ratio

The applicability of the study can be widened if the optimal size of the gas-liquid contactor is known at various inlet air humidity ratio. The results can be used as a guide in determining the optimal size of the 3-fluid gas-liquid contactor for various climatic regions where the ambient air humidity ratio is lower or higher compared to the ambient condition in Tokyo.

Table 9.4 presents the conditions for the contactor size optimization at various inlet air humidity ratio. The selected range for the inlet air humidity ratio is from 17 to 27 g·kg(DA)$^{-1}$. This corresponds to a relative humidity of 50 to 80% relative to the standard ambient humidity ratio during summer in Tokyo. The inlet air flow rate of 0.033 kg·s^{-1} (1.5 m·s^{-1}) is for the ventilation rate of medium-size office space.

Table 9.4 Conditions for volume optimization at various inlet air humidity ratio

Conditions	Parameter	Value
Inlet air	Temperature T_a	34°C
	Humidity ratio x_a	17~27 g·kg(DA)$^{-1}$
	Mass flow rate $\dot{m}_a$	0.033 kg·s^{-1}
Inlet solution	Temperature T_s	17.5
	IL mass fraction X_{IL}	75%
	Mass flow rate $\dot{m}_s$	0.06 kg·s^{-1}
Inlet cooling water	Temperature T_{cw}	17.0°C
	Mass flow rate $\dot{m}_{cw}$	0.1 kg·s^{-1}
Constraints	Outlet air humidity ratio x_{oa}	12.59 g·kg(DA)$^{-1}$

	Air pressure drop ΔP_a	23.15 Pa
GA	Population size *PS*	2000
	Maximum generation *MG*	100
	Crossover rate *CR*	0.9
	Mutation rate *MR*	0.1

Fig. 9.8(a) shows the results for the outlet air humidity ratio at various inlet air humidity ratio. The results are close to the value of the outlet air humidity ratio constraint for the entire range of the inlet air humidity ratio. Fig. 9.8(b) depicts the calculation results for the air pressure drop at various inlet air humidity ratio. Some air pressure drop results are slightly farther from the value of the constraint when compared to the results of the outlet air humidity ratio.

Fig. 9.8(c) graphs the optimal size of the 3-fluid gas-liquid contactor at various inlet air humidity ratio. The results suggest that if the original size of the 3-fluid gas-liquid contactor is taken as constraint, the results would be limited until the value of 19.5 $g \cdot kg(DA)^{-1}$ for the inlet air humidity ratio. This value results in an optimal size of 0.008 m^3, which is equal to the original size of the 3-fluid gas-liquid contactor. In order to satisfy the outlet humidity ratio constraint at inlet air humidity ratio greater than 19.5 $g \cdot kg(DA)^{-1}$, larger sizes of the 3-fluid gas-liquid contactor are necessary.

Fig. 9.8(d) shows the behavior of the wetting ratio for the optimal size of the gas-liquid contactor at various inlet air humidity ratio. The wetting ratio decreases as the inlet condition of the air humidity ratio increases. This is due to the increasing volume requirement for the gas-liquid contactor in order to satisfy the outlet humidity ratio constraint as the inlet air humidity ratio increases.

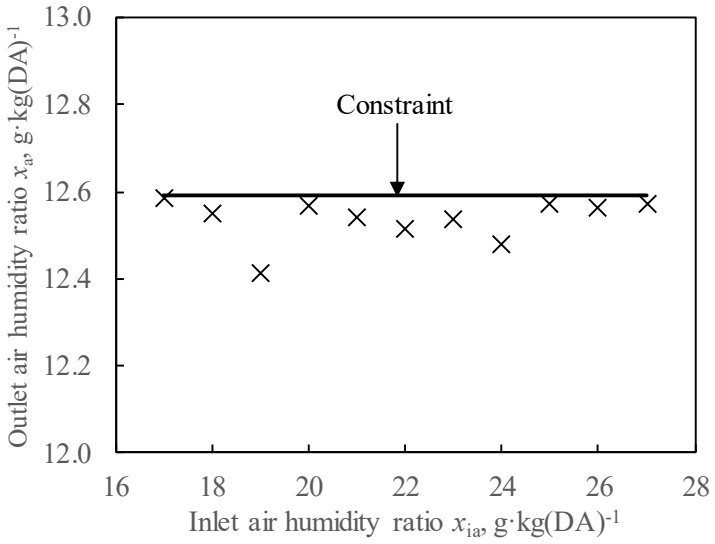

(a)

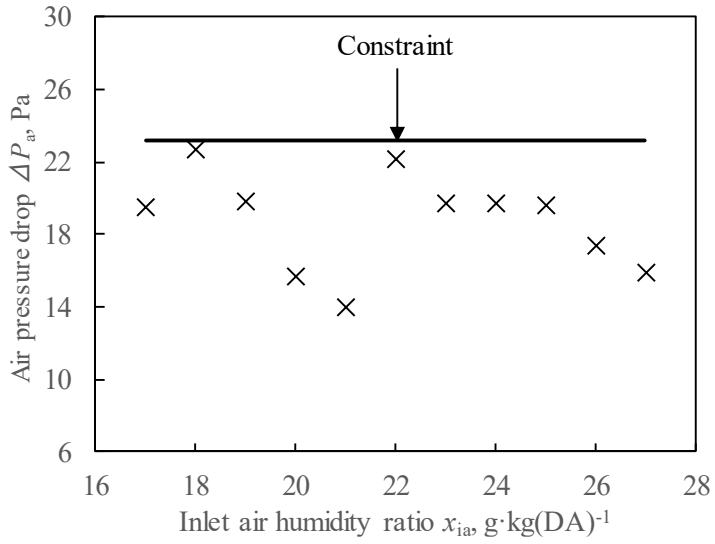
Constraint
Air pressure drop ΔP_a, Pa
Inlet air humidity ratio x_{ia}, g·kg(DA)$^{-1}$
30
26
22
18
14
10
6
16
18
20
22
24
26
28

(b)

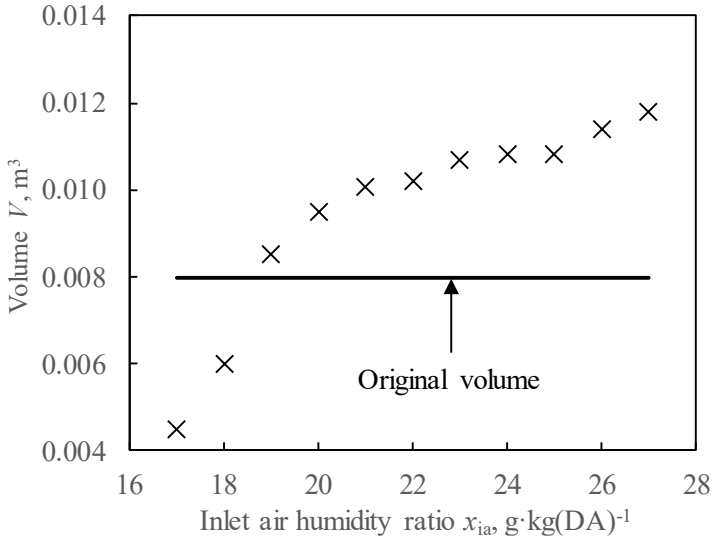
Volume V, m^3
Original volume
Inlet air humidity ratio x_{ia}, g·kg(DA)$^{-1}$
0.014
0.012
0.010
0.008
0.006
0.004
16
18
20
22
24
26
28

(c)

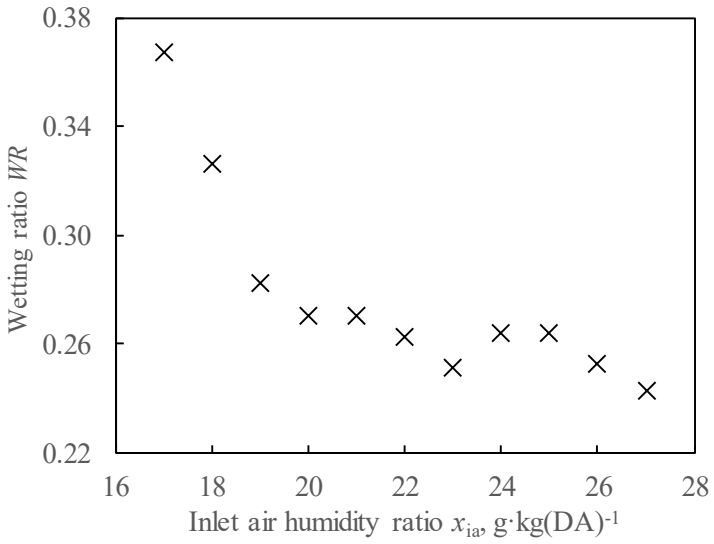

(d)

Fig. 9.8(a) Outlet air humidity ratio, (b) air pressure drop, (c) minimum volume, and (d) wetting ratio at varying inlet air humidity ratio.

9.6 Advantage of the 3-fluid gas-liquid contactor

A performance comparison was carried out to clarify the advantages of the 3-fluid gas-liquid contactor against a conventional 2-fluid gas-liquid contactor. Using the same condition for the inlet air and IL inlet solution, performance calculations were carried out from the gas-liquid contactor with cooling water (3-fluid) and without cooling water (2-fluid).

Table 9.5 Conditions for the performance calculation of a 3-fluid and a conventional 2-fluid gas-liquid contactor.

Conditions	Parameter	3-fluid	2-fluid
Inlet air	Temperature T_a	34°C	34°C
	Humidity ratio x_a	19.5 g·kg(DA)$^{-1}$	19.5 g·kg(DA)$^{-1}$
	Mass flow rate $\dot{m}_a$	0.033 kg·s^{-1}	0.033 kg·s^{-1}
Inlet solution	Temperature T_s	17.5	17.5
	IL mass fraction X_{IL}	75%	75%
	Mass flow rate $\dot{m}_s$	0.06 kg·s^{-1}	0.06 kg·s^{-1}
Inlet cooling water	Temperature T_{cw}	17.0°C	-
	Mass flow rate $\dot{m}_{cw}$	0.1 kg·s^{-1}	-
GA	Population size *PS*	2000	2000
	Maximum generation *MG*	100	100
	Crossover rate *CR*	0.9	0.9
	Mutation rate *MR*	0.1	0.1

Fig. 9.9(a) compares the performance of the 3-fluid and 2-fluid gas-liquid contactor. In both devices, the volume requirement increases as the required outlet air

humidity ratio become smaller (severe). The 3-fluid gas-liquid can reach an outlet air humidity ratio of about 8.4 g·kg(DA)$^{-1}$ at the largest value of the range for the dimensions. On the other hand, the smallest outlet air humidity achieved by the 2-fluid gas-liquid contactor is only 9.9 g·kg(DA)$^{-1}$. From these results, the superiority of the 3-fluid gas-liquid contactor over a conventional 2-fluid gas-liquid contactor is clarified.

Compared to the size of the 2-fluid gas-liquid contactor that achieved an outlet air humidity ratio of 9.9 g·kg(DA)$^{-1}$, the 3-fluid gas-liquid can achieve the same value for the outlet air humidity ratio at a smaller size. A size reduction of about 56% can be realized when the 3-fluid gas-liquid contactor is used to achieve the same outlet air humidity ratio at the listed operating conditions.

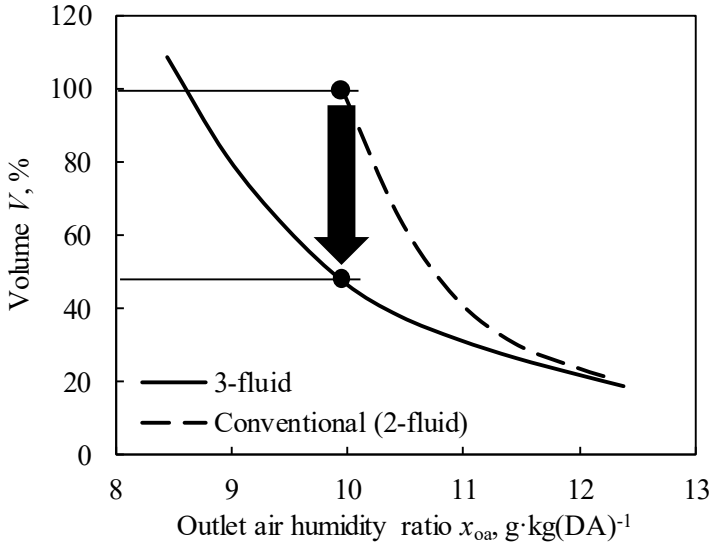

Fig. 9.9 Performance comparison of 3-fluid and conventional 2-fluid (no cooling water) gas-liquid contactor.

10. Conclusions and future plan

The use of air conditioning systems for thermal comfort has been demonstrated to be a necessity due to the rising daily temperatures not only in subtropical regions but also in temperate zones. Generally, air conditioning systems employing the vapor compression cycle have been widely used to accomplish both cooling and dehumidification. However, the method of dehumidifying the air using the vapor compression cycle has been proven experimentally and theoretically by many researchers to be energy inefficient due to the utilization of both deep cooling to condense the water from the air. The potential of using liquid desiccant air conditioning systems has been suggested as an alternative to the vapor compression system because of their ability to precisely dehumidify the air in an energy-efficient way. This innovative technology uses the hygroscopic properties of liquid desiccants to separate the water vapor from the gas mixture. One problem in modeling liquid desiccant air conditioning systems is the complex heat, mass, and momentum phenomena occurring inside the gas-liquid contactor which are sometimes not clarified especially for new pairs of liquid desiccant and gas-liquid contactor. Hence, mathematical modeling, control strategy development, and optimization of these systems are necessary research tasks to improve the design and performance of these systems.

10.1 Conclusions

In this research, a 3-fluid liquid desiccant air conditioning system has been experimentally and theoretically investigated. This system incorporates a 3-fluid gas-liquid contactor, which incorporates cooling water to partially remove the heat of condensation absorbed by the solution. However, the structure of the 3-fluid gas-liquid contactor and the transfer phenomena occurring inside become highly complex. Moreover, a newly developed ionic liquid desiccant is utilized and its physical properties along with its wetting characteristics need to be clarified.

In line with the objectives of this research, the conclusions are described as follows:

The 3-fluid gas-liquid contactor was modeled by incorporating a partial wetting equation for the estimation of the wetting ratio. The partial wetting model was developed applying the principle of minimum energy and minimum wetting rates. The 3-fluid gas-liquid contactor model was validated by comparing the predicted results from the mathematical model with the experimental data. A parametric study was carried out to investigate the effect of the dimensions on the performance of the gas-liquid contactor. It was clarified that increasing the length, the height, or the width decreases the outlet air humidity ratio due to the increase in transfer area and contact time. On the other hand, increasing the length of the contactor increases the air pressure drop while increasing both

the height and the width decreases the air pressure drop. The wetting ratio decreases as the length and width of the contactor increase due to a decrease in solution flow rate per unit area. On the other hand, change in the height of the contactor does not significantly affect the wetting ratio since the top area is not changed and the solution flow rate per unit area remains the same.

Contactor size optimization of the 3-fluid gas-liquid contactor was carried out to determine the optimal size of the gas-liquid contactor at various conditions. The optimal size of the 3-fluid gas-liquid contactor was determined at various air flow rates and various inlet air humidity ratio. The advantage of the 3-fluid gas-liquid contactor against a conventional 2-fluid gas-liquid contactor was clarified. The results show the superiority of 3-fluid gas-liquid contactors over conventional 2-fluid gas-liquid contactors by achieving lower outlet air humidity ratio at the smallest volume from the range of the dimensions. A possible reduction in size of more than 50% can be achieved by the 3-fluid gas-liquid contactor compared to a conventional 2-fluid contactor for a standard air conditioning requirement during summer in Tokyo.

10.2 Future plan

Many different tasks can be done for the continuation of this research study. These tasks include:

1. Further experimentation in order to gather a solid experimental database.
2. Carry out more optimization problems applying other relevant parameters and constraints.
3. System modeling employing the mathematical model of the 3-fluid gas-liquid contactor.

References

1) Earth Observatory, 2020. World of Change: Global Temperatures, Earth Observatory. Accessed March 9, 2020.
2) History.com Editors, 2015. Ice Age, A&E Television Networks. Accessed March 9, 2020.
3) Varassi, J., 2011. Global Cooling: The History of Air Conditioning, ASME Public Information. Accessed on March 9, 2020.
4) Yamaguchi, S., Saito, K., 2013. Numerical and experimental performance analysis of rotary desiccant wheels. International Journal of Heat and Mass Transfer, 60, 51–60.
5) Varela, R.J., Yamaguchi, S., Giannetti, N., Saito, K., Harada, M., Miyauchi, H., 2018. General correlations for the heat and mass transfer coefficients in an air-solution contactor of a liquid desiccant system and an experimental case application. International Journal of Heat and Mass Transfer, 120, 851–860.
6) ASHRAE, 2017. ASHRAE Handbook—Fundamentals SI Edition, Atlanta/USA.
7) Katejanekarn, T., Chirarattananon, S., Kumar, S., 2009. An experimental study of a solar-regenerated liquid desiccant ventilation pre-conditioning system. Solar Energy, 83, 920–933.
8) Kovak, B., Heimann, P.R., Hammel, J., 1997. The sanitizing effects of desiccant-based cooling. ASHRAE Journal, 39, 60–64.
9) Zhang, T., Liu, X., Jiang, J., Chang, X., Jiang, Y., 2013. Experimental analysis of an internally-cooled liquid desiccant dehumidifier. Building and Environment, 63, 1–10.
10) Factor, H.M., Grossman, G., 1980. A packed bed dehumidifier/regenerator for solar air conditioning with liquid desiccants. Solar Energy, 24, 541–550.
11) Abdul-Wahab, S.A., Zurigat, Y.H., Abu-Arabi, M.K., 2004. Predictions of moisture removal rate and dehumidification effectiveness for structured liquid desiccant air dehumidifier. Energy, 29 19–34.
12) Khalid Ahmed, C.S., Gandhidasan, P., Al-Farayedhi, A.A., 1997. Simulation of a hybrid liquid desiccant based air-conditioning system. Applied Thermal Engineering. 17, 125–134.
13) Yin, Y., Zhang, X., Wang, G., Luo, L., 2008. Experimental study on a new internally cooled/heated dehumidifier/regenerator of liquid desiccant systems. International Journal of Refrigeration, 31, 1664–1671.
14) Dai, Y.J., Wang, R.Z., Zhang, H.F., Yu, J.D.,2001. Use of liquid desiccant cooling to improve the performance of vapor compression air conditioning. Applied Thermal Engineering. 21, 1185–1202.
15) Kessling, W., Laevemann, E., Kapfhammer, C., 1998. Energy storage for desiccant cooling systems component development. Solar Energy, 64, 209–221.

16) Varela, R.J., Giannetti, N., Ariyadi, H., Yamaguchi, S., Saito, K., Wang, X.M., Nakayama, H., 2019. A practical heat and mass transfer model between the air and ionic liquid solution in an internally cooled dehumidifier with partial wetting. Proc. of the 25th IIR International Congress of Refrigeration.
17) Luo, Y., Shao, S., Xu, H., Tian, C., Yang, H., 2014. Experimental and theoretical research of a fin-tube type internally-cooled liquid desiccant dehumidifier. Applied Energy, 133, 127–134.
18) Sato, T., Varela, R.J., Yamaguchi, S., Saito, K., Nakayama, H., 2018. Experimental study on a finned-tube internally cooled contactor for liquid desiccant air conditioning systems with ionic liquid. Proc. of the International Refrigeration and Air Conditioning Conference.
19) Yamaguchi, S., Jeong, J., Saito, K., Miyauchi, H., Harada, M., 2011. Hybrid liquid desiccant air-conditioning system: Experiments and simulations. Applied Thermal Engineering, 31, 3741–3747.
20) Yamaguchi, S., Jeong, J., Saito, K., Miyauchi, H., Harada, M., 2011. Hybrid liquid desiccant air- conditioning system: Experiments and simulations. Applied Thermal Engineering, 31, 3741–3747.
21) Shaji Mohan, B., Tiwari, S., Maiya, M.P., 2015 Experimental investigations on performance of liquid desiccant-vapor compression hybrid air conditioner. Applied Thermal Engineering, 77, 153–162.
22) Bassuoni, M.M., 2011. An experimental study of structured packing dehumidifier/regenerator operating with liquid desiccant. Energy, 36, 2628–2638.
23) Bansal, P., Jain, S., Moon, C., 2011. Performance comparison of an adiabatic and an internally cooled structured packed-bed dehumidifier. Applied Thermal Engineering, 31, 14–19.
24) Gommed, K., Grossman, G., Prieto, J., Ortiga, J., Coronas, A., 2015. Experimental comparison between internally and externally cooled air-solution contactors. Science and Technology for the Built Environment, 21, 267–274.
25) Liu, X.H., Chang, X.M., Xia, J.J., Jiang, Y., 2009. Performance analysis on the internally cooled dehumidifier using liquid desiccant. Building and Environment, 44, 299–308.
26) Ren, R.J., Charles, J., Wang, X.C., Nie, F.X., Romero, C., Neti, S., Zheng, Y., Hoenig, S., Chen, C., Cao, F., Bonner, R., Pearlman, H., 2017. Corrosion testing of metals in contact with calcium chloride hexahydrate used for thermal energy storage. Materials and Corrosion, 68, 1046–1056.
27) Liu, J., Liu, X., Zhang, T., 2016. Performance comparison of three typical types of internally-cooled liquid desiccant dehumidifiers. Building and Environment, 103, 134–145.

28) Guiñon, J.L., Garcia-Anton, J., Pérez-Herranz, V., Lacoste, G., 1994. Corrosion of carbon steels, stainless steels, and titanium in aqueous lithium bromide solution. Corrosion, 50, 240–246.
29) Park, M.S., Howell, J.R., Vliet, G.C., Peterson, J., 1994. Numerical and experimental results for coupled heat and mass transfer between a desiccant film and air in cross-flow. International Journal of Heat and Mass Transfer, 37, 395–402.
30) Jain, S., Dhar, P.L., Kaushik, S.C., 2000. Experimental studies on the dehumidifier and regenerator of a liquid desiccant cooling system. Applied Thermal Engineering, 20, 253–267.
31) Peng, C.S.P., Howell, J.R., 1981. Optimization of liquid desiccant systems for solar-geothermal dehumidification and cooling. Journal of Energy, 5, 401–408.
32) Bentounes, N., Jaffrin, A., 1998. Optimization of heat and mass transfers in counterflow corrugated-plate liquid-gas exchangers used in a greenhouse dehumidifier. European Physical Journal Applied Physics, 3, 295–308.
33) An, S., Wang, J., Liu, J., 2007. Some optimization on the design of liquid desiccant air conditioning system, Proc. of the 5th International Symposium on Heating, Ventilating and Conditioning.
34) Dai, Y.J., Xiong, Z.Q., Mei, L., Wang, R.Z., 2007. Analysis and optimization on performance of parallel two stage solar liquid desiccant dehumidifier, Proc. of the Solar World Congress of the International Solar Energy Society.
35) Lee, S.J., Lee, C.J., 2010. Optimization design of liquid desiccant cooling system. Korea Journal of Air-Conditioning and Refrigeration Engineering, 22, 419–428.
36) Chen, L., Chen, Q., Li, Z. Gou, Z.Y., 2010. Moisture transfer resistance method for liquid desiccant dehumidification analysis and optimization. Chinese Science Bulletin, 55, 1445–1453.
37) Jiang, J.J., Liu, X.H., Zhang, T., 2011. Performance optimization of liquid desiccant air-conditioning processes, Proc. of the 7th International Symposium on Heating, Ventilating and Air Conditioning.
38) Ge, G., Xiao, F., Xu, X., 2011. Model-based optimal control of a dedicated outdoor air-chilled ceiling system using liquid desiccant and membrane-based total heat recovery. Applied Energy, 88, 4180–4190.
39) Audah, N., Ghaddar, N., Ghali, K., 2011. Optimized solar-powered liquid desiccant system to supply building fresh water and cooling needs. Applied Energy, 88, 3726–3736.
40) Ge, G., Xiao, F., Wang, S., 2012. Optimization of a liquid desiccant based dedicated outdoor air-chilled ceiling system serving multi-zone spaces, Proc. of the 8th Conference on System Simulation in Buildings.
41) Zhang, T., Liu, X., Jiang, Y., 2012. Performance optimization of heat pump driven liquid desiccant dehumidification systems. Energy and Buildings, 52, 132–144.

42) Ge, G., Moghaddam, G.D., Ramin; N., Simonson, C.J., Besant, R.W., 2013. Analytical model based performance evaluation, sizing and coupling flow optimization of liquid desiccant run-around membrane energy exchanger systems. Energy and Buildings, 61, 248–257.
43) Seenivasan, D., Selladurai, V., Senthil, P., 2014. Optimization of liquid desiccant dehumidifier performance using Taguchi Method. Advances in Mechanical Engineering, 6, 1–6.
44) Qi, R., Lu, L., 2014. Energy consumption and optimization of internally cooled/heated liquid desiccant air-conditioning system: A case study in Hong Kong. Energy, 73, 801–808.
45) Wang, X., Cai, W., Lu, J., Sun, Y., 2014. Optimization of liquid desiccant regenerator with multiobject particle swarm optimization algorithm. Industrial and Engineering Chemistry Research, 53, 19293–19303.
46) Wang, X., Cai, W., Lu, J., 2015. Energy saving strategy development in liquid desiccant dehumidifier by genetic algorithm, Proc. of the 10th IEEE Conference on Industrial Electronics and Applications.
47) Wang, X., Cai, W., Lu, J., Sun, Y., Zhao, L., 2015. Model-based optimization strategy of chiller driven liquid desiccant dehumidifier with genetic algorithm. Energy, 82, 939–948.
48) Yuan, F., Chen, Q., 2015. A property diagram-based method for synthesis and parameter optimization of heat and mass transfer in moist air-water/aqueous solution systems. International Journal of Heat and Mass Transfer, 87, 189–200.
49) Qi, R., Lu L., Huang, Y., 2015. Parameter analysis and optimization of the energy and economic performance of solar-assisted liquid desiccant cooling system under different climate conditions. Energy Conversion and Management, 106, 1387–1395.
50) Muslmani, M., Ghaddar, N., Ghali, K., 2016. Optimized strategy for combined liquid desiccant dehumidification membrane with chilled ceiling and displacement ventilation system, Proc. of the 6th International Conference on Energy Research and Development.
51) Ja, M.K., Dubey, S., Hoong, C.F., Mohan Das, E.T., 2016. Optimization of solar (thermal) powered membrane based multi-effect regenerator, Proc. of the 10th ASME International Conference on Energy Sustainability.
52) Fakhrabadi, F., Kowsary, F., 2016. Optimal design of a hybrid liquid desiccant-regenerative evaporative air conditioner. Energy and Buildings, 133, 141–154.
53) Tu, M., Huang, H., Liu, Z.H., Chen, H.X., Ren, C.Q., Chen, G.J., Hu, Y., 2017. Factor analysis and optimization of operational parameters in a liquid desiccant air-conditioning system. Energy, 139, 767–781.
54) Sanaye, S., Taheri, M., 2018. Modeling and multi-objective optimization of a modified hybrid liquid desiccant heat pump (LD-HP) system for hot and humid regions. Applied Thermal Engineering, 129, 212–229.

55) Zhang, L., Song, X., Zhang, X., 2018. Analysis and optimization of total heat recovery devices by using liquid desiccant as a coupling fluid in air-conditioning systems. Energy and Buildings, 172, 493–504.
56) Song, X., Zhang, L., Zhang, X., 2018. NTUm-based optimization of heat or heat pump driven liquid desiccant dehumidification systems regenerated by fresh air or return air. Energy, 158, 269–280.
57) Zhang, N., Yin, S.Y., Li, M., 2018. Model-based optimization for a heat pump driven and hollow fiber membrane hybrid two-stage liquid desiccant air dehumidification system. Applied Energy, 228, 12–20.
58) Liu, X., Liu, X., Zhang, T., Xie, Y., 2018. Experimental analysis and performance optimization of a counter-flow enthalpy recovery device using liquid desiccant. Building Services Engineering Research and Technology, 39, 679–697.
59) Chen, Q., Kum Ja, M., Li, Y. Chua, K.J., 2018. Thermodynamic optimization of a vacuum multi-effect membrane distillation system for liquid desiccant regeneration. Applied Energy, 230, 960–973.
60) Ou, X., Cai, W., He, X., 2019. Model-based optimization strategy for a liquid desiccant cooling and dehumidification system. Energy and Buildings, 194, 21–32.
61) Liang, C., Zeng, S., 2018. Multi-objective design optimization of hollow fiber membrane-based liquid desiccant module using particle swarm optimization algorithm. Heat Transfer Engineering, 39, 1608–1618.
62) Lof, G.O.G., Cooling with solar energy. Proc. of the 1955 Congress on Solar Energy.
63) Peng, C.S.P., Howell, J.R., 1981. Analysis and design of efficient absorbers for low-temperature desiccant air conditioners. ASME Journal of Solar Energy Engineering, 103, 67–74.
64) Chung, T., Wu, H., 1998. Dehumidification of air by aqueous triethylene glycol solution in a spray tower. Separation Science and Technology, 33, 1213–1224.
65) Esarrag, E., 2007. Moisture removal rate for air dehumidification by triethylene glycol in a structured packed column. Energy Conversion and Management, 48, 327–332.
66) Studak, J.W., Peterson, J.L., 1988. A preliminary evaluation of alternative liquid desiccants for hybrid desiccant air conditioner. Proc. of the Fifth Symposium on Improving Buildings in Hot and Humid Climates.
67) Conde, M.R., 2004. Properties of aqueous solutions of lithium and calcium chlorides: formulations for use in air conditioning equipment design. International Journal of Thermal Sciences, 43, 367–382.
68) Luo, Y., Shao, S., Qin, F., Tian, C., Yang, H., 2012. Investigation on feasibility of ionic liquids used in solar liquid desiccant air conditioning system. Solar Energy, 86, 2718–2724.

69) Butt, H.J., Graf, K., Kappl, M., 2013. Physics and Chemistry of Interfaces. Wiley-VCH, Germany.
70) 舛谷　乙彦, 勝田　正文, 2015. イオン液体用いた CO2 圧縮/吸収ハイブリッドサイクルにおける吸収器での熱·物質移動特性―管内流動促進と伝熱性能の関係(In Japanese)―. Waseda University, Japan.
71) Chung, T., Ghosh, T.K., 1996. Comparison between random and structured packings for dehumidification of air by lithium chloride solutions in a packed column and their heat and mass transfer correlations. Industrial and Engineering Chemistry Research, 35, 192–198.
72) Liu, J., Liu, X., Zhang, T., 2016. Performance comparison of three typical types of internally cooled liquid desiccant dehumidifiers. Building and Environment, 103, 134–145.
73) Zhang, F., Wu, Y.T., Geng, J., Zhang, Z., 2008. An investigation of falling liquid films on a vertical heated/cooled plate. International Journal of Multiphase Flow, 34, 13–28.
74) Ponter, A.B., Davies, G.A., Beaton, W., Ross, T.K., 1967. The measurement of contact angles under equilibrium and mass-transfer conditions. International Journal of Heat and Mass Transfer, 10, 733–736.
75) Bejan, A., 2006. Advanced Engineering Thermodynamics, John Wiley & Sons, USA.
76) H. Helmholtz, 1869/1871. Zur Theorie der stationären Ströme in reibenden Flüssigkeiten. Verhandlungen des naturhistorisch-medizinischen Vereins zu Heidelberg, 5, 1–7.
77) Hamilton, W.R., 1834. On a general method in dynamics. Philosophical Transactions of the Royal Society, part II, 247–308.
78) Hamilton, W.R., 1835. Second essay on a general method in dynamics. Philosophical Transactions of the Royal Society, part I, 95–144.
79) Onsager, L., 1931. Reciprocal relations in irreversible processes I. Physical Review, 37, 405–426.
80) Onsager, L., 1931. Reciprocal relations in irreversible processes II. Physical Review, 38, 2265–2279.
81) Ziman, J.M., 1956. The general variational principle of transport theory. Canadian Journal of Physics, 34, 1256–1273.
82) Prigogine, I., 1961. Introduction to thermodynamics of irreversible processes, Interscience/John Wiley & Sons, USA.
83) Bejan, A., Lorente, S., 2008. Design with Constructal Theory, Hoboken, John Wiley & Sons, USA.
84) Kiss, E., 1994. On the validity of the principle of minimum entropy production. Periodica Polytechnica Ser. Chem. Eng., 38, 183–197.

85) Reis, A.H., 2014. Use and validity of principles of extremum of entropy production in the study of complex systems. Annals of Physics, 346, 22–27.
86) Grandy, W.T., 2008. Entropy and the Time Evolution of Macroscopic Systems, Oxford University Press, USA.
87) Zivi, S.M., 1964. Estimation of steady-state steam void-fraction by means of the principle of minimum entropy production. ASME Journal of Heat Transfer, 86, 247–251.
88) Giannetti, N., Kunita, D., Yamaguchi, S., Saito, K., 2018. Annular flow stability within small-sized channels. International Journal of Heat and Mass Transfer, 116, 1153–1162.
89) N. Brauner, J. Rovinsky, D.M. Maron, 1996. Determination of the interface curvature in stratified two-phase systems by energy considerations. International Journal of Multiphase Flow, 22, 1167–1185.
90) Chakrabarti, D.P., Das, G., Ray, S., 2005. Pressure drop in liquid-liquid two phase horizontal flow: Experiment and prediction. Chemical Engineering and Technology, 28, 1003–1009.
91) Paulus, D.M., Gaggioli, R.A., 2004. Some observations of entropy extrema in fluid flow. Energy, 29, 2487–2500.
92) Dabirian, R., Thompson, L., Mohan, R.S., Shoham, O., Avila, C., 2013. Prediction of two-phase flow splitting in looped lines based on energy minimization. Society of Petroleum Engineers, SPE 166197, 1–11.
93) Mittermaier, M., Schulze, P. Ziegler, F., 2014. A numerical model for combined heat and mass transfer in a laminar liquid falling film with simplified hydrodynamics. International Journal of Heat and Mass Transfer, 70, 990–1002.
94) Andberg, J.W., Vliet, G.C., 1987. A simplified model for absorption of vapors into liquid films flowing over cooled horizontal tubes. ASHRAE Transactions, 93, 2454–66.
95) Papaefthimiou, V.D., Koronaki, I.P., Karampinos, D.C., Rogdakis, E.D., 2012. A novel approach for modelling LiBr–H2O falling film absorption on cooled horizontal bundle of tubes. International Journal of Refrigeration, 35, 1115–1122.
96) Babadi, F., Farhanieh, B., 2005. Characteristics of heat and mass transfer in vapor absorption of falling film flow on a horizontal tube. International Communications in Heat and Mass Transfer, 32, 1253–1265.
97) Giannetti, N., Yamaguchi, S., Saito, K., 2016. Wetting behaviour of a liquid film on an internally-cooled desiccant contactor. International Journal of Heat and Mass Transfer, 101, 958–969.
98) Mikielewicz, J., Moszynski, J. R., 1976. Minimum thickness of a liquid film flowing vertically down a solid surface. International Journal of Heat and Mass Transfer, 19, 771–776.

99) Dokowicz, M., Nowicki W., 2017. Morphological hysteresis of droplets wetting a series of triangular grooves. International Journal of Heat and Mass Transfer, 115, 131–137.
100) de Gennes, P.G., Brochard-Wyart, F., Quéré, D., 2004. Capillarity and Wetting Phenomena: Drops, Bubbles, Pearls, Waves. Springer, New York.
101) Chang, C.C., Sheng, Y.J., Tsao, H.K., 2016. Wetting hysteresis of nanodrops on nanorough surfaces. Physical Review, 94, 1–8.
102) Johnson, R.E., Dettre, R.H., 1964. Contact angle hysteresis. III. Study of an idealized heterogeneous surface. The Journal of Physical Chemistry, 68, 1744–1750.
103) de Jonghe, V., Chatain, D., 1995. Experimental study of wetting hysteresis on surfaces with controlled geometrical and/or chemical defects. Acta Metallurgica et Materialia, 43, 1505–1515.
104) Shanahan, M.E.R., 1995. Simple theory of "stick-slip" wetting hysteresis. Langmuir 11, 1041–1043.
105) Jin, W., Koplik, J., 1997. Wetting hysteresis at molecular scale. Physical Review Letters, 78, 1520–1523.
106) Kabov, O.A., Zaitsev, D.V., 2013. The effect of wetting hysteresis on drop spreading under gravity. Doklady Physics, 58, 292–295.
107) Soolaman, D.M., Yu, H.Z., 2005. Water microdroplets on molecularly tailored surfaces: correlation between wetting hysteresis and evaporation mode switching. The Journal of Physical Chemistry B, 109, 17967–17973.
108) Emelyanenko, A.M., Ermolenko, N.V., Boinovich, L.B., 2004. Contact angle and wetting hysteresis measurements by digital image processing of the drop on a vertical filament. Colloids Surfaces A, 239, 25–31.
109) Hobler, T., 1964. Minimum surface wetting (in Polish). Chemia Stosow, 2B, 145–159.
110) Picknett, R.G., Bexon, R., 1977. The evaporation of sessile or pendant drops in still air. Journal of Colloid Interface Science, 61, 336–350.
111) Wassenaar, R.H., 1996. Measured and predicted effect of flowrate and tube spacing on horizontal tube absorber performance. International Journal of. Refrigeration, 19, 347–355.
112) Islam, R., Wijeysundera, N.E., Ho, J.C., 2003. Evaluation of heat and mass transfer coefficients for falling-films on tubular absorbers. International Journal of Refrigeration, 26, 197–204.
113) Islam Md., R., Wijeysundera, N.E., Ho, J.C., 2004. Simplified models for coupled heat and mass transfer in falling-film absorbers. International Journal of Heat and Mass Transfer, 47, 395–406.
114) Danckwerts, P., 1955. Gas absorption accompanied by a two-step chemical reaction. Chemical Engineering Science. 456–463.

115) Cussler, E.L., 2009. Diffusion Mass Transfer in Fluid Systems, Cambridge, UK.
116) Kays, W.M., Crawford, M.E., 1980. Convective Heat and Mass Transfer, McGraw-Hill, USA.
117) 瀬下　裕, 藤井　雅雄, 1992. コンパクト熱交換器(In Japanese), Japan.
118) Karami, S., Farhanieh, B., 2009. A numerical study on the absorption of water vapor into a film of aqueous LiBr falling along a vertical plate. Heat Mass Transfer, 46, 197–207.
119) Incropera, F.P., Bergman, T.L., Lavine, A.S., DeWitt, D.P., 2011. Fundamentals of Heat and Mass Transfer, USA.
120) JSME, 1999. JSME Steam Tables, Japan.
121) Srinivas, N., Deb, K., 2007. Multi-objective optimization using non-dominated sorting in genetic algorithms. Evolutionary Computation, 2, 221–248.
122) Sanaye, S., Hajabdollahi, H., 2010. Thermal-economic multi-objective optimization of plate fin heat exchanger using genetic algorithm. Applied Energy, 87, 1893–1902.
123) Xie, G.N., Sunden, B., Wang, Q.W., 2008. Optimization of compact heat exchangers by a genetic algorithm. Applied Thermal Engineering, 28, 895–906.
124) Whitman, W.G., 1923. The Two-Film Theory of gas absorption. Chemical and Metallurgical Engineering, 29, 146–148.

Appendix

1. Packed bed gas-liquid contactor model

The packed bed gas-liquid contactor presented in Fig. 1.1(a) is divided into differential control elements as shown in Fig. 1.1(b). Here, the solution refers to the mixture of water and lithium chloride (LiCl).

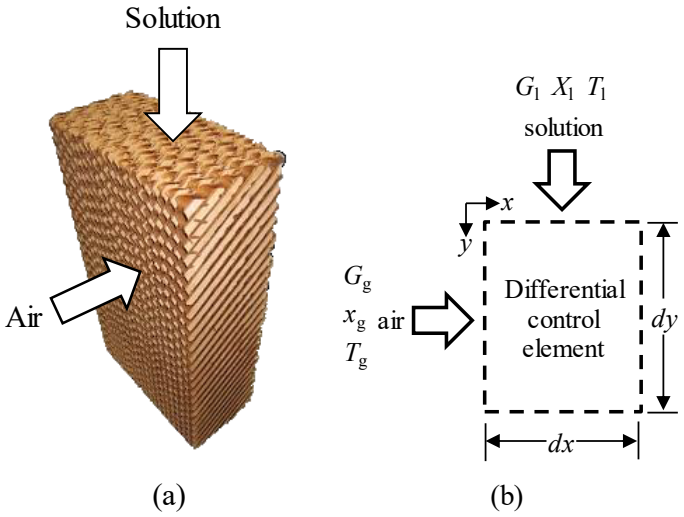

Fig. 1.1 (a) Structured packed bed and (b) differential control element for the packed bed.

1.1 Simplified geometry for the air channel

Fig. 1.2 illustrates the geometry of the air channel inside the packed bed. The actual geometry (Fig. 1.2(1)) is bell-shaped but to simplify the calculation for the hydraulic diameter, a triangular geometry (Fig. 1.2(2)) for the air channel is assumed.

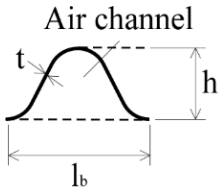

(1) Actual geometry

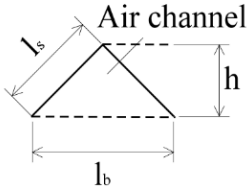

(2) Simplified geometry

Fig. 1.2 Illustration of the: (1) actual geometry and (2) simplified geometry of air channel inside the structured packed bed.

1.2 Assumptions

The following were adopted as simplifying assumptions for the mathematical analysis of the adiabatic liquid desiccant air conditioning system:

(a) Transfer flow is steady-state and one-dimensional.

(b) Heat and mass transfer is between the bulk air and the bulk solution.

(c) The flow of the solution is laminar, non-wavy, and fully developed.

(d) The packed bed is completely wetted by the aqueous LiCl.

(e) Thermodynamic equilibrium exists, and no shear force is acting on the gas-liquid interface.

(f) Mass transport across the falling film is by diffusion only, mass transfer by convection is not considered.

(g) There is no chemical reaction and viscous dissipation.

(h) Dufour and Soret effects are neglected.

1.3 Governing equations

Fig. 1.3 shows the concentration profiles of the water species in the air and the solution. Since mass transfer is in a direction of decreasing concentration, water species in the figure diffuses from the air to the LiCl solution. This condition depicts the mass transport in a dehumidification process wherein the air is in a higher vapor pressure compared with the solution. In the regeneration process, the transfer flow is reversed as the solution is at a higher temperature resulting in higher vapor pressure compared with the air.

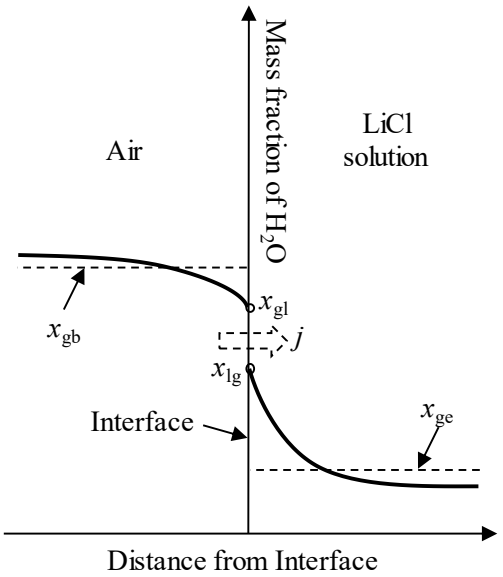

Fig. 1.3 Concentration profiles of water species in the air and solution.

The governing equations for both fluids are derived applying the previously specified assumptions, the directions of the contacting fluids in Fig. 1.1, and the one-dimensional transfer flow illustrated in Fig. 1.3. These conservation equations are first expressed in semi-discrete partial differential equations and are later fully discretized by applying the forward difference method.

Governing equations for the air

The mass of the dry air is conserved in the flow direction and is expressed in conservation form as

$$\frac{\partial G_{\mathrm{gb}}}{\partial x} = 0 \qquad (\mathrm{kg \cdot m^{-2} \cdot s^{-1}}) \qquad (1.1)$$

where G_{gb} indicates the mass flux of the gas bulk.

The moist air conservation of mass is the equality between the change in water mass fraction in the x direction and the mass transfer of water vapor from the air to the solution, that is

$$G_{\mathrm{gb}} \frac{\partial x_{\mathrm{gb}}}{\partial x} = -j_{\mathrm{gb-lb}} C_{\mathrm{sa}} dx \qquad (\mathrm{kg \cdot m^{-2} \cdot s^{-1}}) \qquad (1.2)$$

where x_{gb} ($\mathrm{kg \cdot kg(DA)^{-1}}$) is the water mass fraction of the gas bulk and $j_{\mathrm{gb\text{-}lb}}$ is the diffusion mass flux of water vapor from the gas bulk to the liquid bulk defined in accordance with Fick's law as

$$j_{\mathrm{gb-lb}} = h_{\mathrm{m,gb-lb}} \left(x_{\mathrm{gb}} - x_{\mathrm{ge}} \right) \qquad (\mathrm{kg \cdot m^{-2} \cdot s^{-1}}) \qquad (1.3)$$

where $h_{\mathrm{m,gb\text{-}gl}}$ ($\mathrm{kg \cdot m^{-2} \cdot s^{-1}}$) denotes the overall mass transfer coefficient, which is discussed in Section 1.5. Here, x_{ge} is the equilibrium water mass fraction of the liquid bulk relative to the gas bulk.

The conservation of energy for the air is the balance between the change in energy in the flow direction and the sensible and latent heat transports from the gas bulk to the liquid bulk, expressed in equation form as

$$G_{\mathrm{gb}} \frac{\partial h_{\mathrm{gb}}}{\partial x} = -\left(q_{\mathrm{gb-lb}} + j_{\mathrm{gb-lb}} h_{\mathrm{c}} \right) C_{\mathrm{sa}} dx \qquad (\mathrm{kW \cdot m^{-2}}) \qquad (1.4)$$

where h_{gb} (kJ·kg^{-1}) represents the enthalpy of the gas bulk and h_c is the enthalpy of condensation for the dehumidification process, which becomes the enthalpy of evaporation h_v for the regeneration process.

$q_{gb\text{-}lb}$ indicates the conductive heat transfer from the gas bulk to the liquid bulk and is derived from the Fourier's law as

$$q_{gb-lb} = h_{h,gb-lb}(T_{gb} - T_{lb}) \quad (kW\cdot m^{-2}) \quad (1.5)$$

where $h_{h,gb\text{-}lb}$ (kW·m^{-2}·K^{-1}) is the heat transfer coefficient from the gas bulk to the liquid bulk and is treated in Section 1.5.

T_{gb} (°C) and T_{lb} denote the gas and liquid bulk temperatures, respectively.

Governing equations for the aqueous lithium chloride

The conservation of mass for the LiCl solution is the change in solution mass flux in the y direction equated to the water vapor diffused to the solution.

$$\frac{\partial G_{lb}}{\partial y} = j_{gb-lb} C_{sa} dy \quad (kg\cdot m^{-2}\cdot s^{-1}) \quad (1.6)$$

Here, G_{lb} represents the mass flux of the liquid bulk.

For the LiCl, assuming no leak or carryover, the mass is conserved inside the system,

$$\frac{\partial (G_{lb} X_{lb})}{\partial y} = 0 \quad (kg\cdot m^{-2}\cdot s^{-1}) \quad (1.7)$$

where X_{lb} (kg(IL) kg(sol)$^{-1}$) is the LiCl mass fraction in the solution.

The conservation of energy for the solution is the balance between the change in energy in the flow direction and the conductive and diffusive transports from the air to the solution, written as

$$\frac{\partial (G_{lb} X_{lb})}{\partial y} = (q_{gb-lb} + j_{gb-lb} h_c) C_{sa} dx \quad (kW\cdot m^{-2}\cdot K^{-1}) \quad (1.8)$$

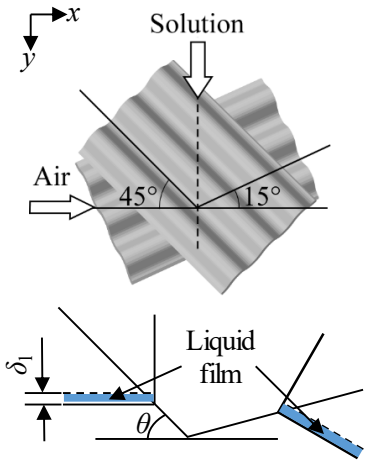

Fig. 1.4 Illustration of the liquid film falling on the inclined corrugated sheets of the packed bed.

Fig. 1.4 illustrates the falling liquid film on the air channel of the packed bed. Consider the left side illustration of the liquid film, the conservation of momentum for the liquid film falling on the inclined surface of the corrugated sheet is the balance between the viscous force and the gravity force acting on the angular direction,

$$\mu_l \frac{\partial^2 u_l}{\partial z^2} = -\frac{\rho_l g}{\sin\theta} \qquad (\text{kg}\cdot\text{m}^{-2}\cdot\text{s}^{-2}) \qquad (1.9)$$

where μ_l (Pa·s), u_l (m·s^{-1}), and g denote the dynamic viscosity of the liquid, the velocity of the liquid, and the standard gravitational acceleration, respectively.

Integrating the momentum equation results to

$$\frac{\partial u_l}{\partial y} = -\frac{\rho_l g}{\mu_l \sin\theta} z + c_1 \qquad (\text{s}^{-1}) \qquad (1.10)$$

Applying the first boundary condition for the momentum conservation, $u_l = 0$ at $y = 0$ (liquid-solid interface), gives the expression for c_1

$$c_1 = \frac{\rho_l g}{\mu_l \sin\theta} \delta_l \qquad (\text{s}^{-1}) \qquad (1.11)$$

Now, integrating the first derivative of the momentum equation,

$$u_l = -\frac{\rho_l g}{\mu_l \sin\theta} \frac{y^2}{2} + c_1 y + c_2 \qquad (\text{m}\cdot\text{s}^{-1}) \qquad (1.12)$$

Substituting the expression for c_1 and the second boundary condition for the momentum conservation, $\partial u_l/\partial y = 0$ at $y = \delta_l$ (gas-liquid interface), results to $c_2 = 0$. Thus, the expression for the velocity profile of the liquid film is

$$u_l = \frac{\rho_l g}{\mu_l \sin\theta}\left(\delta_l y - \frac{y^2}{2}\right) \quad (\mathrm{m\cdot s^{-1}}) \qquad (1.13)$$

1.4 Initial conditions

Initial conditions are important to solve the system of equations organized in the previous section. The initial or input conditions depend on the experimental conditions, which are listed in mathematical form as follows:

At $x = 0$ (air entry)

$$T_{gb} = T_{ig},\ x_{gb} = x_{ig},\ u_{gb} = u_{ig} \qquad (1.14)$$

where T_{ig}, x_{ig}, u_{gb} ($\mathrm{m\cdot s^{-1}}$), and u_{ig} are the inlet gas temperature, the inlet gas water mass fraction, the gas bulk velocity, and the inlet gas velocity, respectively.

At $y = 0$ (LiCl solution entry)

$$T_{lb} = T_{il},\ G_{lb} = G_{il},\ X_{lb} = X_{il} \qquad (1.15)$$

where T_{il}, G_{il}, and X_{il} are the inlet liquid temperature, the inlet liquid mass flux, and the inlet liquid (LiCl) mass fraction, respectively.

1.5 Heat and mass transfer coefficients

The heat and mass transfer coefficients are necessary to solve the systems of equations, specifically the heat and mass transfers inside the packed bed. These heat and mass transfer coefficients can be correlated to a dimensionless number, which involves that corresponding transfer coefficient itself.

Gas-side heat and mass transfer coefficients

The heat transfer coefficient from the gas bulk to the gas-liquid interface $h_{h,gb\text{-}gl}$ is correlated to the Nusselt number as

$$\mathrm{Nu_{gb}} = f\left(\mathrm{Re_{gb}}, \mathrm{Pr_{gb}}\right) = \frac{h_{h,gb-gl} d_{h,gb}}{\lambda_{gb}} \qquad (1.16)$$

where $\mathrm{Nu_{gb}}$, $\mathrm{Re_{gb}}$, and $\mathrm{Pr_{gb}}$ denote the Nusselt number, the Reynolds number, and the Prandtl number of the gas bulk, respectively. λ_{gb} ($\mathrm{kW \cdot m^{-1} \cdot K^{-1}}$) is the thermal conductivity of the gas bulk determined in accordance with the ASHRAE Handbook of Fundamentals[6].

$d_{\mathrm{h,gb}}$ is the hydraulic diameter of the gas bulk or the characteristic length in general term and is estimated by considering the simplified triangular geometry of the air channel in Fig. 1.2 and the liquid film on the inclined surface of the corrugated sheet shown.

$$d_{\mathrm{h,gb}} = \frac{4A_{\mathrm{ac,c}}}{P_{\mathrm{ac,w}}} = \frac{4\left[l_{\mathrm{b}}(h-t)/2 - \delta_{\mathrm{l},\theta} l_{\mathrm{s}}\right]}{2l_{\mathrm{s}}} \quad (\mathrm{kW \cdot m^{-2} \cdot K^{-1}}) \quad (1.17)$$

where $A_{\mathrm{ac,c}}$ and $P_{\mathrm{ac,w}}$ (m) represent the cross-sectional area and the wetted perimeter of the air channel, respectively.

To derive the expression for the film thickness flowing on the inclined sheet of the packed bed $\delta_{\mathrm{l},\theta}$, the continuity of Γ_{l} (mass flow rate of the liquid film per unit length of the contactor) across the thickness of the film is taken

$$\Gamma_{\mathrm{l}} = \int_0^{\delta_{\mathrm{l},\theta}} \rho_{\mathrm{l}} u_{\mathrm{l}} dy = \frac{\rho_{\mathrm{l}}^2 g}{\mu_{\mathrm{l}}} \int_0^{\delta_{\mathrm{l},\theta}} \left(\delta_{\mathrm{l},\theta} y - \frac{y^2}{2}\right) dz \quad (\mathrm{kg \cdot m^{-2} \cdot s^{-1}}) \quad (1.18)$$

Integrating the above equation gives the expression for the film thickness

$$\delta_{\mathrm{l},\theta} = \left(\frac{3\mu_{\mathrm{l}}\Gamma_{\mathrm{l}} \sin\theta}{\rho_{\mathrm{l}}^2 g}\right)^{1/3} \quad (\mathrm{m}) \quad (1.19)$$

where Γ_{l} is described as

$$\Gamma_{\mathrm{l}} = \frac{\dot{m}_{\mathrm{l}}}{L} = \frac{G_{\mathrm{l}} LW}{n\varepsilon(L/l_{\mathrm{b}})l_{\mathrm{s}}} = \frac{G_{\mathrm{l}} W l_{\mathrm{b}}}{n\varepsilon l_{\mathrm{s}}} \quad (\mathrm{kg \cdot m^{-1} \cdot s^{-1}}) \quad (1.20)$$

On the other hand, the mass transfer coefficient from the gas bulk to the gas-liquid interface $h_{\mathrm{m,gb\text{-}gl}}$ is correlated to the Sherwood number as

$$\mathrm{Sh_{gb}} = f\left(\mathrm{Re_{gb}}, \mathrm{Sc_{gb}}\right) = \frac{h_{\mathrm{m,gb-gl}} d_{\mathrm{h,gb}}}{\rho_{\mathrm{gb}} D_{\mathrm{gb}}} \quad (1.21)$$

where $\mathrm{Sc_{gb}}$, ρ_{gb} ($\mathrm{kg \cdot m^{-3}}$), and D_{gb} ($\mathrm{m^2 \cdot s^{-1}}$) indicate the Schmidt number, the density, and the diffusivity coefficient of the gas bulk, respectively, and are estimated based on ASHRAE[6].

Liquid-side heat and mass transfer coefficients

The liquid-side heat and mass transfer coefficients are derived in the same manner as the gas-side transfer coefficients were derived but applying the liquid-side physical properties.

The correlation of the heat transfer coefficient from the gas-liquid interface to the liquid bulk $h_{\mathrm{h,gl\text{-}lb}}$ with the Nusselt number is written as

$$\mathrm{Nu_{lb}} = f(\mathrm{Re_{lb}}, \mathrm{Pr_{lb}}) = \frac{h_{\mathrm{h,gl-lb}}\delta_{\mathrm{l}}}{\lambda_{\mathrm{lb}}} \tag{1.22}$$

where $\mathrm{Nu_{lb}}$, $\mathrm{Re_{lb}}$, and $\mathrm{Pr_{lb}}$ are the Nusselt number, the Reynolds number, and the Prandtl number of the liquid bulk, respectively. λ_{lb} is the thermal conductivity of the liquid bulk and is calculated according to the formulations developed by Conde[67].

The mass transfer coefficient from the gas-liquid interface to the liquid bulk $h_{\mathrm{m,gl\text{-}lb}}$ is correlated as

$$\mathrm{Sh_{lb}} = f(\mathrm{Re_{lb}}, \mathrm{Sc_{lb}}) = \frac{h_{\mathrm{m,gl-lb}}\delta_{\mathrm{l}}}{\rho_{\mathrm{lb}} D_{\mathrm{lb}}} \tag{1.23}$$

where $\mathrm{Sc_{lb}}$, ρ_{lb} , and D_{lb} denote the Schmidt number, the density, and the mass diffusivity of the liquid bulk, respectively, and are estimated from the formulations of Conde[112].

Overall heat and mass transfer coefficients

There are two methods to describe interphase transport rates. One method is to define the transfer rate for each phase by determining the single-phase transfer coefficient and the concentration of species at the interface of the two fluids together with the bulk concentrations as suggested by the "Two-Film Theory" of Whitman[124]. A simplification in this approach is that the liquid film is non-wavy, and the film thickness is constant, which is practically not the case with the falling film inside the inclined sheet of the packed bed. The other method is to use the overall mass transfer coefficient, the water concentration in the gas bulk, and the equivalent water concentration in the liquid bulk to determine the overall mass transfer coefficient. Also, the solute concentration in the liquid bulk and equivalent solute concentration in the gas bulk can be used instead of the species concentration in the gas bulk and the equivalent species concentration in the liquid bulk, respectively, for volatile solutes. These mass transfer principles apply equally to heat transfer using the heat transfer analogs.

Consistent with the assumption that the heat and mass transfers are between the bulk properties of the air and solution, the overall heat and mass transfer coefficients are used to calculate the heat and mass transports. To help conceptualize and formulate the

overall heat and mass transfer coefficients, an illustration of the equivalent circuits for the heat and mass transfers between the air and solution is shown in Fig. 1.5.

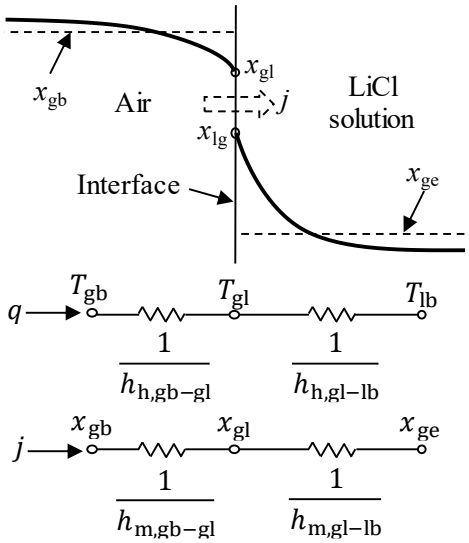

Fig. 1.5 Equivalent circuits for the heat and mass transfers between the air and solution.

Since the gas-side and liquid-side transfer resistances are in series and continuity of heat and mass flux at the interface is assumed, the overall heat and mass transfer coefficients can be determined by adding the single-phase resistances as follows:

$$\frac{1}{h_{\mathrm{h,gb-lb}}} = \frac{1}{h_{\mathrm{h,gb-gl}}} + \frac{1}{h_{\mathrm{h,gl-lb}}} = \frac{d_{\mathrm{h,gb}}}{\mathrm{c}_1 \lambda_{\mathrm{gb}} \mathrm{Re}_{\mathrm{gb}}^{\mathrm{c}_2} \mathrm{Pr}_{\mathrm{gb}}^{\mathrm{c}_3}} + \frac{\delta_{\mathrm{l}}}{\mathrm{c}_4 \lambda_{\mathrm{lb}} \mathrm{Re}_{\mathrm{lb}}^{\mathrm{c}_5} \mathrm{Pr}_{\mathrm{lb}}^{\mathrm{c}_6}} \quad (\mathrm{m^2 \cdot s \cdot kW^{-1}}) \quad (1.24)$$

$$\frac{1}{h_{\mathrm{m,gb-lb}}} = \frac{1}{h_{\mathrm{m,gb-gl}}} + \frac{1}{h_{\mathrm{m,gl-lb}}} = \frac{d_{\mathrm{h,gb}}}{\mathrm{c}_1 \rho_{\mathrm{gb}} D_{\mathrm{gb}} \mathrm{Re}_{\mathrm{gb}}^{\mathrm{c}_2} \mathrm{Sc}_{\mathrm{gb}}^{\mathrm{c}_3}} + \frac{\delta_{\mathrm{l}}}{\mathrm{c}_4 \rho_{\mathrm{lb}} D_{\mathrm{lb}} \mathrm{Re}_{\mathrm{lb}}^{\mathrm{c}_5} \mathrm{Sc}_{\mathrm{lb}}^{\mathrm{c}_6}} \quad (\mathrm{m^2 \cdot s \cdot kg^{-1}}) \quad (1.25)$$

where c_1 to c_6 are constants and are estimated by fitting the experimental results with the above nonlinear equations of the heat and mass transfer coefficients.

1.6 Air pressure drop

The pressure drop is a necessary parameter in optimization studies of air conditioning systems because it contributes to the power consumption of the system. To determine the pressure loss of the air passing through the structured packed bed, the relationship of the friction factor to the pressure drop is used and is defined as

$$f = -\frac{(\Delta P_{\mathrm{gb}}/L)d_{\mathrm{h}}}{\rho_{\mathrm{gb}}u_{\mathrm{gb,e}}^2} \tag{1.26}$$

where ΔP_{gb} is the pressure drop of the gas bulk, which is usually presented as a pressure drop per length of the contactor ($\Delta P_{\mathrm{gb}}/L$) for easy comparison with other types of contactors. $u_{\mathrm{gb,e}}$ is the effective gas bulk velocity, which is determined from the mass balance of the gas bulk entering and exiting the packed bed,

$$\rho_{\mathrm{gb}}u_{\mathrm{gb,e}}\left(A_{\mathrm{ac,c,15}} + A_{\mathrm{ac,c,45}}\right) = \rho_{\mathrm{gb}}u_{\mathrm{gb,e,15}}A_{\mathrm{ac,c,15}} + \rho_{\mathrm{gb}}u_{\mathrm{gb,e,45}}A_{\mathrm{ac,c,45}} \quad (\mathrm{kg\cdot s^{-1}}) \tag{1.27}$$

where $A_{\mathrm{ac,c,15}}$ and $A_{\mathrm{ac,c,45}}$ are the cross-sectional areas of the air channel for the sheets at 15° and 45° angles (Fig. 1.1), respectively. $u_{\mathrm{gb,e,15}}$ and $u_{\mathrm{gb,e,45}}$ are the effective gas bulk velocities flowing through the 15° and 45° angle sheets, which is estimated as follows:

$$u_{\mathrm{gb,e,\theta}} = \frac{u_{\mathrm{gb}}}{\varepsilon \cos\theta} \quad (\mathrm{m\cdot s^{-1}}) \tag{1.28}$$

where ε is the surface roughness of the packed bed and θ (°) is the inclination angle of the sheets.

To estimate the friction factor, an empirical correlation is developed using the experimental data of the pressure drop.

1.7 Numerical analysis

In order for the mathematical model to be suitable for numerical computation, the model specifically the governing equations need to be discretized. The derivatives are approximated by finite difference method, specifically by forward (two-point) difference method and since the system is modeled in a steady-state behavior, the packed bed is partitioned only in the domain of space. Fig. 1.6 illustrates the differential control element and stencil for the conservation equations of the adiabatic packed bed. The length (x-direction) and the height (y-direction) are divided into uniformly spaced grids represented by i_0, ⋯, i_{n} and j_0, ⋯, j_{n}, respectively. With these, the spatial derivatives from the governing equations are transformed into finite differences and a system of algebraic equations or discrete equations are derived which are implemented in a computer using a programming language.

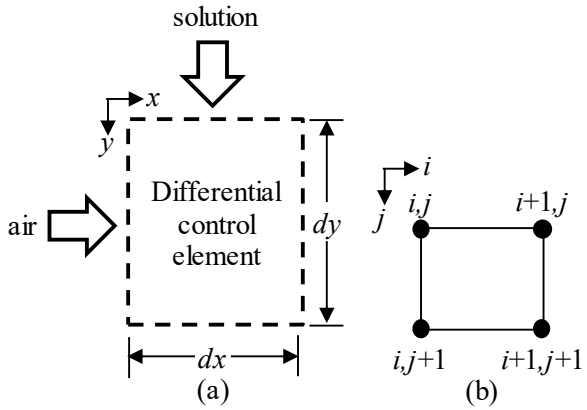

Fig. 1.6 Illustration of the: (a) differential control element and (b) stencil for the conservation equations of the adiabatic packed bed.

2. Experiment and validation of the packed bed gas-liquid contactor

2.1 Experimental apparatus

A schematic diagram of the packed bed liquid desiccant air conditioning system is shown in Fig. 2.1. The packed bed liquid desiccant system is divided into three sections: the test section, the solution condition control section, and the air condition control section.

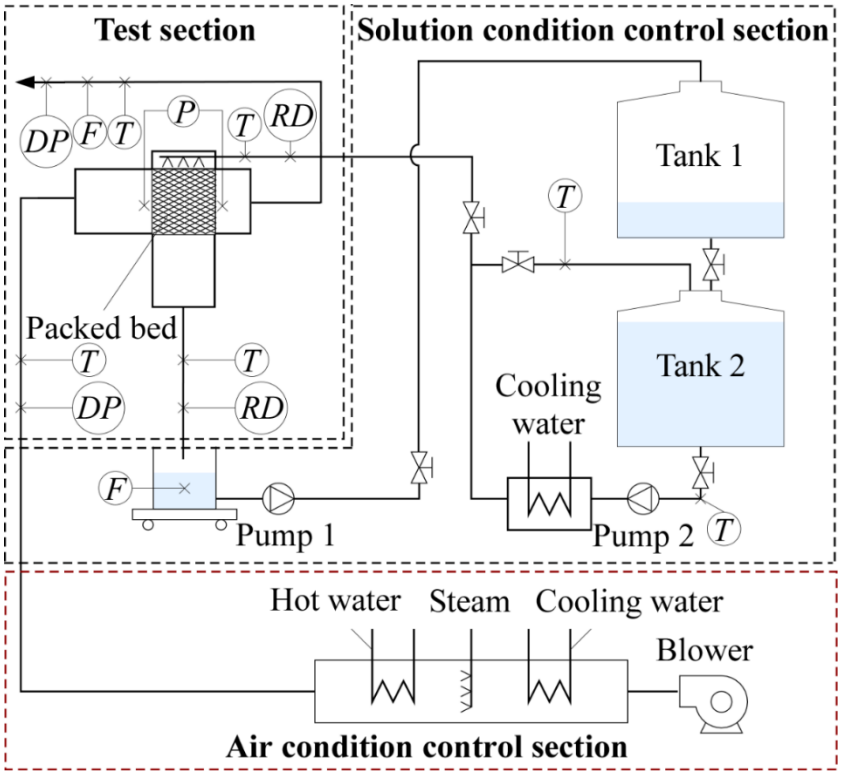

Fig. 2.1 Schematic diagram of the packed bed liquid desiccant air conditioning system.

Fig. 2.2 presents a photo of the test section highlighting the main component of the system, which is the structured packed bed contactor. The air and the solution flow through the packed bed contactor in a crossflow configuration. This type of flow configuration between the air and solution not only benefits from low air pumping head but also from low solution particle carryover compared with counterflow configuration.

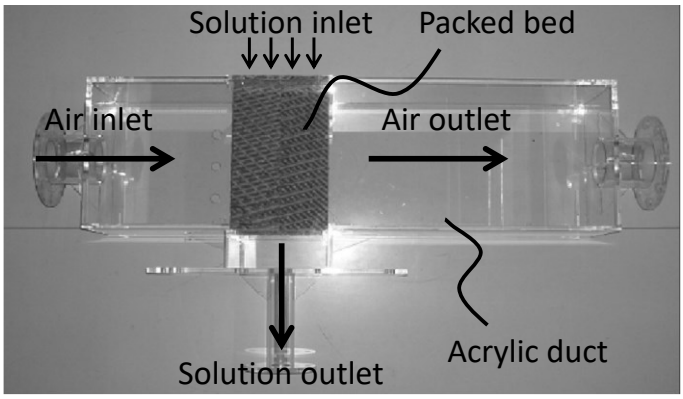

Fig. 2.2 Photo of the test section.

Structured packed bed contactors are preferable compared with random packed bed gas-liquid contactors due to their large surface area per unit volume, lower air pressure drop, and organized geometrical configuration. Fig. 2.3 illustrates the construction of the structured packed bed contactor. It is formed by packing together a special kind of corrugated cellulose paper capable of undergoing repeated wetting and drying cycles without performance degradation. The packed bed has a 460 $m^2 \cdot m^{-3}$ surface contact area (C_{sa}) and a 45˚ by 15˚ flute angle configuration.

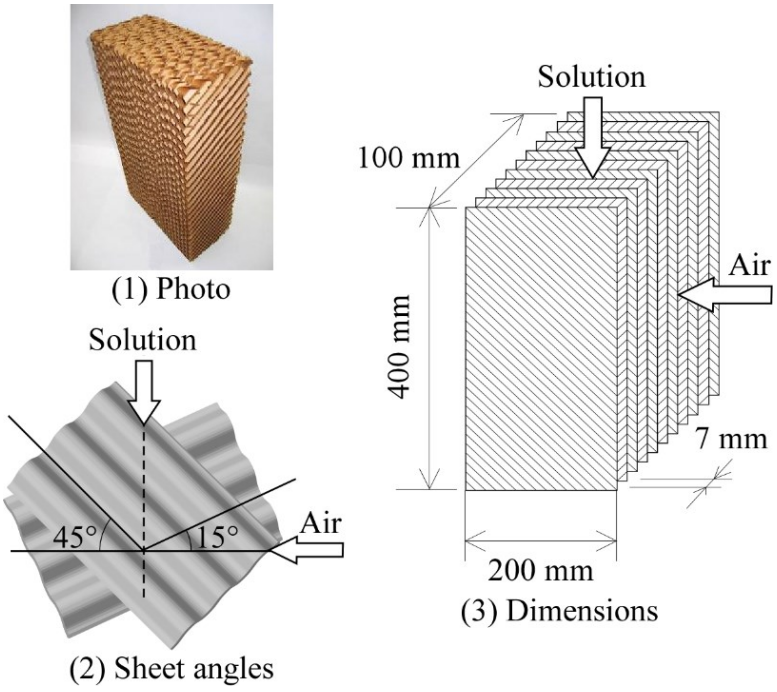

Fig. 2.3 Construction of the structured packed bed gas-liquid contactor.

The liquid desiccant used in this system is lithium chloride (LiCl). It is mixed with the right amount of water to get the required mass fraction of LiCl in the liquid desiccant solution.

Fig. 2.4 shows a photo of the LiCl solution distributor. The solution is distributed by equally spaced holes located at the bottom of the box. From the top of the gas-liquid contactor, the solution flows through the packed bed by gravity.

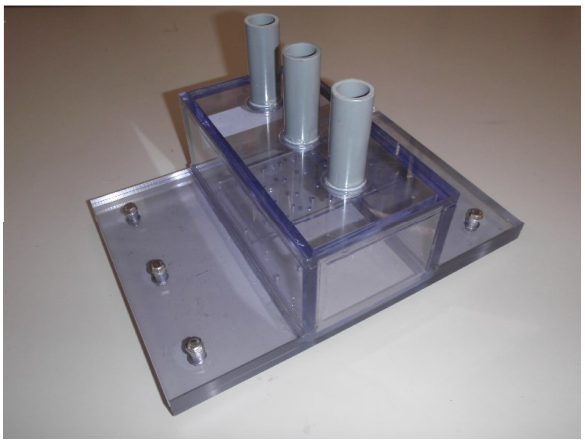

Fig. 2.4 Photo of the LiCl solution distributor.

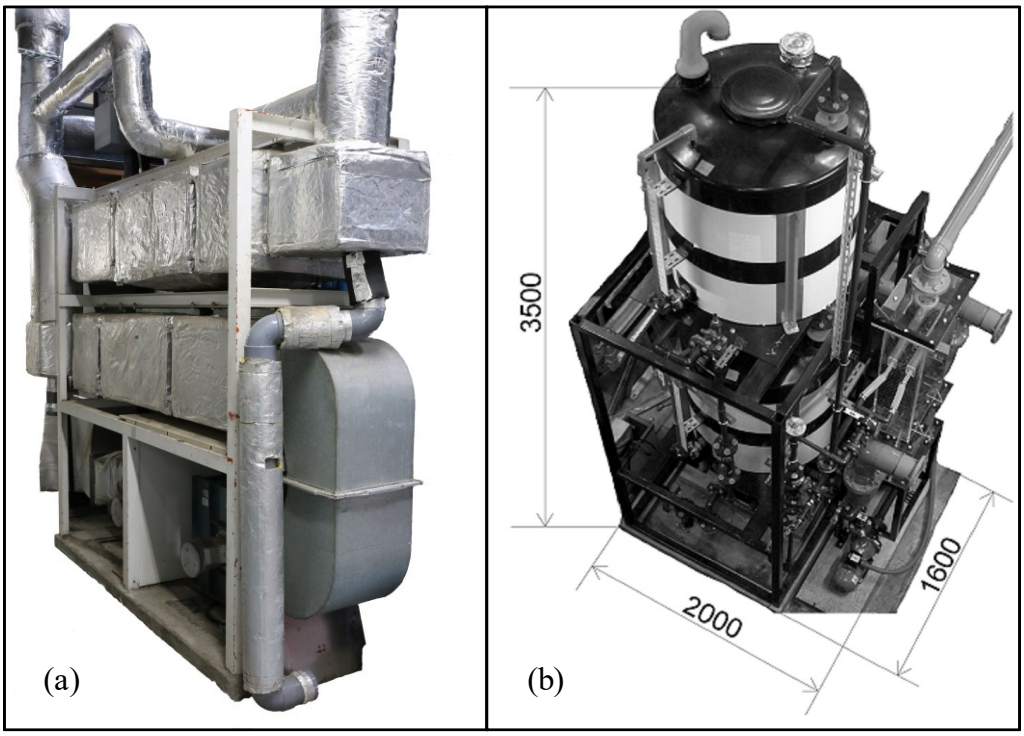

Fig. 2.5 Photo of the (a) air and (b) solution condition control sections.

A photo of the air condition control section is shown in Fig. 2.5(a). The control section is composed of a blower, two heat exchangers (for heating and cooling), and a Fig. 2.1 state into the test section.

Fig. 2.5(b) displays a photo of the solution condition control section. It consists two solution tanks (for concentrated and diluted LiCl solution), two pumps, and a heat exchanger. This control section regulates and supplies the LiCl solution at the specified condition.

Batch type experiments were carried out one after the other; that is regeneration after the dehumidification process. The dehumidification process starts with Tank 2 filled with approximately 500 li of concentrated LiCl solution and the control valve between Tank 1 and Tank 2 closed. For the regeneration experiments, the flow control valve between the two tanks is opened and the cooling water is replaced by heating water.

Table 1 lists the specifications of the measuring instruments used in the experiments. The physical properties listed in the table, which are indicated in Fig. 2.1 as measurement points represent the flow rate, temperature, dewpoint temperature, relative density, and air pressure, respectively. The solution flow rate was evaluated by measuring the rate of change of the solution weight at the dehumidifier outlet.

Table 1 Specifications of the measuring instruments.

Property	Measuring instrument	Accuracy
F (air)	Annubar flow meter	
T (air)	T type thermocouple,	±0.5°C
T (sol)	PT100 resistance temperature detectors	±0.15°C
DP	Cooled mirror dewpoint hygrometer	±0.2°C
RD	Specific gravity hydrometer	±0.001 $[kg \cdot m^{-3}]_{liq} \cdot [kg^{-1} \cdot m^3]_{H20}$
P	Differential pressure gauge	±1.5%

2.2 Experimental results

Table 2 and Table 3 summarize the experimental data from the dehumidification and regeneration experiments, respectively. In both processes, the standard ambient air condition during summer in Tokyo was used as the reference condition for the inlet air. Two sets of experiments were carried out to investigate the effect of the air velocity and the solution flow rate on the performance of the packed bed for both dehumidification and regeneration processes.

Table 2 Dehumidification experimental data.

u_{gb}	T_{ig}	T_{og}	x_{ig}	x_{og}	G_{il}	T_{il}	T_{ol}	X_{il}	X_{ol}	$h_{h,gb\text{-}lb}$	$h_{m,gb\text{-}lb}$
G_{il} = 5.0 $kg \cdot m^{-2} \cdot s^{-1}$											
0.44	33.98	20.32	19.49	7.12	4.96	17.07	21.07	29.74	29.66	11.34	11.28
0.54	33.95	20.17	19.40	8.06	5.04	17.02	21.42	29.88	29.80	14.70	10.98
0.62	34.02	20.86	19.42	7.64	5.02	16.99	21.96	29.78	29.70	15.21	14.35
0.72	34.04	21.17	19.46	7.95	5.00	17.00	22.39	30.03	29.92	17.28	15.46
0.81	34.02	21.61	19.54	8.23	5.13	16.99	22.71	29.81	29.69	18.22	16.82
0.91	34.06	21.70	19.46	8.73	4.89	17.07	23.60	30.04	29.91	21.57	17.08
0.99	34.04	22.40	19.46	8.93	5.00	17.03	23.66	29.81	29.67	20.56	18.16

1.09	33.95	22.29	19.54	9.14	4.92	17.01	24.43	30.13	30.00	24.15	19.13
1.29	34.02	22.92	19.45	9.89	4.94	17.00	24.71	29.18	29.02	26.39	20.86
1.47	33.92	23.47	19.45	10.33	4.98	17.04	25.24	29.19	29.01	28.35	22.25
1.65	34.05	23.87	19.51	10.66	4.94	17.02	25.97	29.42	29.23	31.41	23.68
1.83	33.94	24.33	19.55	11.09	4.83	17.00	26.73	29.80	29.53	33.47	24.10
2.02	33.95	24.55	19.44	11.32	4.95	17.05	26.65	29.34	29.23	36.63	26.32
2.03	33.95	24.90	19.59	11.22	4.83	17.01	27.19	29.86	29.63	35.23	26.75
2.20	33.97	25.04	19.50	11.71	4.78	17.06	27.71	29.60	29.36	38.67	26.87
2.21	34.00	25.12	19.43	11.41	4.81	17.12	27.99	29.91	29.67	39.23	28.37
2.37	33.99	25.15	19.47	11.83	4.78	16.98	28.10	29.55	29.30	42.40	28.77
2.38	34.04	25.39	19.54	11.65	4.88	17.07	28.37	29.97	29.72	41.58	29.74
u_{gb} = 1.5 m·s^{-1}											
1.51	33.93	27.45	19.46	13.07	1.94	17.02	31.67	29.67	29.34	21.67	15.87
1.51	33.96	26.73	19.45	12.66	2.08	16.98	31.44	29.89	29.56	25.66	17.09
1.51	33.96	26.60	19.45	12.50	2.27	16.90	30.64	29.67	29.37	23.61	17.06
1.51	33.99	26.36	19.44	12.30	2.43	16.94	30.23	29.72	29.46	24.04	17.54
1.51	33.94	25.83	19.42	11.89	2.69	17.03	29.92	29.85	29.57	25.91	18.52
1.51	34.00	25.51	19.54	11.81	2.80	16.95	29.63	29.92	29.65	27.11	18.72
1.51	33.94	25.50	19.49	11.63	2.96	17.01	29.35	30.07	29.87	26.21	18.85
1.51	34.02	25.09	19.56	11.58	3.10	16.95	28.98	29.89	29.63	27.61	19.18
1.51	34.02	25.10	19.48	11.34	3.21	17.00	28.90	30.07	29.81	27.21	19.63
1.50	33.97	24.73	19.52	11.01	3.61	16.93	28.08	30.03	29.90	26.96	20.33
1.51	34.03	24.74	19.48	11.02	3.95	16.96	27.14	29.68	29.39	25.28	20.18
1.51	34.02	24.14	19.55	10.70	4.24	17.01	26.78	29.90	29.69	28.18	21.20
1.50	34.02	24.26	19.50	10.65	4.55	16.97	26.41	29.82	29.51	25.87	20.80
1.50	34.05	23.25	19.47	9.96	5.59	17.00	25.18	30.11	29.94	29.46	22.90
1.50	34.00	23.30	19.55	9.70	6.09	17.01	24.77	30.15	30.06	28.09	23.60
1.50	34.00	23.05	19.40	9.61	6.66	17.02	24.33	30.13	29.94	28.50	23.85
1.51	33.98	22.95	19.60	9.35	7.46	17.03	23.69	30.19	30.09	28.29	24.75
1.51	34.01	22.41	19.49	9.49	7.72	17.04	23.48	29.77	29.64	30.83	24.65
1.50	34.05	22.40	19.50	9.34	8.35	17.05	23.13	29.90	29.82	29.98	24.69
1.50	34.05	22.44	19.49	9.19	9.40	17.07	22.59	29.96	29.83	28.78	24.95

Table 3 Regeneration experimental data.

u_{gb}	T_{ig}	T_{og}	x_{ig}	x_{og}	G_{il}	T_{il}	T_{ol}	X_{il}	X_{ol}	$h_{h,gb-lb}$	$h_{m,gb-lb}$
G_{il} = 5.0 kg·m^{-2}·s^{-1}											
0.41	33.99	47.55	19.51	30.18	5.06	49.99	47.56	30.05	30.11	12.84	6.99
0.50	34.00	47.46	19.52	29.61	5.07	50.03	47.08	30.05	30.03	15.76	7.92
0.55	34.05	47.39	19.50	29.33	5.00	50.02	46.78	30.01	30.08	17.73	8.56
0.63	33.92	47.29	19.34	28.56	5.00	50.04	46.67	30.08	30.15	20.32	8.94
0.72	34.07	46.98	19.43	28.13	5.05	50.08	46.33	30.07	30.15	22.00	9.68
0.78	33.91	46.95	19.58	27.50	5.03	49.96	45.92	30.05	30.14	24.31	9.36
0.87	33.98	46.52	19.51	27.14	4.96	49.94	45.62	29.98	29.94	25.52	10.11
0.99	34.05	45.97	19.46	26.45	4.98	50.09	45.11	30.09	30.19	24.86	10.15
1.11	34.04	45.51	19.60	25.90	5.03	50.10	44.66	30.08	30.17	25.41	10.20
1.15	34.02	46.06	19.54	26.18	4.96	50.06	44.61	29.95	29.89	31.92	11.56
1.28	34.01	45.73	19.42	25.98	5.03	50.06	44.49	29.95	29.86	34.12	13.02
1.31	33.93	45.65	19.59	25.28	5.05	50.04	44.26	30.14	30.23	33.13	11.24
1.36	34.06	45.50	19.62	25.51	5.00	50.05	44.06	29.92	30.02	34.01	11.99

1.51	34.06	45.32	19.44	24.87	5.10	50.05	43.89	29.93	30.04	36.87	11.97
1.75	34.04	45.12	19.49	24.63	5.03	50.06	43.54	29.91	30.03	44.57	14.17
1.94	34.06	44.68	19.46	24.18	5.07	50.02	43.18	29.88	30.00	45.74	14.33
2.12	34.04	44.35	19.54	23.86	4.98	50.01	42.84	29.95	29.88	48.04	14.96
2.30	34.07	44.10	19.47	23.63	4.96	50.12	42.57	29.94	29.92	50.23	15.70
u_{gb} = 1.5 m·s^{-1}											
1.51	34.03	43.39	19.51	22.42	2.22	50.05	40.69	29.79	29.92	33.31	7.85
1.51	33.09	43.50	19.62	22.62	2.36	50.02	40.85	29.87	30.00	33.31	8.19
1.51	34.02	43.77	19.64	22.97	2.62	50.04	41.25	29.94	30.07	33.77	8.96
1.50	34.01	44.14	19.42	23.11	2.82	50.06	41.58	29.91	30.05	36.30	9.59
1.51	33.98	44.01	19.51	23.36	2.90	50.04	41.52	29.90	30.03	35.33	10.27
1.51	34.05	44.47	19.45	23.68	3.31	50.00	42.26	29.97	30.10	37.03	10.90
1.51	34.01	44.55	19.43	24.00	3.43	49.99	42.58	30.05	30.19	38.80	12.62
1.52	34.06	44.79	19.59	24.40	3.94	50.02	42.91	29.99	30.05	37.58	12.31
1.50	34.00	44.84	19.44	24.38	4.12	49.99	43.11	29.91	30.03	36.68	11.76
1.52	33.96	44.88	19.41	24.71	4.39	50.03	43.55	30.04	30.16	37.06	13.30
1.53	33.94	45.16	19.40	25.29	5.15	49.97	44.07	30.02	30.11	38.10	14.57
1.48	33.99	45.61	19.59	25.95	6.15	50.04	44.67	29.98	30.08	37.00	14.33
1.50	34.00	45.63	19.44	26.01	6.45	49.97	44.84	29.87	29.72	37.87	14.50
1.48	33.99	46.03	19.57	26.38	7.03	50.05	45.34	30.08	30.09	38.98	14.99
1.48	34.08	45.84	19.62	26.35	7.11	49.92	45.29	29.95	29.97	37.81	14.91
1.50	33.98	45.95	19.55	26.50	7.54	50.03	45.47	29.88	30.00	38.19	14.85
1.52	33.99	46.04	19.47	27.00	7.66	49.94	45.52	30.11	30.21	41.05	18.02
1.51	33.98	46.14	19.57	27.02	8.60	50.01	45.94	29.90	29.99	39.11	16.21
1.54	34.00	46.05	19.42	27.34	8.80	50.04	46.11	30.05	30.14	39.12	18.65
1.51	34.07	46.50	19.46	28.11	9.96	50.11	46.69	29.87	29.78	40.71	19.13

2.3 Effect of air flow rate on the overall heat and mass transfer coefficients

As depicted in Fig. 2.6, higher air flow rates result in higher heat and mass transfer coefficients. This is because higher air flow rates produce higher air Reynolds number, which gives higher heat and mass transfer coefficients. It can also be observed that the increase in the heat transfer coefficient is considerably high, especially for the regeneration results, compared to the mass transfer coefficient. The heat transfer coefficients in the regeneration side are higher compared to those of the dehumidification side due to the higher dry bulb temperature of the air in the regeneration side. On the other hand, the values for the dehumidification mass transfer coefficients are twice in magnitude compared to the regeneration mass transfer coefficients. This is because the mass diffusivity of the water species in the air is more than four orders in magnitude than the water species in the LiCl solution, and since the vapor pressure of the air in the dehumidification side is higher than the vapor pressure of the solution, the result is high mass transfer coefficients in the dehumidification side.

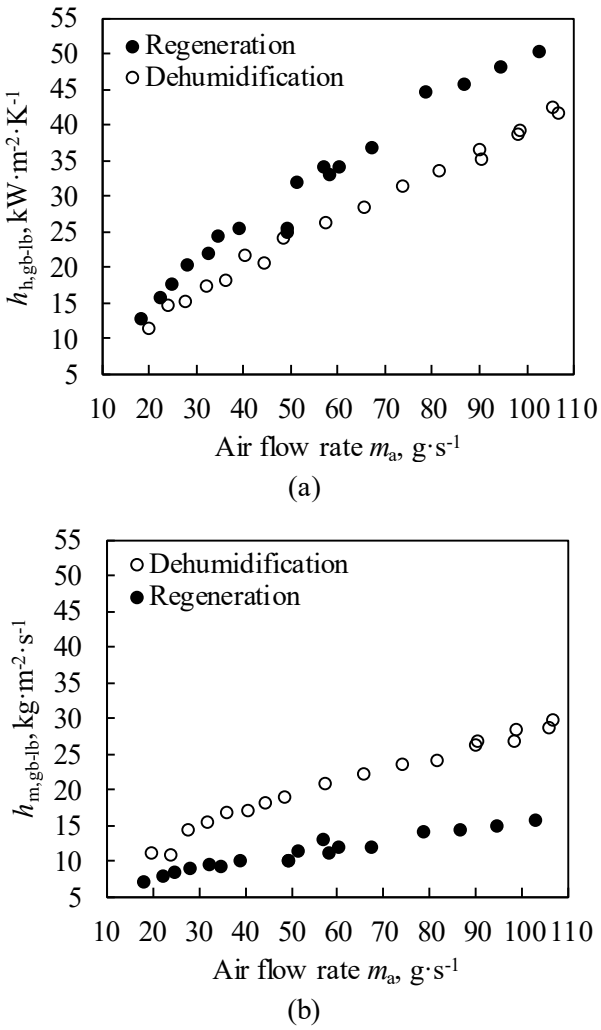

Fig. 2.6 Effect of air velocity on the overall (a) heat and (b) mass transfer coefficients.

2.4 Effect of air flow rate on the outlet air humidity ratio and temperature

Fig. 2.7(a) and (b) show the effect of the air flow rate on the process outlet air humidity ratio and temperature. Fundamentally, the heat and mass transfer coefficients increase as the air mass flow rate increases. However, the contact time between the air and the solution is shorter at higher air velocities. The effect of decreased contact time is more dominant than the increased heat and mass transfer coefficients, thus, both the outlet humidity ratio and temperature increase as the air flow rate increases. This implies that a proper selection of the air flow rate should be made based on the requirement of the actual system while considering also other factors such as air pressure drop.

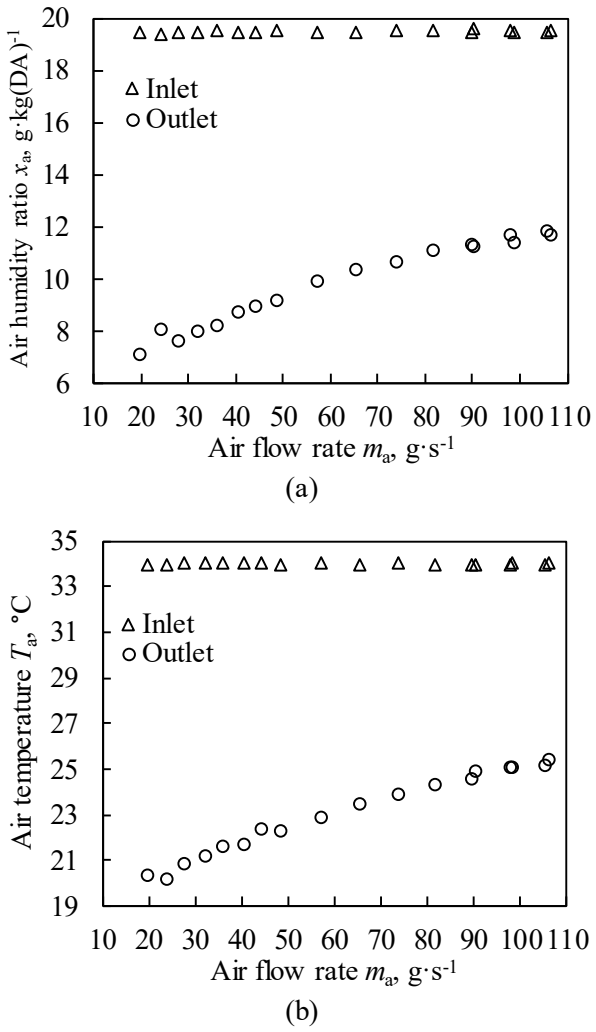

Fig. 2.7 Effect of the air velocity on the outlet air (a) humidity ratio and (b) temperature of the dehumidification process.

Fig. 2.8 presents the results for the regeneration side. The outlet air humidity ratio and temperature decrease as the air flow rate increases. The longer contact time between the air and the solution resulted in higher heat and mass transfer between the air and the solution. Although the heat and mass transfer coefficients are higher at higher air flow rates, the heat and mass transfer between the air and the solution were negatively affected by the shorter contact time at higher air velocities.

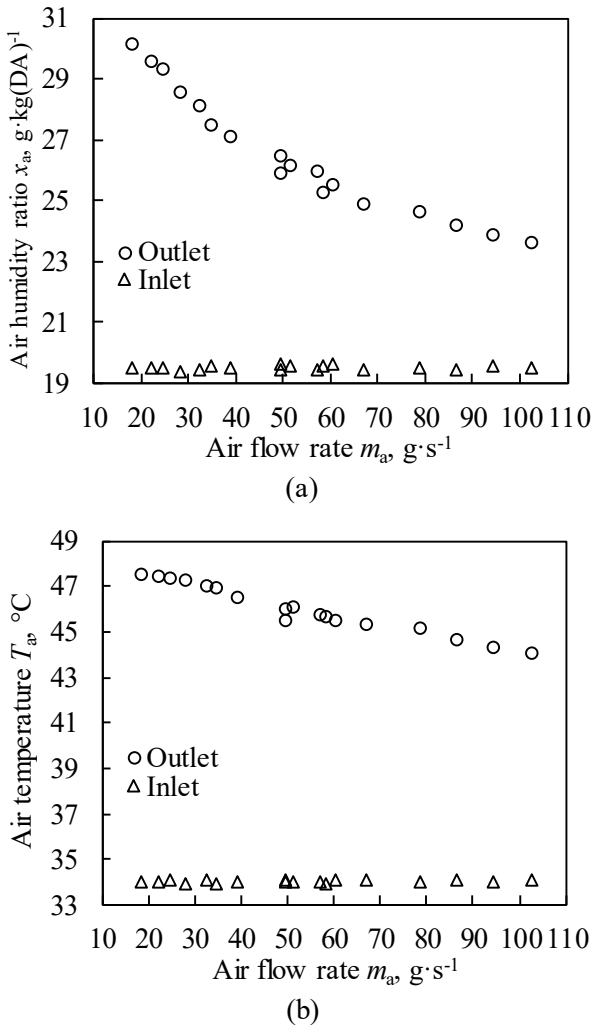

Fig. 2.8 Effect of the air velocity on the outlet air (a) humidity ratio and (b) temperature of the regeneration process.

2.5 Effect of solution flow rate on the overall heat and mass transfer coefficients

Fig. 2.9 shows the effect of the solution flow rate on the overall heat and mass transfer coefficients. The heat and mass transfer coefficients slightly increase as the solution flow rate increases with the slope of the mass transfer coefficient slightly steeper than the heat transfer coefficient. However, compared to the effect of the air flow rate, the effect of the solution flow rate is less significant, especially for the heat transfer coefficient. It can also be depicted from the graphs that the values for the heat transfer coefficient are higher compared to those of the mass transfer coefficient especially on the regeneration side, which is more than twice in magnitude.

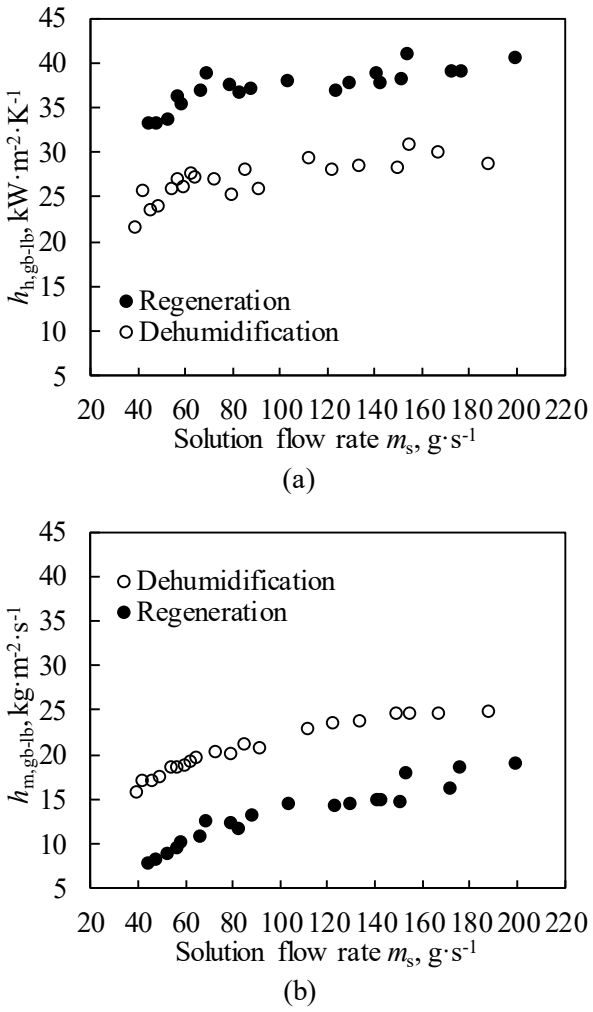

Fig. 2.9 Effect of solution flow rate on the overall (a) heat and (b) mass transfer coefficients.

2.6 Effect of solution flow rate on the outlet air humidity ratio and temperature

Fig. 2.10(a) and (b) depict the effect of the solution flow rate on the process air humidity ratio and temperature, respectively. Both properties benefit from larger dehumidification capacities at higher solution flow rates, and as a result, both decrease as the solution flow rate increases. The downside is that higher solution flow rates produce thicker films and results in larger air pressure drops. Aside from larger air pressure drops, higher solution flow rates also require larger pumping power, becoming both a disadvantage in terms of air fan and solution pumping power consumption. Hence, proper consideration of the power consumption and solution flow rate should be made based on the system application.

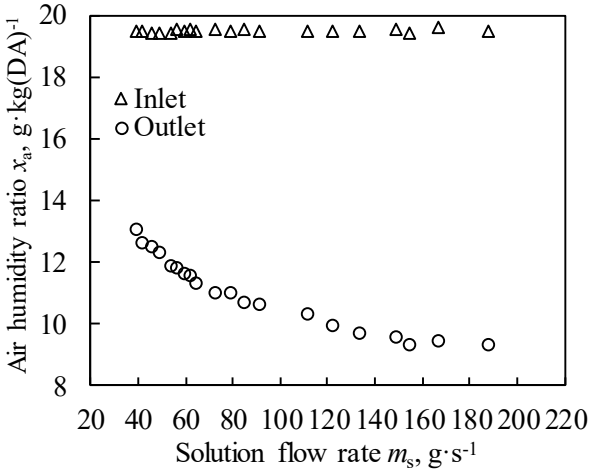

(a)

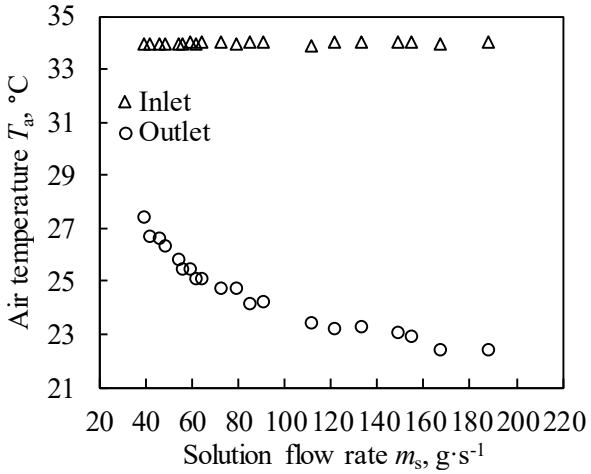

(b)

Fig. 2.10 Effect of the solution flow rate on the outlet air (a) humidity ratio and (b) temperature of the dehumidification process.

Fig. 2.11 depicts the effect of the solution flow rate on the outlet air humidity ratio and temperature for the regeneration side. The trend is opposite to that of the dehumidification process similar to the contradicting trend between the dehumidification and regeneration results from the air flow rate experiments. However, the effect on the performance of the system is the same, that is, the dehumidification and regeneration performance increase as the solution flow rate increases.

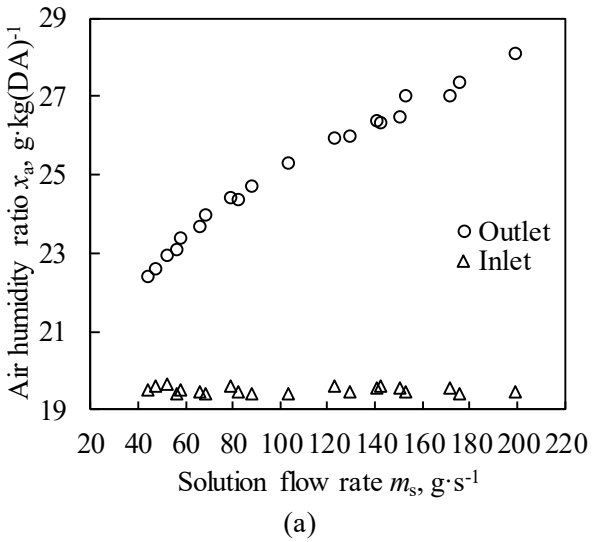

(a)

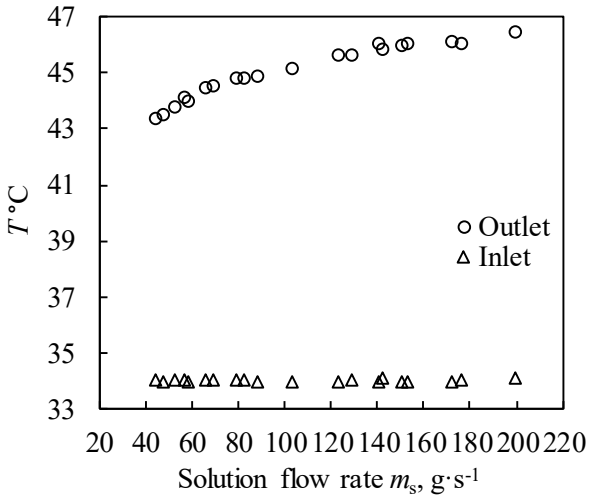

(b)

Fig. 2.11 Effect of the solution flow rate on the outlet air (a) humidity ratio and (b) temperature of the regeneration process.

3. Source code of the 3-fluid gas-liquid contactor

```
#include "stdafx.h"
#include "Property_air_ver3.h"
#include "property_water_ver2.1.1.h"
#include "Property_IonicLiquid_ver2.h"
#include "CNewtonRaphsonMethodPlus.h"

using namespace std;

int main() {

	//Initialize timer
	clock_t start_time, end_time;
	start_time = clock();

	//Declare data containers
	int i, j, k, mesh_x, mesh_y, mesh_z, n, pass;
	double L, H, W, V;
	const int x = 50;
	const int y = 30;
	const int z = 200;

	//Make csv file
	ofstream Results("Results.csv");
	Results << "Rea" << "," << "Res" << "," << "ma" << "," << "ms" << "," << "mcw" << "," << "deltaP" << "," << "xao" << "," << "Tao" << "," << "WR" << "," << "V" << "," << "L" << "," << "H" << "," << "W" "," << "mesh_x" << "," << "mesh_y" << "," << "mesh_z\n";

	//Contactor dimensions
	const double Lo = 0.2; //Original length [m]
	const double Ho = 0.4; //Original height [m]
	const double Wo = 0.1; //Original width [m]
	double Vo = Lo * Ho * Wo; //Original volume [m^3]
	const double D_t_o = 0.007381; //Tube outer diameter [m]
	const double D_t_i = 0.005381; //Tube inner diameter [m]
	const double A_fin = Lo * Ho / 170 - (M_PI * pow(D_t_o, 2) / 4); //Area of one side of the fin of a control volume [m^2]
	const double t_fin = 0.0001; //Fin thickness [m]
	const double P_f = 0.00442 - t_fin; //Distance between adjacent fins [m]
	const double P_t_v = 0.02; //Vertical tube pitch [m]

	const double A_t_ow = M_PI * D_t_o * P_f / 2; //Half of the surface area of the outer wall for one control volume [m^2]
```

```
        const double A_t_iw = M_PI * D_t_i * (P_f + t_fin) / 2; //Surface area of the
inner wall for one control volume [m^2]
        const double A_tot = A_fin + A_t_ow; //Total fin and tube area, one side of CV

        //Mesh and differential element
        const int mesh_x_o = 10; //Original number of mesh in the x-direction, 10
columns of tubes
        const int mesh_y_o = 17; //Original number of mesh in the y-direction, 17 rows
of tubes
        const int mesh_z_o = 23; //Original number of mesh in the z-direction, 23 fins
        const double dx = Lo / mesh_x_o; //Differential length [m]
        const double dy = Ho / mesh_y_o; //Differential height [m]

        const double dz = Wo / mesh_z_o; //Differential width[m]
        const double D_f = pow(4 * dx * dy / M_PI, 0.5); //Parameter for the fin
efficiency [m^2]

        //Experimental data
        //Inlet air
        double T_ig_exp = 34.0; //Temperature [deg.C]
        double x_ig_exp = 0.0195; //Humidity ratio [kg/kg(DA)]
        double u_ig_exp = 1.5;          //Velocity [m/s]
        double T_dp_ig_exp = 24.35; //Dewpoint temperature [deg.C]

        //Outlet air
        double T_og_exp = 24.1959053551196; //Temperature [deg.C]
        double x_og_exp = 0.01259; //Humidity ratio [kg/kg(DA)]
        double T_dp_og_exp = 20.9; //Dewpoint temperature [deg.C]
        double deltaP_og_exp = 23.15; //Pressure drop

        //Inlet solution
        double G_il_exp = 3.0; //Mass flux [kg/m^2/s]
        double T_il_exp = 17.5; //Temperature [deg.C]
        double X_il_exp = 0.75; //IL mass fraction  [kg/kg]
        double x_il_exp = IL_hr_tX(T_il_exp, X_il_exp * 100); //Equilibrium humidity
ratio [kg/kg]

        //Outlet solution
        double T_ol_exp = 24.3513089133334; //Temperature [deg.C]20.58,15.5
        double X_ol_exp = 0.713988625645277; //IL mass fraction [kg/kg]

        //Inlet cooling water
        double T_icw_exp = 17.0; //Temperature [deg.C]
        double m_icw_total_exp = 6.0 / 60; //Total flow rate [kg/s]
        double m_icw_mesh_exp = m_icw_total_exp / mesh_x_o * 2; //Mass flow rate
per pass [kg/s]
```

```
        //Outlet cooling water
        double T_ocw_exp = 20.5; // Temperature [deg.C], average value of 5 passes

        //Calculated properties from the experimental data
        //Inlet air
        double rho_ig_exp = air_rho_tx(T_ig_exp, x_ig_exp); //Density [kg(DA)/m^3]
        double H_ig_exp = air_h_tx(T_ig_exp, x_ig_exp) / 1000.0; //Enthalpy
[kJ/kg(DA)]
        double lambda_ig_exp = air_lambda_tx(T_ig_exp, x_ig_exp) / 1000; //Thermal
conductivity [kW/m/K]
        double c_p_ig_exp = air_cp_tx(T_ig_exp, x_ig_exp); //Specific heat [J/kg/K]
        double TD_ig_exp = air_alpha_tx(T_ig_exp, x_ig_exp); //Thermal diffusivity
[m^2/s]
        double D_ig_exp = air_D_t(T_ig_exp); //Mass diffusivity [m^2/s]
        double myu_ig_exp = air_myu_tx(T_ig_exp, x_ig_exp); //Dynamic viscosity
[Pa-s]
        double Pr_ig_exp = air_Pr_t(T_ig_exp, x_ig_exp); //Prandtl number

        //Outlet air
        double H_og_exp = air_h_tx(T_og_exp, x_og_exp) / 1000.0; //Enthalpy
[kJ/kg(DA)]

        //Inlet solution
        double m_il_total_exp = G_il_exp * Lo * Wo; //Total mass flow rate [kg/s]
        double m_il_mesh_exp = m_il_total_exp / mesh_x_o / mesh_z_o / 2; //Mass
flow rate per mesh [kg/s]
        double Gamma_il_exp = m_il_mesh_exp / dx; //Flowrate per unit length of the
contactor [kg/m/s]
        const double g = 9.80665;// Standard gravitational acceleration [m/s^2]
        double rho_il_exp = IL_rho_tX(T_il_exp, X_il_exp * 100); //Density [kg/m^3]
        double H_il_exp = IL_h_tw(T_il_exp, X_il_exp * 100); //Enthalpy [kJ/kg]
        double myu_il_exp = IL_myu_tX(T_il_exp, X_il_exp * 100); //Dynamic
viscosity [Pa-s]
        double lambda_il_exp = IL_lambda_tX(T_il_exp, X_il_exp * 100) / 1000;
//Thermal conductivity [kW/m/K]
        double sigma_il_exp = IL_sigma_tX(T_il_exp, X_il_exp * 100); //Surface
tension of the solution [N/m]
        double delta_il_exp = pow((3 * Gamma_il_exp * myu_il_exp / pow(rho_il_exp,
2) / g), 0.333333333); //Film thickness [m]
        double u_l_max_exp = rho_il_exp * g * pow(delta_il_exp, 2) / 2 / myu_il_exp;
//Maximum (gas-liquid interface) velocity [m/s]
        double u_l_ave_exp = 2 * u_l_max_exp / 3; //Average velocity [m/s]
        double We_il_exp = sigma_il_exp / rho_il_exp / pow(u_l_ave_exp, 2) /
delta_il_exp; //Weber number
        double Re_il_exp = 4 * Gamma_il_exp / myu_il_exp; //Reynolds number
```

```
        double Pr_il_exp = IL_nyu_tX(T_il_exp, X_il_exp * 100) /
IL_alpha_tX(T_il_exp, X_il_exp * 100); //Prandtl number
        double D_il_exp = IL_D_X(X_il_exp * 100); //Diffusivity [m^2/s]
        double c_p_il_exp = IL_Cp_tX(T_il_exp, X_il_exp * 100); //Specific heat
[kJ/kg/K]
        double TD_il_exp = IL_alpha_tX(T_il_exp, X_il_exp * 100); //Thermal
diffusivity [m^2/s]

        //Inlet and outlet air mass flow rate
        double m_ig_total_exp = rho_ig_exp * u_ig_exp * (Ho * Wo - (D_t_o * Wo *
17 + (t_fin + 2 * delta_il_exp) * Ho * 23)); //Total mass flow rate [kg(DA)/s]
        double m_ig_mesh_exp = m_ig_total_exp / mesh_y_o / mesh_z_o; //Mass flow
rate per mesh [kg(DA)/s]
        double m_og_mesh_exp = m_ig_mesh_exp; //Mass flow rate [kg(DA)/s]

        //Outlet solution
        double m_ol_exp = m_il_mesh_exp * X_il_exp / X_ol_exp;; //Mass flow rate
[kg/m^2/s]
        double G_ol_exp = m_ol_exp / Lo / Wo * mesh_x_o * mesh_z_o; //Mass flux
[kg/m^2/s]
        double H_ol_exp = IL_h_tw(T_ol_exp, X_ol_exp * 100); //Enthalpy
[kJ/kg(DA)]

        //Inlet cooling water
        double H_icw = sc_hl(101.325, T_icw_exp); //Enthalpy [kJ/kg]
        double u_cw = m_icw_mesh_exp / 1000 * 4 / M_PI / pow(D_t_i, 2); //Velocity
[m/s]

        //Outlet cooling water
        double m_ocw = m_icw_mesh_exp; //[kg/s]
        double H_ocw = sc_hl(101.325, T_ocw_exp); //Enthalpy [kJ/kg]
        double nyu_ocw = sc_nyul(101.325, T_ocw_exp); //Kinematic viscosity [m^2/s]
        double Pr_ocw = sc_Prl(101.325, T_ocw_exp); //Prandtl number
        double Re_ocw = u_cw * D_t_i / nyu_ocw; //Reynolds number
        double k_ocw = sc_laml(101.325, T_ocw_exp); //Thermal conductivity
[W/m/K]

        //Initialize partial wetting parameter
        //Asks if the flow is increasing or decreasing
        char type_of_flow;
        type_of_flow = 'D';
        //cout << "Enter the letter 'I' for increasing flow rate condition or the letter 'D'
for deacreasing flow rate condition: ";
        //cin >> type_of_flow;

        //Nusselt number of the air
```

```
        //double Nu_gb = 7.54; //For laminar flow in tubes with rectangular cross section (Kays and Crawford, 1993, page 125)

        //Thermal conductivity of the tube wall
        const double lambda_w = 0.236; //[kW/m/K]

        //Declare variables for calculation properties in a mesh
        //Air
        static double u_gb_dry_mesh[y + 2][x + 2][z + 2] = { 0.0 };
        static double u_gb_wet_mesh[y + 2][x + 2][z + 2] = { 0.0 };
        static double m_gb_mesh[y + 2][x + 2][z + 2] = { 0.0 };
        static double T_gb_mesh[y + 2][x + 2][z + 2] = { 0.0 };
        static double H_gb_mesh[y + 2][x + 2][z + 2] = { 0.0 };
        static double x_gb_mesh[y + 2][x + 2][z + 2] = { 0.0 };
        static double rho_gb_mesh[y + 2][x + 2][z + 2] = { 0.0 };
        static double lambda_gb_mesh[y + 2][x + 2][z + 2] = { 0.0 };
        static double c_p_gb_mesh[y + 2][x + 2][z + 2] = { 0.0 };
        static double TD_gb_mesh[y + 2][x + 2][z + 2] = { 0.0 };
        static double D_gb_mesh[y + 2][x + 2][z + 2] = { 0.0 };
        static double T_dp_gb_mesh[y + 2][x + 2][z + 2] = { 0.0 };
        static double x_dp_gb_mesh[y + 2][x + 2][z + 2] = { 0.0 };
        static double Re_gb_dry_mesh[y + 2][x + 2][z + 2] = { 0.0 };
        static double Re_gb_wet_mesh[y + 2][x + 2][z + 2] = { 0.0 };
        static double Nu_gb_dry_mesh[y + 2][x + 2][z + 2] = { 0.0 };
        static double Nu_gb_wet_mesh[y + 2][x + 2][z + 2] = { 0.0 };
        static double deltaP_gb_mesh[y + 2][x + 2][z + 2] = { 0.0 };
        static double myu_gb_mesh[y + 2][x + 2][z + 2] = { 0.0 };
        static double f_gb_dry_mesh[y + 2][x + 2][z + 2] = { 0.0 };
        static double f_gb_wet_mesh[y + 2][x + 2][z + 2] = { 0.0 };
        static double Pr_gb_mesh[y + 2][x + 2][z + 2] = { 0.0 };

        //Solution
        static double m_lb_mesh[y + 2][x + 2][z + 2] = { 0.0 };
        static double T_lb_mesh[y + 2][x + 2][z + 2] = { 0.0 };
        static double x_lb_mesh[y + 2][x + 2][z + 2] = { 0.0 };
        static double X_lb_mesh[y + 2][x + 2][z + 2] = { 0.0 };
        static double H_lb_mesh[y + 2][x + 2][z + 2] = { 0.0 };
        static double Gamma_lb_mesh[y + 2][x + 2][z + 2] = { 0.0 };
        static double rho_lb_mesh[y + 2][x + 2][z + 2] = { 0.0 };
        static double myu_lb_mesh[y + 2][x + 2][z + 2] = { 0.0 };
        static double lambda_lb_mesh[y + 2][x + 2][z + 2] = { 0.0 };
        static double sigma_lb_mesh[y + 2][x + 2][z + 2] = { 0.0 };
        static double delta_lb_mesh[y + 2][x + 2][z + 2] = { 0.0 };
        static double u_l_max_mesh[y + 2][x + 2][z + 2] = { 0.0 };
        static double u_l_ave_mesh[y + 2][x + 2][z + 2] = { 0.0 };
        static double delta_lb_wr[y + 2][x + 2][z + 2] = { 0.0 };
```

```
static double u_l_max_wr[y + 2][x + 2][z + 2] = { 0.0 };
static double u_l_ave_wr[y + 2][x + 2][z + 2] = { 0.0 };
static double We_lb_mesh[y + 2][x + 2][z + 2] = { 0.0 };
static double Re_lb_mesh[y + 2][x + 2][z + 2] = { 0.0 };
static double Pr_lb_mesh[y + 2][x + 2][z + 2] = { 0.0 };
static double Ga_lb_b_mesh[y + 2][x + 2][z + 2] = { 0.0 };
static double Re_lb_b_mesh[y + 2][x + 2][z + 2] = { 0.0 };
static double D_lb_mesh[y + 2][x + 2][z + 2] = { 0.0 };
static double Nu_lb_mesh[y + 2][x + 2][z + 2] = { 0.0 };
static double c_p_lb_mesh[y + 2][x + 2][z + 2] = { 0.0 };
static double TD_lb_mesh[y + 2][x + 2][z + 2] = { 0.0 };

//Cooling water
static double m_cw_mesh[y + 2][x + 2][z + 2] = { 0.0 };
static double T_cw_mesh[y + 2][x + 2][z + 2] = { 0.0 };
static double H_cw_mesh[y + 2][x + 2][z + 2] = { 0.0 };
static double nyu_cw_mesh[y + 2][x + 2][z + 2] = { 0.0 };
static double Pr_cw_mesh[y + 2][x + 2][z + 2] = { 0.0 };
static double Re_cw_mesh[y + 2][x + 2][z + 2] = { 0.0 };
static double k_cw_mesh[y + 2][x + 2][z + 2] = { 0.0 };
static double Nu_cw_mesh[y + 2][x + 2][z + 2] = { 0.0 };
static double f_mesh[y + 2][x + 2][z + 2] = { 0.0 };

//Gas-Liquid interface
static double T_gl_mesh[y + 2][x + 2][z + 2] = { 0.0 };
static double x_gl_mesh[y + 2][x + 2][z + 2] = { 0.0 };
static double X_gl_mesh[y + 2][x + 2][z + 2] = { 0.0 };

//Tube inner and outer wall
static double T_iw_mesh[y + 2][x + 2][z + 2] = { 0.0 };
static double T_ow_mesh[y + 2][x + 2][z + 2] = { 0.0 };

//Hydraulic diameters and fin efficiencies
static double d_h_dry_mesh[y + 2][x + 2][z + 2] = { 0.0 };
static double d_h_wet_mesh[y + 2][x + 2][z + 2] = { 0.0 };
static double n_f_gb_mesh[y + 2][x + 2][z + 2] = { 0.0 };
static double n_f_lb_mesh[y + 2][x + 2][z + 2] = { 0.0 };

//Heat of condensation/vaporization, heat and mass transfer coefficients
static double h_v_mesh[y + 2][x + 2][z + 2] = { 0.0 };
static double h_h_gb_gl_mesh[y + 2][x + 2][z + 2] = { 0.0 };
static double h_h_gb_lb_mesh[y + 2][x + 2][z + 2] = { 0.0 };
static double h_h_gb_ls_mesh[y + 2][x + 2][z + 2] = { 0.0 };
static double h_h_gl_ls_mesh[y + 2][x + 2][z + 2] = { 0.0 };
static double h_h_gb_gs_mesh[y + 2][x + 2][z + 2] = { 0.0 };
static double h_h_w_mesh[y + 2][x + 2][z + 2] = { 0.0 };
```

```
static double h_h_cw_mesh[y + 2][x + 2][z + 2] = { 0.0 };
static double h_h_gb_cw_mesh[y + 2][x + 2][z + 2] = { 0.0 };
static double h_m_gb_gl_mesh[y + 2][x + 2][z + 2] = { 0.0 };
static double h_m_gl_lb_mesh[y + 2][x + 2][z + 2] = { 0.0 };
static double h_m_gb_lb_mesh[y + 2][x + 2][z + 2] = { 0.0 };

//Contact angles, transfer areas, wetting ratio
static double theta_a_mesh[y + 2][x + 2][z + 2] = { 0.0 };
static double theta_r_mesh[y + 2][x + 2][z + 2] = { 0.0 };
static double A_gl_mesh[y + 2][x + 2][z + 2] = { 0.0 };
static double A_ls_mesh[y + 2][x + 2][z + 2] = { 0.0 };
static double A_gs_mesh[y + 2][x + 2][z + 2] = { 0.0 };
static double wr_gl_mesh[y + 2][x + 2][z + 2] = { 0.0 };
static double wr_ls_mesh[y + 2][x + 2][z + 2] = { 0.0 };

//Heat and mass transfer
static double q_gb_gl_mesh[y + 2][x + 2][z + 2] = { 0.0 };
static double q_gb_gs_mesh[y + 2][x + 2][z + 2] = { 0.0 };
static double q_lb_ls_mesh[y + 2][x + 2][z + 2] = { 0.0 };
static double q_gb_lb_mesh[y + 2][x + 2][z + 2] = { 0.0 };
static double q_gl_ls_mesh[y + 2][x + 2][z + 2] = { 0.0 };
static double q_w_mesh[y + 2][x + 2][z + 2] = { 0.0 };
static double q_iw_cw_mesh[y + 2][x + 2][z + 2] = { 0.0 };
static double j_gb_lb_mesh[y + 2][x + 2][z + 2] = { 0.0 };
static double j_gb_gl_mesh[y + 2][x + 2][z + 2] = { 0.0 };
static double j_gl_lb_mesh[y + 2][x + 2][z + 2] = { 0.0 };
static double m_gb_dp_mesh[y + 2][x + 2][z + 2] = { 0.0 };


//Declare variables for outlet property calculation
//Outlet air
double m_og_pre;
double m_og_total_pre;
double H_og_pre;
double x_og_pre;
double T_og_pre;
double T_dp_og_pre;
double deltaP_og_pre;
double H_og_diff;
double x_og_diff;
double T_og_diff;
double T_dp_og_diff;
double deltaP_og_diff;

//Outlet solution
double m_ol_total_pre;
```

```
double H_ol_pre;
double X_ol_pre;
double m_ol_pre;
double G_ol_pre;
double T_ol_pre;
double x_ol_pre;
double T_dp_ol_pre;
double H_ol_diff;
double X_ol_diff;
double T_ol_diff;
double G_ol_diff;

//Outlet cooling water, initialize
double m_ocw_pre;
double m_ocw_total_pre;
double H_ocw_pre;
double T_ocw_ave_pre;
double m_icw_pre;
double m_icw_total_pre;
double H_icw_pre;
double T_icw_ave_pre;
double T_icw_diff;

//Others
double wr_gl_ave;
double Re_gb_ave;
double Re_lb_ave;

//For parametric study
for (pass = 3; pass < 11; pass +=1) { //L = 0.2, 5 passes
for (mesh_y = 5; mesh_y < 18; mesh_y += 1) { //H = 0.2, 8.5 meshes = 9
for (mesh_z = 23; mesh_z < 93; mesh_z += 3) { //W = 0.2, 46 meshes

//pass = 5;
//mesh_y = 17;
//mesh_z = 23;

//Calculate new dimensions
mesh_x = pass * 2;
L = mesh_x * dx;
H = mesh_y * dy;
W = mesh_z * dz;
V = L * H * W;

//Stream out dimensions
cout << "pass = " << pass << "\n";
```

```
        cout << "mesh_y = " << mesh_y << "\n";
        cout << "mesh_z = " << mesh_z << "\n";

        //Caculate air properties
        double m_ig_mesh_pre = m_ig_total_exp / mesh_y / mesh_z / 2; //Mass flow
rate per mesh [kg/s]

        //Calculate solution properties
        double G_il_pre = m_il_total_exp / L / W; //Mass flux [kg/m^2/s]
        double m_il_mesh_pre = m_il_total_exp / mesh_x / mesh_z / 2; //Mass flow rate
per mesh [kg/s]
        double Gamma_il_pre = m_il_mesh_pre / dx; //Flowrate per unit length of the
contactor [kg/m/s]
        double delta_il_pre = pow((3 * Gamma_il_pre * myu_il_exp / pow(rho_il_exp,
2) / g), 0.333333333); //Film thickness [m]
        double u_l_max_pre = rho_il_exp * g * pow(delta_il_pre, 2) / 2 / myu_il_exp;
//Maximum (gas-liquid interface) velocity [m/s]
        double u_l_ave_pre = 2 * u_l_max_pre / 3; //Average velocity [m/s]
        double We_il_pre = sigma_il_exp / rho_il_exp / pow(u_l_ave_pre, 2) /
delta_il_pre; //Weber number
        double Re_il_pre = 4 * Gamma_il_pre / myu_il_exp; //Reynolds number

        //Calculate cooling water properties
        double m_icw = m_icw_total_exp / pass;
        u_cw = m_icw / 1000 * 4 / M_PI / pow(D_t_i, 2);

        //Initial conditions
        //Air inlet
        for (i = 1; i < mesh_y + 1; i++) {
                for (k = 1; k < mesh_z + 1; k++) {
                        m_gb_mesh[i][1][k] = m_ig_mesh_pre;
                        T_gb_mesh[i][1][k] = T_ig_exp;
                        x_gb_mesh[i][1][k] = x_ig_exp;
                        rho_gb_mesh[i][1][k] = rho_ig_exp;
                        H_gb_mesh[i][1][k] = H_ig_exp;
                        lambda_gb_mesh[i][1][k] = lambda_ig_exp;
                        c_p_gb_mesh[i][1][k] = c_p_ig_exp;
                        TD_gb_mesh[i][1][k] = TD_ig_exp;
                        D_gb_mesh[i][1][k] = D_ig_exp;
                        T_dp_gb_mesh[i][1][k] = T_dp_ig_exp;
                        myu_gb_mesh[i][1][k] = myu_ig_exp;
                        Pr_gb_mesh[i][1][k] = Pr_ig_exp;
                }
        }

        //Solution intlet
```

```
for (n = 1; n < pass + 1; n++) {
	for (j = n * 2 - 1; j < n * 2 + 1; j++) {
		for (k = 1; k < mesh_z + 1; k++) {
			m_lb_mesh[1][j][k] = m_il_mesh_pre;
			Gamma_lb_mesh[1][j][k] = Gamma_il_pre;
			delta_lb_mesh[1][j][k] = delta_il_pre;
			u_l_max_mesh[1][j][k] = u_l_max_pre;
			u_l_ave_mesh[1][j][k] = u_l_ave_pre;
			We_lb_mesh[1][j][k] = We_il_pre;
			Re_lb_mesh[1][j][k] = Re_il_pre;
			X_lb_mesh[1][j][k] = X_il_exp;
			T_lb_mesh[1][j][k] = T_il_exp;
			T_gl_mesh[1][j][k] = T_il_exp;
			x_lb_mesh[1][j][k] = x_il_exp;
			rho_lb_mesh[1][j][k] = rho_il_exp;
			H_lb_mesh[1][j][k] = H_il_exp;
			myu_lb_mesh[1][j][k] = myu_il_exp;
			lambda_lb_mesh[1][j][k] = lambda_il_exp;
			sigma_lb_mesh[1][j][k] = sigma_il_exp;
			Pr_lb_mesh[1][j][k] = Pr_il_exp;
			D_lb_mesh[1][j][k] = D_il_exp;
			c_p_lb_mesh[1][j][k] = c_p_il_exp;
			TD_lb_mesh[1][j][k] = TD_il_exp;
		}
	}
}

//Cooling water outlet
for (n = 1; n < pass + 1; n++) {
	for (j = n * 2 - 1; j < n * 2; j++) {
		T_cw_mesh[1][j][1] = T_ocw_exp;
	}
}

//Initialize number of iterations
int num_of_iter = 1;

//Convergence to the experimental value of the inlet cooling water
CNewtonRaphsonMethodPlus T_icw_conv;
T_icw_conv.Initialize();

//Initial cooling water outlet
for (n = 1; n < pass + 1; n++) {
	for (j = n * 2 - 1; j < n * 2; j++) {
		T_icw_conv.SetValiable(n - 1, T_cw_mesh[1][j][1]);
	}
```

```
        }

        //Initialize Newton-Raphson parameters
        T_icw_conv.SetAcc(1.0);
        T_icw_conv.SetPrint(false, false);
        T_icw_conv.SetDelta(1.0 + 1e-1);
        T_icw_conv.SetError(0.2);

        for (T_icw_conv.MainLoopInit(); T_icw_conv.MainLoopCheck();
T_icw_conv.MainLoopReinit()) {
                for (T_icw_conv.SubLoopInit(); T_icw_conv.SubLoopCheck();
T_icw_conv.SubLoopReinit()) {

                        //Cooling water outlet
                        for (n = 1; n < pass + 1; n++) {
                                for (j = n * 2 - 1; j < n * 2; j++) {
                                        T_icw_conv.GetValiable(n - 1,
T_cw_mesh[1][j][1]);
                                }
                        }

                        for (n = 1; n < pass + 1; n++) {
                                for (j = n * 2 - 1; j < n * 2; j++) {
                                        m_cw_mesh[1][j][1] = m_icw;
                                        H_cw_mesh[1][j][1] = sc_hl(101.325,
T_cw_mesh[1][j][1]);
                                        nyu_cw_mesh[1][j][1] = sc_nyul(101.325,
T_cw_mesh[1][j][1]);
                                        Pr_cw_mesh[1][j][1] = sc_Prl(101.325,
T_cw_mesh[1][j][1]);
                                        Re_cw_mesh[1][j][1] = u_cw * D_t_i /
nyu_cw_mesh[1][j][1];
                                        k_cw_mesh[1][j][1] = sc_laml(101.325,
T_cw_mesh[1][j][1]);
                                }
                        }

                        //Control volume calculations
                        //Governing equations
                        for (n = 1; n < pass + 1; n++) {
                                for (i = 1; i < mesh_y + 1; i++) {
                                        for (j = n * 2 - 1; j < n * 2 + 1; j++) {
                                                if (j % 2 == 1) {
                                                        for (k = 1; k < mesh_z + 1; k++) {
```

```
                                                    //Wetting ratio, gas-liquid
area, and solid-liquid area
                                                    theta_a_mesh[i][j][k] =
0.00008 * pow(X_lb_mesh[i][j][k] * 100, 2) - 0.0149 * X_lb_mesh[i][j][k] * 100 +
1.94; //Advancing contact angle [deg.]
                                                    theta_r_mesh[i][j][k] =
0.00008 * pow(X_lb_mesh[i][j][k] * 100, 2) - 0.0150 * X_lb_mesh[i][j][k] * 100 +
1.48; //Receeding contact angle [deg.]

                                                    //Determine if flow is
increasing or decreasing flow rate
                                                    if (type_of_flow == 'I') {
                                                        wr_gl_mesh[i][j][k]
= 0.83 * pow(theta_a_mesh[i][j][k], -0.90) * pow((Re_lb_mesh[i][j][k] /
pow(We_lb_mesh[i][j][k], 3)), 0.07); //Partial wetting model
                                                    //Assign the value of
1 to the wetting ratio if it is greater than 1
                                                    if
(wr_gl_mesh[i][j][k] > 1) {

        wr_gl_mesh[i][j][k] = 1;
                                                    }
                                                }

                                                    else if (type_of_flow ==
'D') {

        Ga_lb_b_mesh[i][j][k] = rho_lb_mesh[i][j][k] * pow(sigma_lb_mesh[i][j][k], 3)
/ pow(myu_lb_mesh[i][j][k], 4) / g; //Galileo number at film breaking

        Re_lb_b_mesh[i][j][k] = 0.025 * pow(Ga_lb_b_mesh[i][j][k], 0.26) *
pow((log(theta_r_mesh[i][j][k]) + 3.45), 3); //Film Reynolds number at breaking

                                                    //Determine whether
Re_s is lower than Re_b, if so, compute the wetting ratio
                                                    if
(Re_lb_mesh[i][j][k] < Re_lb_b_mesh[i][j][k]) {

        wr_gl_mesh[i][j][k] = 0.83 * pow(theta_r_mesh[i][j][k], -0.90) *
pow((Re_lb_mesh[i][j][k] / pow(We_lb_mesh[i][j][k], 3)), 0.07); //Partial wetting
model
                                                    }

                                                    //Assign the value of
1 to the wetting ratio if Re_s is >= Re_b
```

```
                                                    else if
(Re_lb_mesh[i][j][k] >= Re_lb_b_mesh[i][j][k]) {

        wr_gl_mesh[i][j][k] = 1;
                                                    }
                                                }

                                                //Complete wetting
assumption
                                                //wr_gl_mesh[i][j][k] = 1.0;
//Complete wetting

                                                delta_lb_wr[i][j][k] =
pow((3 * Gamma_lb_mesh[i][j][k] * myu_lb_mesh[i][j][k] / pow(rho_lb_mesh[i][j][k],
2) / g / wr_gl_mesh[i][j][k]), 0.333333333); //Film thickness [m]
                                                u_l_max_wr[i][j][k] =
rho_lb_mesh[i][j][k] * g * pow(delta_lb_wr[i][j][k], 2) / 2 / myu_lb_mesh[i][j][k];
////Maximum (gas-liquid interface) velocity [m/s]
                                                u_l_ave_wr[i][j][k] = 2 *
u_l_max_wr[i][j][k] / 3; // Average solution velocity [m/s]

                                                //Effective air velocity and
effective hydraulic diameter
                                                u_gb_dry_mesh[i][j][k] =
m_gb_mesh[i][j][k] / rho_gb_mesh[i][j][k] / ((0.5 * P_f * dy) - (0.5 * P_f * D_t_o));
//Effective air velocity on dry area
                                                u_gb_wet_mesh[i][j][k] =
m_gb_mesh[i][j][k] / rho_gb_mesh[i][j][k] / ((0.5 * P_f * dy) - (0.5 * P_f * D_t_o) -
(delta_lb_wr[i][j][k] * dy)); //Effective air velocity on wet area
                                                d_h_dry_mesh[i][j][k] = 4 *
((0.5 * P_f * dy) - (0.5 * P_f * D_t_o)) / (dy + P_f); //Effective hydraulic diameter on
dry area
                                                d_h_wet_mesh[i][j][k] = 4 *
((0.5 * P_f * dy) - (0.5 * P_f * D_t_o) - (delta_lb_wr[i][j][k] * dy)) / (dy + P_f);
//Effective hydraulic diameter on wet area

                                                //Air Reynolds number
                                                Re_gb_dry_mesh[i][j][k] =
rho_gb_mesh[i][j][k] * u_gb_dry_mesh[i][j][k] * d_h_dry_mesh[i][j][k] /
myu_gb_mesh[i][j][k]; //On dry area
                                                Re_gb_wet_mesh[i][j][k] =
rho_gb_mesh[i][j][k] * u_gb_wet_mesh[i][j][k] * d_h_wet_mesh[i][j][k] /
myu_gb_mesh[i][j][k]; //On wet area

                                                //Air Nusselt number and
friction factor based on dry area, Fujii and Seshimo
```

```
                                                    if (Re_gb_dry_mesh[i][j][k]
<= 400) {

        Nu_gb_dry_mesh[i][j][k] = 2.1 * pow(Re_gb_dry_mesh[i][j][k] *
Pr_gb_mesh[i][j][k] * d_h_dry_mesh[i][j][k] / (2 * dx), 0.38); //Nusselt number for low
Reynolds number

        f_gb_dry_mesh[i][j][k] = 0.43 + 35.1 * pow(Re_gb_dry_mesh[i][j][k] *
d_h_dry_mesh[i][j][k] / (2 * dx), -1.07) / ((2 * dx) / d_h_dry_mesh[i][j][k]); //Friction
factor for low Reynolds number
                                                    }

                                                    else if
(Re_gb_dry_mesh[i][j][k] > 400) {

        Nu_gb_dry_mesh[i][j][k] = 0.12 * pow(Re_gb_dry_mesh[i][j][k], 0.64);
//Nusselt number for high Reynolds number

        f_gb_dry_mesh[i][j][k] = 0.26 + 27.0 * pow(Re_gb_dry_mesh[i][j][k], -1.27);
//Friction factor for low Reynolds number
                                                    }

                                                    //Air Nusselt number and
friction factor based on wet area, Fujii and Seshimo
                                                    if (Re_gb_wet_mesh[i][j][k]
<= 400) {

        Nu_gb_wet_mesh[i][j][k] = 2.1 * pow(Re_gb_wet_mesh[i][j][k] *
Pr_gb_mesh[i][j][k] * d_h_wet_mesh[i][j][k] / (2 * dx), 0.38); //Nusselt number for low
Reynolds number

        f_gb_wet_mesh[i][j][k] = 0.43 + 35.1 * pow(Re_gb_wet_mesh[i][j][k] *
d_h_wet_mesh[i][j][k] / (2 * dx), -1.07) / ((2 * dx) / d_h_wet_mesh[i][j][k]); //Friction
factor for low Reynolds number
                                                    }

                                                    else if
(Re_gb_wet_mesh[i][j][k] > 400) {

        Nu_gb_wet_mesh[i][j][k] = 0.12 * pow(Re_gb_wet_mesh[i][j][k], 0.64);
//Nusselt number for high Reynolds number

        f_gb_wet_mesh[i][j][k] = 0.26 + 27.0 * pow(Re_gb_wet_mesh[i][j][k], -1.27);
//Friction factor for low Reynolds number
                                                    }
```

```
                                                                    //Air pressure drop
                                                                    deltaP_gb_mesh[i][j][k] =
(f_gb_dry_mesh[i][j][k] * (1.0 - wr_gl_mesh[i][j][k]) * dx * rho_gb_mesh[i][j][k] *
pow(u_gb_dry_mesh[i][j][k], 2) / 2 / d_h_dry_mesh[i][j][k]) +

        (f_gb_wet_mesh[i][j][k] * wr_gl_mesh[i][j][k] * dx * rho_gb_mesh[i][j][k] *
pow(u_gb_wet_mesh[i][j][k], 2) / 2 / d_h_wet_mesh[i][j][k]); //
                                                                    //f_gb_mesh[i][j][k] = 96 /
Re_gb_mesh[i][j][k]; //General correlation for open rectangular duct (Incroperta et al.,
2011, page 553)

                                                                    //Heat transfer coefficient of
the air
                                                                    h_h_gb_gl_mesh[i][j][k] =
Nu_gb_wet_mesh[i][j][k] * lambda_gb_mesh[i][j][k] / d_h_wet_mesh[i][j][k]; //From
the air to the gas-liquid interface [kW/m^2/K]
                                                                    h_h_gb_gs_mesh[i][j][k] =
Nu_gb_dry_mesh[i][j][k] * lambda_gb_mesh[i][j][k] / d_h_dry_mesh[i][j][k]; //From
the air to the liquid-solid interface [kW/m^2/K]

                                                                    //Mass transfer coefficient
of the air
                                                                    h_m_gb_gl_mesh[i][j][k] =
h_h_gb_gl_mesh[i][j][k] * 1000 / rho_gb_mesh[i][j][k] / c_p_gb_mesh[i][j][k];
//Reynolds Analogy [m/s]
                                                                    //h_m_gb_gl_mesh[i][j][k]
= h_h_gb_gl_mesh[i][j][k] * 1000 / rho_gb_mesh[i][j][k] / c_p_gb_mesh[i][j][k] *
pow((D_gb_mesh[i][j][k] / TD_gb_mesh[i][j][k]), 0.66666667); //Chilton-Colburn
Analogy [m/s]

                                                                    //Heat transfer coefficient of
the solution
                                                                    Nu_lb_mesh[i][j][k] =
0.4764 * pow(Re_lb_mesh[i][j][k], 0.0477) * pow(Pr_lb_mesh[i][j][k], 0.334);
//Nusselt number (Karami et al.)
                                                                    double Lc_lb =
delta_lb_wr[i][j][k];//Characteristic length = film thickness [m]
                                                                    h_h_gl_ls_mesh[i][j][k] =
Nu_lb_mesh[i][j][k] * lambda_lb_mesh[i][j][k] / Lc_lb; //Heat transfer coefficient of
the solution film [kW/m^2/K]
                                                                    //Nu_lb_mesh[i][j][k] =
1.88; //Nusselt number

                                                                    //Mass transfer coefficient
of the solution
```

```
                                                    h_m_gl_lb_mesh[i][j][k] = 2 * pow((u_l_max_wr[i][j][k] * D_lb_mesh[i][j][k] / M_PI / dy), 0.5); //Penetration theory [m/s]
                                                    //h_m_gl_lb_mesh[i][j][k] = D_lb_mesh[i][j][k] / delta_lb_wr[i][j][k]; //Film theory [m/s]
                                                    //h_m_gl_lb_mesh[i][j][k] = h_h_gl_ls_mesh[i][j][k] / rho_lb_mesh[i][j][k] / c_p_lb_mesh[i][j][k] * pow((D_lb_mesh[i][j][k] / TD_lb_mesh[i][j][k]), 0.66666667); //Chilton-Colburn Analogy [m/s]

                                                    //Heat transfer coefficient of the wall
                                                    h_h_w_mesh[i][j][k] = lambda_w / log(D_t_o / D_t_i) / M_PI / P_f; //Heat transfer coefficient of the wall [kW/m^2/K]

                                                    //Heat transfer coefficient of the cooling water
                                                    f_mesh[i][j][k] = 0.316 * pow(Re_cw_mesh[i][j][k], -0.25); //Friction factor
                                                    Nu_cw_mesh[i][j][k] = f_mesh[i][j][k] * (Re_cw_mesh[i][j][k] - 1000) * Pr_cw_mesh[i][j][k] / 8 / (1 + 12.7 * pow((f_mesh[i][j][k] / 8), 0.5) * (pow(Pr_cw_mesh[i][j][k], 0.66666667) - 1)); //Nusselt number (Gnielinski correlation)
                                                    h_h_cw_mesh[i][j][k] = Nu_cw_mesh[i][j][k] * k_cw_mesh[i][j][k] / 1000 / D_t_i; //Heat transfer coefficient [kW/m^2/K]

                                                    //Enthalpy of vaporization/condensation of water
                                                    h_v_mesh[i][j][k] = sat_hv(100) - sat_hl(100); //Enthalpy of vaporization/condensation [kJ/kg]

                                                    //Surface areas
                                                    n_f_lb_mesh[i][j][k] = pow((1 + h_h_gl_ls_mesh[i][j][k] * pow((D_f - D_t_o), 2) * pow((D_f / D_t_o), 0.5) / 6 / lambda_w / (t_fin / 2)), -1); //Fin efficiency towards the solution
                                                    n_f_gb_mesh[i][j][k] = pow((1 + h_h_gb_gs_mesh[i][j][k] * pow((D_f - D_t_o), 2) * pow((D_f / D_t_o), 0.5) / 6 / lambda_w / (t_fin / 2)), -1); //Fin efficiency towards the air
                                                    wr_ls_mesh[i][j][k] = wr_gl_mesh[i][j][k]; //Liquid-solid wetting ratio
                                                    A_gl_mesh[i][j][k] = wr_gl_mesh[i][j][k] * (A_fin + A_t_ow); //Area of the gas-liquid area [m^2]
```

```
                                                    A_ls_mesh[i][j][k] =
wr_ls_mesh[i][j][k] * (n_f_lb_mesh[i][j][k] * A_fin + A_t_ow); //Area of the liquid-
solid area [m^2]
                                                    A_gs_mesh[i][j][k] = (1.0 -
wr_ls_mesh[i][j][k]) * (n_f_gb_mesh[i][j][k] * A_fin + A_t_ow); //Area of the gas-
solid area [m^2]
                                                    //A_gs_mesh[i][j][k] =
n_f_gb_mesh[i][j][k] * A_fin + A_t_ow; //For 0 solution flow calculation

                                                    //Total gas-liquid mass
transfer coefficient
                                                    h_m_gb_lb_mesh[i][j][k] =
1 / (1 / rho_gb_mesh[i][j][k] / A_gl_mesh[i][j][k] / h_m_gb_gl_mesh[i][j][k] + 1 /
rho_lb_mesh[i][j][k] / A_gl_mesh[i][j][k] / h_m_gl_lb_mesh[i][j][k]); //[kg/s]

                                                    //Total gas-liquid heat
transfer coefficient
                                                    h_h_gb_lb_mesh[i][j][k] =
1 / (1 / A_gl_mesh[i][j][k] / h_h_gb_gl_mesh[i][j][k] + 1 / A_gl_mesh[i][j][k] /
h_h_gl_ls_mesh[i][j][k]); //[kW/K]

                                                    //Gas-liquid property
calculation
                                                    q_gb_lb_mesh[i][j][k] =
h_h_gb_lb_mesh[i][j][k] * (T_gb_mesh[i][j][k] - T_lb_mesh[i][j][k]); //Heat transfer
from the gas bulk to the liquid bulk [kW]
                                                    T_gl_mesh[i][j][k] =
T_lb_mesh[i][j][k] + q_gb_lb_mesh[i][j][k] / A_gl_mesh[i][j][k] /
h_h_gl_ls_mesh[i][j][k]; //Gas-liquid temperature [deg.C]
                                                    q_gb_gl_mesh[i][j][k] =
h_h_gb_gl_mesh[i][j][k] * A_gl_mesh[i][j][k] * (T_gb_mesh[i][j][k] -
T_gl_mesh[i][j][k]); //Heat transfer from the gas bulk to the gas-liquid interface [kW]
                                                    j_gb_lb_mesh[i][j][k] =
h_m_gb_lb_mesh[i][j][k] * (x_gb_mesh[i][j][k] - x_lb_mesh[i][j][k]); //Overall mass
transfer [kg/s]
                                                    X_gl_mesh[i][j][k] =
X_lb_mesh[i][j][k] + j_gb_lb_mesh[i][j][k] / rho_lb_mesh[i][j][k] /
h_m_gl_lb_mesh[i][j][k] / A_gl_mesh[i][j][k]; // IL mass fraction at the gas-liquid
interface
                                                    j_gl_lb_mesh[i][j][k] =
rho_lb_mesh[i][j][k] * A_gl_mesh[i][j][k] * h_m_gl_lb_mesh[i][j][k] *
(X_gl_mesh[i][j][k] - X_lb_mesh[i][j][k]); //Mass transfer from the gas-liquid interface
to the liquid bulk [kg/s]
                                                    x_gl_mesh[i][j][k] =
x_lb_mesh[i][j][k] + j_gb_lb_mesh[i][j][k] / rho_lb_mesh[i][j][k] /
```

```
h_m_gl_lb_mesh[i][j][k] / A_gl_mesh[i][j][k]; // Humidity ratio of the air at the gas-liquid interface
                                                    j_gb_gl_mesh[i][j][k] = rho_gb_mesh[i][j][k] * A_gl_mesh[i][j][k] * h_m_gb_gl_mesh[i][j][k] * (x_gb_mesh[i][j][k] - x_gl_mesh[i][j][k]); //Mass transfer from the gas bulk to the gas-liquid interface [kg/s]

                                                    //Total air-solid heat transfer coefficient
                                                    h_h_gb_ls_mesh[i][j][k] = 1 / (1 / A_gl_mesh[i][j][k] / h_h_gb_gl_mesh[i][j][k] + 1 / A_ls_mesh[i][j][k] / h_h_gl_ls_mesh[i][j][k]);

                                                    //Overall air-water heat transfer coefficient
                                                    h_h_gb_cw_mesh[i][j][k] = 1 / (1 / (A_gs_mesh[i][j][k] * h_h_gb_gs_mesh[i][j][k] + h_h_gb_ls_mesh[i][j][k]) + 1 / A_t_ow / h_h_w_mesh[i][j][k] + 1 / A_t_iw / h_h_cw_mesh[i][j][k]); //[kW/K]


                                                    //Tube outer wall and inner wall temperatures
                                                    T_iw_mesh[i][j][k] = T_cw_mesh[i][j][k] + h_h_gb_cw_mesh[i][j][k] * (T_gb_mesh[i][j][k] - T_cw_mesh[i][j][k]) / A_t_iw / h_h_cw_mesh[i][j][k]; //[deg.C], from the cooling water towards the air
                                                    T_ow_mesh[i][j][k] = T_iw_mesh[i][j][k] + h_h_gb_cw_mesh[i][j][k] * (T_gb_mesh[i][j][k] - T_cw_mesh[i][j][k]) / h_h_w_mesh[i][j][k] / A_t_ow;
                                                    //T_ow_mesh[i][j][k] = (T_gb_mesh[i][j][k] * h_h_gb_gs_mesh[i][j][k] * A_gs_mesh[i][j][k] + T_gl_mesh[i][j][k] * h_h_gl_ls_mesh[i][j][k] * A_ls_mesh[i][j][k] - h_h_gb_cw_mesh[i][j][k] * (T_gb_mesh[i][j][k] - T_cw_mesh[i][j][k])) /

          //(h_h_gb_gs_mesh[i][j][k] * A_gs_mesh[i][j][k] + h_h_gl_ls_mesh[i][j][k] * A_ls_mesh[i][j][k]); //[deg.C], from the air towards the cooling water calculation
                                                    //T_iw_mesh[i][j][k] = T_ow_mesh[i][j][k] - h_h_gb_cw_mesh[i][j][k] * (T_gb_mesh[i][j][k] - T_cw_mesh[i][j][k]) / A_t_ow / h_h_w_mesh[i][j][k]; //[deg.C], from the air towards the cooling water calculation

                                                    //Outer tube to inner tube heat transfer
                                                    q_w_mesh[i][j][k] = h_h_w_mesh[i][j][k] * A_t_ow * (T_ow_mesh[i][j][k] - T_iw_mesh[i][j][k]); //[kW]
```

```
                                                        //q_w_mesh[i][j][k] =
h_h_w_mesh[i][j][k] * (A_ls_mesh[i][j][k] + A_gs_mesh[i][j][k]) *
(T_ow_mesh[i][j][k] - T_iw_mesh[i][j][k]); //[kW], from the air towards the cooling
water calculation

                                                        //Inner tube to cooling water
heat transfer
                                                        q_iw_cw_mesh[i][j][k] =
h_h_cw_mesh[i][j][k] * A_t_iw * (T_iw_mesh[i][j][k] - T_cw_mesh[i][j][k]); //[kW]

                                                        //Liquid to solid heat
transfer
                                                        q_lb_ls_mesh[i][j][k] =
h_h_gl_ls_mesh[i][j][k] * A_ls_mesh[i][j][k] * (T_lb_mesh[i][j][k] -
T_ow_mesh[i][j][k]); //[kW]

                                                        //Gas to solid heat transfer
                                                        q_gb_gs_mesh[i][j][k] =
h_h_gb_gs_mesh[i][j][k] * A_gs_mesh[i][j][k] * (T_gb_mesh[i][j][k] -
T_ow_mesh[i][j][k]); //[kW]

                                                        //Condensation
                                                        x_dp_gb_mesh[i][j][k] =
air_x_tphi(T_gb_mesh[i][j][k], 1); //Humidity ratio at dewpoint temperature
                                                        if (T_gb_mesh[i][j][k] <=
T_dp_gb_mesh[i][j][k]) {

            m_gb_dp_mesh[i][j][k] = m_gb_mesh[i][j][k] * (x_gb_mesh[i][j][k] -
x_dp_gb_mesh[i][j][k]); //Condensation rate, if gas bulk temperature is lower than the
dewpoint temperature
                                                        }
                                                        else if (T_gb_mesh[i][j][k]
> T_dp_gb_mesh[i][j][k]) {

            m_gb_dp_mesh[i][j][k] = 0; //No condensation of gas bulk temperature is higher
than the dewpoint temperature
                                                        }

                                                        //Air
                                                        m_gb_mesh[i][j + 1][k] =
m_gb_mesh[i][j][k]; //Mass flow rate [kg/s]
                                                        x_gb_mesh[i][j + 1][k] =
(m_gb_mesh[i][j][k] * x_gb_mesh[i][j][k] - j_gb_gl_mesh[i][j][k] -
m_gb_dp_mesh[i][j][k]) / m_gb_mesh[i][j + 1][k]; //Humidity ratio [kg/kg(DA)]
                                                        H_gb_mesh[i][j + 1][k] =
(m_gb_mesh[i][j][k] * H_gb_mesh[i][j][k] - q_gb_gl_mesh[i][j][k] -
```

```
(j_gb_gl_mesh[i][j][k] + m_gb_dp_mesh[i][j][k]) * h_v_mesh[i][j][k] -
q_gb_gs_mesh[i][j][k]) / m_gb_mesh[i][j + 1][k]; //Enthalpy [kJ/kg]
                                                    T_gb_mesh[i][j + 1][k] =
air_t_hx(H_gb_mesh[i][j + 1][k] * 1000, x_gb_mesh[i][j + 1][k]); //Temperature
[deg.C]
                                                    rho_gb_mesh[i][j + 1][k] =
air_rho_tx(T_gb_mesh[i][j + 1][k], x_gb_mesh[i][j + 1][k]); //Density [kg/m^3]
                                                    lambda_gb_mesh[i][j +
1][k] = air_lambda_tx(T_gb_mesh[i][j + 1][k], x_gb_mesh[i][j + 1][k]) / 1000;
//Thermal conductivity [kW/m/K]
                                                    c_p_gb_mesh[i][j + 1][k] =
air_cp_tx(T_gb_mesh[i][j + 1][k], x_gb_mesh[i][j + 1][k]); //Specific heat [J/kg/K]
                                                    TD_gb_mesh[i][j + 1][k] =
air_alpha_tx(T_gb_mesh[i][j + 1][k], x_gb_mesh[i][j + 1][k]); //Thermal diffusivity
[m^2/s]
                                                    D_gb_mesh[i][j + 1][k] =
air_D_t(T_gb_mesh[i][j + 1][k]); //Mass diffusivity [m^2/s]
                                                    myu_gb_mesh[i][j + 1][k] =
air_myu_tx(T_gb_mesh[i][j + 1][k], x_gb_mesh[i][j + 1][k]); //Dynamic viscosity [Pa-
s]
                                                    Pr_gb_mesh[i][j + 1][k] =
air_Pr_t(T_gb_mesh[i][j + 1][k], x_gb_mesh[i][j + 1][k]); //Prandtl number
                                                    T_dp_gb_mesh[i][j + 1][k]
= air_td_x(x_gb_mesh[i][j + 1][k]); //Dewpoint temperature [deg.C]

                                                    //Liquid bulk
                                                    m_lb_mesh[i + 1][j][k] =
m_lb_mesh[i][j][k] + j_gb_gl_mesh[i][j][k] + m_gb_dp_mesh[i][j][k]; //Mass flow rate
[kg/s], with condensation
                                                    H_lb_mesh[i + 1][j][k] =
(m_lb_mesh[i][j][k] * H_lb_mesh[i][j][k] + q_gb_gl_mesh[i][j][k] +
(j_gb_gl_mesh[i][j][k] + m_gb_dp_mesh[i][j][k]) * h_v_mesh[i][j][k] -
q_lb_ls_mesh[i][j][k]) / m_lb_mesh[i + 1][j][k]; //With condensation
                                                    X_lb_mesh[i + 1][j][k] =
(m_lb_mesh[i][j][k] * X_lb_mesh[i][j][k]) / m_lb_mesh[i + 1][j][k]; //IL mass fraction
                                                    T_lb_mesh[i + 1][j][k] =
IL_t_hw(H_lb_mesh[i + 1][j][k], X_lb_mesh[i + 1][j][k] * 100); //Temperature [deg.C]
                                                    Gamma_lb_mesh[i +
1][j][k] = m_lb_mesh[i + 1][j][k] / dx; //Flowrate per unit length of the contactor
[kg/m/s]
                                                    x_lb_mesh[i + 1][j][k] =
IL_hr_tX(T_lb_mesh[i + 1][j][k], X_lb_mesh[i + 1][j][k] * 100); //Equilibrium
humidity ratio [kg/kg]
                                                    rho_lb_mesh[i + 1][j][k] =
IL_rho_tX(T_lb_mesh[i + 1][j][k], X_lb_mesh[i + 1][j][k] * 100); //Density [kg/m^3]
```

```
                                                    myu_lb_mesh[i + 1][j][k] =
IL_myu_tX(T_lb_mesh[i + 1][j][k], X_lb_mesh[i + 1][j][k] * 100); //Dynamic viscosity
[Pa-s]
                                                    lambda_lb_mesh[i +
1][j][k] = IL_lambda_tX(T_lb_mesh[i + 1][j][k], X_lb_mesh[i + 1][j][k] * 100) / 1000;
//Thermal conductivity [kW/m/K]
                                                    delta_lb_mesh[i + 1][j][k] =
pow((3 * Gamma_lb_mesh[i + 1][j][k] * myu_lb_mesh[i + 1][j][k] /
pow(rho_lb_mesh[i + 1][j][k], 2) / g), 0.333333333); //Film thickness
                                                    u_l_max_mesh[i + 1][j][k]
= rho_lb_mesh[i + 1][j][k] * g * pow(delta_lb_mesh[i + 1][j][k], 2) / 2 / myu_lb_mesh[i
+ 1][j][k]; //Maximum (gas-liquid interface) velocity [m/s]
                                                    u_l_ave_mesh[i + 1][j][k] =
2 * u_l_max_mesh[i + 1][j][k] / 3; //Average velocity [m/s]
                                                    sigma_lb_mesh[i + 1][j][k]
= IL_sigma_tX(T_lb_mesh[i + 1][j][k], X_lb_mesh[i + 1][j][k] * 100); //Surface
tension [N/m]
                                                    We_lb_mesh[i + 1][j][k] =
sigma_lb_mesh[i + 1][j][k] / rho_lb_mesh[i + 1][j][k] / pow(u_l_ave_mesh[i + 1][j][k],
2) / delta_lb_mesh[i + 1][j][k]; //Weber number
                                                    Re_lb_mesh[i + 1][j][k] = 4
* Gamma_lb_mesh[i + 1][j][k] / myu_lb_mesh[i + 1][j][k]; //Reynolds number
                                                    Pr_lb_mesh[i + 1][j][k] =
IL_nyu_tX(T_lb_mesh[i + 1][j][k], X_lb_mesh[i + 1][j][k] * 100) /
IL_alpha_tX(T_lb_mesh[i + 1][j][k], X_lb_mesh[i + 1][j][k] * 100); //Prandtl number
                                                    D_lb_mesh[i + 1][j][k] =
IL_D_X(X_lb_mesh[i + 1][j][k] * 100); //Mass diffusivity [m^2/s]
                                                    c_p_lb_mesh[i + 1][j][k] =
IL_Cp_tX(T_lb_mesh[i + 1][j][k], X_lb_mesh[i + 1][j][k] * 100); //Specific heat
[kJ/kg/K]
                                                    TD_lb_mesh[i + 1][j][k] =
IL_alpha_tX(T_lb_mesh[i + 1][j][k], X_lb_mesh[i + 1][j][k] * 100); //Thermal
diffusivity [m^2/s]


                                                    //Cooling water
                                                    m_cw_mesh[i][j][k + 1] =
m_cw_mesh[i][j][k]; //Mass flow rate [kg/s]
                                                    H_cw_mesh[i][j][k + 1] =
(m_cw_mesh[i][j][k] * H_cw_mesh[i][j][k] - q_iw_cw_mesh[i][j][k]) /
m_cw_mesh[i][j][k + 1]; //Enthalpy [kJ/kg]
                                                    T_cw_mesh[i][j][k + 1] =
water_t_hp(H_cw_mesh[i][j][k + 1], 101.325); //Temperature [deg.C]
                                                    nyu_cw_mesh[i][j][k + 1] =
sc_nyul(101.325, T_cw_mesh[i][j][k + 1]); //Kinematic viscosity [m^2/s]
                                                    Re_cw_mesh[i][j][k + 1] =
u_cw * D_t_i / nyu_cw_mesh[i][j][k + 1]; // Reynolds number
```

```
                                                    Pr_cw_mesh[i][j][k + 1] =
sc_Prl(101.325, T_cw_mesh[i][j][k + 1]); // Prandtl number
                                                    k_cw_mesh[i][j][k + 1] =
sc_laml(101.325, T_cw_mesh[i][j][k + 1]); // Thermal conductivity [kW/m/K]
                                                }

                                                //Assign initial values for the next
control volume
                                                m_cw_mesh[i][j + 1][k - 1] =
m_cw_mesh[i][j][k - 1];
                                                H_cw_mesh[i][j + 1][k - 1] =
H_cw_mesh[i][j][k - 1];
                                                T_cw_mesh[i][j + 1][k - 1] =
T_cw_mesh[i][j][k - 1];
                                                nyu_cw_mesh[i][j + 1][k - 1] =
nyu_cw_mesh[i][j][k - 1];
                                                Re_cw_mesh[i][j + 1][k - 1] =
Re_cw_mesh[i][j][k - 1];
                                                Pr_cw_mesh[i][j + 1][k - 1] =
Pr_cw_mesh[i][j][k - 1];
                                                k_cw_mesh[i][j + 1][k - 1] =
k_cw_mesh[i][j][k - 1];

                                        }
                                        else if (j % 2 == 0) {
                                                for (k = mesh_z; k > 0; k--) {

                                                        //Wetting ratio, gas-liquid
area, and solid-liquid area
                                                        theta_a_mesh[i][j][k] =
0.00008 * pow(X_lb_mesh[i][j][k] * 100, 2) - 0.0149 * X_lb_mesh[i][j][k] * 100 +
1.94; //Advancing contact angle [deg.]
                                                        theta_r_mesh[i][j][k] =
0.00008 * pow(X_lb_mesh[i][j][k] * 100, 2) - 0.0150 * X_lb_mesh[i][j][k] * 100 +
1.48; //Receeding contact angle [deg.]

                                                        //Determine if flow is
increasing or decreasing flow rate
                                                        if (type_of_flow == 'I') {
                                                                wr_gl_mesh[i][j][k]
= 0.83 * pow(theta_a_mesh[i][j][k], -0.90) * pow((Re_lb_mesh[i][j][k] /
pow(We_lb_mesh[i][j][k], 3)), 0.07); //Partial wetting model
                                                                //Assign the value of
1 to the wetting ratio if it is greater than 1
                                                                if
(wr_gl_mesh[i][j][k] > 1) {
```

```
        wr_gl_mesh[i][j][k] = 1;
                                                    }
                                                }

                                                else if (type_of_flow ==
'D') {

        Ga_lb_b_mesh[i][j][k] = rho_lb_mesh[i][j][k] * pow(sigma_lb_mesh[i][j][k], 3)
/ pow(myu_lb_mesh[i][j][k], 4) / g; //Galileo number at film breaking

        Re_lb_b_mesh[i][j][k] = 0.025 * pow(Ga_lb_b_mesh[i][j][k], 0.26) *
pow((log(theta_r_mesh[i][j][k]) + 3.45), 3); //Film Reynolds number at breaking

                                                    //Determine whether
Re_s is lower than Re_b, if so, compute the wetting ratio
                                                    if
(Re_lb_mesh[i][j][k] < Re_lb_b_mesh[i][j][k]) {

        wr_gl_mesh[i][j][k] = 0.83 * pow(theta_r_mesh[i][j][k], -0.90) *
pow((Re_lb_mesh[i][j][k] / pow(We_lb_mesh[i][j][k], 3)), 0.07); //Partial wetting
model
                                                    }

                                                    //Assign the value of
1 to the wetting ratio if Re_s is >= Re_b
                                                    else if
(Re_lb_mesh[i][j][k] >= Re_lb_b_mesh[i][j][k]) {

        wr_gl_mesh[i][j][k] = 1;
                                                    }
                                                }

                                                //Complete wetting
assumption
                                                //wr_gl_mesh[i][j][k] = 1.0;
//Complete wetting

                                                delta_lb_wr[i][j][k] =
pow((3 * Gamma_lb_mesh[i][j][k] * myu_lb_mesh[i][j][k] / pow(rho_lb_mesh[i][j][k],
2) / g / wr_gl_mesh[i][j][k]), 0.333333333); //Film thickness [m]
                                                u_l_max_wr[i][j][k] =
rho_lb_mesh[i][j][k] * g * pow(delta_lb_wr[i][j][k], 2) / 2 / myu_lb_mesh[i][j][k];
////Maximum (gas-liquid interface) velocity [m/s]
                                                u_l_ave_wr[i][j][k] = 2 *
u_l_max_wr[i][j][k] / 3; // Average solution velocity [m/s]
```

```
                                                    //Effective air velocity and
effective hydraulic diameter
                                                    u_gb_dry_mesh[i][j][k] =
m_gb_mesh[i][j][k] / rho_gb_mesh[i][j][k] / ((0.5 * P_f * dy) - (0.5 * P_f * D_t_o));
//Effective air velocity on dry area
                                                    u_gb_wet_mesh[i][j][k] =
m_gb_mesh[i][j][k] / rho_gb_mesh[i][j][k] / ((0.5 * P_f * dy) - (0.5 * P_f * D_t_o) -
(delta_lb_wr[i][j][k] * dy)); //Effective air velocity on wet area
                                                    d_h_dry_mesh[i][j][k] = 4 *
((0.5 * P_f * dy) - (0.5 * P_f * D_t_o)) / (dy + P_f); //Effective hydraulic diameter on
dry area
                                                    d_h_wet_mesh[i][j][k] = 4 *
((0.5 * P_f * dy) - (0.5 * P_f * D_t_o) - (delta_lb_wr[i][j][k] * dy)) / (dy + P_f);
//Effective hydraulic diameter on wet area

                                                    //Air Reynolds number
                                                    Re_gb_dry_mesh[i][j][k] =
rho_gb_mesh[i][j][k] * u_gb_dry_mesh[i][j][k] * d_h_dry_mesh[i][j][k] /
myu_gb_mesh[i][j][k]; //On dry area
                                                    Re_gb_wet_mesh[i][j][k] =
rho_gb_mesh[i][j][k] * u_gb_wet_mesh[i][j][k] * d_h_wet_mesh[i][j][k] /
myu_gb_mesh[i][j][k]; //On wet area

                                                    //Air Nusselt number and
friction factor based on dry area, Fujii and Seshimo
                                                    if (Re_gb_dry_mesh[i][j][k]
<= 400) {

        Nu_gb_dry_mesh[i][j][k] = 2.1 * pow(Re_gb_dry_mesh[i][j][k] *
Pr_gb_mesh[i][j][k] * d_h_dry_mesh[i][j][k] / (2 * dx), 0.38); //Nusselt number for low
Reynolds number

        f_gb_dry_mesh[i][j][k] = 0.43 + 35.1 * pow(Re_gb_dry_mesh[i][j][k] *
d_h_dry_mesh[i][j][k] / (2 * dx), -1.07) / ((2 * dx) / d_h_dry_mesh[i][j][k]); //Friction
factor for low Reynolds number
                                                    }

                                                    else if
(Re_gb_dry_mesh[i][j][k] > 400) {

        Nu_gb_dry_mesh[i][j][k] = 0.12 * pow(Re_gb_dry_mesh[i][j][k], 0.64);
//Nusselt number for high Reynolds number

        f_gb_dry_mesh[i][j][k] = 0.26 + 27.0 * pow(Re_gb_dry_mesh[i][j][k], -1.27);
//Friction factor for low Reynolds number
```

```
                                                    }

                                                    //Air Nusselt number and
friction factor based on wet area, Fujii and Seshimo
                                                    if (Re_gb_wet_mesh[i][j][k]
<= 400) {

        Nu_gb_wet_mesh[i][j][k] = 2.1 * pow(Re_gb_wet_mesh[i][j][k] *
Pr_gb_mesh[i][j][k] * d_h_wet_mesh[i][j][k] / (2 * dx), 0.38); //Nusselt number for low
Reynolds number

        f_gb_wet_mesh[i][j][k] = 0.43 + 35.1 * pow(Re_gb_wet_mesh[i][j][k] *
d_h_wet_mesh[i][j][k] / (2 * dx), -1.07) / ((2 * dx) / d_h_wet_mesh[i][j][k]); //Friction
factor for low Reynolds number
                                                    }

                                                    else if
(Re_gb_wet_mesh[i][j][k] > 400) {

        Nu_gb_wet_mesh[i][j][k] = 0.12 * pow(Re_gb_wet_mesh[i][j][k], 0.64);
//Nusselt number for high Reynolds number

        f_gb_wet_mesh[i][j][k] = 0.26 + 27.0 * pow(Re_gb_wet_mesh[i][j][k], -1.27);
//Friction factor for low Reynolds number
                                                    }

                                                    //Air pressure drop
                                                    deltaP_gb_mesh[i][j][k] =
(f_gb_dry_mesh[i][j][k] * (1.0 - wr_gl_mesh[i][j][k]) * dx * rho_gb_mesh[i][j][k] *
pow(u_gb_dry_mesh[i][j][k], 2) / 2 / d_h_dry_mesh[i][j][k]) +

        (f_gb_wet_mesh[i][j][k] * wr_gl_mesh[i][j][k] * dx * rho_gb_mesh[i][j][k] *
pow(u_gb_wet_mesh[i][j][k], 2) / 2 / d_h_wet_mesh[i][j][k]); //
                                                    //f_gb_mesh[i][j][k] = 96 /
Re_gb_mesh[i][j][k]; //General correlation for open rectangular duct (Incroperta et al.,
2011, page 553)

                                                    //Heat transfer coefficient of
the air
                                                    h_h_gb_gl_mesh[i][j][k] =
Nu_gb_wet_mesh[i][j][k] * lambda_gb_mesh[i][j][k] / d_h_wet_mesh[i][j][k]; //From
the air to the gas-liquid interface [kW/m^2/K]
                                                    h_h_gb_gs_mesh[i][j][k] =
Nu_gb_dry_mesh[i][j][k] * lambda_gb_mesh[i][j][k] / d_h_dry_mesh[i][j][k]; //From
the air to the liquid-solid interface [kW/m^2/K]
```

```
                                                                    //Mass transfer coefficient
of the air
                                                                    h_m_gb_gl_mesh[i][j][k] =
h_h_gb_gl_mesh[i][j][k] * 1000 / rho_gb_mesh[i][j][k] / c_p_gb_mesh[i][j][k];
//Reynolds Analogy [m/s]
                                                                    //h_m_gb_gl_mesh[i][j][k]
= h_h_gb_gl_mesh[i][j][k] * 1000 / rho_gb_mesh[i][j][k] / c_p_gb_mesh[i][j][k] *
pow((D_gb_mesh[i][j][k] / TD_gb_mesh[i][j][k]), 0.66666667); //Chilton-Colburn
Analogy [m/s]

                                                                    //Heat transfer coefficient of
the solution
                                                                    Nu_lb_mesh[i][j][k] =
0.4764 * pow(Re_lb_mesh[i][j][k], 0.0477) * pow(Pr_lb_mesh[i][j][k], 0.334);
//Nusselt number (Karami et al.)
                                                                    double Lc_lb =
delta_lb_wr[i][j][k];//Characteristic length = film thickness [m]
                                                                    h_h_gl_ls_mesh[i][j][k] =
Nu_lb_mesh[i][j][k] * lambda_lb_mesh[i][j][k] / Lc_lb; //Heat transfer coefficient of
the solution film [kW/m^2/K]
                                                                    //Nu_lb_mesh[i][j][k] =
1.88; //Nusselt number

                                                                    //Mass transfer coefficient
of the solution
                                                                    h_m_gl_lb_mesh[i][j][k] =
2 * pow((u_l_max_wr[i][j][k] * D_lb_mesh[i][j][k] / M_PI / dy), 0.5); //Penetration
theory [m/s]
                                                                    //h_m_gl_lb_mesh[i][j][k] =
D_lb_mesh[i][j][k] / delta_lb_wr[i][j][k]; //Film theory [m/s]
                                                                    //h_m_gl_lb_mesh[i][j][k] =
h_h_gl_ls_mesh[i][j][k] / rho_lb_mesh[i][j][k] / c_p_lb_mesh[i][j][k] *
pow((D_lb_mesh[i][j][k] / TD_lb_mesh[i][j][k]), 0.66666667); //Chilton-Colburn
Analogy [m/s]

                                                                    //Heat transfer coefficient of
the wall
                                                                    h_h_w_mesh[i][j][k] =
lambda_w / log(D_t_o / D_t_i) / M_PI / P_f; //Heat transfer coefficient of the wall
[kW/m^2/K]

                                                                    //Heat transfer coefficient of
the cooling water
                                                                    f_mesh[i][j][k] = 0.316 *
pow(Re_cw_mesh[i][j][k], -0.25); //Friction factor
```

```
                                                    Nu_cw_mesh[i][j][k] =
f_mesh[i][j][k] * (Re_cw_mesh[i][j][k] - 1000) * Pr_cw_mesh[i][j][k] / 8 / (1 + 12.7 *
pow((f_mesh[i][j][k] / 8), 0.5) * (pow(Pr_cw_mesh[i][j][k], 0.66666667) - 1)); //Nusselt
number (Gnielinski correlation)
                                                    h_h_cw_mesh[i][j][k] =
Nu_cw_mesh[i][j][k] * k_cw_mesh[i][j][k] / 1000 / D_t_i; //Heat transfer coefficient
[kW/m^2/K]

                                                    //Enthalpy of
vaporization/condensation of water
                                                    h_v_mesh[i][j][k] =
sat_hv(100) - sat_hl(100); //Enthalpy of vaporization/condensation [kJ/kg]

                                                    //Surface areas
                                                    n_f_lb_mesh[i][j][k] =
pow((1 + h_h_gl_ls_mesh[i][j][k] * pow((D_f - D_t_o), 2) * pow((D_f / D_t_o), 0.5) / 6
/ lambda_w / (t_fin / 2)), -1); //Fin efficiency towards the solution
                                                    n_f_gb_mesh[i][j][k] =
pow((1 + h_h_gb_gs_mesh[i][j][k] * pow((D_f - D_t_o), 2) * pow((D_f / D_t_o), 0.5) /
6 / lambda_w / (t_fin / 2)), -1); //Fin efficiency towards the air
                                                    wr_ls_mesh[i][j][k] =
wr_gl_mesh[i][j][k]; //Liquid-solid wetting ratio
                                                    A_gl_mesh[i][j][k] =
wr_gl_mesh[i][j][k] * (A_fin + A_t_ow); //Area of the gas-liquid area [m^2]
                                                    A_ls_mesh[i][j][k] =
wr_ls_mesh[i][j][k] * (n_f_lb_mesh[i][j][k] * A_fin + A_t_ow); //Area of the liquid-
solid area [m^2]
                                                    A_gs_mesh[i][j][k] = (1.0 -
wr_ls_mesh[i][j][k]) * (n_f_gb_mesh[i][j][k] * A_fin + A_t_ow); //Area of the gas-
solid area [m^2]
                                                    //A_gs_mesh[i][j][k] =
n_f_gb_mesh[i][j][k] * A_fin + A_t_ow; //For 0 solution flow calculation

                                                    //Total gas-liquid mass
transfer coefficient
                                                    h_m_gb_lb_mesh[i][j][k] =
1 / (1 / rho_gb_mesh[i][j][k] / A_gl_mesh[i][j][k] / h_m_gb_gl_mesh[i][j][k] + 1 /
rho_lb_mesh[i][j][k] / A_gl_mesh[i][j][k] / h_m_gl_lb_mesh[i][j][k]); //[kg/s]

                                                    //Total gas-liquid heat
transfer coefficient
                                                    h_h_gb_lb_mesh[i][j][k] =
1 / (1 / A_gl_mesh[i][j][k] / h_h_gb_gl_mesh[i][j][k] + 1 / A_gl_mesh[i][j][k] /
h_h_gl_ls_mesh[i][j][k]); //[kW/K]
```

```
                                                                //Gas-liquid property
calculation
                                                                q_gb_lb_mesh[i][j][k] =
h_h_gb_lb_mesh[i][j][k] * (T_gb_mesh[i][j][k] - T_lb_mesh[i][j][k]); //Heat transfer
from the gas bulk to the liquid bulk [kW]
                                                                T_gl_mesh[i][j][k] =
T_lb_mesh[i][j][k] + q_gb_lb_mesh[i][j][k] / A_gl_mesh[i][j][k] /
h_h_gl_ls_mesh[i][j][k]; //Gas-liquid temperature [deg.C]
                                                                q_gb_gl_mesh[i][j][k] =
h_h_gb_gl_mesh[i][j][k] * A_gl_mesh[i][j][k] * (T_gb_mesh[i][j][k] -
T_gl_mesh[i][j][k]); //Heat transfer from the gas bulk to the gas-liquid interface [kW]
                                                                j_gb_lb_mesh[i][j][k] =
h_m_gb_lb_mesh[i][j][k] * (x_gb_mesh[i][j][k] - x_lb_mesh[i][j][k]); //Overall mass
transfer [kg/s]
                                                                X_gl_mesh[i][j][k] =
X_lb_mesh[i][j][k] + j_gb_lb_mesh[i][j][k] / rho_lb_mesh[i][j][k] /
h_m_gl_lb_mesh[i][j][k] / A_gl_mesh[i][j][k]; // IL mass fraction at the gas-liquid
interface
                                                                j_gl_lb_mesh[i][j][k] =
rho_lb_mesh[i][j][k] * A_gl_mesh[i][j][k] * h_m_gl_lb_mesh[i][j][k] *
(X_gl_mesh[i][j][k] - X_lb_mesh[i][j][k]); //Mass transfer from the gas-liquid interface
to the liquid bulk [kg/s]
                                                                x_gl_mesh[i][j][k] =
x_lb_mesh[i][j][k] + j_gb_lb_mesh[i][j][k] / rho_lb_mesh[i][j][k] /
h_m_gl_lb_mesh[i][j][k] / A_gl_mesh[i][j][k]; // Humidity ratio of the air at the gas-
liquid interface
                                                                j_gb_gl_mesh[i][j][k] =
rho_gb_mesh[i][j][k] * A_gl_mesh[i][j][k] * h_m_gb_gl_mesh[i][j][k] *
(x_gb_mesh[i][j][k] - x_gl_mesh[i][j][k]); //Mass transfer from the gas bulk to the gas-
liquid interface [kg/s]

                                                                //Total air-solid heat
transfer coefficient
                                                                h_h_gb_ls_mesh[i][j][k] = 1
/ (1 / A_gl_mesh[i][j][k] / h_h_gb_gl_mesh[i][j][k] + 1 / A_ls_mesh[i][j][k] /
h_h_gl_ls_mesh[i][j][k]);

                                                                //Overall air-water heat
transfer coefficient
                                                                h_h_gb_cw_mesh[i][j][k] =
1 / (1 / (A_gs_mesh[i][j][k] * h_h_gb_gs_mesh[i][j][k] + h_h_gb_ls_mesh[i][j][k]) + 1 /
A_t_ow / h_h_w_mesh[i][j][k] + 1 / A_t_iw / h_h_cw_mesh[i][j][k]); //[kW/K]

                                                                //Tube outer wall and inner
wall temperatures
```

```
                                                    T_iw_mesh[i][j][k] =
T_cw_mesh[i][j][k] + h_h_gb_cw_mesh[i][j][k] * (T_gb_mesh[i][j][k] -
T_cw_mesh[i][j][k]) / A_t_iw / h_h_cw_mesh[i][j][k]; //[deg.C], from the cooling
water towards the air
                                                    T_ow_mesh[i][j][k] =
T_iw_mesh[i][j][k] + h_h_gb_cw_mesh[i][j][k] * (T_gb_mesh[i][j][k] -
T_cw_mesh[i][j][k]) / h_h_w_mesh[i][j][k] / A_t_ow;
                                                    //T_ow_mesh[i][j][k] =
(T_gb_mesh[i][j][k] * h_h_gb_gs_mesh[i][j][k] * A_gs_mesh[i][j][k] +
T_gl_mesh[i][j][k] * h_h_gl_ls_mesh[i][j][k] * A_ls_mesh[i][j][k] -
h_h_gb_cw_mesh[i][j][k] * (T_gb_mesh[i][j][k] - T_cw_mesh[i][j][k])) /

        //(h_h_gb_gs_mesh[i][j][k] * A_gs_mesh[i][j][k] + h_h_gl_ls_mesh[i][j][k] *
A_ls_mesh[i][j][k]); //[deg.C], from the air towards the cooling water calculation
                                                    //T_iw_mesh[i][j][k] =
T_ow_mesh[i][j][k] - h_h_gb_cw_mesh[i][j][k] * (T_gb_mesh[i][j][k] -
T_cw_mesh[i][j][k]) / A_t_ow / h_h_w_mesh[i][j][k]; //[deg.C], from the air towards
the cooling water calculation

                                                    //Outer tube to inner tube
heat transfer
                                                    q_w_mesh[i][j][k] =
h_h_w_mesh[i][j][k] * A_t_ow * (T_ow_mesh[i][j][k] - T_iw_mesh[i][j][k]); //[kW]
                                                    //q_w_mesh[i][j][k] =
h_h_w_mesh[i][j][k] * (A_ls_mesh[i][j][k] + A_gs_mesh[i][j][k]) *
(T_ow_mesh[i][j][k] - T_iw_mesh[i][j][k]); //[kW], from the air towards the cooling
water calculation

                                                    //Inner tube to cooling water
heat transfer
                                                    q_iw_cw_mesh[i][j][k] =
h_h_cw_mesh[i][j][k] * A_t_iw * (T_iw_mesh[i][j][k] - T_cw_mesh[i][j][k]); //[kW]

                                                    //Liquid to solid heat
transfer
                                                    q_lb_ls_mesh[i][j][k] =
h_h_gl_ls_mesh[i][j][k] * A_ls_mesh[i][j][k] * (T_lb_mesh[i][j][k] -
T_ow_mesh[i][j][k]); //[kW]

                                                    //Gas to solid heat transfer
                                                    q_gb_gs_mesh[i][j][k] =
h_h_gb_gs_mesh[i][j][k] * A_gs_mesh[i][j][k] * (T_gb_mesh[i][j][k] -
T_ow_mesh[i][j][k]); //[kW]

                                                    //Condensation
```

```
                                                    x_dp_gb_mesh[i][j][k] =
air_x_tphi(T_gb_mesh[i][j][k], 1); //Humidity ratio at dewpoint temperature
                                                    if (T_gb_mesh[i][j][k] <=
T_dp_gb_mesh[i][j][k]) {

            m_gb_dp_mesh[i][j][k] = m_gb_mesh[i][j][k] * (x_gb_mesh[i][j][k] -
x_dp_gb_mesh[i][j][k]); //Condensation rate, if gas bulk temperature is lower than the
dewpoint temperature
                                                    }
                                                    else if (T_gb_mesh[i][j][k]
> T_dp_gb_mesh[i][j][k]) {

            m_gb_dp_mesh[i][j][k] = 0; //No condensation of gas bulk temperature is higher
than the dewpoint temperature
                                                    }

                                                    //Air
                                                    m_gb_mesh[i][j + 1][k] =
m_gb_mesh[i][j][k]; //Mass flow rate [kg/s]
                                                    x_gb_mesh[i][j + 1][k] =
(m_gb_mesh[i][j][k] * x_gb_mesh[i][j][k] - j_gb_gl_mesh[i][j][k] -
m_gb_dp_mesh[i][j][k]) / m_gb_mesh[i][j + 1][k]; //Humidity ratio [kg/kg(DA)]
                                                    H_gb_mesh[i][j + 1][k] =
(m_gb_mesh[i][j][k] * H_gb_mesh[i][j][k] - q_gb_gl_mesh[i][j][k] -
(j_gb_gl_mesh[i][j][k] + m_gb_dp_mesh[i][j][k]) * h_v_mesh[i][j][k] -
q_gb_gs_mesh[i][j][k]) / m_gb_mesh[i][j + 1][k]; //Enthalpy [kJ/kg]
                                                    T_gb_mesh[i][j + 1][k] =
air_t_hx(H_gb_mesh[i][j + 1][k] * 1000, x_gb_mesh[i][j + 1][k]); //Temperature
[deg.C]
                                                    rho_gb_mesh[i][j + 1][k] =
air_rho_tx(T_gb_mesh[i][j + 1][k], x_gb_mesh[i][j + 1][k]); //Density [kg/m^3]
                                                    lambda_gb_mesh[i][j +
1][k] = air_lambda_tx(T_gb_mesh[i][j + 1][k], x_gb_mesh[i][j + 1][k]) / 1000;
//Thermal conductivity [kW/m/K]
                                                    c_p_gb_mesh[i][j + 1][k] =
air_cp_tx(T_gb_mesh[i][j + 1][k], x_gb_mesh[i][j + 1][k]); //Specific heat [J/kg/K]
                                                    TD_gb_mesh[i][j + 1][k] =
air_alpha_tx(T_gb_mesh[i][j + 1][k], x_gb_mesh[i][j + 1][k]); //Thermal diffusivity
[m^2/s]
                                                    D_gb_mesh[i][j + 1][k] =
air_D_t(T_gb_mesh[i][j + 1][k]); //Mass diffusivity [m^2/s]
                                                    myu_gb_mesh[i][j + 1][k] =
air_myu_tx(T_gb_mesh[i][j + 1][k], x_gb_mesh[i][j + 1][k]); //Dynamic viscosity [Pa-
s]
                                                    Pr_gb_mesh[i][j + 1][k] =
air_Pr_t(T_gb_mesh[i][j + 1][k], x_gb_mesh[i][j + 1][k]); //Prandtl number
```

```
                                                    T_dp_gb_mesh[i][j + 1][k] = air_td_x(x_gb_mesh[i][j + 1][k]); //Dewpoint temperature [deg.C]

                                                    //Liquid bulk
                                                    m_lb_mesh[i + 1][j][k] = m_lb_mesh[i][j][k] + j_gb_gl_mesh[i][j][k] + m_gb_dp_mesh[i][j][k]; //Mass flow rate [kg/s], with condensation
                                                    H_lb_mesh[i + 1][j][k] = (m_lb_mesh[i][j][k] * H_lb_mesh[i][j][k] + q_gb_gl_mesh[i][j][k] + (j_gb_gl_mesh[i][j][k] + m_gb_dp_mesh[i][j][k]) * h_v_mesh[i][j][k] - q_lb_ls_mesh[i][j][k]) / m_lb_mesh[i + 1][j][k]; //With condensation
                                                    X_lb_mesh[i + 1][j][k] = (m_lb_mesh[i][j][k] * X_lb_mesh[i][j][k]) / m_lb_mesh[i + 1][j][k]; //IL mass fraction
                                                    T_lb_mesh[i + 1][j][k] = IL_t_hw(H_lb_mesh[i + 1][j][k], X_lb_mesh[i + 1][j][k] * 100); //Temperature [deg.C]
                                                    Gamma_lb_mesh[i + 1][j][k] = m_lb_mesh[i + 1][j][k] / dx; //Flowrate per unit length of the contactor [kg/m/s]
                                                    x_lb_mesh[i + 1][j][k] = IL_hr_tX(T_lb_mesh[i + 1][j][k], X_lb_mesh[i + 1][j][k] * 100); //Equilibrium humidity ratio [kg/kg]
                                                    rho_lb_mesh[i + 1][j][k] = IL_rho_tX(T_lb_mesh[i + 1][j][k], X_lb_mesh[i + 1][j][k] * 100); //Density [kg/m^3]
                                                    myu_lb_mesh[i + 1][j][k] = IL_myu_tX(T_lb_mesh[i + 1][j][k], X_lb_mesh[i + 1][j][k] * 100); //Dynamic viscosity [Pa-s]
                                                    lambda_lb_mesh[i + 1][j][k] = IL_lambda_tX(T_lb_mesh[i + 1][j][k], X_lb_mesh[i + 1][j][k] * 100) / 1000; //Thermal conductivity [kW/m/K]
                                                    delta_lb_mesh[i + 1][j][k] = pow((3 * Gamma_lb_mesh[i + 1][j][k] * myu_lb_mesh[i + 1][j][k] / pow(rho_lb_mesh[i + 1][j][k], 2) / g), 0.333333333); //Film thickness
                                                    u_l_max_mesh[i + 1][j][k] = rho_lb_mesh[i + 1][j][k] * g * pow(delta_lb_mesh[i + 1][j][k], 2) / 2 / myu_lb_mesh[i + 1][j][k]; //Maximum (gas-liquid interface) velocity [m/s]
                                                    u_l_ave_mesh[i + 1][j][k] = 2 * u_l_max_mesh[i + 1][j][k] / 3; //Average velocity [m/s]
                                                    sigma_lb_mesh[i + 1][j][k] = IL_sigma_tX(T_lb_mesh[i + 1][j][k], X_lb_mesh[i + 1][j][k] * 100); //Surface tension [N/m]
                                                    We_lb_mesh[i + 1][j][k] = sigma_lb_mesh[i + 1][j][k] / rho_lb_mesh[i + 1][j][k] / pow(u_l_ave_mesh[i + 1][j][k], 2) / delta_lb_mesh[i + 1][j][k]; //Weber number
                                                    Re_lb_mesh[i + 1][j][k] = 4 * Gamma_lb_mesh[i + 1][j][k] / myu_lb_mesh[i + 1][j][k]; //Reynolds number
```

```
                                                    Pr_lb_mesh[i + 1][j][k] =
IL_nyu_tX(T_lb_mesh[i + 1][j][k], X_lb_mesh[i + 1][j][k] * 100) /
IL_alpha_tX(T_lb_mesh[i + 1][j][k], X_lb_mesh[i + 1][j][k] * 100); //Prandtl number
                                                    D_lb_mesh[i + 1][j][k] =
IL_D_X(X_lb_mesh[i + 1][j][k] * 100); //Mass diffusivity [m^2/s]
                                                    c_p_lb_mesh[i + 1][j][k] =
IL_Cp_tX(T_lb_mesh[i + 1][j][k], X_lb_mesh[i + 1][j][k] * 100); //Specific heat
[kJ/kg/K]
                                                    TD_lb_mesh[i + 1][j][k] =
IL_alpha_tX(T_lb_mesh[i + 1][j][k], X_lb_mesh[i + 1][j][k] * 100); //Thermal
diffusivity [m^2/s]


                                                    //Cooling water
                                                    m_cw_mesh[i][j][k - 1] =
m_cw_mesh[i][j][k]; //Mass flow rate [kg/s]
                                                    H_cw_mesh[i][j][k - 1] =
(m_cw_mesh[i][j][k] * H_cw_mesh[i][j][k] - q_iw_cw_mesh[i][j][k]) /
m_cw_mesh[i][j][k - 1]; //Enthalpy [kJ/kg]
                                                    T_cw_mesh[i][j][k - 1] =
water_t_hp(H_cw_mesh[i][j][k - 1], 101.325); //Temperature [deg.C]
                                                    nyu_cw_mesh[i][j][k - 1] =
sc_nyul(101.325, T_cw_mesh[i][j][k - 1]); //Kinematic viscosity [m^2/s]
                                                    Re_cw_mesh[i][j][k - 1] =
u_cw * D_t_i / nyu_cw_mesh[i][j][k - 1]; //Reynolds number
                                                    Pr_cw_mesh[i][j][k - 1] =
sc_Prl(101.325, T_cw_mesh[i][j][k - 1]); //Prandtl number
                                                    k_cw_mesh[i][j][k - 1] =
sc_laml(101.325, T_cw_mesh[i][j][k - 1]); //Thermal conductivity [kW/m/K]
                                                }

                                                //Assign initial values for the next
control volume

                                                m_cw_mesh[i + 1][j - 1][k + 1] =
m_cw_mesh[i][j][k + 1];

                                                H_cw_mesh[i + 1][j - 1][k + 1] =
H_cw_mesh[i][j][k + 1];

                                                T_cw_mesh[i + 1][j - 1][k + 1] =
T_cw_mesh[i][j][k + 1];

                                                nyu_cw_mesh[i + 1][j - 1][k + 1] =
nyu_cw_mesh[i][j][k + 1];

                                                Re_cw_mesh[i + 1][j - 1][k + 1] =
Re_cw_mesh[i][j][k + 1];

                                                Pr_cw_mesh[i + 1][j - 1][k + 1] =
Pr_cw_mesh[i][j][k + 1];

                                                k_cw_mesh[i + 1][j - 1][k + 1] =
k_cw_mesh[i][j][k + 1];
```

```
                                        }
                                    }
                                }
                            }

                            //Outlet conditions
                            //Outlet air
                            m_og_pre = 0.0;
                            m_og_total_pre = 0.0;
                            H_og_pre = 0.0;
                            x_og_pre = 0.0;
                            T_og_pre = 0.0;
                            T_dp_og_pre = 0.0;
                            deltaP_og_pre = 0.0;
                            H_og_diff = 0.0;
                            x_og_diff = 0.0;
                            T_og_diff = 0.0;
                            T_dp_og_diff = 0.0;
                            deltaP_og_diff = 0.0;

                            for (i = 1; i < mesh_y + 1; i++) {
                                for (k = 1; k < mesh_z + 1; k++) {
                                    for (n = 1; n < pass + 1; n++) {
                                        for (j = n * 2 - 1; j < n * 2 + 1; j++) {
                                            deltaP_og_pre = deltaP_og_pre +
deltaP_gb_mesh[i][j][k];
                                        }
                                    }
                                    deltaP_gb_mesh[i][mesh_x][k] = deltaP_og_pre;
                                    deltaP_og_pre = 0.0;
                                }
                            }

                            for (i = 1; i < mesh_y + 1; i++) {
                                for (k = 1; k < mesh_z + 1; k++) {
                                    m_og_pre = m_og_pre +
m_gb_mesh[i][mesh_x][k] * 2;
                                }
                            }
                            m_og_total_pre = m_og_pre;

                            for (i = 1; i < mesh_y + 1; i++) {
                                for (k = 1; k < mesh_z + 1; k++) {
                                    x_og_pre = x_og_pre +
m_gb_mesh[i][mesh_x][k] * x_gb_mesh[i][mesh_x][k] * 2;
```

```
                                        H_og_pre = H_og_pre +
m_gb_mesh[i][mesh_x][k] * H_gb_mesh[i][mesh_x][k] * 2;
                                        deltaP_og_pre = deltaP_og_pre +
deltaP_gb_mesh[i][mesh_x][k];
                                }
                        }

                        x_og_pre = x_og_pre / m_og_total_pre;
                        H_og_pre = H_og_pre / m_og_total_pre;
                        deltaP_og_pre = deltaP_og_pre / mesh_y / mesh_z;
                        T_og_pre = air_t_hx(H_og_pre * 1000, x_og_pre);
                        T_dp_og_pre = air_td_x(x_og_pre);
                        H_og_diff = H_og_exp - H_og_pre;
                        x_og_diff = x_og_exp - x_og_pre;
                        T_og_diff = T_og_exp - T_og_pre;
                        T_dp_og_diff = T_dp_og_exp - T_dp_og_pre;
                        deltaP_og_diff = deltaP_og_exp - deltaP_og_pre;

                        //Screen output
                        cout << "x_og_pre: " << x_og_pre << "[kg/kg(DA)]\t";
                        cout << "T_og_pre: " << T_og_pre << "[deg. C]\t";
                        //cout << "H_og_pre: " << H_og_pre << "[kJ/kg]\n";
                        //cout << "T_dp_og_pre: " << T_dp_og_pre << "[deg. C]\n";
                        cout << "deltaP_og_pre: " << deltaP_og_pre << "[Pa]\t";
                        //cout << "x_og_diff: " << x_og_diff << "[kg/kg(DA)]\t";
                        //cout << "T_og_diff: " << T_og_diff << "[deg. C]\t";
                        //cout << "H_og_diff: " << H_og_diff << "[kJ/kg]\n";
                        //cout << "T_dp_og_diff: " << T_dp_og_diff << "[deg. C]\n";
                        //cout << "deltaP_og_diff: " << deltaP_og_diff << "[Pa]\t";

                        //Outlet solution
                        m_ol_total_pre = 0.0;
                        H_ol_pre = 0.0;
                        X_ol_pre = 0.0;
                        m_ol_pre = 0.0;
                        G_ol_pre = 0.0;
                        T_ol_pre = 0.0;
                        x_ol_pre = 0.0;
                        T_dp_ol_pre = 0.0;
                        H_ol_diff = 0.0;
                        X_ol_diff = 0.0;
                        T_ol_diff = 0.0;
                        G_ol_diff = 0.0;

                        for (n = 1; n < pass + 1; n++) {
                                for (j = n * 2 - 1; j < n * 2 + 1; j++) {
```

```
                                    for (k = 1; k < mesh_z + 1; k++) {
                                        m_ol_pre = m_ol_pre +
m_lb_mesh[mesh_y][j][k] * 2;
                                    }
                                }
                            }
                            m_ol_total_pre = m_ol_pre;
                            G_ol_pre = m_ol_total_pre / L / W;

                            for (n = 1; n < pass + 1; n++) {
                                for (j = n * 2 - 1; j < n * 2 + 1; j++) {
                                    for (k = 1; k < mesh_z + 1; k++) {
                                        H_ol_pre = H_ol_pre +
H_lb_mesh[mesh_y][j][k] * m_lb_mesh[mesh_y][j][k] * 2;
                                        X_ol_pre = X_ol_pre +
X_lb_mesh[mesh_y][j][k] * m_lb_mesh[mesh_y][j][k] * 2;
                                    }
                                }
                            }

                            H_ol_pre = H_ol_pre / m_ol_total_pre;
                            X_ol_pre = X_ol_pre / m_ol_total_pre;
                            T_ol_pre = IL_t_hw(H_ol_pre, X_ol_pre * 100);
                            x_ol_pre = IL_hr_tX(T_ol_pre, X_ol_pre * 100);
                            T_dp_ol_pre = IL_td_tw(T_ol_pre, X_ol_pre * 100);
                            H_ol_diff = H_ol_exp - H_ol_pre;
                            X_ol_diff = X_ol_exp - X_ol_pre;
                            T_ol_diff = T_ol_exp - T_ol_pre;
                            G_ol_diff = G_ol_exp - G_ol_pre;

                            //Screen output
                            //cout << "H_ol_pre: " << H_ol_pre << "[kJ/kg]\n";
                            //cout << "X_ol_pre: " << X_ol_pre * 100 << "[%]\n";
                            cout << "T_ol_pre: " << T_ol_pre << "[deg. C]\n";
                            //cout << "x_ol_pre: " << x_ol_pre << "[kg/kg]\n";
                            //cout << "T_dp_ol_pre: " << T_dp_ol_pre << "[deg. C]\n";
                            //cout << "G_ol_pre: " << G_ol_pre << "[kg/m^2/s]\n";
                            //cout << "H_ol_diff: " << H_ol_diff << "[kJ/kg]\n";
                            //cout << "X_ol_diff: " << X_ol_diff * 100 << "[%]\n";
                            //cout << "T_ol_diff: " << T_ol_diff << "[deg. C]\n";
                            //cout << "G_ol_diff: " << G_ol_diff << "[kg/m^2/s]\n";

                            //Wetting ratio
                            wr_gl_ave = 0.0;
                            Re_lb_ave = 0.0;
                            for (i = 1; i < mesh_y + 1; i++) {
```

```
                    for (j = 1; j < mesh_x + 1; j++) {
                        for (k = 1; k < mesh_z + 1; k++) {
                            wr_gl_ave = wr_gl_ave +
wr_gl_mesh[i][j][k];
                            Re_lb_ave = Re_lb_ave +
Re_lb_mesh[i][j][k];
                        }
                    }
                }
                wr_gl_ave = wr_gl_ave / (mesh_y * mesh_x * mesh_z);
                Re_lb_ave = Re_lb_ave / (mesh_y * mesh_x * mesh_z);

                //Outlet cooling water
                m_ocw_pre = 0.0;
                m_ocw_total_pre = 0.0;
                H_ocw_pre = 0.0;
                T_ocw_ave_pre = 0;
                m_icw_pre = 0.0;
                m_icw_total_pre = 0.0;
                H_icw_pre = 0.0;
                T_icw_ave_pre = 0;
                T_icw_diff = 0;

                for (n = 1; n < pass + 1; n++) {
                    for (j = n * 2 - 1; j < n * 2; j++) {
                        m_ocw_pre = m_ocw_pre + m_cw_mesh[1][j][1];
                        H_ocw_pre = H_ocw_pre + H_cw_mesh[1][j][1]
* m_cw_mesh[1][j][1];
                    }
                }
                m_ocw_total_pre = m_ocw_pre;
                H_ocw_pre = H_ocw_pre / m_ocw_total_pre;
                T_ocw_ave_pre = water_t_hp(H_ocw_pre, 101.325);

                //Inlet cooling water
                for (n = 1; n < pass + 1; n++) {
                    for (j = n * 2; j < n * 2 + 1; j++) {
                        m_icw_pre = m_icw_pre +
m_cw_mesh[mesh_y][j][1];
                        H_icw_pre = H_icw_pre +
H_cw_mesh[mesh_y][j][1] * m_cw_mesh[mesh_y][j][1];
                    }
                }
                m_icw_total_pre = m_icw_pre;
                H_icw_pre = H_icw_pre / m_icw_total_pre;
                T_icw_ave_pre = water_t_hp(H_icw_pre, 101.325);
```

```
                        T_icw_diff = T_icw_exp - T_icw_ave_pre;

                        //Screen outlet
                        cout << "T_ocw_ave_pre: " << T_ocw_ave_pre << "[deg. C]\n";
                        cout << "T_icw_ave_pre: " << T_icw_ave_pre << "[deg. C]\n";
                        //cout << "T_icw_diff: " << T_icw_diff << "[deg. C]\n\n";

                        for (n = 1; n < pass + 1; n++) {
                                for (j = n * 2; j < n * 2 + 1; j++) {
                                        T_icw_conv.SetResult(n - 1,
T_cw_mesh[mesh_y][j][1], T_icw_exp);
                                }
                        }

                        num_of_iter += 1;
                        //cout << "No. of iter. = " << num_of_iter << "\n";
                }
        }

        /*if (deltaP_og_exp >= deltaP_og_pre && x_og_exp >= x_og_pre && V <=
Vo) {

                //Write results to csv file
                Results << m_ig_total_exp << "," << m_il_total_exp << "," <<
m_icw_total_exp << "," << deltaP_og_pre << "," << x_og_pre << "," << T_og_pre <<
"," << wr_gl_mesh[mesh_y][mesh_x][mesh_z] << "," << V << "," << L << "," << H <<
"," << W << "," << mesh_x << "," << mesh_y << "," << mesh_z << "\n";
        }*/
        Results << Re_gb_wet_mesh[1][1][1] << "," << Re_lb_ave << "," <<
m_ig_total_exp << "," << m_il_total_exp << "," << m_icw_total_exp << "," <<
deltaP_og_pre << "," << x_og_pre << "," << T_og_pre << "," << wr_gl_ave << "," <<
V << "," << L << "," << H << "," << W << "," << mesh_x << "," << mesh_y << "," <<
mesh_z << "\n";

        }
        }
        }


        //Record time
        end_time = clock();
        double run_time = (double)(end_time - start_time) / 1000; // [sec]
        cout << "total run time: " << run_time << "[sec]\n";
        Results << "total run time: " << run_time << "[sec]\n";

        //CMD prompt pause
```

```
        system("pause");
        return 0;
}
```

早稲田大学　博士（工学）　学位申請　研究業績書

(List of research achievements for application of doctorate (Dr. of Engineering), Waseda University)

氏 名 Richard Jayson VARELA　　印

（As of June, 2020）

種 類 別 (By Type)	題名、　発表・発行掲載誌名、　発表・発行年月、　連名者（申請者含む）(theme, journal name, date & year of publication, name of authors inc. yourself)
論文 ①	Experimental investigation of the wetting characteristics of an aqueous ionic liquid solution on an aluminum fin-tube substrate, International Journal of Refrigeration, April 2018, Richard Jayson Varela, Niccolo Giannetti, Seiichi Yamaguchi, Kiyoshi Saito, Xin-Ming Wang, Hiroshi Nakayama.
②	General correlations for the heat and mass transfer coefficients in an air-solution contactor of a liquid desiccant system and an experimental case, International Journal of Heat and Mass Transfer, May 2018, Richard Jayson Varela, Seiichi Yamaguchi, Niccolo Giannetti, Kiyoshi Saito, Masatoshi Harada, Hikoo Miyauchi.
③	Semitheoretical prediction of the wetting characteristics of aqueous ionic liquid solution on an aluminum finned-tube desiccant contactor, Journal of Fluids Engineering, December 2018, Niccolo Giannetti, Richard Jayson Varela, Hifni Ariyadi, Seiichi Yamaguchi, Kiyoshi Saito, Xin-Ming Wang, Hiroshi Nakayama.
国際発表 ④	Liquid desiccant air conditioning system as an alternative to vapor compression system, 10th International Mechanical Engineering Research Conference, January 2020, Richard Jayson Varela, Seiichi Yamaguchi, Kiyoshi Saito, Masatoshi Harada, Hikoo Miyauchi.
⑤	A practical heat and mass transfer model between air and ionic liquid solution in an internally cooled dehumidifier with partial wetting, 25th International Congress of Refrigeration, August 2019, Richard Jayson Varela, Niccolo Giannetti, Hifni Ariyadi, Seiichi Yamaguchi, Kiyoshi Saito, Xin-Ming Wang, Hiroshi Nakayama.
6	Numerical simulation of a transcritical CO_2 heat pump under intermittent operation for energy savings in vending machines, ERICAE 2017, October 2017, Richard Jayson Varela, Keisuke Ohno, Seiichi Yamaguchi, Kiyoshi Saito.
⑦	Correlations for the heat and mass transfer coefficients in a structured packed bed regenerator, International Sorption Heat Pump Conference 2017, August 2017, Richard Jayson Varela, Seiichi Yamaguchi, Niccolo Giannetti, Kiyoshi Saito, Masatoshi Harada, Hikoo Miyauchi.
⑧	Derivation and validation of dimensionless models for the heat and mass transfer coefficients of a structured packed bed dehumidifier, Second International Conference on Energy and Indoor Environment for Hot Climates, February 2017, Richard Jayson Varela, Seiichi Yamaguchi, Niccolo Giannetti, Kiyoshi Saito, Masatoshi Harada, Hikoo Miyauchi.
9	Design and simulation of a double-skin roof module for day and nighttime natural ventilation, 3rd Annual International Mechanical Engineering Research Conference, January 2013, Richard Jayson Varela, Nicanor Buenconsejo Jr.
⑩	Transfer characteristics of a fin-tube-type regenerator for liquid desiccant systems with ionic liquid, 30th International Symposium on Transport Phenomena, November 2019, Takuri Ogiwara, Richard Jayson Varela, Seiichi Yamaguchi, Kiyoshi Saito, Hiroshi Nakayama, XinMing Wang.

早稲田大学　博士（工学）　学位申請　研究業績書

(List of research achievements for application of doctorate (Dr. of Engineering), Waseda University)

種 類 別 By Type	題名、　発表・発行掲載誌名、　発表・発行年月、　連名者（申請者含む）(theme, journal name, date & year of publication, name of authors inc. yourself)
⑪	Semi-theoretical model of the wetting characteristics of aqueous ionic liquid on an aluminium finned-tube desiccant contactor, 25th International Congress of Refrigeration, August 2019, Niccolo Giannetti, Richard Jayson Varela, Hifni Ariyadi, Seiichi Yamaguchi, Kiyoshi Saito, Xin-Ming Wang, Hiroshi Nakayama.
⑫	Experimental study on a finned-tube internally cooled contactor for liquid desiccant air conditioning systems with ionic liquid, 17th International Refrigeration and Air Conditioning Conference, July 2018, Takahiro Sato, Richard Jayson Varela, Seiichi Yamaguchi, Kiyoshi Saito, Hiroshi Nakayama, Xin-Ming Wang.
発表 ⑬	Performance optimization of a packed bed liquid desiccant air conditioning system, 2016 Japan Society of Refrigeration and Air Conditioning Engineers Annual Conference, September 2016, Richard Jayson Varela, Seiichi Yamaguchi, Kiyoshi Saito, Masatoshi Harada, Hikoo Miyauchi.
⑭	Effect of gas-liquid contactor structure on the dehumidification performance of a liquid desiccant system, 26th Environmental Engineering Symposium, June 2016, Richard Jayson Varela, Seiichi Yamaguchi, Kiyoshi Saito, Masatoshi Harada, Hikoo Miyauchi.
⑮	Numerical simulation of a CO_2 heat pump for hybrid desiccant air conditioning system, 2015 Japan Society of Refrigeration and Air Conditioning Engineers Annual Conference, October 2015, Richard Jayson Varela, Keisuke Ohno, Seiichi Yamaguchi, Kiyoshi Saito.